The effect of extensional flow on shear viscosity

By:

Richard Hodgkinson

A thesis submitted in partial fulfilment of the requirements for the degree of
Doctor of Philosophy

The University of Sheffield
Faculty of Engineering
Department of Chemical and Biological Engineering

Original submission date: 28th February 2017

Corrections submission date: 23rd August 2017

I.   Disclaimer

I hereby declare that this PhD thesis is my own work and has not been submitted to a previous institution for assessment purposes. Consummate to this, the formulation of and volition to investigate the hypothesis in section 3.1 was my own, and not in any way specified or pre-empted at the start of this PhD.

As of the date indicated, this work has yet to be published in any external journals or literature.

I further declare that all sources used, including personal communications were relevant, have been appropriately acknowledged in the text and cited in the references chapter.

R. Hodgkinson   *23/8/2017*

_____   _____

Richard Hodgkinson   Date

II. Preface and acknowledgements

Many, if not the majority of PhD projects, find their own paths. New ideas are generated, and unexpected outcomes found. Looking back from where I am now, writing this thesis, this PhD was certainly no different, but perhaps a little more convoluted than most.

This PhD started out focussed on further developing an in-line rheometer already under investigation at the University Of Sheffield. It is not described in any detail in this thesis, except that it formed a prelude to investigating an alternative design in chapter 2. A broad introduction to the curios and facets of rheology is presented in chapter 1.

Two interesting outcomes came from this. For reasons discussed, the new design would have been of little use for shear rheometry, but it does hold some promise as an extensional rheometer. More importantly in terms of shear rheometry however, one of the hypothesised shortcomings of proposed design appeared to be a new proposition to the field of experimental fluid mechanics: that of extensional flow affecting shear rheology.

The hypothesised shortcoming was taken further in chapter 3. Evidence was found to support such a hypothesis in literature, and a suitable experimental technique using two-phase flow identified. A technique was required to control the structure of the two-phase flow, investigated and developed in chapter 4. Considerations, presented in chapter 5, were made addressing the key dimensions of the hyperbolic converging channel used, which, as far as could be ascertained, have never been critically assessed in literature. With the use of two-phase flow and the application of particle image velocimetry techniques, there exist only two suitable optical configurations. These are outlined and their requirements identified in chapter 6: both are studied here. Chapter 7 details the experimental setup and procedures used, as well as looking more closely at the influence of optics. Experiments are conducted in chapter 8 and specific conclusions drawn which initially support the hypothesis. The achievements made during this PhD, avenues for future work, and thoughts on future experiment improvements are summarised in chapter 9.

At the time of writing, a set of demanding extension-free "shear history recreation" experiments still need to be performed, as detailed in section 8.4. The programming parameters for the rheometer (a TA instruments DHR2) are given in table 8.6, and figure 8.28 clearly shows that the software does indeed accept the desired strain-time profile descriptions. This instrument is brand new, and property of separate research group. Unfortunately, the wrong chiller has been supplied for the Peltier stage, an issue that will not be rectified much

before the 25th of March 2017, well after submission of this thesis. Prior to this, the use of another instrument had been envisaged (an Anton Paar MCR502, also property of another external group). However it was identified by the author that in between evaluating and requiring use of this instrument a serious eccentricity issue had developed. As of the time of writing an expensive repair is under negotiation. Advanced instruments such as these are also necessary to accurately measure very low viscosities such as that of the silicone oil and certainly the glycerol-water mixture used in validation work. The viscosities are below the capabilities of older instruments available, or would of necessitated capillary rheometry methods. In such cases, mixing relationships, manufacturer data, or literature extrapolation have instead been used to date, as presented in chapter 6. When the DHR2 rheometer is finally commissioned, it is hoped to perform both the shear history tests and obtain accurate viscosity values for these low viscosity fluids.

Looking back on the PhD, it has involved consideration of surface wettability, two phase flow, and optics. It has also required several pieces of code to be written, and almost all of the experimental equipment has been both designed and built by the author, using self-taught skills on equipment accrued during the period of the PhD. This is in addition to embarking on a path through the field of extensional rheology, one few experimentalists would arguably choose to tread. I hope that the hypothesis and outcomes prove insightful to an interested individual in the future - or perhaps moreover - that some of the development work presented here fortuitously assists their own.

With regards the issues of viewing through a two-phase interface – a crucial requirement of this work – the author concludes with the comment "…if only I were an Archer fish".

R. Hodgkinson.

III.   Abstract

Shear rheology is conventionally studied under pure shearing flows, rather than more realistic mixed flows. Moving parallel surfaces and capillary rheometery are examples of the former, whilst the latter occurs whenever a flow accelerates or decelerates creating an additional component of extension, e.g. on passing through an industrial extrusion die. We postulate and gather supporting evidence that shear rheology is a function of not only shear, but both shear and extension rate, a factor with important consequences for fibre spinning and extrusion operations. The direction, as well as rate, of extensional deformation is important. A novel two-phase flow, planar extension experiment is developed and the surface coatings necessary to control the interface structure identified. Shear viscosity evolution is monitored, in-situ, under extensional flow, by optically measuring shear rates either side of a test fluid – reference fluid interface; issues due to optical refraction are critically addressed. Preliminary evidence is shown for a 1.2wt% 4×10^6MW PEO solution that parallel (+ve) extensional flow, on the order of $11.5 s^{-1}$, causes a reduction in shear viscosity, and perpendicular (-ve) causes an increase in shear viscosity, supporting the hypothesis. A framework for a comparison experiment, with the same shear history but without extension, is presented.

As part of this work, design criteria for planar hyperbolic extensional channels are critically assessed. In particular, expanding a hyperbola entrance region would maximise total Hencky strain, yet this region is almost never given rationalised consideration in literature. In this region the basis for the hyperbolic profile breaks down, and a new profiling strategy and channel form are presented, which is found to only differ significantly in this inlet region. A useful design limit of 130 degrees on channel inlet angle is identified. The new profile is compared to a hyperbolic profile through the use of CFD for wall slip flow, and a slight improvement in extension rate uniformity along the centreline found. Deviations are contrasted against assumptions made in the profiling strategy: comments are made with regards the possibility for "internal" shear to occur, and non-uniform extension rates are accordingly found to exist between streamlines in these channels despite the use of full wall slip in the simulations.

Contents

List of figures

corrective prism, and a single fluid phase

List of tables

Chapter 1.

Introduction to rheology.

Chapter 1: Introduction to rheology.

1.1   Importance of rheology

Rheology is the study of the response, or flow, of matter to an applied stress. The flow behaviour of fluids, of interest here, is widely important. It defines how much energy is required to pump a fluid in a pipe and the characteristics of engine lubricants. It defines the sensual characteristics of foodstuffs and is key to the functioning of cosmetic products such as hair gel. One-coat paints and "non-slump" adhesives rely heavily on fluid rheology. The production of synthetic fibres used in textiles, forming polymer sheets, and the moulding of plastic objects used in everyday applications is strongly linked to the rheology of the polymer melts.

The term "rheology" is normally associated with fluids. However, it applies perhaps to anything that can be made to flow. Gasses flow, and still exhibit a value of viscosity. Materials that are on appearance solid may also in be flowing, but slowly. Glass windows over many centuries flow under gravity, becoming thicker at their base. Similarly, one of the world's longest running experiments is the so called "pitch drop" experiment (The University Of Queensland, 2013). The amount of stress might also be important, gels are apparently solid, but only deform above a critical stress. Fluids can also exhibit elastic properties as elaborated shortly, another phenomenon normally associated with solids. In fact rheological tests may bear many of the same concepts to their solid materials counterparts.

To measure rheology, well defined steady flows are required. This departs from more complex flows in practical situations, and especially where complex, turbulent flow is present. Thus one could ask how useful are rheological measures in such disparate situations? Take turbulent flows as an example. Firstly, the Reynolds number, the ratio of inertial to viscous forces, tells us if a flow is likely to be turbulent. Secondly, the addition of a few parts per million of polymer to a turbulent pipe flow greatly reduces the pressure drop by subtly altering the fluid rheology. Understanding fluid rheology through well-defined flows is important as it fundamentally underpins the mechanics of these more complex scenarios - without this, we could not hope to fully understand such flows.

This chapter provides a general overview as to what rheometric responses exist to imposed strains. The aim is not to provide a full and exhaustive overview of the nuances in which each "behaviour" can act. Rather, the aim is to provide an illustration of what complex and esoteric factors might complicate the design of any new rheometric technique, should they not be realised.

1.2 Viscosity, and the dependence with shear rate

In the following, the term "simple" is used to describe a homogeneous fluid that contains only small, isotropic molecules with no noteworthy large scale molecular or particulate structure. For example, water, glycerol, are "simple" in this framework, whilst suspensions or polymers are "complex".

For the simplest of fluids, the resistance to deformation under an applied force would be described by a single, constant value – the fluid viscosity.

The viscosity (or more accurately here, the shear viscosity) is defined as the ratio between the shear force applied to a fluid element and the resulting deformation rate. This is illustrated in figure 1.1. Two flat, parallel plates with area A, spacing δy, and velocity difference δu, driven by a force F, move relative to each other, separated by a fluid. Laminar flow, infinitely large plates, and zero slip at the wall are assumed. The shear rate is defined by equation 1.1, and shear stress by equation 1.2. The viscosity, or specifically the "dynamic viscosity", is defined by equation 1.3, with SI units of Pa.s. Kinematic viscosity is defined as the dynamic viscosity divided by the fluid density. Poise (1P = 0.1Pa.s) and Stokes are also commonly used units for dynamic and kinematic viscosity, respectively.
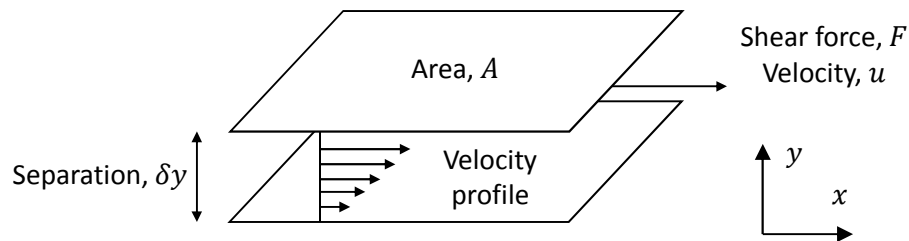
Figure 1.1: Simple shear between infinite parallel plates

$$\dot\gamma = \frac{\delta u}{\delta y} \qquad (\,1.1\,)$$

$$\sigma = \frac{F}{A} \qquad (\,1.2\,)$$

$$\mu = \frac{\sigma}{\dot\gamma} \qquad (\,1.3\,)$$

Nominal viscosity values include air at 18.2µPa.s, water at 1.0020mPa.s and glycerol at 1.408Pa.s (20°C) (NPL, 2016). These fluids feature a linear increase in shear force with shear rate, or a "Newtonian" shear behaviour. Oils are also Newtonian, providing they are free of

additives (as highlighted in section 6.3). Crude oil is in fact non-Netwonian, whilst the oils themselves are Newtonian, solid wax particles and dispersed water droplets contained within the crude serve to create non-Newtonian behaviours (Rønningsen, 2012).

Many fluids display a non-constant value of shear viscosity with respect to shear rate, and are usually referred to as "non-Newtonian". Examples of such fluids include those showing shear thinning or "pseudoplastic" behaviour (for example paints), shear thickening or "diliant" behaviours (corn starch solution) and Bingham plastic behaviours with a characteristic yield stress. These are represented in figure 1.2. The distinction between a highly shear thinning and a Bingham plastic behaviour can be debated as they are practically similar.

Note that this strict definition of "non-Newtonian" requires care. Boger fluids are a special class of fluids engineered to have a near-constant shear viscosity, but still feature viscoelastic effects. Such fluids are used to test the predictions of viscoelastic constitutive equations that do not predict a shear-dependent viscosity.
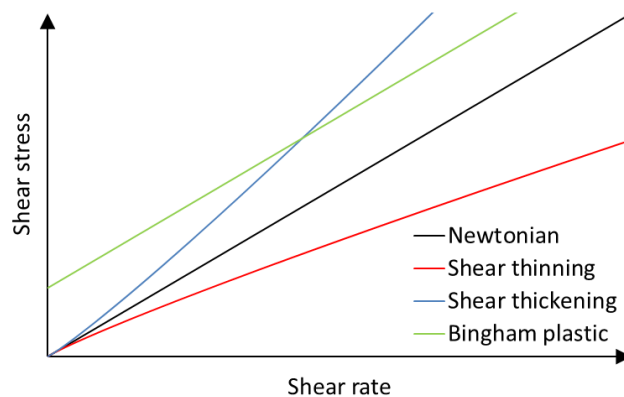
Figure 1.2: Examples of viscosity dependance with shear rate

A range of empirical equations of the form $\mu = f(\dot{\gamma})$ are used to describe shear dependent behaviour. Perhaps examples of the most common descriptions are the "power law" and "Carreau" relationships, equations 1.4 and 1.5 respectively. In the power law model, μ is the effective viscosity, k is the viscosity index, $\dot{\gamma}$ the shear rate and n the power law parameter. Setting $n = 1$ gives Newtonian behaviour, whilst $n > 1$ gives shear thickening and $n < 1$ shear thinning. The Carreau relation adds limits on the maximum and minimum values that the viscosity can asymptote to, μ_0 and μ_{inf} at zero and infinite shear rates respectively. The λ parameter is referred to as a relaxation timescale (units of time), though this is a shear rate dependent parameter here rather than a time dependent behaviour discussed next.

$$\mu(\dot{\gamma}) = k\dot{\gamma}^{n-1} \qquad\qquad (1.4)$$

$$\mu(\dot{\gamma}) = \mu_{inf} + \left(\mu_0 - \mu_{inf}\right)(1 + (\lambda\dot{\gamma})^2)^{\frac{n-1}{2}} \qquad\qquad (1.5)$$

1.3   Time dependent behaviours

The models for shear dependent fluids assumed that the shear viscosity changes instantly with a change in shear rate. However, some form of micro scale change in the fluid must be responsible for the change in viscosity (here we include changes in, and also the straining of, such structure). Such a change would take a finite time (or strain) to occur; this would thus result in time dependent rheological behaviour. Any system that features some time dependence to deformation could equally be referred to as having a sensitivity to flow history.

There are two main "groups" of terms usually attributed to describe time-dependent rheological behaviour. The first is viscoelasticity; the second is thixotropy/rheopecticity. As viscoelasticity and thixotropy are somewhat similar and occasionally used interchangeably in literature, a digression is presented in an attempt to clarify the issue. Both behaviours are thus grouped here, in that unless a sufficient period of time has been permitted after the application of deformation, the behaviour is different to that observed at steady state. Timescales may vary, but Barnes (1997) echoes the comment of structural change in the context of thixotropic systems, saying that "…they will always take a finite time to bring about the rearrangements needed in the microstructural elements that result in shear thinning".

A system features viscoelasticity when it displays the ability to both store and dissipate energy. This is typical of polymer solutions and melts, where polymer chains can be uncoiled and stretched under flow and return to coiled configurations under rest. A consequence of this is that, on the application of a change in deformation rate, the elastic component stretches (or relaxes) until an equilibrium condition is achieved. This takes time to occur, and over this time the viscosity would appear to change as a result. The Deborah number (De) defines the ratio of stress relaxation time to the time scale of observation. For De < 1, a fluid behaves in a viscous manner. For De > 1, elastic effects are dominant.

The most basic description of a viscoelasticity is that of the Maxwell model in equation 1.6, shown in terms of shearing deformations only (Bird et al., 1987). Mechanical analogies are often used to represent viscoelastic behaviour, using combinations of springs and dashpots. This is shown in figure 1.3.

$$\tau_{yx} + \frac{\mu}{G}\frac{\partial \tau_{yx}}{\partial t} = -\mu \dot{\gamma}_{yx} \qquad (1.6)$$

(From Bird et al. (1987))

Reference point   Dashpot   Spring

Shear stress

Resulting shear deformation is sum across elements
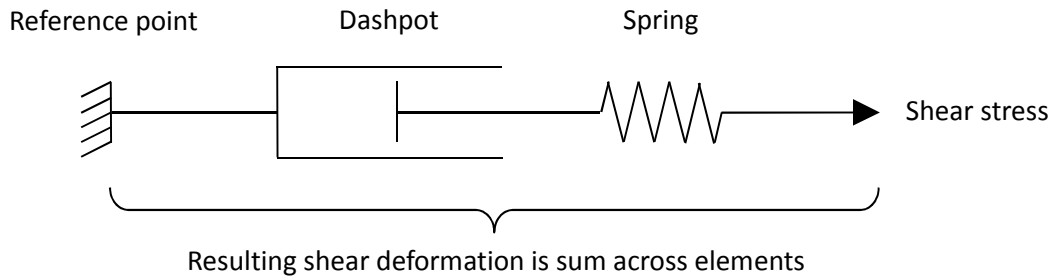
Figure 1.3: Maxwell model represented in spring and dashpot form

In equation 1.6 τ_{yx}, corresponds to the shear stress, and $\dot{\gamma}_{yx}$ the shear rate. In steady state behaviour $\frac{\partial \tau_{yx}}{\partial t} = 0$ and the fluid behaves in a Newtonian manner. This equates to the dashpot in figure 1.3, and the spring extension remains constant with respect to time.

When the shear stress changes in time, $\frac{\partial \tau_{yx}}{\partial t} \neq 0$, or the spring length in figure 1.3 is increasing. The imposed shear rate is then shared between the spring and dashpot. Figure 1.4 below shows the response of this system for a step change in shear rate, with the resulting time dependence time clearly apparent.
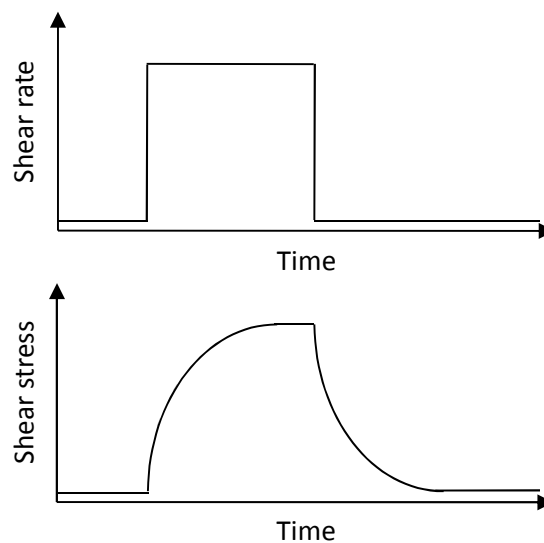
Figure 1.4: Illustration of the Maxwell model response to a step change in shear rate

As discussed in Bird et al. (1987), the Maxwell model states that at a particular time, the stresses acting on a fluid depend on the rate of strain at that time t, as well as all previous times t', with progressively reduced weighting further back in history. This is the classical origin of the term "memory fluid", though as will be elaborated shortly systems without elasticity can also demonstrate a sensitivity to history.

The series dashpot-spring system of the Maxwell model can be further modified. Two more examples are that of the Jeffreys model, and the generalised Maxwell model. The Jeffreys model adds a dashpot in parallel with the spring of the Maxwell model (Siginer, 2014) shown in figure 1.5. This parallel combination of a dashpot and spring constitutes the Kelvin-Voight model for creep. The generalised Maxwell model, shown below in figure 1.6, connects a series of n spring-dashpot chains in parallel. This model allows a spectrum of viscosities and relaxation timescales to be modelled.
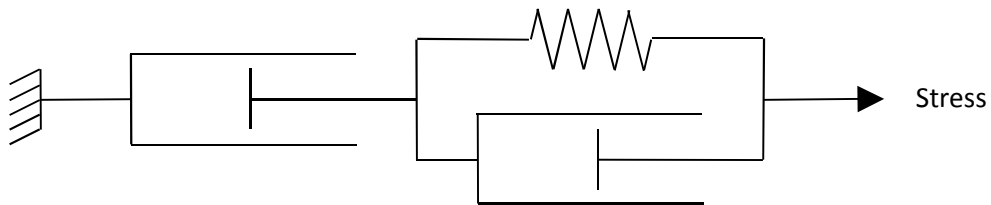
Figure 1.5: Jeffreys model represented in spring and dashpot form
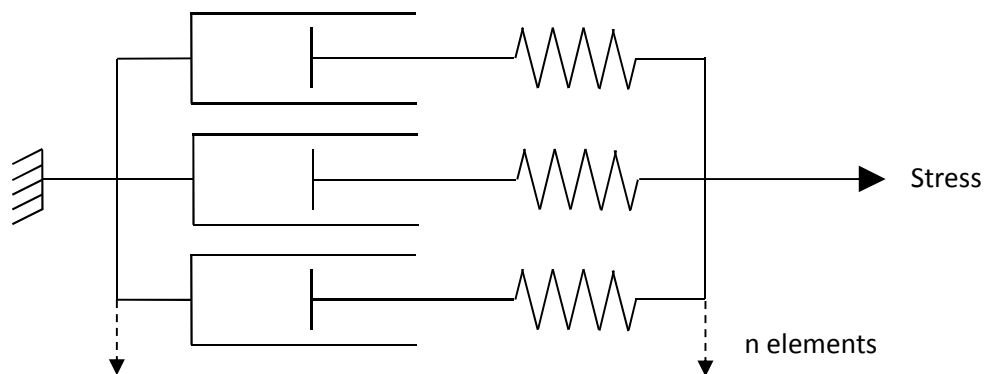
Figure 1.6: Generalised Maxwell model represented in spring and dashpot form

There are many more viscoelastic models in existence. Those described here are linear models, non-linear models also exist. However, they are all fundamentally based on the elastic characteristics described here.

Thixotropy on the other hand, is a rather more ill-defined concept. Thixotropy has its roots in history, since which subsequent discoveries have strained the original meaning. An excellent charting of issue of definition is presented in Bauer and Collins (1967) and more recently by

Barnes (1997), with reference to further issues of nomenclature (such as the exact meaning of dilatancy).

The original term of thixotropy was coined to describe gel-sol-gel transitions where, upon agitation, the gel would become liquid (reducing in viscosity). Under rest, the gel would then gradually reform over time (increasing in viscosity) in a reversible manner. Rheopecticity is a related but rarer fluid behaviour, where the shear viscosity increases with the time over which a constant rate of shear has been applied. The definitions used for thixotropy vary, from the most lax that do not include time dependent behaviour (i.e. describing simple shear thinning), to the most specific connected directly to this original reversible gel-sol-gel process and the yield stress of the gels. Whatever the definition, the general trend of usage, however, appears to be in referring to systems which undergo changes in microstructure. This is from a competition between break-down processes under flow that decrease viscosity, and build-up processes under rest that increase viscosity. The generally accepted form of this behaviour is illustrated in figure 1.7 below, with the structure break-down processes typically being faster than the rebuilding processes.
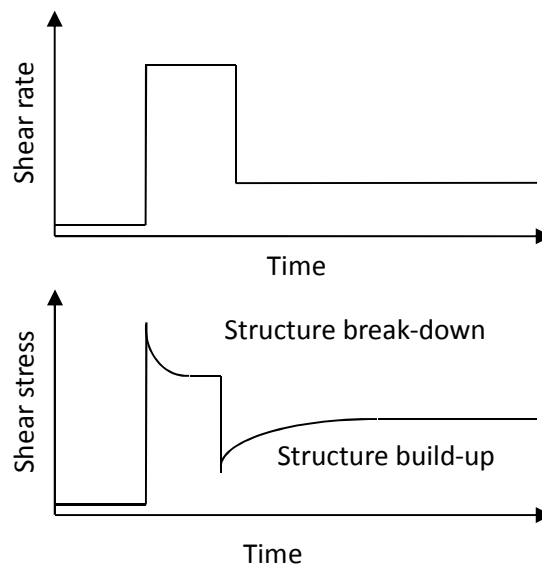
Figure 1.7: Generally accepted rheological response of thixotropy

From this, there are in effect two behaviours that produce time dependence, one elastic, and one structural. Note that whilst the idea of a memory fluid arose from viscoelasticity, and is sometimes attributed to those systems that will attempt to "spring back" to an original configuration on a release of stress; it is apparent that thixotropic systems must display "memory" of past conditions too.

There is overlap between these two behaviours which creates issues with the definition of "thixotropy". From a practical perspective, a fluid that has elastic characteristics (such as a polymer solution) will also feature interactions between the lengthy molecules, on some level structural changes will also occur under deformation. Indeed, the simplest viscoelastic models do not predict a shear thinning dependence of viscosity, which is characteristic of almost all polymer solutions. Conversely, Barnes (1997) highlights that the large scale microstructures in thixotropic gels exhibit degree of elasticity when not fully broken down, and highlights the significant difficulties of interpreting the differences from elastic and "thixotropic" effects in experiments. Indeed some of the systems tested by early investigators are commented as demonstrating elastic recoil (Bauer and Collins, 1967).

When a broad definition of thixotropy as a "shear thinning fluid exhibiting time dependence" is used (Bauer and Collins (1967) - corresponding with that proposed by the Joint Committee of Rheology) this can directly fit that of a viscoelastic, shear thinning fluid, even if it did not necessarily undergo the gradual rebuilding of structure usually inferred by thixotropy. An example is given by Barnes (1997) where thixotropy is used to cover "all time effects in a movement to non-linear behaviour" in the context of polymeric systems, even if thixotropy does not conventionally infer significant viscoelasticity. Conversely, describing a thixotropic as "viscoelastic" would be inaccurate if elastic stresses were not involved. It is easy to see why viscoelasticity and thixotropy may be used interchangeably without due care.

This "mechanistic" description seems the best way to reconcile the situation. The consequences of these elastic and structural behaviours are rather different. However the timescales of these phenomena are vastly different. Viscoelastic responses are usually rapid in the order of seconds at most, whilst structural changes may take many minutes if not hours to rebuild a microstructure at rest. Barnes (1997) also follows a similar trend, noting the timescale and mechanistic differences between viscoelasticity and thixotropy.

It is probable that this issue of nomenclature will continue to be an issue in literature. A further way of clarifying the situation is that elasticity in fluids gives rise to a number of additional phenomena which would not be present if a system simply had a time and shear dependent viscosity. These will be highlighted in the next section.

1.4 Additional behaviours in shear flows arising from viscoelasticity

In addition to time dependent behaviour, viscoelasticity adds a number of further behaviours that make it distinct from it being a solely time-sensitive rheological phenomenon.

The first and most obvious one of these is the ability of the material to store energy. If a stress is applied and removed, the material will recoil if Deborah number is sufficiently large. The classic and widely used example is that of bouncing "silly putty". A ball of the material will bounce with short timescales of applied stress (De >> 1), but with longer timescales of applied stress (i.e. left on a surface under the force of gravity) the ball will flow into a puddle (Macosko, 1994). This response is tested using oscillatory shear experiments, where the phase relationship between stress and strain is characteristic of elastic and viscous behaviours at the timescales being probed by the experiment. If a shear strain γ is applied such that it varies with time, $\gamma = \gamma_0 \cos \omega t$, the resulting stress σ follows equation 1.7 below (from Whorlow (1992)) – assuming the system is linear. Contributions are present from stresses in phase (G', elastic modulus) and 90 degrees out of phase (G'', loss modulus) with the applied strain. The ability of a viscoelastic fluid to return to an initial shape via elasticity may have given rise to the term "memory fluid", but only an elastic fluid will exhibit an elastic modulus.

$$\sigma = \gamma_0(G' \cos \omega t - G'' \sin \omega t) \qquad \text{(1.7)}$$

(From Whorlow (1992))

The accumulation of elastic tension in viscoelastic fluids gives rise to further, less expected phenomenon. A 3D fluid packet is shown in figure 1.8 on the following page is subject to simple shear under stress σ (equation 1.8). In a Newtonian system under steady shear only one force acts, that of shear stress, σ_{xy} ($\sigma_{xy} = \sigma_{yx}$). In a viscoelastic system however, the accumulation of elastic strain produces a force acting perpendicular to the surfaces of a fluid packet. Two normal stress differences (eliminating hydrostatic pressure) can be defined, $N_1 = \sigma_{xx} - \sigma_{yy}$ and $N_2 = \sigma_{yy} - \sigma_{zz}$.

In practice, N_1 is relatively straightforward to measure as it represents a force attempting to separate two sliding surfaces. N_2, on the other hand, is rather more difficult to measure. N_1 is usually positive for polymer solutions (i.e. attempting to separate the shearing surfaces in a conventional rheometer), and N_2 smaller and negative (Wang, 2013). The parameter N_1 is commonly used as a measure of elasticity, particularly so before the advent of oscillatory flow techniques.

$$\sigma = \begin{pmatrix} \sigma_{xx} & \sigma_{xy} & 0 \\ \sigma_{yx} & \sigma_{yy} & 0 \\ 0 & 0 & \sigma_{zz} \end{pmatrix} \qquad (1.8)$$
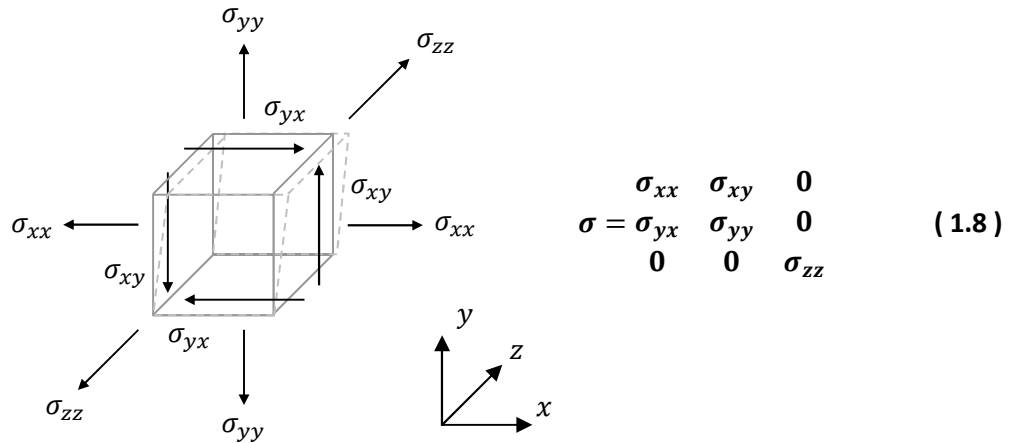
Figure 1.8: Definition of shear and normal forces acting on a fluid packet. The dashed lines indicate the shear deformation occurring. Equation 1.8 is the associated stress tensor.

These normal forces give rise to a range of related phenomena. One example is that of the "Weissenberg rod climbing" effect. If a rotating rod is inserted into a non-elastic fluid, centrifugal forces generate a surface depression in the vicinity of the rod. With an elastic fluid, the strain accumulated in the polymer chains (aligned circumferentially around the axis of rotation by shear) causes a notional force directed towards the rod. This force causes the fluid to climb the rotating rod as illustrated in figure 1.9. Bird et al. (1987) shows more rigorously that both the normal stress differences, N_1 and N_2, contribute to this effect.
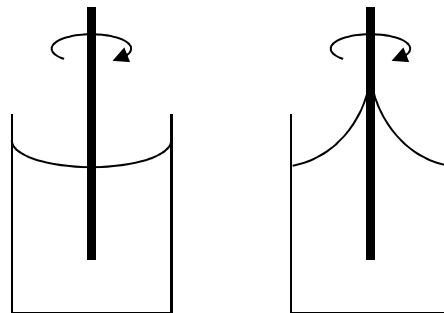
Figure 1.9: Weissenberg rod climbing effect. Left: Non-elastic fluid, right: Elastic fluid.

Aside from the behaviour in free containers, normal forces have important effects when a bounding wall is removed, allowing the elastic strains to relax. Two examples of this are die swell, and the so called "hole pressure error". Die swell, figure 1.10, occurs when a viscoelastic materials leaves an extruder die and increases in cross sectional dimensions as a result. This phenomenon is important in the extrusion of plastic products. Hole pressure error, figure 1.11, occurs when the streamlines of a viscoelastic fluid pass over a manometer port or otherwise non-flush mounted pressure transducer. This was first reported by Broadbent et al. (1968). The

11

tension in streamlines attempts to "lift" fluid out of the port and is directly related to N_1 and N_2 (Bird et al., 1987), thus resulting in a reduction in the pressure recorded. This phenomenon was not realised in early work with viscoelastic systems, and Macosko (1994) comments that it "created quite a stir" when these errors were realised. The tendency of the streamlines to avoid curvature gives rise to another related and quite unusual effect. Streamlines around particles are curved, and as a result the particles migrate into ordered lines when under flow (Bird et al., 1987). This therefore affects the rheology of particulate suspensions and could conceivably affect tracer particles too.
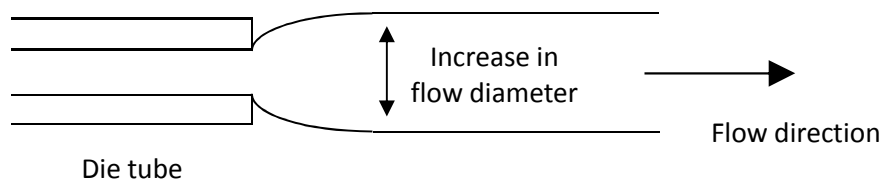
Figure 1.10: Die swell of a viscoelastic material
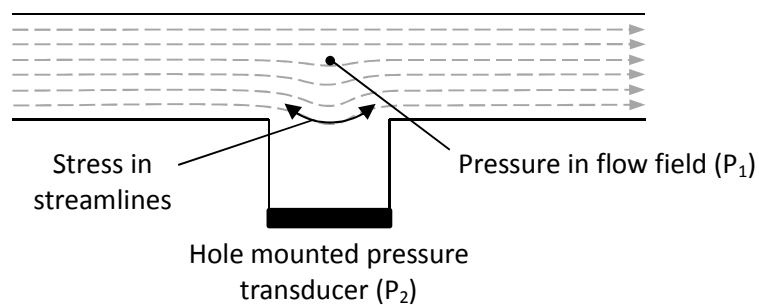
Figure 1.11: Curvature of streamlines near a hole or pressure tap giving rise to hole pressure error ($P_1 > P_2$) with viscoelastic fluids

Aside from the above examples, there are many other situations where elastic systems produce striking differences from their Newtonian counterparts. It was already mentioned in the introduction that the addition of a few ppm of polymer to a fluid dramatically reduces turbulent drag. Another example is that on a contraction/expansion, vortices occur upstream of a contraction, whilst with a Newtonian fluid vortices occur downstream of the expansion. Both of these examples feature an additional component of extensional as well as shear flow. Extensional flows will be described next.

1.5 Extensional flow

There are two forms of deformation: Simple shear already described, and that of extension (or "elongation" – the terms being used interchangeably here). Shear describes forces and motions applied and directed parallel to surfaces of a fluid particle respectfully, whilst extension

describes those normal to it. The normal force definitions are identical to those in the previous sections. To satisfy conservation of volume, extension of a fluid packet in one or more directions requires a reduction in size of other dimensions. Depending on the geometry, extensional flows may be described as planar, uniaxial extension, or uniaxial compression (figure 1.12).
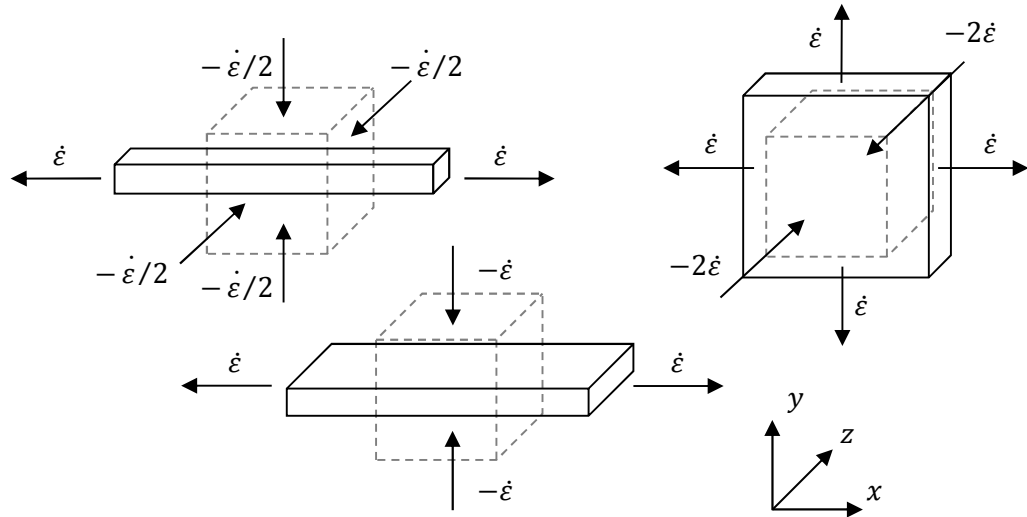
Figure 1.12: Principle forms of extensional flows, $\dot{\varepsilon}$ denotes elongation rate.

Top left: Uniaxial, top right: Biaxial, bottom: Planar. Stresses are defined as in figure 1.8.

As shown for figure 1.12 here, $\sigma_e = \sigma_{xx} - \sigma_{yy}$ corresponds to the uniaxial and planar extensional normal stress differences, and $\sigma_e = \sigma_{xx} - \sigma_{zz}$ for biaxial. Infinitesimal strain (Or "Cauchy strain") ε_{inf} is the relative increase in length of a fluid packet compared to its original length (equation 1.9). For a finite change in length, Hencky strain is used, defined as the integration of a series of infinitesimal strains (equation 1.10). Hencky strain is used when quantifying the total stretch applied to a fibre or flow field. Strain rate, $\dot{\varepsilon}$, is simply the rate of change of strain with respect to time (equation 1.11). Extensional viscosity, η_e, is defined similarly to shear viscosity as the ratio of the normal force difference σ_e acting on a fluid element to the strain rate (equation 1.12).

A parameter known as the "Trouton ratio" is defined as the ratio of shear to extensional viscosity (equation 1.13). This ratio takes a constant value for a particular flow field for Newtonian fluids under all situations. Trouton (Trouton, 1906) showed the extensional viscosity of pitch to be 3 times that of the shear viscosity under uniaxial extensional flow, as predicted by theory. However, for complex fluids as the deformation rate is increased from very low values, this value begins to deviate. For polymers (or polymer solutions), extensional viscosities can often be orders of magnitude higher than the shear viscosity, and often show tension

thickening whilst the fluid is shear thinning in character. Table 1.1 summarises the velocities in each type of extensional flow, the Trouton ratios for Newtonian fluids, and the complementary shear rate used for a particular test elongation rate (summarised from Brujan (2011)). More information on the origin of these quantities is noted in chapter 3.

$$\varepsilon_{inf} = \frac{\delta l}{l} \qquad \textbf{(1.9)} \qquad\qquad \eta_e = \frac{\sigma_e}{\dot{\varepsilon}} \qquad \textbf{(1.12)}$$

$$\varepsilon_{hencky} = \int_L^l \frac{\delta l}{l} = \ln\left(\frac{l}{L}\right) \qquad \textbf{(1.10)} \qquad\qquad T_r = \frac{\mu}{\eta_e} \qquad \textbf{(1.13)}$$

$$\dot{\varepsilon} = \delta\varepsilon/\delta t \qquad \textbf{(1.11)}$$

	Uniaxial	Biaxial	Planar
u_x	$\dot{\varepsilon}$	$\dot{\varepsilon}$	$\dot{\varepsilon}$
u_y	$-\dot{\varepsilon}/2$	$\dot{\varepsilon}$	$-\dot{\varepsilon}$
u_z	$-\dot{\varepsilon}/2$	$-2\dot{\varepsilon}$	0
Shear rate for T_r	$\sqrt{3}\dot{\varepsilon}$	$\sqrt{12}\dot{\varepsilon}$	$2\dot{\varepsilon}$
T_r(Newtonian)	3	6	4

Table 1.1: Summary of extensional flow fields, shear rates for evaluating the Trouton ratio, and Trouton ratios for Newtonian fluids. Summarised from information in Brujan (2011).

Extensional flows are generated in any operation where a fluid packet is compressed in one direction, or otherwise physically drawn out in another orthogonal direction. This is crucial fibre spinning, blow moulding, and extrusion. The anomalously high extensional viscosity of polymers defines the ability of a fibre to be spun, or the very high pressure drops encountered in extrusion operations. A practical example of the effects of extensional viscosity is the "tubeless siphon" where a continuous column of fluid is drawn up from a free surface (see, for example, the historical review of Petrie (2006b). A classification is also commonly used where extensional flows are classed as "strong" flows, in that they have the ready ability to uncoil and stretch polymer chains. In comparison shear flows are classed as "weak" flows.

In the following section, a few examples will be given of techniques applied for the measurement of extensional viscosity (as well as shear viscosity). Key factors complicates extensional viscosity measurement. The rigorous definition requires that a steady pure extensional flow is imposed, and the stress allowed to reach steady state at $t = \infty$. Unlike shear flows however, it is impossible (with one specialised exception) to obtain steady state extensional flow. A fibre either snaps or pressure drops become excessive before this is achieved. This means that measured extensional viscosities are transient. Furthermore, they

are a function of the whole deformation history, which is difficult to control during a single experiment and not necessarily comparable between different experiments. Secondly, producing pure extensional flows without shear is difficult, and some flows may have mixed kinematics (shear and extension). Bird et al. (1977), p187 summarises that "Measuring $\bar{\eta}$ has proven to be an extremely difficult task".

Despite the importance of extensional viscosity in many industries, the complications and dangers caused by this "transient" extensional viscosity, and interpretation of the results from different experiments and flow types, are well attested to by Petrie (2006a). The example given of the (in)famous "M1 Muddle" (James and Walters, 1993) where a standardised test fluid was tested in different laboratories on different experiments, exemplifies the current situation. This is reproduced in figure 1.13 below. For the same extension rates, extensional viscosities varied by 100 – 1000 times between methodologies. Even though (and partly due to) extensional viscosity being so difficult to measure, there exists a prevalent use of technical standardised "metrics" in industry to assess extensional characteristics (such as melt flow index, or MFI described shortly). Such measurements are highly complex mixed flows and poorly relate to rheological quantities, but as many real world flows are both transient and mixed in nature they are nonetheless useful, arguably more so sometimes than a true measurement of extensional viscosity.
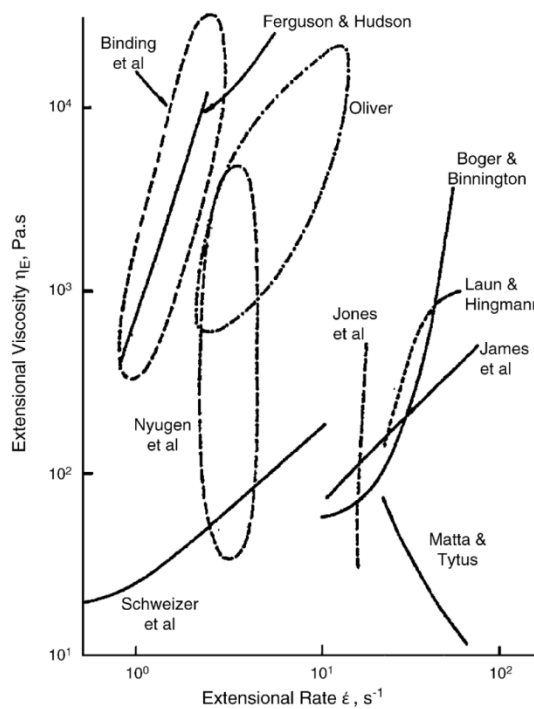
Figure 1.13: M1 Muddle plot

(reproduced from Petrie (2006a), after James and Walters (1993))

15

1.6   Indirect influences on rheology

There are a few "indirect" routes which may affect the rheometry of test fluids during experiments that should be noted. The effects can be (very broadly) grouped into those that are "reversible", and those that are "irreversible", the latter corresponding to some form of sample degradation or damage. These are intended as examples, and the list is non-exhaustive.

The first example of reversible phenomena is that caused by viscous dissipation. Shearing dissipates heat, and whilst Newtonian fluids are not sensitive to shear, their viscosity is sensitive to temperature changes (like almost all fluids). An uncontrolled temperature rise of a sample can directly appear as a viscosity decrease. This can be seen if glycerol is sheared in a rheometer at a high rate for an extended period of time. The Nahme number (Na) for a particular geometry describes the significance of shear heating effects.

Apart from the presence of walls necessary to generate shear, they may also result in a phenomenon called wall slip. In some test systems such as particle suspensions, particles may migrate away from the bounding walls under shear. This results in a thin low viscosity layer next to the walls and an apparent "slip" of the test fluid against these surfaces.

Further phenomena may occur by virtue of the fluid rheology itself. Two examples arise from thixotropy and multi-valued stress strain relationships. It was previously stated that the rebuilding timescales for thixotropic liquids can be long. This means that sample loading and handling may affect the measured rheology. A multivalued rheometric profile in terms of shear rate at certain values of shear stress creates a phenomenon called "shear banding", something that has only been observed in recent years with the development of suitable imaging techniques (see, for example Mair and Callaghan (1996)). Shear banding is in contrast to the geometrical assumption of a homogeneous shear field across the geometry of a conventional rheometer, complicating the results of such measurements.

In terms of sample degradation, the work of James and Saringer (James and Saringer, 1980, James and Saringer, 1982) considered a range of issues that highlight the importance of sample stability. Their work involved PEO (polyethylene oxide) solutions – Unlike studying natural gums such as Xanthan and Guar that are occasionally used in literature, degradation might not be anticipated for stored PEO solutions. Despite this, they found that their master solutions had a tendency to slowly age over about a month. Furthermore, they also found apparent degradation in the presence of high extension rates, i.e. through chain breakage. This mirrors precautionary principles of other groups in the use of fresh samples in the course of such

experiments. Their work was conducted at ambient temperatures, when high temperatures are used (such as with polymer melts) thermal degradation of samples with time also becomes a problem.

More unusually, they also report finding the presence of long fibres (mm in length) of apparently undissolved PEO in their experiments, as well as irregular networks of PEO in electron microscopy samples. Initially this was attributed to strain induced crystallisation (another phenomenon that would irreversibly affect a test fluid rheology) but was later thought to be due to the gentle sample preparation method. Solutions for light scattering experiments were thoroughly mixed and filtered, which they hypothesise would have broken up these networks; in agreement with the change in results in their experiments when the samples were subject to intense shearing. This indicates that the exact preparation method of samples, and particularly filtering operations, have an important consequence on the resulting sample rheology.

1.7   Standard techniques for shear rheology measurement

In order to measure the shear rheology of a fluid, it is necessary to apply some form of force to cause the fluid to flow. Conventionally, this is achieved by mechanically moving one surface relative to another (a drag flow), or by an externally imposed pressure drop between static surfaces (a pressure driven flow). Combinations of these two approaches are possible, as well as the use of other driving forces (i.e. gravitational and electro kinetic flows), however these are outside of the scope of this introduction. We also note that historically some consideration was given to whether experiments should be "stress" or "strain" controlled where a surface is mechanically moved. This was more relevant before the advent of modern control systems in which either condition can easily be achieved. All the techniques listed here assume that steady laminar isothermal flow is produced: i.e. non-time dependant, free of secondary motion and at a homogeneous temperature, notwithstanding complications from edge/end effects etc.

Parallel plate rheometers do exist (in accordance with figure 1.1 shown earlier) that operate with a linear sliding motion. However as the shearing duration is necessarily limited, rotational geometries are more often used. Three standard "formats" exist: the cone and plate geometry (figure 1.14), the parallel plate geometry (figure 1.15) and variations of concentric cylinder (or "Couette") geometry (figure 1.16). These are illustrated on the following page.
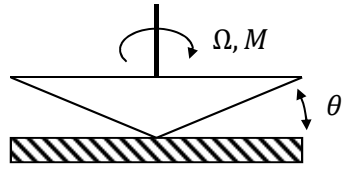
Figure 1.14: Cone and plate rheometer   **Figure 1.15: Parallel plate rheometer**
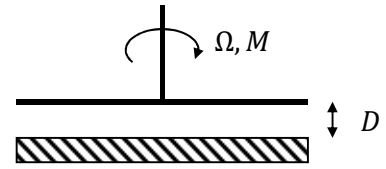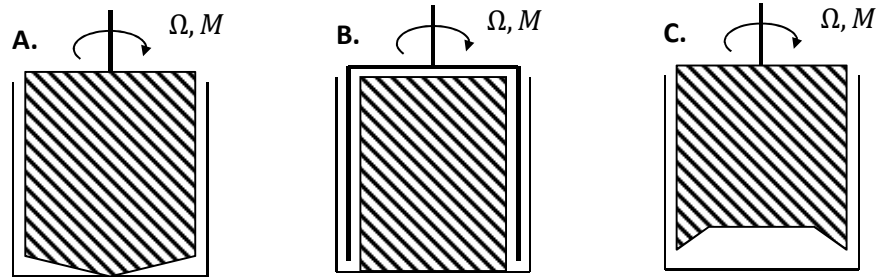
Figure 1.16: Variations of the concentric cylinder rheometer

The cone and plate geometry (figure 1.14) features an upper cone which is rotated at an angular velocity Ω whilst the lower plate is held stationary, and the torque, M is measured via some suitable means. Whilst the velocity difference between the surface of the cone and the lower plate varies linearly with respect to radius, so does the shear gap by virtue of the cone angle θ, thereby producing a constant rate of shear across the sample radius. Cone angles are usually on the order of a few degrees, and often truncated at the tip for the last few hundred microns or so to avoid "jamming" of particles in the extremely small gap.

Figure 1.15 shows a similar rotating parallel plate geometry with the places separated by a distance D. Due to the use of parallel plates, the shear rate now varies linearly from zero at the centre to a maximum at the plate edge. If multiple data points are taken at different angular velocities however, equation 1.14 (derived in Macosko (1994)) can be used to provide true shear rate – shear stress data, where R is the radius of the disks, M is the measured torque at a data point, and $\dot{\gamma}_R$ is the shear rate at radius R (at the edge of the disks).

$$\tau_{12}(R) = \frac{M}{2\pi R^3}\left[3 + \frac{d\ln M}{d\ln\dot{\gamma}_R}\right] \qquad (\textbf{1.14})$$

A rough insight into how this correction functions can be gained by noting that at a single rotation rate, the torque contribution comes from shear rates at locations between $r = 0$ and $r = R$, which is of little use for accurate work. However, on an increase in rotation rate a new higher band of shear is introduced at the disk edges. The torque contribution from shear rates less than this is effectively known from the previous data point. The requirement of a suitable

derivative term is thus evident in equation 1.14. Whilst this additional analysis is required for parallel plate geometries, there are a number of advantages over the cone and plate geometry. The flat plates permit easier loading for solid samples. The ability to vary the gap permits a wider range of shear rates, the ability to delay edge failure, and the ability to correct for wall slip (Macosko, 1994).

Due to the geometries used, both the cone & plate and parallel plate geometries permit ready measurement of normal stress data by the force attempting to separate the shearing surfaces. For the cone and plate geometry, this directly relates to N_1. For the parallel plate geometry, $N_1 - N_2$ can be determined. Through using a combination of the two techniques, N_2 can be found (Macosko, 1994).

Figure 1.16 shows three "variations" of concentric cylinder geometry. Generally the inner cylinder is rotated whilst the outer walls are held fixed. Shearing principally occurs in the gap between the rotating cylinder and the static walls. A narrow gap in relation to the cylinder radius is necessary if a constant shear rates across the gap is assumed (relations are available for determining true shear rates, similar to those for the parallel disks).

The principle aim of these differing geometries is to minimise end effects. Geometry A achieves this by incorporating a cone and plate geometry on the end of the cylinder. Geometry B achieves this by minimising the end surface of the cylinder. Geometry C uses a trapped pocket of air in the cylinder end, thus almost eliminating shear in this location. Different advantages and disadvantages exist between these geometries. For example, geometry A is relatively simple to manufacture and fill, however precision gap setting is required due to the cone and plate geometry. Geometry B does not require precision height setting and is particularly useful for low viscosity fluids. However, the geometry is more difficult to manufacture and fill, and the rotating cylinder must be thin not only to reduce end effects, but also to enable the same shear rates on the inner and outer walls to be assumed. Compared to the cone and plate / parallel plate geometries, the concentric cylinder geometry does not permit ready measurement of normal stresses.

All three techniques suffer or are affected to varying degrees by sample evaporation, inertia, mechanical symmetry / eccentricity, and the potential presence of secondary flows. Sample evaporation can create high viscosity layers or crusts on samples, one mitigating method is to use an atmosphere saturated with solvent vapour. Mechanical symmetry and eccentricity (or bearing runout) is particularly important, especially when shallow cone angles or narrow gaps

are employed. All three techniques, but especially the cone and plate and parallel plate techniques, are sensitive to the shape of the sample edge. Sample loss may also occur (with low viscosity samples at high shear rates) and edge failure (a common issue with high viscosity samples). Wall slip is also a ubiquitous problem, and techniques have been developed for the different approaches to detect and compensate for this.

Modern commercial rotational rheometers designed around these three geometries have progressed into quite advanced instruments. Aside from featuring interchangeable geometry types, the gaps required by these geometries can be automatically set on many systems by utilising the normal force measurements. Sample temperature control is virtually ubiquitous, and precision air bearings and motor designs have been developed to allow near frictionless, high accuracy, low inertia drives which permit oscillatory as well as steady shear tests. Software packages permit automatic corrections for remaining inertia, and allow high accuracy feedback control of the instrument.

We now turn our attention to the other standard technique for rheometry, that of pressure driven flow, usually in the form of "capillary" rheometry. Flow is pumped at a known flow rate Q through a precision narrow bore tube (sometimes slits are also used) of length L and radius R. The flow is driven by a known pressure P, either from a driving piston, pressurised gas applied to a holding reservoir, or gravity. The flow is allowed to exit the capillary into atmospheric pressure. This is shown in figure 1.17 below. As the flow is now pressure driven, an additional assumption that the fluid is incompressible and pressure does not affect viscosity has to be made, compared to drag flow techniques.
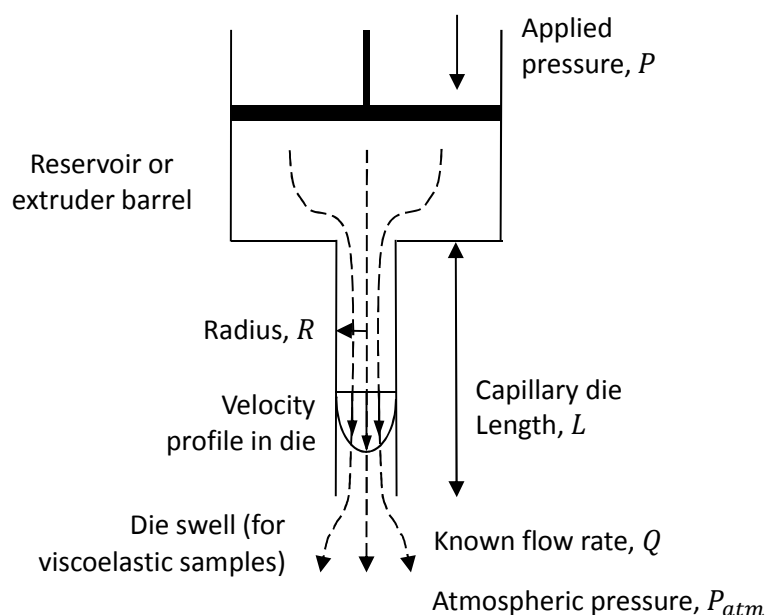
Figure 1.17: Capillary rheometer

20

Under fully developed flow conditions, the pressure drop along the capillary, p_c, increases linearly with length and corresponds directly to the wall shear stress, τ_w, as per equation 1.15 (Macosko (1994).

$$\tau_w = \frac{R}{2} \frac{p_c}{L}$$

(1.15)

Any form of laminar pipe flow, however, features a velocity distribution across the diameter of the pipe, as illustrated in figure 1.17, from (usually) zero at the walls to a maximum in the centre. For a Newtonian fluid, the velocity profile is parabolic. As a result, the shear rate is not constant across the capillary radius, and furthermore, the shape of the velocity profile itself is a direct function of the rheology of the fluid under test, so a velocity profile cannot be assumed a priori.

There are three main corrections that are used in association with capillary rheometry: the Bagley correction (or plots), the Mooney correction, and the Weissenberg-Rabinowitsch correction. Useful examples of applying these three corrections are given in lecture materials such as Morrison (2014). The latter deals with the non-uniform shear rates across the capillary diameter.

In order to perform meaningful rheological measurements, the pressure drop across a capillary featuring fully developed flow is required (p_c in equation 1.15). However, the pressure drop between that applied in the reservoir or by the extruder ram and atmospheric pressure at the capillary end are a combination of factors. This includes mechanical resistance of rams, extensional entrance flows between the reservoir and the capillary, flow development in the capillary, and any effects resulting from the flow leaving the capillary into ambient conditions. Bagley plots are used to determine p_c, by evaluating at least two capillaries of the same radius but different lengths, for each of the flow rates used. Plotting the recorded pressure drop against capillary length L and extrapolating back to the Y axis allows the additional pressure loses to be determined, and thus p_c, by their subtraction. This correction applies at only one flow rate. An alternative method to achieve this is to use two pressure transducers situated across a section of capillary with fully developed flow. This is the usual approach for in-line techniques introduced in chapter 2. Whilst they are subject to the issues of hole pressure error previously noted in section 1.4 for viscoelastic fluids, if the mountings are identical using the pressure drop between the sensors eliminates this issue.

The Mooney correction accounts for wall slip. For a thin slip layer next to the capillary wall, and a constant applied wall shear stress, a characteristic "slip velocity" results which reduces the velocity gradient near the walls, and thus reduces the apparent viscosity. If the diameter of the capillary is increased with constant wall shear stress, this slip velocity remains the same, but becomes a progressively smaller fraction of the velocity magnitude in the capillary. For an infinite diameter capillary, the significance of wall slip vanishes. The Mooney correction uses different radius capillaries (usually with the same L/R ratio), and extrapolates to a capillary of infinite size on a plot of apparent wall shear rate against inverse radius at constant wall shear stress.

The Weissenberg-Rabinowitsch correction allows the true wall shear rate to be determined at a particular value of wall shear stress (equation 1.16, derived in Macosko (1994)). The correction functions in much a similar manner to the correction previously described for the parallel plate geometry. Whilst at a single data point (of flow rate) a range of shear rates are present, collecting a set of data of Q against p_c allows the derivative in equation 1.16 to be evaluated and the true wall shear rate to be found.

$$\dot{\gamma}_w = \frac{1}{4}\dot{\gamma}_{aw}\left[3 + \frac{d\ln Q}{d\ln p_c}\right] \quad \text{where} \quad \dot{\gamma}_{aw} = \frac{4Q}{\pi R^3} \qquad \text{(1.16)}$$

The swell of a sample on leaving the capillary, as shown in figure 1.17, can be used to give an approximate indication of viscoelastic normal forces.

A greatly simplified version of capillary rheometry is used for characterising the properties of polymer melts is that of MFI (or melt flow index) previously mentioned. Standardised test procedures are used across industry. A sample is heated in a barrel to a defined temperature. This sample is then forced through a pre-described capillary die by a piston, of specified diameter, driven by a load mass. After 10 minutes, the mass of sample extruded through the die in grams is used as the MFI index (ASTM International, 2013). Whilst difficult to relate to fundamental rheological properties and a combination of both shear and extensional flows, the MFI is a useful index for process control.

Despite the potential requirement for a number of corrections, capillary rheometry uses a simple experiment which avoids many of the issues associated with the free surfaces in standard rotational approaches. The major disadvantage with capillary rheometry however is that the flow field is non-homogeneous (particles experience different shear rates for different

periods of time as they transit the capillary) and as a result time dependency cannot be analysed. This is exemplified somewhat in the Bagley plots of Laun and Hirsch (1989), where thixotropy caused an apparent reduction in viscosity as the capillary length was increased.

1.8   Techniques for extensional rheology measurement

Due to the difficulties previously described in extensional rheology measurement, no universally accepted techniques are apparent for it, and a significant number of different approaches have been attempted in literature. Different techniques are attributable broadly to the state and viscosity of the sample. For samples such as rubbers and polymer melts that can be gripped and are self-suspending under their own weight, experiments more akin to those for solid samples have been used (e.g. the Sentmanat Extensional Rheometer (Xpansion Instruments, 2014)). As extensional techniques with fluid samples are considered later in this thesis and the issues between techniques are quite disparate, a brief outline of experimental approaches used to generate such extensional flows is presented here.

The first set of techniques rely on the samples having sufficiently high extensional viscosities that they can form stable filaments or threads when drawn out in free conditions, even if only for a transient period. This mitigates the issues of wall shear from bounding walls, but generally introduces other problems. The first example is that of "fibre spinning" experiments, shown in figure 1.18 on the following page. A thread is drawn out between a nozzle and a take up roller, and the force required to perform this (usually the force acting on the nozzle) is measured. The extension rate is evaluated optically via imaging the fibre profile and knowing the flow rate. This technique was used in the SLR (Spin Line Rheometer), a now discontinued instrument, however a description is given in Jones et al. (1987). The same arrangement can also be achieved by drawing a fibre up from a free surface into a nozzle, akin to the tubeless siphon effect. Rather than continuously spinning a fibre, a second approach to producing fibres is to take a sample held between two parallel plates, and rapidly move the plates apart, forming a "bridge" between them. This technique is used in the CaBER (Thermo Fisher Scientific, 2015) and similar FiSER (Cambridge Polymer Group, 2016) commercial instruments (summarised in figure 1.19). In both instruments, the force on the endplate is measured and the midpoint diameter of the filament is recorded by a laser micrometer, providing measures (subject to suitable corrections) of extensional stress and strain rate. The difference between the two techniques is that in the CaBER instrument, a step strain is applied between the plates and the rate of extension is uncontrolled, dictated by hydrodynamic and capillary forces. In the FiSER instrument, the rate of separation of the end places is controlled in order to produce a more constant rate of extension.

Whether the fibre is continuously spun, or transiently stretched, these techniques are limited as beyond some critical level of strain, the fibre will snap. As fluid viscosity is further decreased, these forms of experiments become less and less useful, and the fluid must be contained or supported in some manner.
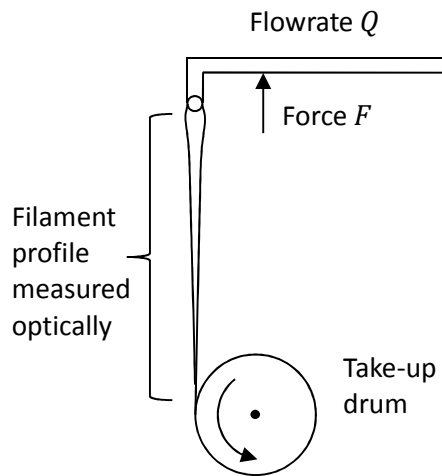
Figure 1.18: Fibre spinning experiment fundamentals
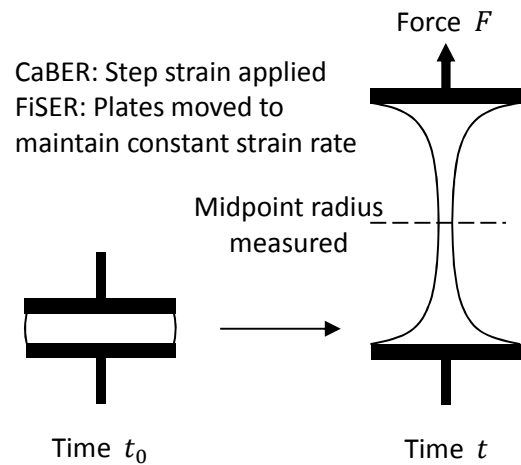
Figure 1.19: CaBER / FiSER experiment fundamentals

The main route by which this is achieved is by arranging the bounding channel walls to produce an extensional flow. The simplest form of this is to use an abrupt contraction (or entrance flow) from a larger to smaller diameter channel, which is normally accompanied by recirculating vortices in the upstream region which control the extension rate (figure 1.20 A). This can be improved by the use of a suitably profiled contraction, which permits better control of the extension rate (figure 1.20 B). Extending this further, a profiled contraction is, broadly speaking, one half of a stagnation flow (figure 1.20 C) (though important differences do exist, briefly noted in chapter 5). All these flows feature shear as well as extension, and a variety of approaches and approximations have been applied for determining extensional viscosity from them in literature. The stagnation flow is a particularly interesting class of flows produced when two symmetric and coaxial streams impinge. Right at the stagnation point located between the two streams the flow is shear free and extension can be maintained for high total strains; however this location can only be accessed by optical measurements. Rather than using a profiled channel to produce stagnation flow, such flows are usually produced in square "cross slot" geometries. Other methods of producing these stagnation flows include the "four roll mill" where four rotating cylinders replace the bounding walls, as originally proposed by Taylor (1934), and opposed jet arrangements.
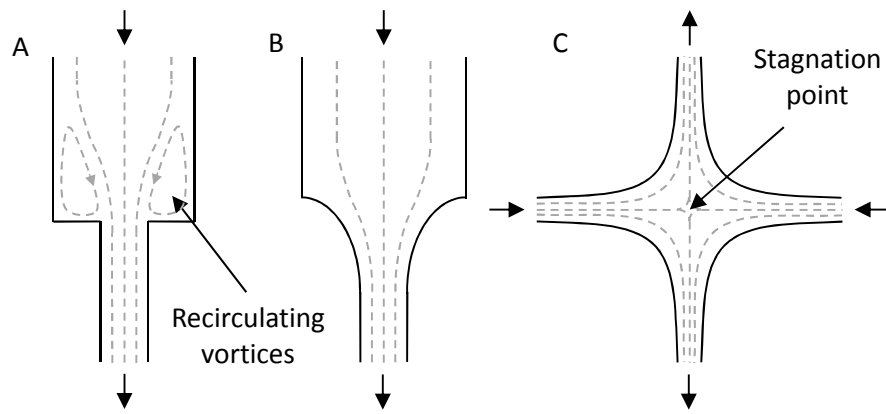
Figure 1.20: Extensional flows between bounding walls.

A: abrupt contraction, B: profiled contraction, C: stagnation flow

One final, interesting approach that produces pure extensional flow without the issues of fibre spinning limitations or bounding walls is that of bubble collapse. Varying the pressure outside a bubble causes the bubble to expand or shrink, producing extensional flow. The size of the bubble can be readily monitored optically and the pressure difference provides a measure of force. Unfortunately, the extension rate away from the bubble surface decreases rapidly with increasing radius (Macosko, 1994).

Reviews of all these approaches, together with further information on the operating fundamentals and limitations, can be found in Whorlow (1992) and Macosko (1994).

Chapter 2.

Initial remit of in-line rheometry.

Chapter 2: Initial remit of in-line rheometry.

At the start of this PhD, the initial remit was that of developing sensors for an "in-line" rheometric device. This was expanded to cover what other approaches would allow in-line rheometry to be achieved. This lead to the hypothesis in chapter 3 and accordingly, a shift in PhD focus. This chapter is intended to elaborate this process, but is by no means exhaustive in nature.

2.1   Requirement for and examples of existing in-line rheometric techniques

The rheological properties of commercial products, the importance of which was noted in chapter 1, are achieved through additives and processing. In terms of the former, the amount of additive must be controlled, as with thickening or gelling agents used in foodstuffs, or the blending of base stocks or viscosity modifiers to produce lubricating oils. Monitoring rheology over time may also be useful after additive incorporation, especially in batch-wise operations (i.e. Pu et al. (2015)). In the latter, processing parameters such as thermal treatments, or the control of polymerisation operations, directly affect rheology. Examples include the heat treatment of cake flours (Chesterton et al., 2015) and spaghetti dough (Marcella Mastromatteo, 2012) where thermal treatments are used to improve properties that have close links with the materials' rheology, and the variable nature of the feedstocks makes continuous control important. A good example of the value of in-line rheometry for polymer processing is that of Broadhead et al. (1996) who used a custom rheometer to directly control a reactive extrusion process. The advantages are reiterated in an application note by TA Instruments (TA Instruments, 2013a). Continuous "in-line" or "on-line" rheological measurement is thus desirable for process control and quality assurance.

The in-line rheometer concept that was under development at the start of this PhD, for which specialist sensors were required, had a number of key shortcomings. Due to the complexity of the approach, results could only be interpreted by a priori CFD modelling of fluid behaviours and application of an "inverse model" approach. As will become evident in this thesis, our lack of a thorough understanding of rheometric behaviours makes this an extremely fragile technique. Secondly, is that there are, in fact, a large number of systems capable of achieving in-line rheometric measurements already on the market, utilising much simpler and much more robust operating principles.

The capability of these commercially available systems vary, and there are several ways they could be categorised. The most relevant consideration is the type of data they supply. At one end of the scale are systems which measure "metrics", such as melt flow index, or MFI. Such measurements do not correspond to traditional rheological variables, but are simple and useful

for process or quality control (which does not usually require fundamental parameters), and as a result have found widespread use. Perhaps one of the most simple rheometers in existence is the manually operated "marsh funnel", used for checking drilling muds (Pitt, 2000). At the other end of the scale are systems which independently generate their own controlled and well defined deformations, and resolve full rheometric data. Between these two lie systems sold as "viscometers" in that a single value of viscosity is obtained. For some, there may be little reason they could not be extended to rheometric data (i.e. modulating a drive speed). For other systems, they may measure parameters more closely related to viscosity, however for some care may be advisable in interpreting their results for more complex fluids (i.e. vibrating fork or torsionially oscillating probe type systems, an example of the former being the Micro Motion systems offered by Emerson Process Management (Emerson Process Management, 2014)).

Rheometric systems can also be segregated by those that are physically "in-line" and operating under externally imposed flows, those attached in some suitable manner "on-line" (i.e. on a side stream, with more flexibility in flow conditions), and those which represent automated conventional rheometers. We can even, perhaps similarly, segregate systems in terms of sampling rate, and contrast this to the process control demands. At one end of the scale, an ideal system would collect data against shear rate in a parallel manner, with the sample corresponding instantaneously to the process. Most systems take shear data in some form of serial manner, with some additional residence delay in piping samples to the device. Automated versions of conventional rheometers would perhaps be the slowest in terms of response if they were produced. The closest example is that of the ThermoHaake Roboflixer (ThermoHaake, 2001) though this system is designed to produce standardised MFI rather than rheological measurements.

Perhaps the most well developed and logical approach for online rheometry is to simply adapt a standard technique such that it resides "on-line", parallel to a process stream. Capillary based techniques are perhaps the most widespread (usually intended for polymer melts), with products (some very similar) are offered by a range of companies. One example is the Göttfert RTR (GÖTTFERT Werkstoff-Prüfmaschinen GmbH, 2014) which is clearly shown as being able to produce full shear viscosity – shear rate curves. Concentric cylinder rheometers have equally been adapted for online applications, such as those offered by Brookfield (Brookfield Engineering Laboratories Inc., 2004). An relatively recent addition to the mix is that of the OLR (Rheology Solutions, 2012), which resembles a system developed by Glasscock et al. (2003), though the deformation mode used is as much a extensional rheometer as a shear rheometer.

We will not attempt to perform a more extensive review of all systems available, except note that Dealy (1990) highlighted the challenges of process rheometry as well as reviewed techniques around that time for polymer melts (Dealy and Broadhead, 1993). Entire lists of commercially available systems appear in publications such as Collyer and Clegg (1998), and indeed, Macosko (1994) summarised this in that "there are a large number of excellent commercial instruments to choose from". An interesting real-world operational evaluation of several process viscometers with different operating principles (including Brookfield's cylindrical rotary viscometer) is detailed in Fricke and Crisalle (1999).

A common factor between almost all commercial rheometric systems is that to achieve rheometric data, measurements at different shear rates are generally performed in a serial manner, with shear rate changing as a function of time (i.e. altering a pump or rotor speed). The device on which this PhD was originally based would have used a constant flowrate and multiple sensors. This highlights the two fundamental approaches through which rheology measurement can be performed: changing shear rate in time, or space. Taking the initial rheometer concept back to fundamentals, the simplest and most direct way to achieve this is by a channel that changes in cross section, i.e. a "wedge".

Arguably, a spatially varying approach to rheometry has limited practical advantages over a temporal approach. Firstly, the flow rate (or some parameter linking to the deformation rates in the material) still needs to be known, even if it is not being varied. Using a positive displacement pump is academic, as the pump could simply be made variable. The choice of flow metering approaches is very restrictive as the fluid rheology is unknown, but options do exist. Secondly, acquiring several points on the rheometric curve instantly, rather than over perhaps 20 seconds, may be of little consequence to many industrial processes; especially when upstream residence time delays in metering or pumping are present (though Broadhead et al. (1996) does highlight a system where system response delays are an issue and in-line, real time measurements would be useful). Using many pressure sensors, depending on their type, could be costly.

The only practical measurements of flow rate without sensitivity to rheological functions is that of Coriolis flowmeters (and potentially, electromagnetic flowmeters). Coriolis flowmeters measure mass flow directly, rather than velocity, and their clean bores and lack of moving parts are advantages. Such devices are used in a capillary-Coriolis viscometer featured in the study of Fricke and Crisalle (1999) and used in the Krohne Viscoline system (KROHNE, 2012) . Of course, a valve-modulated version of this instrument could again resolve rheometric data, but for the

purposes of this chapter a spatially varying rheometer / Coriolis flowmeter combination will be taken forward to consider, at least academically, how this might be achieved.

We should note that in addition to the on-line / in-line rheometric approaches briefly highlighted, there are two very promising new fields under active development at the present time: that of "UVP+PD", or ultrasound velocity profile and pressure drop measurement, and the same technique, but using NMR to map the velocity profile (see for example Powell et al. (1994), and strategies given in Gibbs et al. (1997)). The velocity profile directly relates to the nature of the fluid's rheological behaviour, and the pressure drop scales the magnitude of viscous losses. Full rheometric shear data can thus be obtained non-invasively, with clean bore systems, and no pumping or flow adjustment requirements. The ultrasound variant has been shown to handle not only liquids, but even systems with suspended solid food chunks (Wiklund and Stading, 2008) and is currently being researched extensively. As the NMR approach does not necessarily need high strength magnetic fields (Goloshevsky et al., 2005), it may only be a matter of time before these systems become commercial products.

Along the same lines of "extending" ultrasound from measuring a flow rate (as in industry) to that of a full velocity profile, it is technically possible to do the same with an electromagnetic flow meter. This has been highlighted in Leeuwen (1997). In recent years "Electromagnetic tomography" has been developed for mapping velocity profiles (Leeungculsatien and Lucas, 2013) but the resolution of the technique is currently rather limited compared ultrasound and NMR approaches.

2.2   Spatially varying "wedge" approaches to rheometry

Aside from the obvious utility of a mechanically variable slit for rheometry (Aho and Syrjälä, 2011, Robin et al., 2010), there are a few examples where spatially varying wedge and slit approaches have been adopted. Fritz (1989) (see Collyer and Clegg (1998) for details) and Horvat et al. (2013) have constructed "stepped" slit dies with two and three step sections respectively. In both cases, the pressure drop across each slit section is measured by a pair of pressure transducers. Rather than steps, Pabedinskas et al. (1991) used a continuous linear wedge, augmented with three pressure transducers. In the patent of Gleissle and Schulze (1993) (under auspices of Göttfert) they describe four configurations, including a cone shaped (circular cross section) tapered capillary, shown with three pressure sensors along its length; a similar arrangement but with a tapered slot (rectangular cross section) capillary; two parallel sided rectangular capillaries of different dimensions, connected in series by a gradual contraction, each capillary section with a pair of pressure transducers; and two differing

diameter circular capillaries connected in series by abrupt expansion-contraction volumes, to which are connected pressure transducers. Thermo Scientific (Jakob and Ruthardt, 2014) have developed an "X-die" for mounting onto other instruments, intended for rapid simple characterisation of samples under shear and extension. This system also features two rectangular capillaries of differing dimensions connected in series by a gradual contraction, with four pressure sensors measuring the pressure drops over the three sections.

All these approaches have in common a heavy requirement for sometimes costly pressure sensors: it is useful to recall some aspects of capillary rheometry in this regard. In a standard capillary rheometer measuring elastic materials, the pressure at each sensor is the pressure of the fluid, plus any normal stresses, inertial contributions, and so called "hole pressure errors". However, as the pressure drop down the capillary is of interest, assuming the flow conditions are identical at both sensors (i.e. a parallel capillary), these additional factors cancel (or are zero). With a tapered capillary, these factors do not cancel, and furthermore, extensional flow is present between measuring locations, which creates an additional pressure drop: Cogswell (1972) proposed that the pressure drop down converging channels is the sum total of that arising from shear and extensional flow, shown below in equation 2.1:

$$P = P_S + P_E \qquad\qquad (\ 2.1\ )$$

A series of parallel instrumented capillaries is thus preferable, however, the abrupt contractions or expansions between parallel die sections result in extensional flows and entrance effects. As a result, for shear rheometry, extraneous measurement of these pressure drops must be avoided. Sensors must be sited away from these regions which creates rather long channel lengths, and accordingly, a pair of transducers is needed across each new capillary section. One compromise is that the pressure drop across these abrupt contractions is however a useful metric for extensional behaviour.

Many advantages are apparent, if rather than measuring pressure drops, wall shear stress is measured directly in such a tapering channel. As shear-induced pressure drop down a channel is in effect an integrated contribution from wall shear stresses, the same analysis procedures could conceivably be applied as for pressure drop measurements (i.e. the Weissenberg Rabinowitsch correction). However, this technique avoids all issues with erroneous contributions to pressure drops that would appear from normal forces, inertia, and hole pressure errors. More specifically, it is also insensitive to pressure drops arising from

extensional flow. Not only is a tapered channel is now viable, it is free of the problem of being discretised into parallel sections and the problems of entrance and end effects: with sufficient and small enough wall shear stress measurement devices many data points could (conceivably) be attained in a more practical channel length.

2.3   Measurement of wall shear stress in a spatially varying "wedge" geometry

The next problem is how to implement such measurements of wall shear stress, a more practically difficult proposition than pressure measurement. Whilst pressure measurement requires a surface that can deform normal to a wall, shear stress requires a surface that can deform parallel to it. Such a surface may also be subject to pressure forces, or must be floating in a flow field such pressure forces are balanced across it (with elastic fluids, this may not be sufficient as normal forces would not necessarily be balanced). Examples of micro electrical mechanical (MEMS) shear stress sensors can be found in literature, however these sophisticated devices are complex, fragile, and certainly not generally suited to practical rheological applications. Particularly, the small length scales behind any "floating" sensors would be highly susceptible to fouling. Dealy et al. (1992) describe a more robust macro scale shear stress sensor that has been used in their work (i.e. see the thesis by Broadhead (1992)), however the issue of test fluid entering the space behind the shear sensitive surface is still present.

A wall shear stress sensor is required that uses relatively conventional technology, is robust, and is both unaffected by or arranged in a manner that makes it insensitive to both high static pressure (i.e. being situated on a extruder, for example) and viscoelastic normal forces. One robust and pressure insensitive option is to use a deformable gel. Gijsen et al. (1997) measured wall shear stresses using speckle pattern interferometry and a deformable gel layer on the inside surface of a channel. Etebari (2006) used ionic polymers to a similar effect. A difficulty exists in making multiple measurements using this gel technique, as unless isolated through some means, the deformation at one location would couple to deformations at other locations. Secondly, differing pressures acting on gel would cause it to deform in a direction downstream. The sensor must therefore also be able to make independent wall shear stress measurements that do not couple to one another.

Taking the concept of "floating" shear stress sensors, the first useful realisation was that the pressure and normal force issues could be removed if the conditions, and thus flow, were identical on either side of a floating shear stress sensor. This means the sensing surface lies on

the symmetry plane of a tapering channel, with shearing acting on either side. This also removes the issues of fowling behind a floating sensor.

The second important realisation is that this surface need not be a series of complex floating "elements" anchored to the cell wall, as akin to standard approaches to shear stress sensing. If freely suspended at an upstream point in the flow field, the increase in tension along such a central surface could be instead measured. This is a much more practical proposition and to a good approximation (noted further later) the stress is independent at each position along the surface length. Figure 2.1 shows such a "tension sensing fin" in the planar arrangement, with an assumption that the parallel bounding walls are placed far away relative to the converging walls. Figure 2.2 shows an alternative, more complex geometry that enables the stresses present on the fin to be identical throughout the channel interior surfaces. Tension in the fin increases running right to left in both diagrams. Such a fin design would be simple to calibrate – All that is needed is the application of known tension loads to the far end.
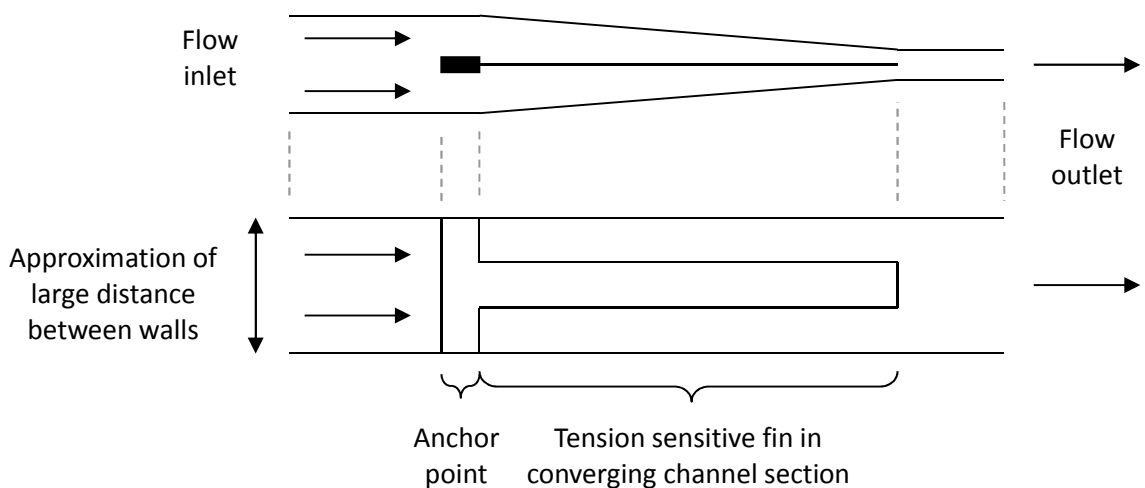
Figure 2.1: Tapering channel equipped with a tension sensitive fin
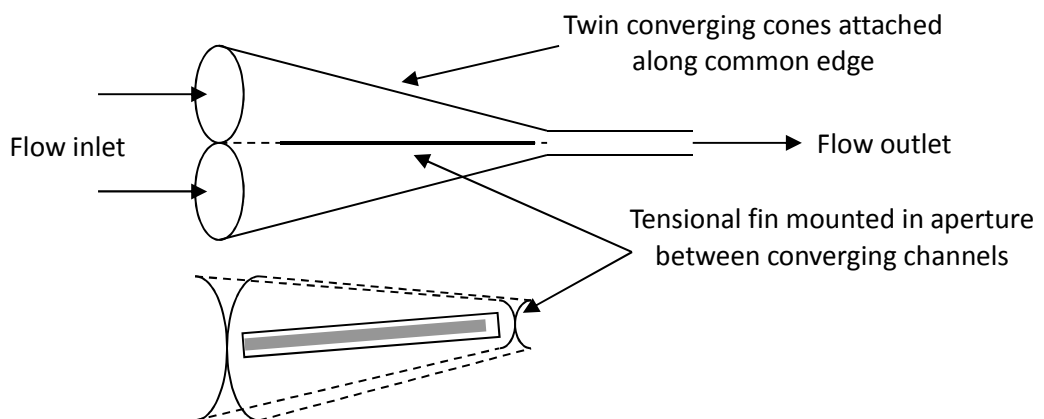
Figure 2.2: Twin conical converging channels to produce axisymmetric wall stresses

There are a multitude of ways that tension can be measured, including optical approaches. Optical approaches cannot, of course, be used when opaque fluids are of interest. Electrical strain gauges are the most direct solution. Commercially available single element strain gauges attached to some form of backing would be far too insensitive, and gluing several end to end, and making the necessary electrical connections, is not practical. Fortunately however, some companies do offer "custom" strain gauge fabrication. This makes a custom strain gauge "fin array", incorporating all the electrical interconnects back to and out through the anchor point, a possibility. As gauges are sensitive to strain, rather than stress, using a custom fin avoids the need for a (test) substrate to which strain gauges are usually attached, thus maximising the sensitivity to tension in the fin.

2.4   Strain gauge fin shear stress rheometer

Before the concept of a tension sensing fin can be considered further, some thought needs to be given as to how the suggested strain gauges might be implemented. Briefly, a strain gauge (sometimes referred to as a "gage") consists of a thin metal foil network in a grid pattern, on top of (and sealed with) a suitable electrically insulating flexible carrier material, typically a thin Kapton film. Other types of gauges, such as piezo resistive gauges, are also in common use. Several strain gauge "elements" may be configured in networks in a single package, here we are discussing the use of several single element gauges to form the custom strain sensitive fin.

An example single element gauge is shown in figure 2.3 overleaf. Straining the package in the direction of strain sensitivity (shown by the arrow) causes the metal foil conductor to become longer and thinner. As a result, the electrical resistance between the ends of the foil conductor varies in a linear manner with applied strain. This strain is usually small, and units of micro-strain ($\mu\varepsilon$) are commonly encountered.

Three main characteristics apply to strain gauges. A strain gauge has a (unloaded) characteristic resistance of usually a few hundred ohms. The gauge factor, or GF, defines the ratio of a fractional change in resistance, dR/R, to an applied strain in a particular direction. For strains directed parallel to the gauge conductors, the gauge factor of bonded foil gauges is nominally about 2 (Omega Engineering, 2009). Strain gauges are also specified with a factor known as the transverse sensitivity (K_t), which describes the relative sensitivity (ratio of gauge factors) to strains applied perpendicular compared to parallel to grid pattern, and is nominally of the order of 10% (Omega Engineering, 2009). As tension forces are acting only in one direction in the conceptual fin, this is unimportant.

Strain sensitive direction
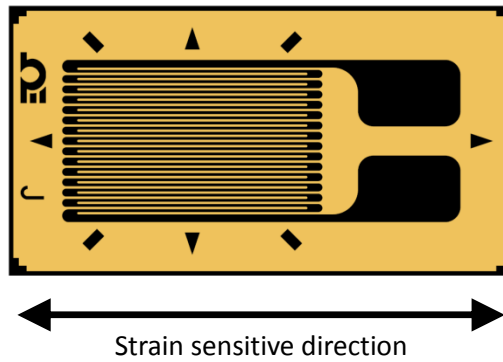
Figure 2.3: Linear pattern strain gauge (SGD-5/350-LY) from Omega Engineering (2015)

Several such strain gauges need to be situated on the fin, and connected, via tracks, back to some suitable location that electrical connections can be readily implemented. Two criteria are important: firstly, minimising the number of interconnects required, and secondly, implementing a network that is temperature compensated: the resistance of a gauge also depends on temperature (and indeed, resistive self-heating) despite the use of materials such as constantan for the foil, and is quite critical given the small strains measured. Strain gauge packages featuring bridge networks are normally used as they are inherently temperature compensated, however they are not suited to this application.

Making two connections to each gauge on the fin is the most versatile approach, but rapidly becomes rather prohibitive in terms of space occupied by solder pads and tracks. On the other hand, wiring the gauges as a "matrix" is difficult to interpret, and cannot readily be implemented as traces would need to bridge one another. The most effective approach is to configure the gauges as a long "potential divider" arrangement. This is shown in figure 2.4 below for five gauges, with the gauges orientated such that they are sensitive tensional forces in the fin (one long "tapped" gauge would be oriented in the wrong direction to the applied strain).
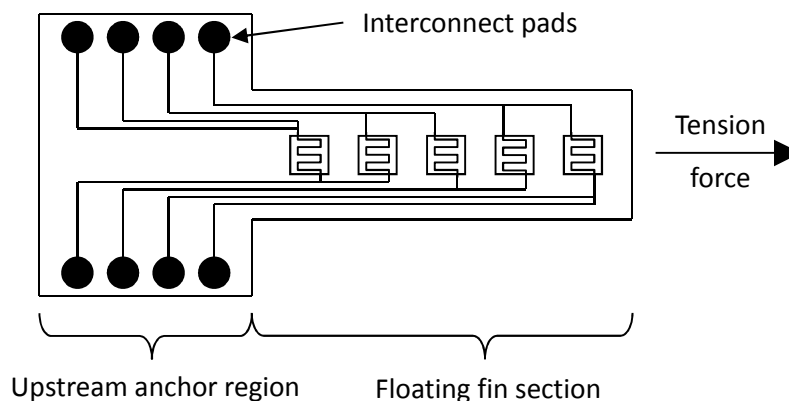
Figure 2.4: Strain gauge "fin" configured as a potential divider network

The voltages developed down a potential divider are dependent on the relative values of the resistances in the divider, not their absolute values. If a supply voltage were simply connected across the ends of the potential divider, the voltage signal from between each successive gauge would thus provide information on tension distribution along the fin, but not the absolute tension in the fin. As a result, a "reference" gauge is also required electrically situated at one end of the potential divider network. This gauge must be made of the same material and in the same thermal and mechanical environment as the other gauges, but arranged to be devoid of stresses. Duplicating the mechanical situation is important, as bonding the reference gauge to a surface would introduce so-called "apparent strain" from thermal expansion, freely suspending the gauge in a thermal well would be ideal. Now, the voltage signals from the network depend on the absolute stresses in the fin, and are insensitive to temperature changes, which affects all the gauges (including the reference gauge) equally. The full layout is simulated for the purposes of explanation in figure 2.5 below using Crocodile Technology (Crocodile Clips Ltd, 2000).
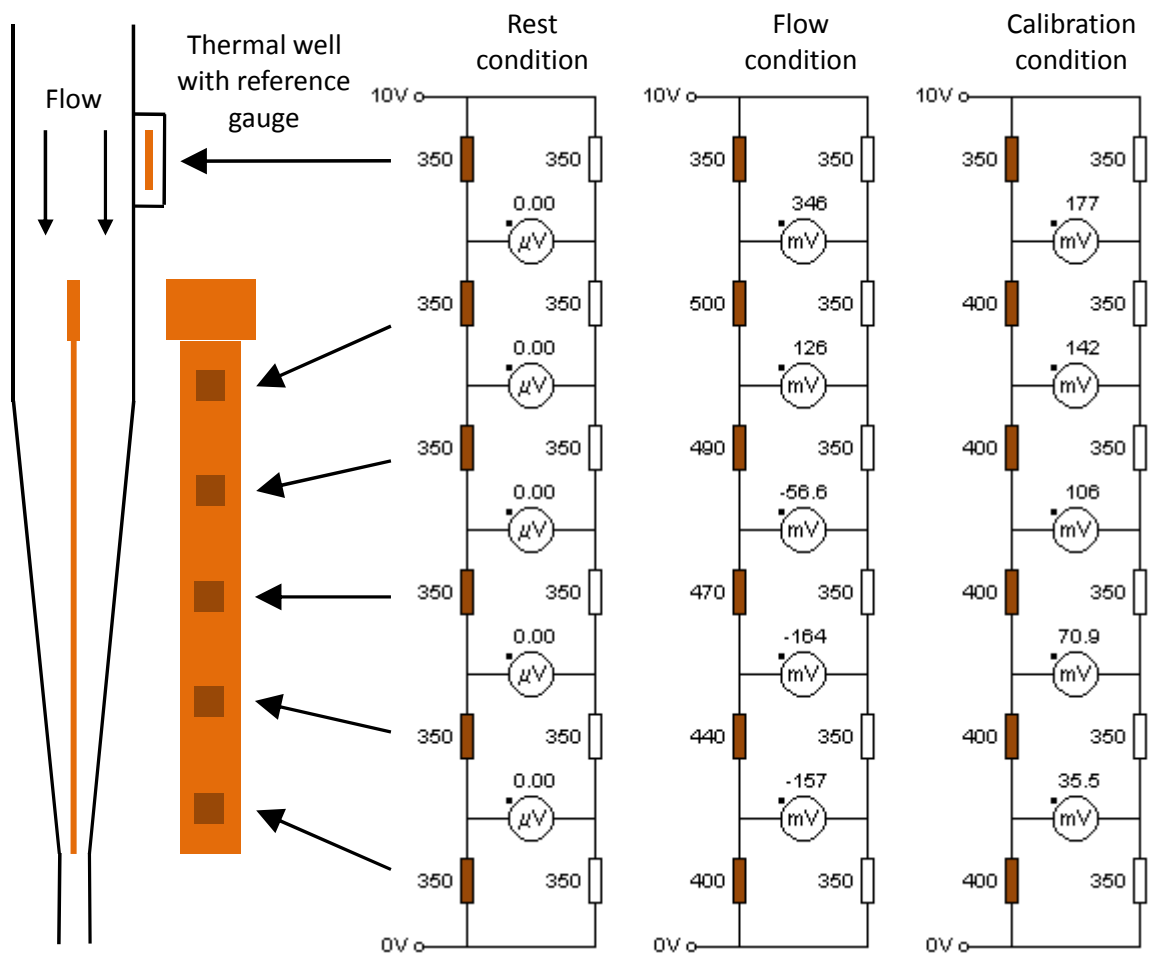
Figure 2.5: Simple simulation of strain gauge fin with 5 gauges. Strain gauges (both loaded and reference) are shown in brown, all other resistors are fixed resistors.

The five gauges shown here, plus the reference gauge, have unloaded (in the "rest" condition) resistance of 350 ohms. They are shown under two loaded conditions: a "flow" condition with highly exaggerated but otherwise qualitative resistance distribution of what might be expected under flow, and a "calibration" condition, emulating a static load applied to the fin end. In the "flow" condition, at the free downstream end of the array, the tension is the lowest, but increases at the fastest rate along the fin due to the high shear stresses. At the anchor end upstream, the tension in the fin is the highest, but increasing at the slowest rate as the shear stresses are lower. The signals are "shown" on the virtual voltmeters measured relative to a fixed resistor array. The voltage distributions shown here will be compared to the main simulations shortly.

In a real situation, these voltmeters would be high gain, high stability differential amplifiers, and the fixed resistor array trimmed to compensate for manufacturing variations in the bridge unloaded resistance (such as to give zero output under no-stress conditions). Some care would equally be necessary in the design of the reference array to ensure that all the elements in it also respond equally with respect to temperature, both any fixed and variable resistors.

2.5   CFD and electrical simulation of strain gauge fin concept

To consider the utility of such a converging channel / strain gauge fin arrangement for measuring shear stresses, a combined CFD and electrical simulation was conducted. Fluent (Ansys, 2012) was used for CFD, and spreadsheet calculations for the electrical network.

A rectangular "wedge" shaped channel with a linear contraction was modelled, featuring an aspect ratio that prefers shear contributions from the contracting walls (at least, to an extent sufficient for signal evaluation purposes). To reduce flow disturbances long entry and exit channel sections are modelled. The strain gauge fin is supported in the channel by an "anchor" region running across the full channel height. This is situated at a location significantly upstream of the contraction to provide developed flow at the contraction onset. Two planes of symmetry are used to aid computation, one in the plane of the fin and the second at half the channel height, perpendicular to the fin. The dimensions of this channel were chosen to be comparable to a real world channel with such a fin, if constructed, given the size of typical strain gauge elements. Figure 2.6 overleaf shows the full and symmetric geometries with the key dimensions labelled. The fin thickness used for the CFD and stress calculations is 25 microns, that of a typical strain gauge (Omega Engineering, 2006). Flow is set up to run right to left to make fin tension increase with increasing X axis coordinate. With a gap reduction of 5

times down the channel length, an increase in shear rate of about 25 times would be expected (albeit rather modest compared to standard rheometric techniques).
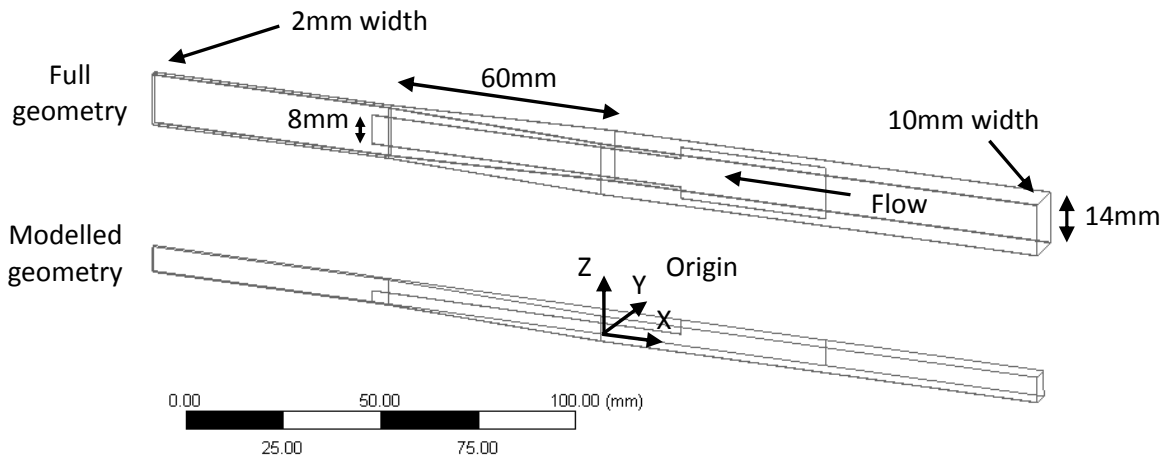
Figure 2.6: The full "wedge" channel geometry used to assess the strain gauge fin concept, and the fraction of this modelled in CFD through the application of two symmetry planes.

Preliminary simulations were conducted to ascertain a "practical" simulation in terms of imposed viscosity, flow rate, and the resulting pressure drop. The test criteria decided on for the main simulations is detailed in table 2.1 below. A power law model in the Fluent package was used, with additional settable limits on the fluid viscosity. A modest 5Pa.s consistency index was used, comparable or less than that of many viscous foodstuffs (For example, honey at 15 Pa.s and mayonnaise at 50 Pa.s (Cole-Parmer Instrument Co. Ltd., 2006)).

Parameter	Units	Condition A	Condition B	Condition C
Mass Flow Rate	kg/s	0.001	0.001	0.001
Density	kg/m^3	1000	1000	1000
Consistency Index, k	Pa.s^n	5	5	5
Power-Law Index, n		0.8	1	1.2
Minimum Viscosity Limit	Pa.s	1	1	1
Maximum Viscosity Limit	Pa.s	25	25	25

Table 2.1: CFD Simulation fluid parameters

In the following contour plots, one quarter of the flow field is depicted due to the symmetry planes. A slice in the X-Z plane at Y=0 (the plane of the fin) is shown to inspect flow fields around the long edge of the fin. Two more slices are shown in the X-Y plane at Z=0 and a

higher Z coordinate (perpendicular to the centreline of the fin) to highlight profile development between the fin and the narrowing cone wall. A third slice, in the Y-Z plane is shown at X=0 (the start of the cone). Due to how the modelling geometry was configured, flow is directed right to left, from positive to negative X coordinate as in figure 2.6. Note the variation in scale bars between plot figures.

Figure 2.7 below shows a pressure drop down the channel for case B (n=1.0). The pressure drop down the channel ranged from 7.3×10^{4} to 6.9×10^{5} Pa from case A to case C, i.e. a maximum of about 100PSI which is at the upper end of practically "amenable" pressure drops. Note, however, these estimates neglect the additional pressure drop from the extensional flow of viscoelastic liquids. As can be seen, about half of the pressure drop is a result of the outlet channel which could be reduced in length. Figure 2.8 and 2.9 show the corresponding velocity plot and wall strain rate plots for case B (qualitatively similar to cases A and C).
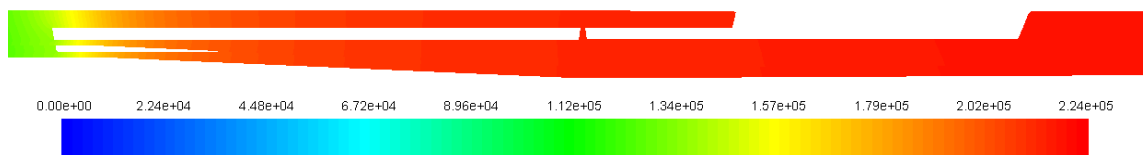
Figure 2.7: Condition B – Static pressure (Pa)
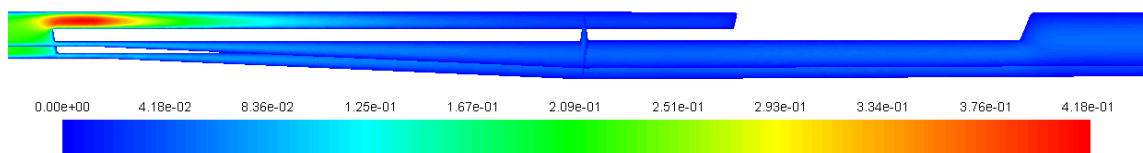
Figure 2.8: Condition B - Velocity magnitude (m/s)
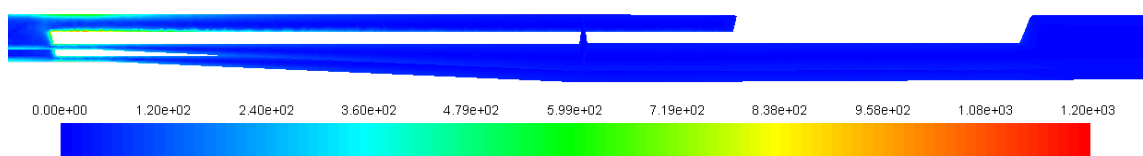
Figure 2.9: Condition B – Strain rate (1/s)

From figure 2.8, we can see that despite the influence of the anchoring section for the fin, both upstream before the anchoring section, and downstream on reaching the contraction zone, the flow is well developed, both across the channel height and width. As the channel narrows, we can see the flow velocity increasing perpendicular to the fin surface and the corresponding increase in strain rates at the fin surface in figure 2.9.

What is quite clear from these plots is that most of the flow bypasses the contraction formed between the fin and channel walls, and travels in the spaces above and below the fin. In this planar geometry, the fin cannot extend to the top and bottom walls as a 2D approximation is desired. However, the fin could be arranged to resemble a "cut-out" of a wall extending the full channel height which would avoid this issue. An improvement in sensitivity vs. pressure drop would be expected as these regions of flow bypass contribute little to the tension in the fin.

Note strain rates in figure 2.9 around $400s^{-1}$ towards the fin end. Similar values are present for cases A (n=0.8) and C (n=1.2). This corresponds to viscosity variations down to 1.5 Pa.s and up to 16.6 Pa.s respectively – Within the limits of 1 to 25 Pa.s set in the model parameters.

Figure 2.10 below shows the shear stress developed on the fin surface for case B. Shear stress values have been exported along the centreline of the fin for the three conditions. At each X location shear stress was reported along the fin, an "element" was formed extending half way to the neighbouring points. The tension contribution from this element was determined from the shear stress, element length, fin height, and multiplied by 2 for flow at either side of the fin. These tension contributions were summed up the fin length (increasing X coordinate), and converted into stress via the fin cross sectional area. As expected, the stresses end up independent of the fin height. The wall shear stress and fin tensional stress are plotted in figure 2.11 for case B (n=1.0).
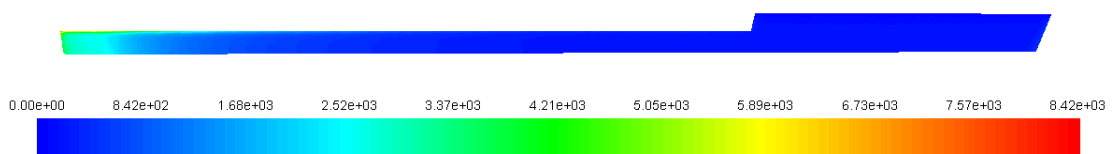
Figure 2.10: Condition B – Wall shear stress (Pascal)
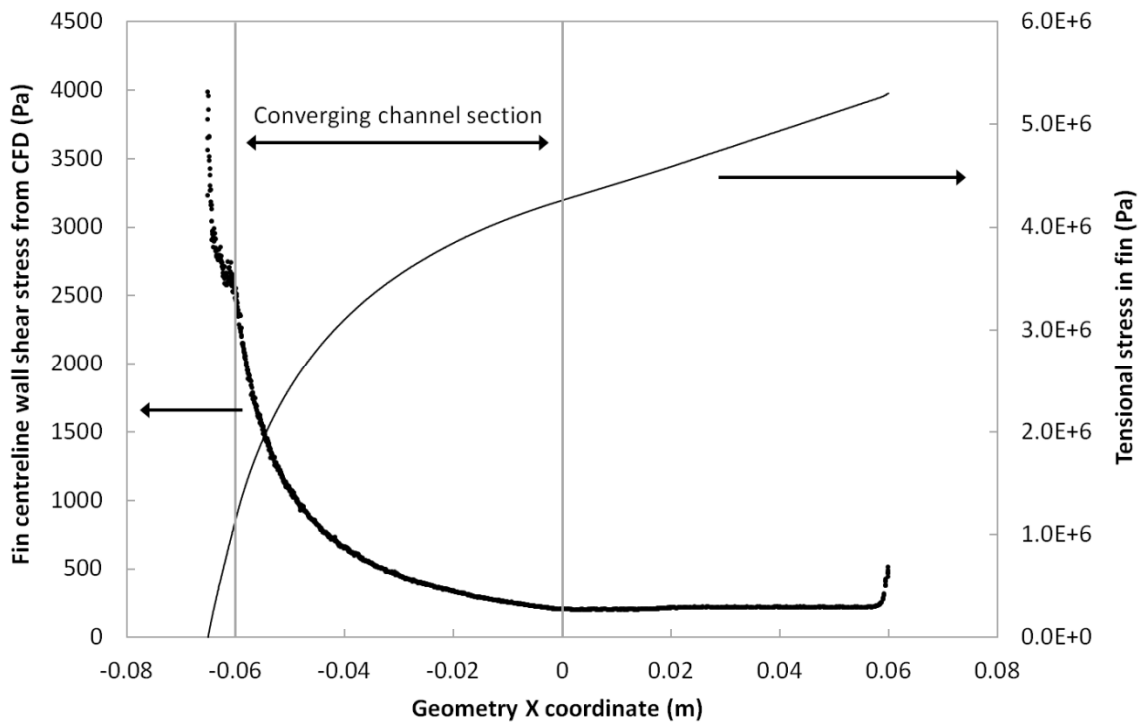
Figure 2.11: Conversion of wall shear stress to tensional stress in the fin for case B (n=1.0)

Figure 2.11 shows an approximately 10 fold increase in wall shear stress compared to the 25 fold increase expected by the geometry: this might be due to flow bypass highlighted earlier causing the linear velocity to thus increase less than expected.

To simulate the response of a strain gauge array, a basis of 25 point-sized strain gauges spaced 2.5mm apart (based on typical grid sizes) was used, situated in the converging section of the channel. Real strain gauges are sensitive to tension over their entire grid area, so in a real world application additional data analysis would be required. Loaded resistances are calculated based on the gauges having a unloaded resistance of 350 ohms, a gauge factor of 2, and the stresses were converted into strains based on the Young's modulus of Kapton (2.5GPa, (DuPont, 2006) – Assuming the metal foil thickness of the gauges is negligible).

It is assumed here that the strain distribution is homogeneous throughout the width of the fin. The unrestricted edges of the fin may render this an approximation, causing stress to be concentrated towards the fin centre, and a detailed analysis would be required. If stress concentration occurred, a coupling of strains may also then also occur along the fin length. Similarly, the stress distribution from a calibration load at one end of the fin needs to be compared to that of applying shear loading down the fin length. The wider the fin, the less of an issue stress concentration would be.

41

The electrical simulation is based on these 25 strain gauges being connected in series, one end is connected to 0V, and the other end is connected through a fixed 350 ohm element (the "reference" strain gauge) to +10V. Summing the resistances enables the current through the series string to be calculated, and from that, the voltage at any measurement point to be determined. The difference between the voltage in this "loaded" array, and an equivalent "unloaded" array (all elements 350 ohms) is multiplied ("amplified") by 1500 times to give the final simulated amplifier output signals.

The results for cases A (n=0.8), B (n=1.0), and C (n=1.2) are plotted in figures 2.12, 2.13, and 2.14 respectively, together with the tension in the fin.
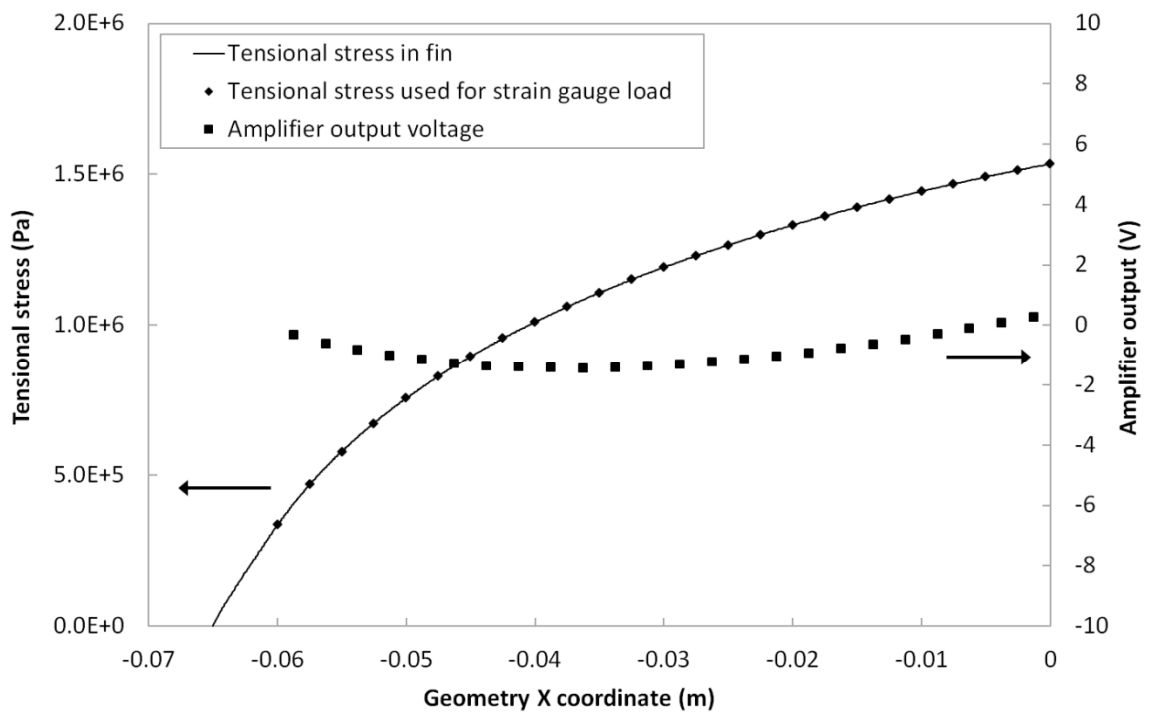
Figure 2.12: Predicted output signal voltages for case A (n=0.8)
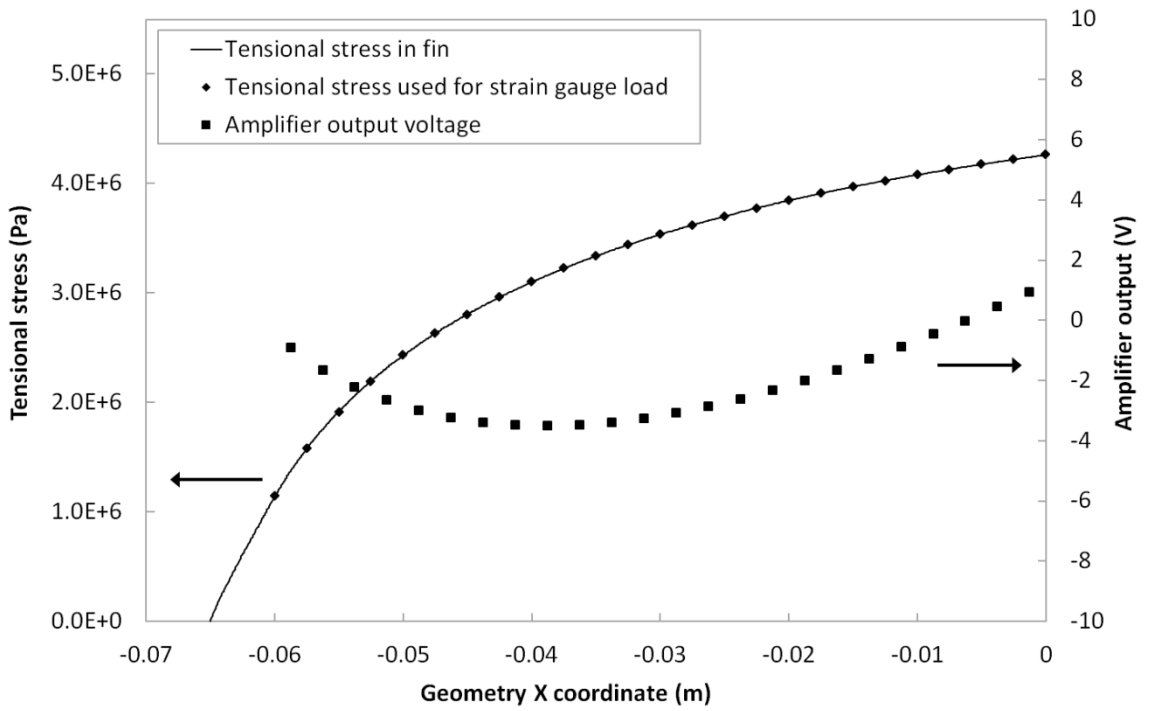
Figure 2.13: Predicted output signal voltages for case B (n=1.0)
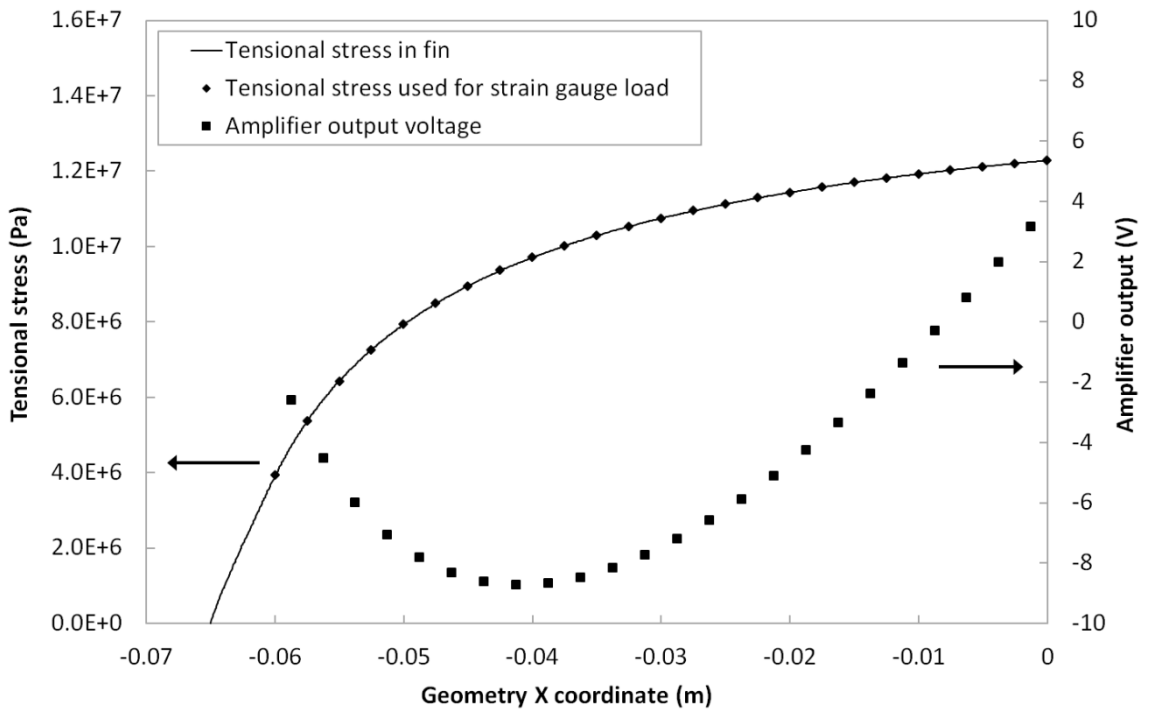
Figure 2.14: Predicted output signal voltages for case C (n=1.2)

In terms of sensitivity to the fluid shearing, we can see from figures 2.12 to 2.14 that the signals developed are of acceptable magnitude. Firstly, the x1500 amplification factor is quite reasonable for strain gauge applications; factors of 10 times this were used on the commercial amplifiers of the in-line rheometer under development at the start of this PhD. Secondly, the maximum stress in the fin of 12MPa is well short of the 69MPa (3% strain) yield point of Kapton

(DuPont, 2006) and (surprisingly) even less than the maximum strain of 5% quoted for Omega's Kapton based KFG series of strain gauges (Omega Engineering, 2006).

These stress figures indicate that higher viscosity systems, higher shear rates and/or longer fins with more measurement points could be comfortably handled. Beyond this the array could be made thicker in cross section, or simply applied to a stiffer substrate (with attention paid to apparent strain due to thermal expansion) for particularly severe applications. On the other hand, if additional sensitivity for the same shearing conditions was desired, there are a few ways this could be achieved. The obvious options would be to increase the signal amplification or apply higher voltages to the array. Similarly to the above, increasing the fin length increases the tensional force, but at the expense of higher pressure drops. Making the fin thinner or fabricating it with a less rigid substrate would increase sensitivity, but both may not be practical for custom fabrication. As noted earlier, increasing the height of the fin spreads the force over a larger fin cross section, and thus has no effect on signals as noted earlier. One option would, however, be to fabricate a fin with inlaid sections of a more flexible material (such as an elastomer) as to concentrate stress in to the strain gauges, as illustrated in figure 2.15. This also mitigates the flow disturbances if the fin was a discontinuous structure. The stress distribution issue highlighted earlier would be more acute.
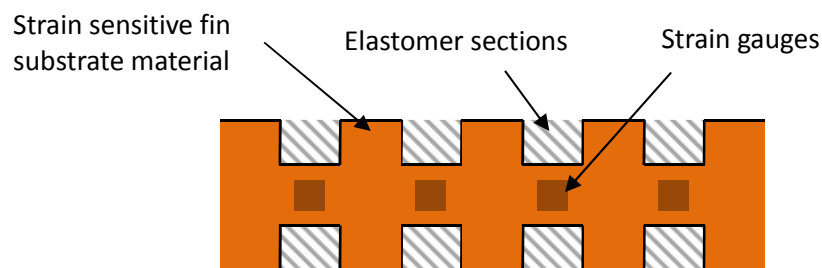
Figure 2.15: Sensitivity enhancement by inlayed elastomer sections in the strain sensitive fin

A simpler option to the above would be to use a more sensitive strain measurement technique. Piezo resistive devices are much more sensitive to strain (i.e. higher gauge factor) than strain gauges, and a strain sensitive fin with many such devices could conceivably fabricated in a single silicon strip. Aside from the cost of such an approach however, the silicon substrate would likely be thicker and feature a much higher Young's modulus than Kapton (around 150GPa (Hopcroft et al., 2010) vs. 2.5GPa) likely negating any advantage. Piezo resistive devices are also more sensitive to temperature changes than metal foil gauges. More exotic flexible sensing materials such as QTC (Quantum tunnelling compound, Peratech Holdco Limited (2016)) could also be considered. This material is however intended for on-off type switching applications; it may not be suitable for a stress sensing application that demands

reproducibility between elements and a simple (in particular independent) behaviour with temperature changes.

In terms of the shape of the signal outputs in figures 2.12, 2.13, and 2.14, we can see that the form resembles that in figure 2.5 shown earlier, providing confidence in the simulations. Two general features occur as the power law index is increased: The minima in signal across the fin length becomes deeper, and shifts towards the free end of the fin (lower X coordinate). By scaling the tensions in the electrical simulations by a constant amount (i.e. equivalent to adjusting the fluid consistency index) the peak becomes lower, but does not move in location. Thus, the shifting of the peak with changing n values is directly related to the change in fluid rheometric behaviour (though complicated by the flow bypass issue noted previously). It can equally be seen that the rate of tension growth along the fin in case C (n=1.2) is relatively faster than that in case A (n=0.8), at the start of the fin, as expected for shear thickening compared to shear thinning behaviour. The lower minima in the shear thickening case is, however, not directly a result of the increased stresses (i.e. higher total tension) in the fin, but most likely influenced by them.

To elaborate, whilst the minima position is directly coupled to the fluid rheology, the actual process that produces the minima in the signals is qualitatively difficult to describe. For example, consider the simplest case of placing a constant tensional force on the fin. Overall, the resistance of the strain gauge array increases, thus the current flowing through the array falls. However, the reference resistance remains fixed. The voltage across this element falls, placing more voltage across the sensing elements. Positive signal voltages thus result, that increases linearly from 0V at the free end of the fin to a positive value at the anchor location. This has been shown with the spread sheet calculations and the "calibration" case in figure 2.5 earlier. Observe that increasing the fin tension in this case would cause higher signal values, yet in the shear thickening case with increased overall fin tension the minima fell to a more negative value; highlighting why it cannot be directly related to fluid consistency. This interplay between current in the array and the reference resistance is occurring similarly in the simulated cases, with all strain gauges affecting the signal from all others. As a result, further qualitative description of this phenomenon is complex and of little benefit, so will not be described further. In a practical situation the same principles applied to conduct this modelling would of course be reversed, rather than direct interpretation of the signal voltages attempted.

Concluding this modelling exercise, it has been demonstrated that a "strain gauge fin" is possible. Such a fin as described features adequate sensitivity to measure relatively viscous

fluids (i.e. >1Pa.s), and routes by which the sensitivity of the technique could be improved have been highlighted. A demonstration of how this technique would be sensitive to rheometric behaviour has also been illustrated.

2.6   Strain gauge fin concept: Physical and manufacturing considerations

In terms of the practical implementation of the proposed strain gauge "fin", some important considerations are worth highlighting. It is necessary that this fin remains in the centre of a channel. Making the fin rigid by ribs would reduce the fin sensitivity to stress, and if extreme, disrupt symmetry assumptions. A thin fin may prove to be unstable even with gravity directed in the direction of fluid flow due to a number of effects, and may even stick to a side wall of the channel through capillary (when wet) or electrostatic (when dry) forces. Small "guide" tabs could be considered to guide the fin, but these would introduce friction and flow disturbances. Ideally, the fin would be situated as part of a "cut-out" of a larger fixed wall, as described earlier, and the gap between the fin and the wall filled with a thin film of flexible elastomer (shown below in figure 2.16) allowing the fin to extend but simultaneously keeping it correctly located.
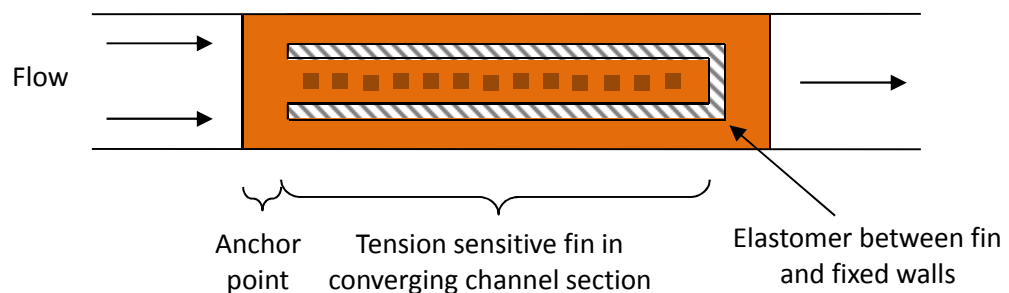
Figure 2.16: Use of elastomer and the concept of the fin as a "cut-out" of a larger fixed wall to prevent secondary flows and stabilise the fin position

There are also manufacturing issues that need consideration which present greater issues. Firstly, strain gauges, when supplied, are not flat. A photograph is shown in figure 2.17 below. Whilst not a problem in conventional use, such a curvature would render a custom fin useless. More specifically, problems may be encountered if a curved fin were restrained into position by the elastomer approach detailed, as the inherent forces may well be unstable over time and temperature.
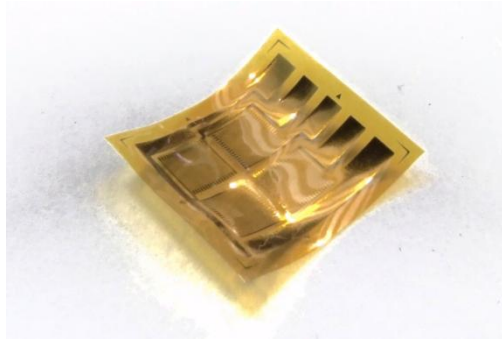
Figure 2.17: Standard (bridge) strain gauge as supplied, exhibiting curvature

Secondly, from discussion with manufacturers strain gauges have a relatively high manufacturing failure rate from open circuit grids. This, again, is not a problem in conventional use, but where an array of tens of grids is being sought, particularly one where all the gauges are interconnected, this could prove less straightforward than desired (i.e. external bridging of open circuit grids). Figure 2.18 shows an "ideal", if slightly optimistic, fin of 27 strain gauges wired in a potential divider arrangement. The gauges are aligned along the centre of the fin, with connecting tracks running to each alternate gauge down each edge. Additional unconnected tracks are incorporated to generate more uniform mechanical properties along the fin. A quote from one company was £1000 for a production run of 5 of these gauges, but with no guarantee that these would be fully operational.

(Actual size: 80.26mm x 7.55mm)
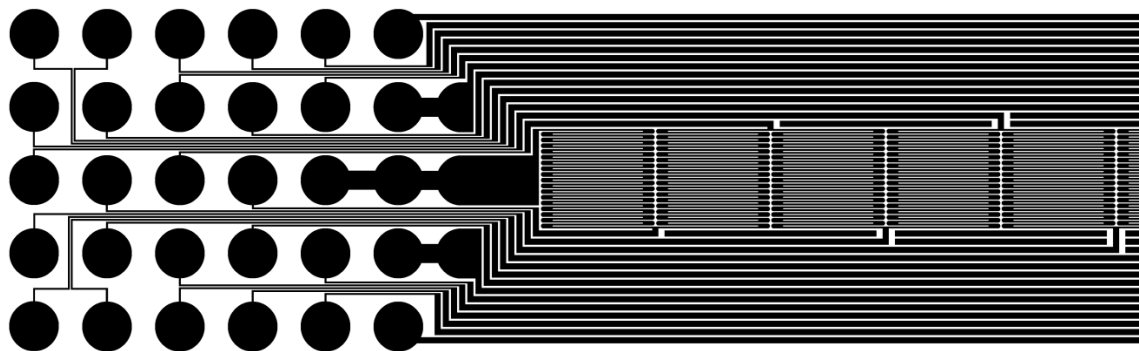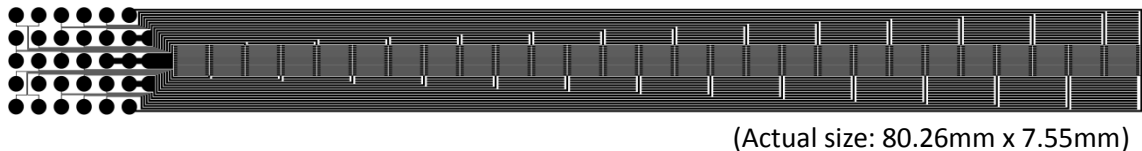
Figure 2.18: Conceptual strain gauge fin design with 27 gauges in a potential divider configuration. Additional unconnected tracks are included enhance mechanical uniformity. Upper image: Full array, lower image: Enlarged view of region around connection pads. Design based on the pattern of Omega Engineering SGD-2/350-LY41 strain gauges.

2.7   Strain gauge fin concept: Fluid dynamics restrictions

Given the manufacturing restrictions highlighted, considerable cost may need to be expended on the production of a custom strain gauge fin, or the "in-house" development and fabrication of a flatter alternative may be required, using some suitable strain sensitive technology.

As a result, we must consider the utility of such an approach for shear rheometry. The most significant drawback of this - and indeed any spatially varying approaches to shear rheometry - is that the deformation rates acting on a fluid packet (i.e. In the Lagrangian description) are not time-steady. The shear rates on a fluid packet rise rapidly as it propagates down the channel. This is aside from the existing (potentially correctable) complication of spatial variations in shear rate across the channel. This means that any rheometric measurements are transient in nature, and these results, especially for time dependent viscoelastic and thixotropic systems, cannot be directly compared to traditional steady state rheometry.

The second issue is that the flow field is kinematically mixed, with both shear and extension present. It is of course accepted that shearing a fluid may affect its shear viscosity, but does extensional flow affect shear viscosity also? If so, then the ability to obtain pure shear viscosity data from such an experiment breaks down.

One area that this concept may be valuable in, however, is in the measurement of extensional, rather than shear rheometry. Converging channels (i.e. profiled versions of the wedge described so far) are used to produce extensional flow in experiments (amongst other techniques) and the pressure drop down such channels is measured. As previously highlighted, the pressure drop down these channels would be the sum total of that due to shear and extension. Conventionally, such experiments either attempt to eliminate wall shear by some form of low viscosity wall lubrication, or alternatively simulate the "inelastic" pressure drop contribution from shear flow and subtract it from those measured experimentally. An example is that of James et al. (1990), however critically they assumed a power law fluid which, in hindsight here, regrettably neglected any transient shear behaviour of the test fluid.

If the strain gauge fin were incorporated into a converging channel equipped with pressure sensors, it would be possible to determine the pressure drop contribution from shearing and directly subtract it from the measured pressure drops, rather than simulating it. This inherently covers both transient shear rheometry and incorporates any effects of extensional flow on shear rheometry, if it were present (both directly, and through influences on resulting velocity profiles). It would be most useful for systems where the shear pressure drop was comparable

or in excess of that due to extension. As with any other pressure drop based extensional experiment, consideration of inertia would still be required as well as that of any normal forces and hole pressure errors (i.e. requiring the use of flush mounted transducers).

Unfortunately, compensating for wall shear in an extensional flow experiment is not as ideal as completely eliminating it. The velocity distribution resulting from shear flow results in a spread of elongation rates and residence times in such experiments, ranging from zero at the wall to a maximum at the channel centreline, a fact underlined by Cogswell (1978). Similarly also to the issues of extensional deformation being present in experiments attempting to measure shear, shear deformation is also present here in an experiment attempting to measure extension. The results from such an experiment are therefore of questionable use for "true" extensional flow rheology.

Whilst of limited value for extensional rheology experiments, mixed shear-extensional flows are, however, far more relevant in real world situations than pure extensional flows. Compared to the previous examples provided section 2.2 where pressure drops across contractions provide a very crude indication of extensional behaviour, this concept would provide a much more pertinent representation. Furthermore, complex modelling to otherwise separate, or the great experimental difficultly in completely eliminating wall shear is avoided. This technique therefore has promise as an on-line, practical, and meaningful indication of fluid extensional characteristics.

2.8   Conclusions

Given the industrial products already available for in- or on-line rheometry, and the promise of ultrasound and NMR techniques, further speculation of alternative approaches is considered of limited benefit.

There are now two directions that this work could be taken.

The first option is, as just described, to develop a new approach to extensional rheometry where the wall shear stresses are directly measured, in-situ, with consideration as application as a high quality "metric" of extensional rheology. The issues of strain gauge array cost, manufacturing reliability, and curvature would need to be addressed.

The second option is to consider further the issue of whether shear rheometry is affected by extensional flow.

The latter option is of rather more interest and value with regards potential contribution to the field of rheology, and was chosen to consider further for the purposes of this PhD.

The following chapter defines this hypothesis more rigorously, highlights supporting evidence, and starts to develop how this may be investigated experimentally.

Chapter 3.

Hypothesis and supporting evidence.

Chapter 3: Hypothesis and supporting evidence.

3.1   Hypothesis

The hypothesis for the remainder of this thesis, as constructed in the last chapter, is that extensional flows have a simultaneous effect on shear viscosity. More specifically, traditionally shear viscosity is supposed such that:

$$\mu = f(\dot{\gamma}, t) \qquad \textbf{(3.1)}$$

Whereas here, it is proposed that:

$$\mu = f(\dot{\gamma}, \dot{\varepsilon}, t) \qquad \textbf{(3.2)}$$

A similar argument can be made that extensional viscosity which is traditionally supposed as:

$$\eta = f(\dot{\varepsilon}, t) \qquad \textbf{(3.3)}$$

Could be considered to be:

$$\eta = f(\dot{\gamma}, \dot{\varepsilon}, t) \qquad \textbf{(3.4)}$$

Here we will concentrate on the former case, that of demonstrating a shear viscosity dependence on extension rate. The latter case will be occasionally highlighted.

3.2 Definition of generalised shear rate

In chapter 1, definitions of stresses and viscosity were defined elementarily, focusing on a single deformation strain rate and the associated stress. For example with a power law fluid:

$$\sigma = (k\dot{\gamma}^{n-1})\dot{\gamma} \qquad\qquad (3.5)$$

When calculations move into more than one dimension the form of the equations is slightly different. For 2D, stresses on a fluid packet are represented by the matrix $\boldsymbol{T}$ as follows (the convention being that $\boldsymbol{\sigma}$ includes contributions from fluid pressure, whereas $\boldsymbol{T}$ does not):

$$\boldsymbol{T} = \begin{bmatrix} T_{11} & T_{12} \\ T_{21} & T_{22} \end{bmatrix} \qquad\qquad (3.6)$$

Parameters T_{11} and T_{22} are extensional stresses in the X and Y directions respectively. For a fluid element that has constant angular momentum, T_{12} and T_{21} are equal, and represent shear stress.

The rate of strain is defined by the tensor $\boldsymbol{D}$, which is given by:

$$\boldsymbol{D} = \frac{1}{2}(\nabla\mathbf{u} + \nabla\mathbf{u}^T) = \begin{bmatrix} \dfrac{\partial u}{\partial x} & \dfrac{\left(\dfrac{\partial v}{\partial x} + \dfrac{\partial u}{\partial y}\right)}{2} \\ \dfrac{\left(\dfrac{\partial v}{\partial x} + \dfrac{\partial u}{\partial y}\right)}{2} & \dfrac{\partial v}{\partial y} \end{bmatrix} \qquad\qquad (3.7)$$

$\nabla\mathbf{u}$ defines the deformation rates acting on a fluid packet. The symmetric form of **D** rejects solid body rotation. Note some sources (e.g. Bird et al. (1987)) exclude the half factor in equation 3.7 whilst others include it, it is included throughout here.

In the case of a Newtonian fluid, the constitutive equation (following sign conventions in Bird et al. (1987)) links the two:

$$\boldsymbol{T} = -2\mu\boldsymbol{D} \qquad\qquad (3.8)$$

Applying only a shear deformation of $\frac{\partial u}{\partial y} = \dot{\gamma}$ with other deformation components equal to zero this produces a shear stress of $T_{12} = -\mu\dot{\gamma}$ as would be expected. Applying a planar elongational deformation of $\frac{\partial u}{\partial x} = -\frac{\partial v}{\partial y} = \dot{\varepsilon}$ produces a elongational stress of $T_{11} - T_{22} = -4\mu\dot{\varepsilon}$, and applying a uniaxial elongational deformation of $\frac{\partial u}{\partial x} = -\frac{1}{2}\frac{\partial v}{\partial y} = -\frac{1}{2}\frac{\partial w}{\partial z} = \dot{\varepsilon}$ produces an elongational stress $T_{11} - T_{22} = -3\mu\dot{\varepsilon}$, hence the Trouton ratios presented in chapter 1.

Importantly, in this form, the extensional and shear strains, and their resulting stresses, remain quite separate.

However, for a power law fluid, the situation is complicated by what deformation rate to use in the power law description. A parameter sometimes referred to as the generalised shear rate is used, shown below in matrix and 2D form (again following Bird et al. (1987)):

$$\dot{\gamma}_{gr} = \sqrt{2\boldsymbol{D} : \boldsymbol{D}}$$ (3.9)

$$\dot{\gamma}_{gr} = \sqrt{2\frac{\partial u}{\partial x}^2 + 2\frac{\partial v}{\partial y}^2 + \underbrace{\left(\frac{\partial u}{\partial y} + \frac{\partial v}{\partial x}\right)^2}}$$ (3.10)

$$\underbrace{\qquad}_{\text{Extension}} \underbrace{\qquad}_{\text{Shear}}$$

The generalised shear rate applied to the power law relation is in the form of:

$$\boldsymbol{T} = -K\dot{\gamma}_{gr}{}^{n-1}\boldsymbol{D}$$ (3.11)

We can see from equation 3.11 that the generalised shear rate parameter includes a dependence on both shear and elongational deformation. As a result, the power law relation infers a dependence of shear viscosity on extension rate, and equally, of extensional viscosity on shear rate. The situation is more complex than this, as this "generalised shear rate" arises from considering only one of three invariant parameters in the generalised Newtonian fluid (or Reiner–Rivlin fluid). Other parameters feature a greater contribution from extensional flows, and as a result the generalised shear rate relation is valid only "for flows that are very nearly shearing " (Bird et al., 1987). Despite this simplification, the generalised shear rate already directly supports the hypothesis. Secondly, Bird et al. (1987) adds "…that engineers have not hesitated to apply this equation to somewhat more complicated flows…". Evidently, if extensional flow does affect shear viscosity, there is no appreciation of this in general engineering use. The importance of "flagging" this by testing the hypothesis is thus underlined.

Note also that the "equivalent" shear rates for calculating Trouton ratios presented in chapter 1 can be shown from the generalised shear rate relation. For example with a planar flow and $\dot{\varepsilon} = 1 \left(\frac{\partial u}{\partial x} = 1, \frac{\partial v}{\partial y} = -1\right)$ produces $\dot{\gamma}_{gr} = 2$. For a uniaxial 3D flow and $\dot{\varepsilon} = 1 \left(\frac{\partial u}{\partial x} = 1, \frac{\partial v}{\partial y} = -\frac{1}{2}, \frac{\partial w}{\partial z} = -\frac{1}{2}\right)$ produces $\dot{\gamma}_{gr} = \sqrt{3}$. For simple shear flow, $\dot{\gamma}_{gr} = \dot{\gamma}$. As a result, the shear viscosity should be evaluated at shear rate of 2 and $\sqrt{3}$ times that of the extension rate respectfully: under these conditions the amount of deformation induced reduction in fluid viscosity would be identical if the shear and extensional deformations influenced the fluid

similarly (aside from the questionable applicability of the generalised shear rate equation to extensional flows).

3.3   Viscoelastic constitutive models under steady state deformation

The Oldroyd-B fluid model describes a class of fluid with a constant shear viscosity, but with an incorporated viscoelastic response arising from a solute dissolved in a solvent liquid. This is one of the simplest viscoelastic fluid models that satisfies independence with respect to the frame of reference (unlike the Maxwell model), and is amenable to analytical analysis.

I am grateful to Chaffin (2015) for discussion and extensive assistance with regards the following material through to the end of section 3.3. More information on the Oldroyd-B model can be found in Hinch (2003).

The Oldroyd-B constitutive equation takes the form of:

$$\boldsymbol{\sigma}_{Tot} = -P\mathbf{1} + 2\mu_s\boldsymbol{D} + \boldsymbol{T} \qquad (\ 3.12\ )$$

where $\boldsymbol{\sigma}_{Tot}$ is the total stresses acting on a fluid packet, $P\mathbf{1}$ is the normal pressure forces acting on the particle faces, $2\mu_s\boldsymbol{D}$ is the force contribution from the Newtonian solvent liquid, and $\boldsymbol{T}$ is the "extra" stress arising from a dissolved solute. Note that neglecting contributions from the solvent liquid ($2\mu_s\boldsymbol{D}$) yields what is referred to as an upper-convected Maxwell model, or UCM (simpler, but less physical and computationally less stable than the OLB model).

Of particular interest here is $\boldsymbol{T}$: this is determined from solving the constitutive equation:

$$\boldsymbol{T} + \lambda\left[(\underline{\boldsymbol{u}} \cdot \nabla)\boldsymbol{T} - [\boldsymbol{L}\boldsymbol{T} + \boldsymbol{T}\boldsymbol{L}^T]\right] = 2\mu_p\boldsymbol{D} \qquad (\ 3.13\ )$$

Without the second term of the equation, stresses have a linear (Newtonian) dependence on shear rates where μ_p is the polymer viscosity. Adding in the second term of the equation incorporates a dependence on viscoelastic behaviour, where λ is the fluid relaxation time (s^{-1}). When λ equals zero, fluid behaviour becomes Newtonian. The term $(\underline{\boldsymbol{u}} \cdot \nabla)\boldsymbol{T}$ is the spatial derivative of stress component $\boldsymbol{T}$ directed along a streamline. As we are considering a Lagrangian steady state situation with respect to strain rates, this term is a priori zero.

The **L** component is defined as follows (for a 2D flowfield):

$$L = \nabla \mathbf{u}^T = \begin{bmatrix} \dfrac{\partial u}{\partial x} & \dfrac{\partial u}{\partial y} \\ \dfrac{\partial v}{\partial x} & \dfrac{\partial v}{\partial y} \end{bmatrix}$$

(3.14)

The component $[LT + TL^T]$ is:

$$[LT + TL^T] = \begin{bmatrix} \dfrac{\partial u}{\partial x} & \dfrac{\partial u}{\partial y} \\ \dfrac{\partial v}{\partial x} & \dfrac{\partial v}{\partial y} \end{bmatrix} \begin{bmatrix} T_{11} & T_{12} \\ T_{12} & T_{22} \end{bmatrix} + \begin{bmatrix} T_{11} & T_{12} \\ T_{12} & T_{22} \end{bmatrix} \begin{bmatrix} \dfrac{\partial u}{\partial x} & \dfrac{\partial v}{\partial x} \\ \dfrac{\partial u}{\partial y} & \dfrac{\partial v}{\partial y} \end{bmatrix}$$

(3.15)

And from matrix multiplication gives the following:

$$[LT + TL^T] = \begin{bmatrix} \dfrac{\partial u}{\partial x}T_{11} + \dfrac{\partial u}{\partial y}T_{12} & \dfrac{\partial u}{\partial x}T_{12} + \dfrac{\partial u}{\partial y}T_{22} \\ \dfrac{\partial v}{\partial x}T_{11} + \dfrac{\partial v}{\partial y}T_{12} & \dfrac{\partial v}{\partial x}T_{12} + \dfrac{\partial v}{\partial y}T_{22} \end{bmatrix} + \begin{bmatrix} \dfrac{\partial u}{\partial x}T_{11} + \dfrac{\partial u}{\partial y}T_{12} & \dfrac{\partial v}{\partial x}T_{11} + \dfrac{\partial v}{\partial y}T_{12} \\ \dfrac{\partial u}{\partial x}T_{12} + \dfrac{\partial u}{\partial y}T_{22} & \dfrac{\partial v}{\partial x}T_{12} + \dfrac{\partial v}{\partial y}T_{22} \end{bmatrix}$$

(3.16)

Noting $\partial u/\partial x = -\partial v/\partial y$ due to mass conservation:

$$[LT + TL^T] = \begin{bmatrix} 2\left(\dfrac{\partial u}{\partial x}T_{11} + \dfrac{\partial u}{\partial y}T_{12}\right) & \dfrac{\partial v}{\partial x}T_{11} + \dfrac{\partial u}{\partial y}T_{22} \\ \dfrac{\partial v}{\partial x}T_{11} + \dfrac{\partial u}{\partial y}T_{22} & 2\left(\dfrac{\partial v}{\partial x}T_{12} + \dfrac{\partial v}{\partial y}T_{22}\right) \end{bmatrix}$$

(3.17)

Thus the constitutive relation (substituting in **D**) becomes:

$$\begin{bmatrix} T_{11} & T_{12} \\ T_{12} & T_{22} \end{bmatrix} - \lambda \begin{bmatrix} 2\left(\dfrac{\partial u}{\partial x}T_{11} + \dfrac{\partial u}{\partial y}T_{12}\right) & \dfrac{\partial v}{\partial x}T_{11} + \dfrac{\partial u}{\partial y}T_{22} \\ \dfrac{\partial v}{\partial x}T_{11} + \dfrac{\partial u}{\partial y}T_{22} & 2\left(\dfrac{\partial v}{\partial x}T_{12} + \dfrac{\partial v}{\partial y}T_{22}\right) \end{bmatrix} = \mu \begin{bmatrix} 2\dfrac{\partial u}{\partial x} & \left(\dfrac{\partial v}{\partial x} + \dfrac{\partial u}{\partial y}\right) \\ \left(\dfrac{\partial v}{\partial x} + \dfrac{\partial u}{\partial y}\right) & 2\dfrac{\partial v}{\partial y} \end{bmatrix}$$

(3.18)

Substituting in shear and elongation rates $\left(\dfrac{\partial u}{\partial y} = \dot{\gamma}, \dfrac{\partial v}{\partial x} = 0, \dfrac{\partial u}{\partial x} = \dot{\varepsilon}, \dfrac{\partial v}{\partial y} = -\dot{\varepsilon}\right)$:

$$\begin{bmatrix} T_{11} & T_{12} \\ T_{12} & T_{22} \end{bmatrix} - \lambda \begin{bmatrix} 2(\dot{\varepsilon}T_{11} + \dot{\gamma}T_{12}) & \dot{\gamma}T_{22} \\ \dot{\gamma}T_{22} & -2\dot{\varepsilon}T_{22} \end{bmatrix} = \mu \begin{bmatrix} 2\dot{\varepsilon} & \dot{\gamma} \\ \dot{\gamma} & -2\dot{\varepsilon} \end{bmatrix}$$

(3.19)

Solving for T_{22}:

$$T_{22} + 2\lambda\dot{\varepsilon}T_{22} = -2\mu\dot{\varepsilon}$$

(3.20)

$$T_{22} = \dfrac{-2\mu\dot{\varepsilon}}{(1 + 2\lambda\dot{\varepsilon})}$$

(3.21)

$$T_{22} = \dfrac{-2\mu\dot{\varepsilon}(1 - 2\lambda\dot{\varepsilon})}{-4\lambda^2\dot{\varepsilon}^2 + 1}$$

(3.22)

$$T_{22} = \frac{2\mu(\dot{\varepsilon} - 2\lambda\dot{\varepsilon}^2)}{4\lambda^2\dot{\varepsilon}^2 - 1} \qquad (3.23)$$

Solving for T_{12}:

$$T_{12} - \lambda\dot{\gamma}T_{22} = \mu\dot{\gamma} \qquad (3.24)$$

And substituting in T_{22}:

$$T_{12} - \lambda\dot{\gamma}\frac{-2\mu\dot{\varepsilon}}{(1 + 2\lambda\dot{\varepsilon})} = \mu\dot{\gamma} \qquad (3.25)$$

$$T_{12} = \mu\dot{\gamma} - \lambda\dot{\gamma}\frac{2\mu\dot{\varepsilon}}{(1 + 2\lambda\dot{\varepsilon})} \qquad (3.26)$$

$$T_{12} = \frac{\mu\dot{\gamma}(1 + 2\lambda\dot{\varepsilon}) - 2\lambda\dot{\gamma}\mu\dot{\varepsilon}}{(1 + 2\lambda\dot{\varepsilon})} \qquad (3.27)$$

$$T_{12} = \frac{\mu\dot{\gamma}}{(1 + 2\lambda\dot{\varepsilon})} \qquad (3.28)$$

Solving for T_{11}:

$$T_{11} - 2\lambda(\dot{\varepsilon}T_{11} + \dot{\gamma}T_{12}) = 2\mu\dot{\varepsilon} \qquad (3.29)$$

$$T_{11} - 2\lambda\dot{\varepsilon}T_{11} - 2\lambda\dot{\gamma}T_{12} = 2\mu\dot{\varepsilon} \qquad (3.30)$$

$$T_{11} = \frac{2\mu\dot{\varepsilon} + 2\lambda\dot{\gamma}T_{12}}{(1 - 2\lambda\dot{\varepsilon})} \qquad (3.31)$$

And substituting in T_{12}:

$$T_{11} = \frac{\dfrac{2\mu\dot{\varepsilon}(1 + 2\lambda\dot{\varepsilon})}{(1 + 2\lambda\dot{\varepsilon})} + 2\lambda\dot{\gamma}\dfrac{\mu\dot{\gamma}}{(1 + 2\lambda\dot{\varepsilon})}}{(1 - 2\lambda\dot{\varepsilon})} \qquad (3.32)$$

$$T_{11} = \frac{2\mu\dot{\varepsilon}(1 + 2\lambda\dot{\varepsilon}) + 2\lambda\dot{\gamma}\mu\dot{\gamma}}{-4\lambda^2\dot{\varepsilon}^2 + 1} \qquad (3.33)$$

$$T_{11} = -\frac{2\mu(\dot{\varepsilon} + 2\lambda\dot{\varepsilon}^2 + \lambda\dot{\gamma}^2)}{4\lambda^2\dot{\varepsilon}^2 - 1} \qquad (3.34)$$

Note that the Oldroyd-B model does not hold under conditions of $\dot{\varepsilon}\lambda >= \frac{1}{2}$. Writing the shear and extensional viscosities based on the above results (i.e. neglecting solvent viscosity):

$$\mu_{shear} = \frac{T_{12}}{\dot{\gamma}} = \frac{\mu}{(1 + 2\lambda\dot{\varepsilon})} \tag{3.35}$$

$$\eta_e = \frac{T_{11} - T_{22}}{\dot{\varepsilon}} = \frac{-2\mu(\dot{\varepsilon} + 2\lambda\dot{\varepsilon}^2 + \lambda\dot{\gamma}^2) - 2\mu(\dot{\varepsilon} - 2\lambda\dot{\varepsilon}^2)}{4\lambda^2\dot{\varepsilon}^2 - 1} \tag{3.36}$$

$$\eta_e = \frac{-2\mu(2\dot{\varepsilon} + \lambda\dot{\gamma}^2)}{4\lambda^2\dot{\varepsilon}^2 - 1} \tag{3.37}$$

From the shear viscosity relation, we can see that for non-extensional flows shear viscosity is both constant with respect to shear rate (Newtonian, as per the model), and equal to μ as would be expected. However, for mixed flow fields, the shear viscosity is shown to be a function of the extension rate, supporting the hypothesis. From the extensional viscosity relation, the apparent extensional viscosity is also a function of both shear and extension rates. More interestingly, whilst the generalised shear rate is not sensitive to the direction (sign) of applied extension, the Oldroyd B model appears to be. This raises an important observation which the following references will underline. This said, it remains to be checked whether there are issues with the above result: when the coordinate system is rotated through 90 degrees, both the extension direction and the plane on which shearing is occurring changes.

3.4   Computational modelling of mixed flows

Evans and Heyes (1990) considered non-equilibrium molecular dynamics (NEMD) simulations of a non-Newtonian liquid under steady (planar) shear, transient shear, and mixed shear-elongational flows with elongation directed both parallel or perpendicular to the shear direction. Simulations were performed on a cubic unit cell, containing upwards of 500 molecules, with this cell then being periodically repeated in all three dimensions. The statement "Another new feature of this work is the simultaneous application of shear and elongational strain rates, which frequently occurs in the complex strain rate distribution found in processing flows" (Evans and Heyes, 1990) underlines the previous comments regarding the practical relevance of mixed flow fields.

Whilst it is clear that Lennard-Jones potentials were used to simulate forces between molecules (and measurements reported likewise in terms of reduced units), it is not immediately obvious to those less familiar with NEMD how complex molecular interactions are represented. For example, references to long chain molecules are not evident. Let it suffice to

say that shear thinning and tension thinning behaviours resulted under steady shear and steady elongation. For transient shear (effective timescales on the order of picoseconds), stress overshoots were observed with a suddenly applied strain field, characteristic of structural changes occurring. Those more accustom to NEMD simulations are recommended to consult the reference for more information.

In the case of extension directed in the streaming direction of flow (shear strain rate $\dot{\gamma} = \partial v_x / \partial Y$, extension rate $\dot{\gamma}_T$ scaled by δ in each direction where $\delta_x = 1$, $\delta_y = -1/2$, and $\delta_z = -1/2$) it was found that shear thinning was enhanced in the presence of extensional flow:

"We ascribe this enhanced shear thinning to the action of the elongational flow in 'dynamically ordering' the fluid along the stream lines of the shear flow (X direction). The elongational flow facilities the mechanism that causes shear thinning in simple fluids."

(Evans and Heyes, 1990)

It was stated that this enhancement was greatest in the limit of small shear and elongation rates: something that might be expected in the real world case of power law fluids that undergo the majority of shear thinning at low shear rates. It was also found that the elongational viscosity at a fixed elongation rate decreased when accompanied by shear flow (of interest in relation to references presented shortly).

In the case of extension directed perpendicular to the streaming direction of flow ($\dot{\gamma} = \partial v_x / \partial Y$, $\delta_x = -1/2$, $\delta_y = 1$, and $\delta_z = -1/2$), it was found that "There is still $\dot{\gamma}$ induced shear thinning in η, when accompanied by a finite $\dot{\gamma}_T$. However, the elongational flow acts to diminish the extent of shear thinning when compared with the unelongated sample" (Evans and Heyes, 1990). It is then noted that "The outcome in any simulation depends on the relative magnitudes of $\dot{\gamma}$ and $\dot{\gamma}_T$ and the competition between the somewhat conflicting preferences of the two flows" (Evans and Heyes, 1990).

These results for parallel and perpendicular mixed flows by Evans and Heyes directly support the stated hypothesis that that shear viscosity is a function of elongation rate, and highlights that the relative orientation of the two flows is important.

They conclude with:

> "These phenomena highlight the shortcomings of present continuum modelling techniques which fail to incorporate these many-body effects. These considerations will surely be important in reproducing the complex flow-rate dependent stream-lines in converging flows involving non-Newtonian liquids"
>
> **(Evans and Heyes, 1990)**

This underlines the importance of informing modelling work by testing the hypothesis.

3.5 Behaviour of liquid crystals

In the work by Evans and Heyes (1990) previously outlined, it was not immediately obvious whether anisotropic or otherwise large scale orientable structures such as polymer chains were simulated. However, liquid crystals are prime examples of the effects of molecular orientation on shear viscosity. Due to their physical anisotropy, liquid crystals (in the simplest case, rod-like molecules which tend to align along the so called director, $\underset{n}{\rightarrow}$) are characterised by 3 viscosities for shear, plus a fourth for rotation and also behave viscoelasticially (Sengupta et al., 2014). If the shear flow is denoted as $\frac{\partial u}{\partial y}$, then η_1 corresponds to a liquid crystal aligned parallel to the X axis, η_2 parallel to the Y axis, and η_3 parallel to the Z axis. With liquid crystals, the effect of this anisotropy can be directed investigated through the application of external (e.g. magnetic or electric) fields. Miesowicz (1946) is regarded as the first to do so, and the folded capillary of Kneppe and Schneider (1981) appears to be regarded as one of the more precise measurements of anisotropic viscosity, both using strong magnetic fields.

It is usually assumed that molecules in shear fields will undergo tumbling due to the vorticity present. However as well as tumbling, sheared liquid crystals may exhibit a flow aligning behaviour, with alignment at a fixed angle with respect to the shear direction (see for example Van Horn and Winter (2000)). The latter is a direct result of the interplay between the anisotropic shear viscosities and the torques produced from the flow field, where an equilibrium angle exists in the shear plane and can be calculated from theory. This is a direct example of "a mutual coupling between flow direction, director orientation and viscosity" (Sengupta et al., 2014); again underlining the hypothesis.

It is interesting to note that a viscous stress perpendicular to the flow direction can be generated when the director lies at an angle to the shear plane, the magnitude of which is

dependent "on the viscosity coefficients η_1 and η_3 and on ϕ...", vanishing "...for $\eta_1 = \eta_3$ or for $\phi = 0$, $\pi/2$" (Sengupta et al., 2014). Very unusually, this stress difference can also be negative (Currie, 1981). Viscoelastic fluid models generate such (at least usually positive) normal stress predictions, but without any dependence on anisotropic viscosities. If anisotropy in viscosities was present during the alignment of polymer chains in a viscoelastic material, should the generation of normal force differences be (or are they in fact) related to it in some manner?

3.6   X-Ray and neutron investigations of molecular alignment under extensional flow

We have just seen that the basics of the field of liquid crystals includes a viscosity dependence on crystal orientation. Whilst liquid crystals have a definite anisotropic shape, it is well known that under extensional flow polymers will uncoil from a coiled configuration at rest, providing the extension rate is greater than that of the polymer relaxation timescale (see chapter 5, and take for example the microstructure in extruded plastics). It is thus reasonable to extend this outside of the field of liquid crystals and more generally to the field of polymer fluid dynamics, and expect aligned, elongated polymers to also show effects on shear viscosity, the main differences arguably being relaxation times involved and the rigidity of the aligned polymer chains. More detailed evidence of alignment effects in extensional flows can be gained from X-Ray and neutron scattering studies. Four (non-exhaustive) examples are presented here: Cinader and Burghardt (1999); Trebbin et al. (2013); Martin et al. (2016) all using X-rays, and McLeish et al. (2009) using neutrons. These all study systems more complex than simple long-chain polymers, and in themselves study very different systems, but are taken here as sufficient to illuminate the argument.

A brief introduction into how scattering techniques resolve orientation is now pertinent. When neutron or x-ray radiation passes around a polymer chain, interference effects result in diffraction patterns. In a system of aligned polymer chains, two vertically disposed (first order) scattering peaks are produced, perpendicular to the alignment direction: i.e. in the channels of the following references horizontal alignment produces vertically disposed peaks, and vertical alignment horizontally disposed peaks. A system of randomly aligned molecules of uniform width would produce a single circular scattering ring. Neutron scattering produces equivalent patterns, but the techniques have different capabilities and requirements between them. WAXS and WANS (wide angle x-ray and wide angle neutron scattering) refers to experiments using a sensor relatively close to the sample, capturing shorter length scale features at large angles, and SAXS and SANS conversely uses a sensor further away, capturing longer length scale features at smaller angles, substantially larger than the wavelength of the incident radiation. The examples cited here used beam line synchrotron radiation sources for X-rays, and for

neutrons the nuclear reactor source at the Institut Laue Langevin (spallation sources may also be used). Experiments are influenced in terms of design by the necessity for (relatively) transparent windows for x-rays or neutrons. Furthermore, it is inescapable that the beams must pass through the entirety of a measuring cell, incorporating diffraction arising from both extensionally dominated flow near the centre and shear-dominated flow near the windows.

Cinader and Burghardt (1999)

Cinader and Burghardt (1999) studied, to quite a thorough degree, the effects of various channel flow geometries with mixed kinematics on the orientation of a commercial thermotropic (liquid crystalline) copolyester melt using in-situ WAXS, building on previous work. Their system under study is known to tumble at low shear rates. With respect to the hypothesis is stated that the TIF (transversely isotropic fluid) model suggests that a tumbling material would experience a significant change in orientation under elongation (particularly if the reorientation of a tumbling orbit transitions to a flow aligning behaviour), whilst a flow aligning material would only experience a minimal change in orientation under stream wise elongation, as it is already aligned due to upstream shear. For the work here we could postulate that the former class of fluids would display a higher sensitivity with respect to shear viscosity under elongational flows. Complementary comments could be made for perpendicular extensional flows where gradual changes for a tumbling regime or flips in molecular orientation at critical elongation rates to a flow aligning nematic are said to occur.

In their work (apparent wall shear rates are estimated at $2.5 - 10s^{-1}$, peak elongation rates estimated at a similar magnitude for a 4:1 sharp contraction) it is found that compared to a straight slit flow reference, in slit-contraction flows, elongation serves to dramatically enhance molecular orientation compared to that at the shear-dominated walls (consistent with previous work in the group). Corroborating with extensional flows being classed as "strong" flows in literature "…the extensional effects of the contraction overpower any difference in the initial conditions" [for different upstream scenarios], and the same is found for slit-expansion flows where upstream orientation is more pronounced.

In contraction flows near the extensionally dominated channel centreline, a parallel orientation state is visible. In slit-expansion flows, a bimodal state of orientation is observed due to the variation in shear and elongation rates through which the X-ray beam propagates (figure 12 of reference). One population near the walls remains directed downstream (at a finite shallow angle to the channel walls, as predicted for a tumbling material), whilst the population in the extensional expansion region lies perpendicular to local streamlines as a result of the

transverse stretching flow (surprisingly, at contrast with the groups earlier work). Weaker but similar orientation effects are seen in gradual expansions (i.e. alignment is a function of elongation rate, as might be expected). Other geometries, such as an obstruction and a 90 degree bend (of square geometry) corner was also investigated. Flow around bends is of interest in chapter 5.

Comments are made as to the difficulty in simulating the flows of LCP (liquid crystalline polymers), particularly with regards the generation of defects and textures which are of practical interest, and that "there is still an urgent need for improved understanding of the behaviour of LCPs under experimentally relevant conditions", underlining the general importance of improving existing fluid models (under extensional flows).

Trebbin et al. (2013)

Trebbin et al. (2013) performed microfocus SAXS measurements and polarised optical microscopy on aqueous solutions of anisotropic cylindrical block copolymer micelles under pressure-driven flow in microchannels. This was to consider the assumption that anisotropic particles align parallel to the flow direction. PDMS was used as an x-ray transparent material from which to fabricate the channel. These measurements were followed by PIV (particle image velocimetry) where the existence of the extensional region is observed, and comparison to CFD flow models set up based on the measured shear thinning behaviour of the micelle solutions.

In their study, the qualitative correlation between orientation information in the X-ray scattering (alignment information) and polarised light measurements (stress information from birefringence) is generally excellent - despite any issues previously of shear near walls which one would expect optical microscopy to better reject. Regions of birefringence also corroborate with extension rate measurements from PIV. Similarly to the previous reference, they find that the particles increase in alignment parallel to the flow direction on entering a narrow channel section along its centreline, and transition from no preferred orientation to a perpendicular alignment at the exit. Equally they conclude this to be a result of perpendicular extension in the expansion zone. This alignment remains stable downstream and is only disrupted by a second contraction-expansion. Also, in an identical manner to the previous reference, parallel alignment to the flow direction is observed near to the channel walls where shear flow dominates in upstream parallel channel sections, a bimodal orientation state is observed across the width of the channel expansion, and in curved channel sections the molecule alignment tracks the flow streamlines. They have found that the perpendicular orientation in the

expansion to be a general feature, displayed by other systems such as different block copolymers, different concentrations, different channel geometries, as well as with other particles including disk-like micelles.

Importantly in terms of evidence of molecular alignment affecting shear viscosity, in their PIV work they observe two different, but hydrodynamically stable velocity profiles across the channel upstream and downstream of the contraction-expansion region. These are reproduced in figure 3.1. Upstream of the contraction, the velocity profile has "a broad but clearly noticeable maximum", and downstream the velocity profile is "nearly flat, similar to plug flow"; they state "...these differences are caused by the different viscosities parallel and perpendicular to the local mean orientation of the micelles (i.e., their orientational distribution), similar to nematic liquid crystals" – As highlighted earlier, and essentially evidence of elongation coupling though to shear viscosity. Similarly, whilst the CFD simulations also show good qualitative agreement to the PIV measurements, the difference in upstream and downstream velocity profiles is not present in their CFD results, a direct result of it only considering an isotropic non-Newtonian, shear thinning fluid description.
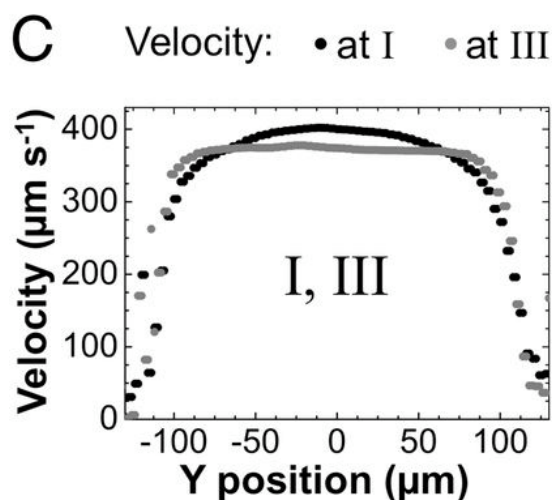
Figure 3.1: Extract reproduced from figure 4 of Trebbin et al. (2013), showing the velocity profiles running across (Y position) their contraction-expansion geometry at two locations. Position (I) is located just upstream of the contraction, and (III) just downstream of the expansion.

Martin et al. (2016)

Martin et al. (2016) performed a very similar structure of work as Trebbin et al. (2013), using SAXS and polarised optical microscopy to study the structural changes in hexadecyl trimethyl ammonium chloride surfactant in a ternary system. Such systems are said to self-assemble to

form stable microstructures referred to as lyotropic liquid crystalline phases. A PDMS based microfluidic geometry is used featuring straight channel flows, contractions and corners (amongst others), and essentially the same qualitative observations are made with regards alignment from the X-ray scattering patterns. Additional comments are made on the effect of flows on the spacing of lamellar, which are found to be affected by extensional regimes (though only modestly in terms of spacing change) and this is monitored to study long term (20s+) relaxation effects after deformation.

Note that there is a very significant difference in polarised light microscopy image appearance from the contraction-expansion regions compared to the previous reference. Previously, a very strong indication was present in the optical images that a parallel-perpendicular orientation shift had occurred in the core of the expansion flow, directly correlating with the SAXS scattering patterns showing transverse alignment. Here, inspecting the centreline of the channel shows it to be generally featureless throughout the contraction-expansion, and predominantly only off-symmetric features are visible. Rotational flow around corners in a separate geometry appears generally similar to the previous reference, but on examination of the figures extinction occurs at 90 degrees around the 180 degree bend. In their discussion they state that "within the constriction, the lamellar structures are highly aligned parallel to the flow, exhibiting an effectively single crystalline order and thus very little birefringence" (i.e. signal in the optical microscopy images). However it may be the case considering the rotational flow that only off parallel/perpendicular alignments are being highlighted. The lack of signal still therefore corresponds to a high degree of alignment, but not directly. Whilst the test fluid differs and the geometries are slightly different, this may well be due to a difference in the optical setups. The previous reference incorporating a quarter-wave plate in some manner, the current reference uses a cross-polarised setup (the exact optical setup is not well documented in either reference).

In this reference, a consideration is presented of the effects of these microstructural changes on rheology. Their test system is shown to be shear thinning (with measured plug-like velocity profiles) and quite history sensitive (min-hours), which mirrors the discussion of relaxation effects on lamellar spacing and that the system is self-assembling in nature. Particularly in terms of rheology is that they consider the effect of extensional flow on shear rheology. To achieve this, the mixture is injected through a needle to load a Couette geometry to keep the timescale comparable with the fluid relaxation time. The samples loaded using the needle show a considerably higher shear viscosity than a standard sheared sample (viscosity measured over time at $0.001s^{-1}$ shear rate), and this is related to the changes in structure from

extensional flow – presumably the expansional flow and die swell (if it occurred) on exiting the needle. This is the only direct experimental example found of the effects of extensional flow on shear viscosity, if albeit this is ex-situ and somewhat qualitative in nature.

McLeish et al. (2009)

As part of their review of the use of SANS for testing molecular rheological models, McLeish et al. (2009) highlight work with linear chains, bimodal linear chain blends and linear/branched polymer blends through a 4:1:4 planar contraction (10 : 2.5 : 10mm contraction – expansion width, 20mm long 2.5mm section, 10mm depth, highest wall shear rates 59s^{-1} with maximum extension rates at the centreline of 11s^{-1}). Similarly to the X-ray work previously highlighted, they too observe an enhancement in parallel alignment of molecules around the contraction region, and an enhancement in perpendicular alignment on exit, for example as per figure 3 (anisotropy plots, linear chains) and figure 5 (2D scattering patterns, branched chains) of the reference. Perpendicular alignment on exit is not however observed for a bimodal blend, a factor attributed to the higher Weissenberg numbers and shorter slit residence times achieved in these experiments (i.e. anisotropy from the entrance region has not been erased by the time the flow reaches the expansion). Interestingly, they also observe, as shown in figure 3 of reference, that the principle stress difference from birefringence decays much faster than the anisotropy from the SANS data, an indication that these two parameters are not directly coupled as might be thought for a completely elastic system.

3.7   Publications investigating the effects of shear on extensional viscosity

Compared to the hypothesis of investigating the effects of extensional rheology on shear, there are examples in literature were the converse has been considered – The effect of shear on extensional rheology: albeit all these were performed in a non-simultaneous manner, e.g. a period of shearing followed by a period of extension. The examples presented here are of the work by Wunderlich and James (1987) and that of Vissmann and Bewersdorff (1990) as they are similar to each other; followed by the notable SHERE (Soulages et al., 2010) and SHEREII experiments (Jaishankar et al., 2012). One of the earliest studies in this area appears to be that of James et al. (1987).

Wunderlich and James (1987) and Vissmann and Bewersdorff (1990)

Wunderlich and James (1987) studied the effects of pre-shear on the extensional rheology of dilute aqueous polyacrylamide (PAM) and surfactant (C$_{16}$TA-Sal +NaBr) solutions, the former with and without additive salts to affect polymer coil extension. To achieve this, they used a rectangular cross section channel with a contraction (presumably radial, given cited references)

in the side wall. Independent control of the flow rate through the main channel and the side channel was used to alter the pre-shear rate and elongation rates respectfully. Pressure taps opposite the contraction entrance, and after the contraction measured the pressure loss over this region of extensional flow; the results being compared as a ratio to the pressure drop for water at identical elongation rates. The elongation rates and shear rates are rather generally defined, the "peak" elongation rate is estimated from a separate equation and the pre-shear rate is based on fluid near the rectangular channel wall being captured into the contraction (flow instabilities reported make this assumption rather fragile, however). Flow regimes in this area were inspected visually with a tracer dye.

Following this, Vissmann and Bewersdorff (1990) conducted a broadly similar study to that of Wunderlich and James but with a revised approach. They studied dilute polyethylene oxide (PEO), polyisobutene (PIB), polyacrylamide (PAM), and surfactant (C_{16}TA-Sal + NaBr) solutions. They recognise the issue that the rectangular channel in the previous reference does not produce a constant shear field, in their experimental work this is replaced by a modified Couette geometry rheometer with interchangeable abrupt orifices in the outer cylinder. A more in-depth consideration of the pressure drops across the orifices used under extensional flow is also performed to provide a value of extensional viscosity (rather than reporting pressure drop ratios); pressure drop from shear flow being part of this. Due to the variation in elongation rates across and down a streamline entering the orifice, an approximation for the elongation rate still has to be used. The pressure taps of the previous study are replaced by placing the rheometer system under positive pressure. Note that whilst neither source comments on this, pressure taps are well known to exhibit "hole pressure errors" with viscoelastic fluids as per chapter 1: certainly locating one tap opposite a contraction which also has a strong shear flow superimposed on it (together studying changes in the shearing rate) which will not assist matters in the first reference. A positive pressure approach is conversely, also not perfect, with upstream and end effects being important. Another complicating matter for the question of molecular alignment (being asked here) is that in both systems, it is not necessarily obvious in what manner an orientation developed in shearing region would translate to (perpendicular or parallel?) in the extensional region.

For the PAM solutions without added salts presented by Wunderlich and James it was found that the contraction pressure drop ratio was enhanced with PAM concentration, increased then decreased with elongation rate, and decreased with increasing application of pre-shear. However, disturbances around the contraction were observed. The reduction in these disturbances at higher shear rates was suggested as an indication that non-Newtonian stresses

had been reduced, thus reducing the extensional viscosity (shear thinning is discounted due to the high Re values in the contraction). Vissmann and Bewersdorff also attempted to characterise a PAM system but also observed instabilities in the orifice inflow, noting the same instabilities commented by Wunderlich and James, and concluded that their experimental setup was unsuitable for studying this system.

On the other hand, both groups studied essentially the same surfactant system, and as Vissmann and Bewersdorff commented, good qualitative agreement was found. The elongational viscosity (or pressure drop ratio) starts off at a low value without pre-shearing, and is dramatically enhanced with pre-shearing. This is attributed by Vissmann and Bewersdorff (and in a similar manner by Wunderlich and James) to the formation of a shear induced state (or network) by the pre-shearing, where the shear viscosity rises rapidly (with a corresponding effect on the extensional viscosity, noting that a Trouton ratio of 3 was maintained). Increasing elongation rates or high shear rates correspondingly served to break down this network and reduce the elongational viscosity.

Vissmann and Bewersdorff studied PEO, worthwhile of comment as this system is used as a test subject in chapter 8, and presumably did not feature instabilities in their tests like the PAM samples. Elongational viscosity was found to be equivalent to the shear viscosity of the Newtonian solvent over a range of elongation rates without shear (agreeing with a reference in fig. 14 of Wunderlich and James). Above a critical amount of pre-shear it was found to increase with shear and generally with elongation rate (contrasting with both the PEO and PAM behaviour in fig. 14 of Wunderlich and James), a phenomenon they attribute to the stretched molecules in shear flow being "orientated in the direction of the elongation in the transition region from shear to elongational flow" (though but no proof of this direction of orientation is presented). Such a requirement for pre-shear before PEO will exhibit non-Newtonian effects under extensional flow is surprising, especially as PEO appears somewhat of a mainstay of extensional rheology samples in literature. Perhaps on account of their dilute system some pre-extension of polymers under shear (which continues for a far longer time/total strains than the extensional flow), if this were occurring, may be necessary to enable inter-molecular hydrodynamic interactions to occur once molecules reach the orifice. They report similar behaviours were found for one of the two PIB solutions examined in regimes where vortices were not formed, but with a lesser dependence on elongation rate. See the source for more details.

SHERE (Soulages et al., 2010) and SHERE II (Jaishankar et al., 2012)

SHERE (Soulages et al., 2010) and SHERE II (Jaishankar et al., 2012) were filament stretching extensional rheology experiments performed on the International Space Station in microgravity. Use of microgravity mitigated filament sagging below the midpoint which would otherwise occur on earth with low viscosity systems and/or low strain rates, permitting extended timescales before filament breakup for evolution analysis .These studies investigated the effect of a period of rotational pre-shear on fluid sample transient extensional viscosity. The sample between two circular plates was rotationally sheared, before the plates were exponentially moved apart (uniaxial extensional flow). During and after the filament extension, the filament radius, shape, and tensile force were monitored as in standard filament stretching experiments. SHERE investigated samples of a dilute high molecular weight polystyrene dissolved in oligomeric styrene oil (forming a Boger fluid). Equivalent experiments were conducted on Earth with a modified FiSER instrument by Anna and McKinley (2008). SHERE II used the same fluid as SHERE, but filled with 6μm PMMA microspheres. Compared to the two references presented previously, with this approach it is not particularly obvious how any orientations developed in the shearing phase would of actually translated to the extensional phase of the experiment.

In SHERE and SHERE II, extensional strain hardening was observed in both the stretching and subsequent elastocapillary phases. In SHERE and SHERE II (at $3s^{-1}$ elongation rate) they found that increasing pre-shear rates had a definite effect in reducing ("delaying") the apparent extensional viscosity of the samples at equivalent points of Hencky strain during the filament stretching phase, attributed to the "orthogonal pre-orientation of the polymer chains with respect to the stretch direction". In SHERE II at $5s^{-1}$ elongation rate, the effects of the pre-shear were found not to be strong enough to affect the extensional viscosity. In SHERE the pre-shear also appeared to enhance the strain hardening in the subsequent elastocapillary thinning regime, which was verified on Earth but had yet to be explained.

In conclusion with regards the effects of pre-shear on extension, the work by Vissmann and Bewersdorff (1990) (for example) generally showed pre-shear to have a rather significant effect on extensional flows. Conversely, the SHERE experiments should it to be very slight (in line with extensional flows overpowering orientation from shear flows). Despite probable differences in pre-orientation, measurement processes, and the different systems studied, such a substantial difference in outcome would not be expected. Either way, there is some evidence of (prior) shear flows affecting extensional rheology in literature.

3.8 Evidence summary

From the references presented, we see that there is a high probability of elongational flow affecting shear viscosity. It has been shown that the models normally used in the modelling of viscoelastic fluids – Even the simple OLB model - capture a shear viscosity dependence on elongation rate. Molecular dynamics has further provided evidence of a direct link between the two parameters. From an experimental standpoint, with combinational X-Ray and polarised light studies, we know that elongational flow fields have a definite effect on molecular alignment. From the field of liquid crystals, we then understand that orientation of molecules (or at least anisotropic structures) generates definite effects on shear viscosity. The X-Ray studies highlighted have even provided preliminary evidence that elongational flows do modify shear viscosity.

It is clear from the pre-sheared extensional flow studies that conversely, shear affects elongational viscosity, despite the complexities of performing accurate extensional flow measurements. However, no evidence has been found so far of the converse being rigorously considered in literature (in an experimental sense, and particularly in a simultaneous manner) apart from general statements surrounding the interplay between flow fields, molecular alignment, and rheology. It appears from the X-Ray data and SHERE experiments at least that extensional flows tend to overpower shear flows in practical settings, so with a suitable experiment we would expect to see a definite dependence of shear rheology on extensional flow. In particular, we would expect this to be dependent on the direction of the extensional and shear flows relative to one another (as found by Evans and Heyes (1990)).

3.9 Principle experimental requirements

In order to measure the shear rheology of a flow field, a known rate of shear is required together with a known shear stress at that location. To test the hypothesis with simultaneous shear and extension, by definition fluid at this location must also be undergoing extensional flow – a complicated proposition. Here we consider how this could be achieved.

The first system worth commenting on is the floating strain gauge fin converging channel design outlined in chapter 2: Recall that this system was side-lined for conventional rheology on the hypothesis that extensional flows might affect shear rheology. Aside from the issues practical issues of the strain gauge fin, and initially, the lack of shear rate measurements provided, the problem is that at the location of shear stress measurement (the fin wall), a fluid packet does not propagate into the converging channel. Thus, the elongation rate of a fluid packet at this location is zero (as noted earlier as per Cogswell (1978)). For shear rates

measured at this location, the wall shear stress is thus only affected by conventional shear rheology.

Taking this concept further, we know from Trebbin et al. (2013) that extensional flow modifies the velocity profile across the channel. We also know, as highlighted in section 2.1, that ultrasound and NMR velocity profiling is capable of mapping the velocity fields and, when combined with a pressure drop measurement, can convert this directly into shear rheometry data. Perhaps in a way, these techniques may enable the known shear stresses at the wall to be "propagated" out to some location in the flow field, where extensional deformation would be occurring. For experimental work on transparent or translucent fluids, the complexity of UVP or NMR could be replaced with simpler optical PIV measurements. Velocity profiling conveniently resolves both shear and elongation rates, making it easy to associate each point on a shear rheometry curve with the appropriate elongation rate.

The problem with such an approach is that firstly, the fluids of interest, as per in the velocity profile plots of Trebbin et al. (2013), are highly shear thinning. This means that a large proportion of the fluid shearing is contained in a narrow, sometimes difficult to resolve region, right at the channel wall. The wall shear stress in any inversion method must presumably be assumed to propagate though this region to reach the central, extensional flow of interest at the channel centre. This makes this approach difficult to perform accurately. Recalling the discussion in section 2.2, the pressure drop measurement which scales viscosity would similarly complicated by the issues of hole pressure measurement errors. These errors would no longer cancel with a converging (as opposed to parallel) channel and flush mounted transducers would again be required. A single point wall shear stress measurement would be better, i.e. by the strain gauge fin or other suitable method, equally as previously discussed, but still not a straightforward proposition.

As a result of the above considerations, what is needed is a method of measuring shear stresses at a location that is also propagating into the contraction, not fixed to a channel wall. Figure 3.2 on the following page shows a simple geometry by which this might be considered, consisting of a rotating cylinder placed off-axis within a larger outer cylinder. The gap between the two cylinders is filled with test fluid which is pulled into the contraction region by rotation of the inner cylinder; regions of parallel and perpendicular elongation relative to the shear direction is indicated. This geometry has in fact recently been investigated by Tian et al. (2016) as a means to produce controllable mixed shear/extensional flows.
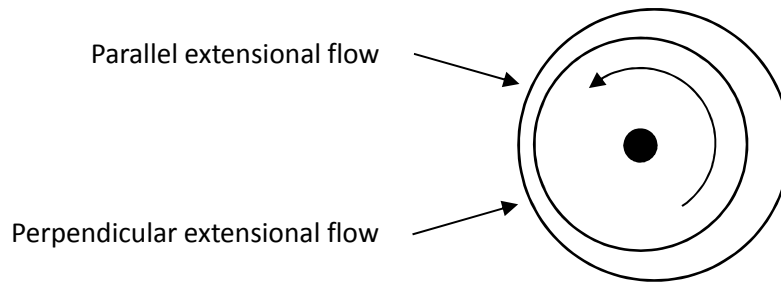
Figure 3.2: Off axis rotating cylinder geometry for generating mixed kinematic flow fields

In this geometry, the surface of the inner rotating cylinder is, in effect, propagating into a contraction zone due to the eccentricity of the setup. The torque on this cylinder, is unfortunately, a function of the shear stress around the entire circumference, which would make analysis almost impossible. Furthermore, elongation rates and flow histories vary dramatically across the gap, and velocity profiles differing from that assumed for Couette flow, induced from extensional flow variations in shear rheology, could not be ruled out.

Let us consider, for a moment, that a (rather difficult to achieve, but nonetheless) micro-electrical mechanical sensor (MEMS device), capable of measuring wall shear stress, is mounted flush to the rotating cylinder wall. This sensor therefore provides a shear stress measurement at one well-defined location, and a location that is propagating into the contraction. Furthermore, suppose that that the shear rate directly above the stress sensing surface was measured by some other means (for example, an optical technique). There is a second problem: For a fluid packet to elongate, a more rigorous definition is that it must be accelerating, or vis, the front face of the fluid packet is travelling along a streamline faster than the rear face. For zero wall slip on the inner cylinder / MEMS sensor surface, a fluid packet may be indeed propagating into the contraction zone, but it cannot elongate, and thus the elongation rate is still zero.

We now realise that what is required, is a method of sensing shear stress, at a location that is propagating into a contraction along with the test fluid, which either allows a velocity gradient along its surface (i.e. wall slip) or otherwise is elongating itself. The key is arguably in the concept of wall slip.

Extensional rheology experiments attempt to minimise or eliminate wall shear, as this introduces shear forces and modifies the distribution of elongation rates as previously mentioned in chapters 1 and 2. Fibre spinning and filament stretching type experiments

eliminate wall shear completely by freely suspending the test fluid, but eliminating the wall also eliminates the capability of performing shear rheology measurements. In extensional flow experiments, artificial wall slip is occasionally attempted by the introduction of a "lubricant" between bounding walls and the test fluid, examples will be highlighted next. Suppose this lubricant is Newtonian (i.e. an oil, water, or other appropriate substance) and suitably immiscible with a test fluid of interest. The force of shearing of the test fluid, on one side of the interface, propagates through the interface (regardless of interfacial slip) to the lubricant phase. This means that, if the viscosity of the lubricant is known, and shear rates in both the lubricant and test phases measured either side of the interface (i.e. optically, via PIV), then the shear viscosity of the test fluid – under extensional flow – could be determined. As both fluids are free to extend, the condition of extensional flow at the measurement location is satisfied.

This key concept is highlighted in figure 3.3 for a 2D, two phase, "wedge" flow. For a real world flow, this measurement would be performed at the mid-plane of an ideally "shallow" aspect ratio channel (defined and illustrated here for stratified flows, and used similarly in later chapters) as an interface span width across channel greater than total thickness of phases. A "tall" aspect ratio would be the converse. This imaging location, assisted by the choice of aspect ratio, eliminates lateral shear across the channel at the measurement location, subject to the critical assumption being made of interface symmetry across the width of such a channel.

We also make the assumption that shear force is continuous across the interface (slip is acceptable, however). This assumption depends on the rheology at the interface being similar to that of the bulk liquid phases, with consideration given to the interfacial shear and extensional rheology (a field of rheology in itself). We can make the assumption that that stresses required to deform the bulk of the liquid phases will be in excess of any interfacial contributions. However, using figure 3.3 as an example, a substantial increase in either shear or extensional interfacial viscosity beyond that typical of the bulk of the phases would serve to divert stress being applied by the "pulling" aqueous phase away from "pulling along" the lubricant phase by shear stresses.
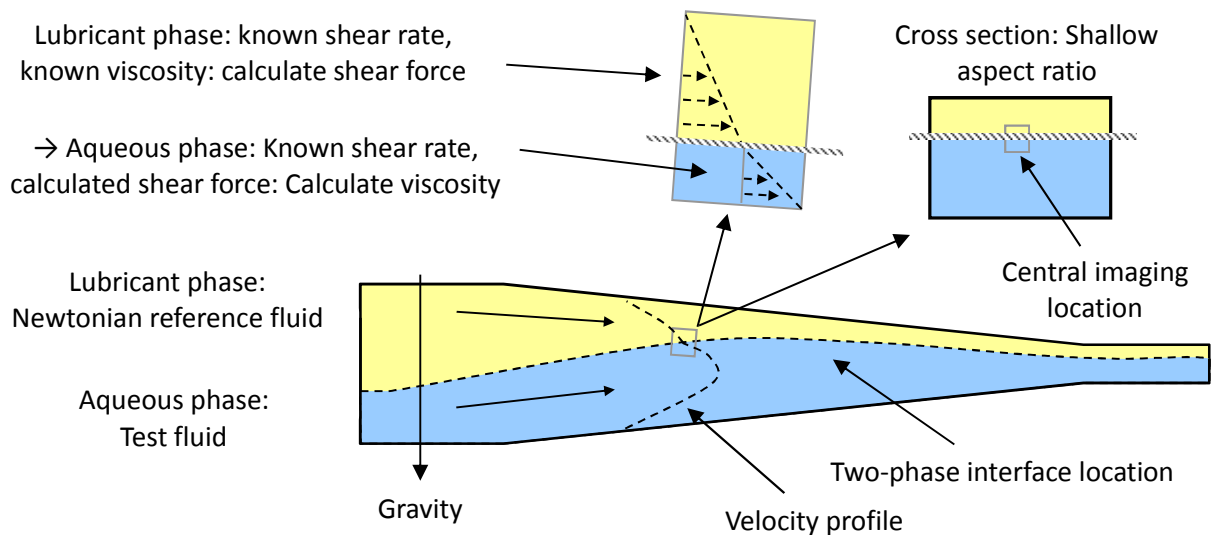
Figure 3.3: Concept of using lubricant to enable shear viscosity measurement within a wedge shaped converging channel

3.10 Review of lubricated extensional experiments

As it is now evident a form of lubricated extensional flow is required, a review of those who have attempted this is relevant. Focus will be specifically in a practical rather than theoretical setting, and concentrating on approaches to and problems with maintaining lubrication, with a few additional comments. Note that as it will become clear, the following sources consider both immiscible and miscible lubrication: using a miscible lubricant in this present study is not practical due to possibility for variation in the reference phase composition, and thus viscosity.

Extensional flow experiments that have implemented lubricated walls can be essentially divided into two categories: Those with non-parallel static walls, and a pressure driven flow (the profiles such walls are considered in chapter 5), and those that "squeeze" a sample between two approaching walls. Arguably systems with rotating lubricated surfaces could also be imagined akin to Tian et al. (2016), where a test and a lubricating fluid would be simultaneously dragged into a contraction. Pressure driven flows with static walls will exclusively be investigated here.

To underline why "squeezing" flows are not suitable, consider for argument examples of Chatraei et al. (1981) and Venerus et al. (2008), (2010). In both, two circular disks squeeze a sample placed between them, the former is pre-lubricated by being immersed in an oil bath, and the latter by lubricant fed in via porous plates which also form the squeezing surfaces. This system is only amenable to studying relatively solid samples which can be easily loaded (gums and polymer melts respectively), not flowing liquids desired here, and equally not with thick

layers of lubrication. However, methods can be imagined by which this system might be adapted to liquid lubrication with liquid samples, for example squeezing liquid phases together in a tank. The major drawback is that this type of experiment is not steady in the Eulerian sense (i.e. at a point) compared to experiments using pressure driven flows. This makes gathering data a one-time exercise and rather more difficult. As such a system offers no other obvious benefits (apart from perhaps a more direct control of extension rates) they will not be considered further.

Following a similar argument that continuously running extensional flows are desired, lubricated converging flows can be divided into two categories: Those that use a pre-lubricated sample (or channel), and those which continuously inject lubricant through some means. The latter is desired here, as in the former the lubricant is stated to (or otherwise would eventually) be squeezed out from the experiment in all cases. Pre-lubricated flows will be noted to trace the development of the lubricated flow technique and comment whether lubrication was successful.

The first significant reference of experimental lubricated extensional flows appears to be that of Shaw (1975). He looked into the extrusion of polyethylene melts through a conical, pre-lubricated (with silicone grease) converging extrusion die to study melt fracture in die entry regions. Extensional flow is thought to have been promoted in preference to shear flow by the lubrication: not only were pressure drops lower with lubrication, but increased melt fracture was also present. This was thought to be due to a much sharper flow convergence angle occurring compared to the unlubricated case, thereby generating higher tensile stresses.

Whilst a review paper, Cogswell (1978) detail a speculative extensional rheometer using lubricated flows (see footnote shortly). They also acknowledge Shaw (1975) and also that of Snelling and Lontz (1960) in a section on lubricated flows, though the form of "lubrication" in the latter is not that sought here.

Around this time, Everage and Ballman (1978) detail a profiled, presumably uniaxial, lubricated extrusion die for polymer (here polystyrene) melts, designed to attach directly to an extruder barrel. Lubricant is continuously fed into the die. They also reference discussion (British Society of Rheology, 1977) of a speculative rheometer "of apparently similar design" (see footnote shortly). In their work, instabilities were found if the sheath to core flow rate was too low and also state that "…details of the design and operation of the rheometer… will be presented elsewhere", but unfortunately no trace of this can be found.

Following this, Winter et al. (1979) present a framework detailing the utility of orthogonal stagnation flows for extensional rheometry. A number of geometries are presented for achieving such flows including an ingenious (if slightly impractical) profiled porous tube. Whilst converging channels do not strictly feature a stagnation point, they also briefly present some of the first images of lubricated uniaxial extensional flows to appear in literature. These flows of aqueous polyacrylamide solution, conducted in a transparent channel, are contrasted directly to flows without lubrication. They found that using insoluble silicone oil as a lubricant generated flow instabilities as "the oil would not uniformly wet the walls". As a result they use (and suggest as a future design consideration) a miscible (water) lubricant layer. Fuller details of these lubricated flows were presented in an obscure conference proceeding (see the reference for details).

Following their previous work, Macosko et al. (1980), (1982) present preliminary results of a lubricated planar stagnation die. This was used on a polystyrene melt with silicone oil (1 Pa.s, temperature not stated) as the lubricant, and dedicated channels were incorporated into the die to distribute the lubricant at the entrance of the polymer melt. Consideration of the pressure measurements is made as to the effectiveness of the wall lubrication. A new die with glass end windows was hypothesised to allow study of the whole flow field.

van Aken and Janeschitz-Kriegl (1980) describe and then present (1981) further results from a lubricated biaxial extensional rheometer used on polystyrene melts. Two identical samples are forced by rams towards a symmetric stagnation point, the force separating the dies being measured. As with Shaw (1975), the samples are pre-coated with a silicone oil, (10^3 Pa.s at 170°C) for lubrication, and similarly the lubricant layer thickness is reduced as "the lubrication layer is pressed out of cylinders together with melt" (van Aken and Janeschitz-Kriegl, 1981); adding additional lubricant though holes was not considered desirable. The effectiveness of lubrication was demonstrated by coloured slices incorporated into the polymer samples during their experiments. However, it was noted that lubrication layer quality varied from other analysis work.

Williams and Williams (1985), detail a lubricated planar stagnation flow rheometer of quite appreciable scale (i.e. 90L samples) which became known as the "CFR" or "Converging Flow Rheometer" in literature[1]. There system is perhaps the only example of a bounded, lubricated

---

[1] The CFR was constructed and operated at the Rutherford Appleton Labs, England. The BSR reference in Everage and Ballman (1978) points to a "speculative" lubricated flow rheometer being considered at this site; as do the comments of Cogswell (1978). It seems likely that these are all the same instrument.

stagnation flow in literature. An experimental comparison of this system later features in Jones et al. (1987), and further analysis of results presented in Binding and Jones (1989) and Zahorski (1992). This system was used to measure, via pressure drops, the extensional properties of a Newtonian (maltose syrup and water) and Boger (maltose syrup, polyacrylamide and water) systems. Careful attention is given in their design to distributing lubricants into the experiment, and allowing some period of fluid relaxation before the test section, which is rarely commented on. Two different lubricants of different densities were required above and below the test fluid to avoid buoyancy issues. They found that slightly miscible lubricants performed best, with both wholly miscible and immiscible lubricants gave rise to "serious problems of stability of flow balance" (presumably between the two symmetric sides of the instrument, but no doubt instigated via some form of interface instability). Further considerations of criteria for stable lubricant interfaces are also mentioned. They also report issues, under some operating conditions, with the (visually observed) lubricant layers being displaced by the sample in the test section before they became ineffective even with their continuous supply into the instrument. For runs with the Boger fluid in contrast to the Newtonian sample, maintaining the stability of the flow field at higher flow rates was found to be very challenging, with "the sample tending to displace the lubricants by sweeping them before it" (unfortunately no images are presented of this). Perhaps due to these difficulties Jones et al. (1987) were in fact looking to phase out this system if a more convenient and easier alternative could be found.

Khan and Larson (1991) performed step (rather than steady rate) lubricated planar extension experiments on polyethylene melts and compared it to step shear data, to test the concept that the response to the two deformations should be related in a simple manner. Pre-lubrication of the channel was performed with a high viscosity silicone fluid, the viscosity a compromise between eliminating shearing deformation in the sample and being squeezed out during the step strains. For their limited strains, no lubrication failure was observed.

The most recent macro-scale lubricated flow work appears to be that by Kim et al. (1994) (accompanied by letters, Dealy (1995) and Pendse and Collier (1995)). See also Collier et al. (1998). They describe an experimental framework for polymer melt extensional flow experiments through profiled converging dies with lubricated flow, where the lubrication is achieved not by greases or flowing lubricants, but by an ingenious skin-core structure of two polymers with a large difference in their melt viscosities. Work has also recently been reported by Soulages et al. (2008a) (see also Soulages et al. (2008b), Abedijaberi et al. (2009)) using a lubricated planar cross slot geometry. However, in their work lubrication is used on the front

and back walls to improve the planar assumption in lieu of optical measurements through the cell, rather than being applied on the profiled side walls of the channel as sought here.

Recently with the growth in interest in microfluidics, this field of research has been applied to extensional rheometry, as summarised in the review by Galindo-Rosales et al. (2013). Most techniques are based on some form of "hydrodynamically focussed" flow where a central core fluid, entering a channel from one end, is "focussed" into a controllable and moveable sheet or thread, by flows of a second fluid brought in either side. This is often achieved in a "cross slot" like geometry as used for stagnation flows, but instead with three inlets and one outlet port.

The geometry in the numerical study by Oliveira et al. (2008), comprising of a flow focusing section, and the same in reverse downstream, is interesting as it would permit significant relaxation timescales prior to an expansion region, without accruing high pressure drops in a narrow channel. Unfortunately no experimental results appear to have been published to date as far as ascertainable – no doubt ensuring a long, thin, stable filament, as well as separating the flows at the second cross slot, might be challenging.

More general information on hydrodynamically focused flows can be found in, for example Dziubinski (2012). What is important is that this focussing effect constitutes an extensional flow field and is essentially akin to lubricated converging channels, conferring the same effects of minimising shear. Furthermore, microfluidic experiments are usually accompanied by optical measurements, so much more information is available concerning the structure adopted by the flow fields.

Concentrating on immiscible flows, Arratia et al. (2008) used this technique to study filament thinning and breakup (to determine the extensional rheology) of dilute polymer aqueous solutions, using an external immiscible fluid to stretch the test fluid. In their geometry, attention made to ensure that the channel walls have uniform wettability (continuous surface of polydimethylsiloxane, PDMS) and treated such that they are hydrophobic, thus continuously wetted by the outer liquid phase (a mineral oil with a small amount of surfactant). Lee et al. (2011) perform a similar piece of work looking at the effect of viscoelasticity and surfactants on thread formation, using a slightly different geometry and different fluid viscosity ratio. Again, an immiscible mineral oil phase with surfactant and aqueous polymer test phase is used and the same considerations are given to wall wettability. Whilst in both references a 2D entrance zone is used and no experimental evidence is presented in either as to the actual flow field cross section; the attention to wall wettability and their channel shapes (50μm wide, 30μm

deep, and channel 200µm wide, 100µm deep respectfully), should presumably of produced filaments travelling down the outlet channels well detached from the bounding walls, as required by their analysis.

In terms of the geometry that the two fluid phases obtain, these fully encapsulated fluid filaments can now be contrasted with the work by Guillot et al. (2006), (2008) and by Wang et al. (2010), Wang and James (2011) both also using immiscible systems.

Guillot et al. (2006), (2008) develop a microfluidic shear rheometer by flowing two immiscible parallel laminar streams side by side in a micro channel, one a reference phase of known viscosity and the other a test phase. The position and shape of the interface is monitored by observing the contact lines on the channel walls. This interface information is then used to compute the viscosity ratio of the test fluid from that of their reference fluid and the imposed flow rates of the two phases (with certain assumptions and approximations being made).

Their work is particularly valuable here, as it is the only reference seen where detailed cross sections of the interface shape are presented, if slightly complicated as unlike the other references presented three channel surfaces are PDMS and one is glass. In Guillot et al. (2006) these images (figure 3 and 4 of the reference, depicting both 100µm x 100µm and 200µm wide by 100µm deep channels, the latter being a "tall" aspect ratio channel as previously defined with respect to the vertical interface) show quite how significant the interface curvature is, and how it is distorted by the non-uniform surface wetting. Figure 4 of the reference is reproduced in figure 3.4 showing the downstream condition in the two geometries.
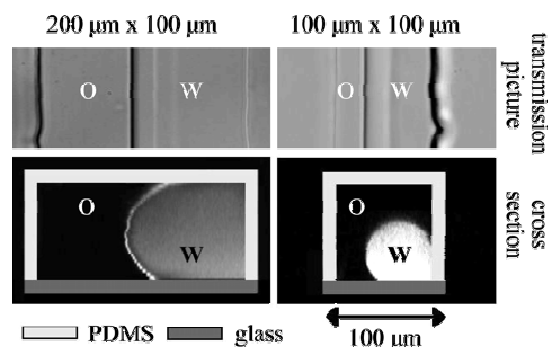
Figure 3.4: Fig 4 reproduced from Guillot et al. (2006). "Cross-sectional picture of the parallel flow between hexadecane (O) and the aqueous phase with rhodamine (W) in a 200 µm x 100 µm and a 100 µm x 100 µm microchannel".

In particular for the square profile channel, the initially roughly symmetrical distribution of the two phases transitions to a completely asymmetrical configuration downstream, with the aqueous phase appearing to preferably wet the glass wall and the oil phase the PDMS walls. In the further development work of Guillot et al. (2008) the 200x100µm channel is adopted, it is stated that this channel shape greatly increases the range of flow rates for which a stable parallel flow may be obtained compared to a square geometry. Furthermore, in this geometry the water phase is (for the conditions shown in the reference) not completely wrapped by the oil phase and remains in contact with the upper and lower channel walls, however the interface is still slightly asymmetrical due to wettings differences and nonetheless still highly curved. Issues of interface curvature and wetting are investigated in chapter 4. Note that Nguyen et al. (2008) used a flow focusing as an alternative approach for the same purpose as that of Guillot et al. (2006), (2008) but with a miscible system producing what is assumed to be a vertical sheet of the focussed test fluid, rather than a two-layer system, though no definite measurements of this are given.

The work by Wang and James (2011) (summarised in Wang et al. (2010)) is perhaps the closest, in terms of flow geometry and layout, to what is desired in the experiments here. Converging flows of viscoelastic (PEO in a water/PEG solution) solutions in a lubricated hyperbolic planar micro channel were studied, for the purpose of extensional rheometry. In particular, the contraction region in their work features a "shallow" aspect ratio as desired relative to horizontal distribution of the lubricants and test phase (26µm wide by 46µm deep), rather than the "tall" aspect ratio of Guillot et al. (2008). The lubricating fluids are brought in either side of the test fluid, and both miscible and immiscible lubricants were tested. The four channel walls were again arranged to all be coated in PDMS. For a miscible lubricant (DI water), in the wide upstream area (500µm wide by 46µm deep) the test phase was bounded on either side by the lubricant, however in the contraction the test fluid was fully enveloped by the lubricating phase. This is highlighted by the authors as being consistent with the work of Cubaud and Mason (2009) who also studied miscible fluids (for both square and planar geometries). This miscible system was however found to be unstable (wobbling) when used with viscoelastic systems. For the stable immiscible case with significant interfacial tension (perflurohexane as the lubricant), the test fluid remained bounded on either side by the lubricants even through the contraction, and even when surfactant was added to lower interface tension (which reduced the stability of the interface). No evidence of the exact profile is presented, however the source indicates that the interface is slightly slanted from the vertical, and that this "confirmed by confocal microscopy". This interface structure would be ideal for the present work, with the channel aspect ratio here, and will be looked at further in the following chapter.

From these four references for micro channel flows, it can be seen that both (presumably) fully encapsulated threads and (essentially) stratified flows have been produced for immiscible micro channel flows. Note that this contrasts to Galindo-Rosales et al. (2013), where these references are presented, as they state for immiscible fluids that "the core fluid remains attached to the top and bottom walls"; the source of this statement is unclear.

In summary from this review, what is clear is that interfacial effects have a crucial role on the flow configuration and stability in multi-phase experiments, particularly for non-melt systems where the viscosities are lower and indeed more analysis work has been performed. As the scale of the experiments is reduced, there appears to be a trend away from miscible systems for stability, (i.e. Winter et al. (1979), Williams and Williams (1985)), towards a slight preference for immiscible systems (i.e. Wang and James (2011)). This can be rationalised through considering surface tension. In larger scale systems surface tension effects are much less dominant than many other forces, contributing little to stability. It can be imagined that surface tension would in fact promote instabilities, if it were favourable for the fluids to form local structures away from the desired near-flat configurations. i.e. the dewetting reported by Winter et al. (1979). Particularly the very large scale of experiments such as the CFR of Williams and Williams (1985) is not desirable even with regards to inertia.

As the scale is reduced, these interfacial effects become increasingly dominant, forcing the fluid to adopt specific structures in lieu of surface wetting properties. Once these structures are formed, however, they may in fact serve to stabilise the flow field as per Wang and James (2011), possibly through restricting the motion of the interface. However, at these length scales gravity becomes insignificant (evident as the interfaces can adopt vertical configurations) and the structure is completely dependent on the design of the channel and the wettability of the bounding walls. This issue of surface wettability and fluid structure will be considered closely in the following chapter.

In a similar manner, we should acknowledge that there have been attempts at modelling the lubrication of flows through extensional geometries, in a simplistic manner in several of the works just detailed, and more specifically also in Secor et al. (1987).

It may be possible to analytically model – or attempt to simulate – what the two phase interface profile will look like in this work. To incorporate all effects and create an accurate prediction would, however, be a challenging study in its own right: many effects are apparent which are difficult even to model independently. For example, we have just seen that

interfacial effects are crucial in determining the flow profile in a real world, 3D channel, a process dictated by the choices of wall materials. Not only are we considering flows of viscoelastic mediums but we are considering them in contact with Newtonian liquids, which do not generate equivalent normal stresses. This is then being applied in an extensional flow situation (which is not fully understood in any case) where differing resistances to flow are expected between the phases. Furthermore, there is always the possibility that there may not even exist a time-stable interface position, which would then call for time-step simulations to resolve. To contrast, the modelling in literature has usually been 2D, analytical, neglected surface tension effects, and utilised simplified fluid models (Secor et al. (1987) applies the shear thinning Carreau model, for example). Rather than attempting in-depth modelling, instead here we move on to some simplified flows in chapter 4 to obtain a real-world appreciation of the situation.

3.11 Framework for experimental measurements

We now have evidence that extensional flow should affect shear viscosity, and an experimental framework by which measurement of shear viscosity under extensional flow could be achieved. Therefore, to test the hypothesis the shear viscosity of a test fluid at two different extension rates must be compared.

The first issue is that it is not simply possible to alter the extension rate in the proposed experiment, and keep all other parameters constant. Changing flow rates through the experiment will alter both elongation and shear rates (amongst other parameters) present at a particular measuring location. It is therefore expedient to compare the difference in shear viscosity under extensional flow, to that under pure shear flow (zero extension) in a conventional rheometer at the same shear rates: i.e. Fixing the shear rate parameter in the comparison.

In chapter 1, it was highlighted that complex fluids can feature time dependent rheological characteristics which has an important impact on this experiment and time dependence was included as a function in the hypothesis statements at the start of this chapter. Here, we are now looking to compare the shear viscosity of a sample, to a sample undergoing elongation and shear at the same shear rate. However, by virtue of the test fluid accelerating down a converging channel as it elongates, the shear rates on the fluid rise rapidly. Thus, for a fluid that does not change shear viscosity instantly on a change in shear rate, the shear viscosity at that point is not steady state in nature, but transient, and a function of the shear rate history. It is therefore not comparable with the viscosity of a sample under steady shear, i.e. from a

conventional rheometric plot (the same issue that detracted from the strain gauge fin rheometer design noted in section 2.7).

As a result of the transient shear, we must now fix the shear history of the measurements being compared. This can be achieved by measuring the shear rates of the test fluid at several points along the converging channel, translating it into a temporal history, and programming a conventional rheometer accordingly. This time history recreation is a powerful tool, as it inherently accounts for many complicating behaviours that come under "time dependent shear". Two of these are stress overshoot, and more applicably, exponential shear.

Stress overshoot is a phenomenon well known about with polymer solutions at the onset of shearing, where a complex evolution of stress occurs (including over and undershoots) before it settles to a steady state (Whorlow, 1992). Discussion with Holland (2015) raised the concern that the measurements of interest are in this stress overshoot region. Exponential shear flow, like extensional flow, is also classed as a "strong" flow, in that it has the ability to align and stretch molecules (Doshi and Dealy, 1987). A pronounced effect on shear viscosity may thus be expected by such a shear history.

Note that, whilst exponential shear imposes molecular alignment and extensions effects similar to the extensional flow of interest, it is both accounted for, and arguably less significant than extensional effects. As the previous scattering references clearly show, alignment appears to coincide essentially with regions of extension, whereas exponential shear would only contribute molecular alignment at an intermediate location between the walls (high shear, but slow rate of change) and the channel centreline (zero shear).

Suppose a coupling was present between extension rate and shear viscosity in these experiments. Furthermore, suppose the behaviour followed that predicted by the simulations of Evans and Heyes (1990): That of extension directed parallel to shear (i.e. +ve extension) causing enhanced shear thinning, and perpendicular to shear (-ve extension) causing reduced shear thinning, or a relative shear thickening. Figure 3.5 and 3.6 summarise this for a hypothetical channel with a contraction (+ve extension) followed by an expansion (-ve extension), for both a Newtonian verification fluid and a shear thinning polymer test solution respectfully. In both cases the shear history is recreated in a second experiment using a conventional shear rheometer, i.e. "without extension". No significant differences are expected for a Newtonian verification fluid with and without extensional flow, aside from experimental

error. For the shear thinning test fluid, we expect to see the shear viscosity falling lower than the comparison experiment in the contraction region and higher in the expansion region.
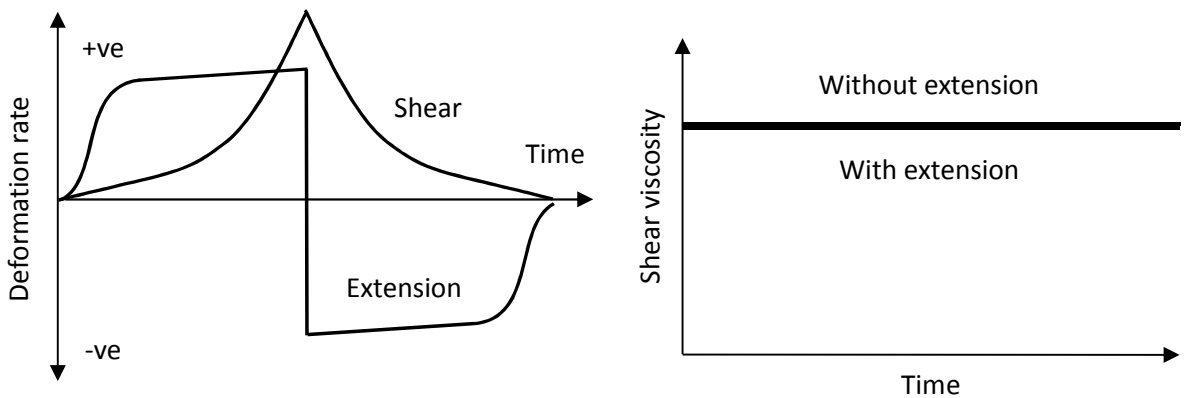
Figure 3.5: Expected experimental results with a Newtonian verification fluid.

Left: Shear and deformation rate histories from the extensional flow experiment.

Right: Shear viscosities from the extensional and reference shear experiments.
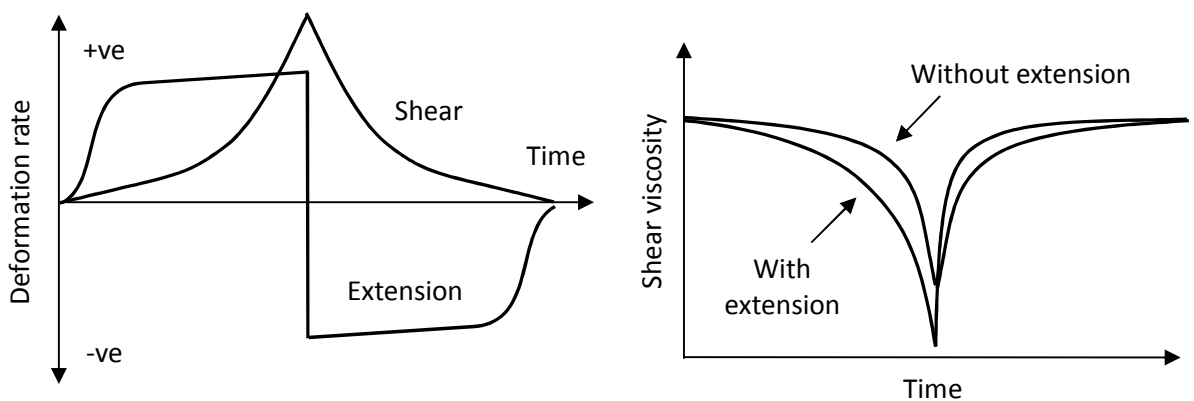
Figure 3.6: Expected experimental results with a shear thinning polymer solution test fluid, qualitatively based on the predictions of Evans and Heyes (1990).

Left: Shear and deformation rate histories from the extensional flow experiment.

Right: Shear viscosities from the extensional and reference shear experiments.

The study of particulate based rheological systems as well as polymers would also be pertinent. For example, fumed silica solutions are known to be thixotropic, but the particles are much less anisotropic and substantially more rigid than polymer molecules (if albeit they can form 3D gel networks under rest). The shear rheology of fumed silica suspensions has been widely studied, see for example Khan and Zoeller (1993), Raghavan and Khan (1995), Raghavan and Khan (1997), Lee et al. (1999), Yziquel et al. (1999), Zhang et al. (2014), and Hasanzadeh et al. (2015). If shear and extensional deformations proved equivalent on an approximately isotropic system, a rheological response might be expected that more closely matched that of the generalised

shear rate description in section 3.2, i.e. sensitive to the magnitude, but not direction of extension.

Despite the complexities of these measurements, the lubricated extensional flow offers some degree of control over the experimental conditions with three main parameters. Varying flow rates of the reference phase and the test phase will affect both the extension rates in the channel, and the position of the interface relative to the channel walls, which controls shear rates. Altering the viscosities of the two phases is also useful to extend this control range. The other parameter is the imaging location in the channel. Whilst it must be varied to map the time history of the flow, the shear and elongation rates, as well as Hencky strain, will also differ at each point, particularly if the flow is mapped from a contraction into an expansion zone.

It is important now to consider, if these changes in shear viscosity were observed under elongation, what they actually represent. They are a function of not only the elongation rate, shear rate, shear rate history for a particular test fluid, but also the elongation rate history (which will not be constant) and equivalently, the total Hencky strain applied to the fluid. As other parameters cannot be held constant, the effect of elongation rate on shear viscosity cannot be mapped, only analysed at one point, and it cannot be cross-compared to other points without speculation. These measurements can in no way be used to fully characterise the fundamental behaviour of a fluid, or indeed be directly applied to a practical problem. These issues of comparing to equivalent conditions is arguably comparable, but even more severe, to general issues in extensional rheology as highlighted by Petrie (2006a).

With these restrictions in mind, why is proving that such a dependence exists of interest? There are two main reasons.

Firstly from a practical perspective it would allow us to better understand "mixed" flows which are much more prevalent in real world situations than pure extensional flows, as stated in chapter 2. Pure rheometric flows may be easier to analyse, but consider the modification of the velocity fields due to extensional flow previously highlighted in Trebbin et al. (2013). The same form of profile modifications would occur in extruder dies. Here, the final morphology across an exudate, and ultimately the mechanical properties of the material are strongly linked to historical deformation of the melt: something of commercial interest, not just for extruded sections, but also spun fibres and blown films. If elongation caused shear thinning as per figure 3.6, this would enhance core velocities, and cause further shear thinning in a cyclic manner. The simplest example of impact on final properties that of chain alignment, responsible for the

anisotropic mechanical properties of products such as plastic sheet. Phenomena such as shear induced crystallisation also occur and are more complex than simple shear thinning, occurring providing both a critical shear rate and a critical total strain (mechanical work) are imposed on a fluid packet (Mykhaylyk et al., 2010). Not only would the onset of which likely affect the fluid rheology, but extension also has an important role to play in this process as well (Fairclough, 2017).

Secondly, highlighting that such an effect occurs has an impact on our understanding of such flows. The effect can be incorporated into improved numerical models, or conversely, it can be noted when a model is validated against often arbitrary real world situations. Improving the accuracy of polymer processing simulations has particular value in commercial extruder and also material design. Furthermore, it was highlighted in section 1.5 that the agreement between extensional flow measurements can be poor, with an example given in section 2.7 of an experiment that simulated the shear contribution to pressure drop and subtracted it from that measured experimentally, i.e. according to equation 2.1. Equation 2.1 would still hold, however this type of experiment that would be directly influenced by shear viscosity dependence on extensional flows, a factor not accounted for when shear contributions to pressure drop are traditionally determined. As noted, only direct measurement of wall shear stress could permit the real shear contribution to pressure drop to be found.

Returning to the hypothesis at the start of this chapter, we have also seen in literature evidence of shear flows affecting extensional rheology. However, all these experiments have similarly been performed in a non-simultaneous manner. This could also be achieved simultaneously with the experiment envisaged, simply by focussing on extension rates in the reference and test fluids rather than shear rates and determining the test fluid extensional viscosity in an analogous manner. This is more difficult however. Surface tension effects between the two phases would need consideration as they impart a normal stress. More importantly, a shear free extensional flow measurement is required, as the reference, which permits real-time control of the elongation rate. The FiSER system (Cambridge Polymer Group, 2016) is the closest option, but such systems are not commonplace. Furthermore, the current disagreement between the results of extensional techniques makes choosing any one technique to use as an experimental "reference" a concern.

Chapter 4.

Flow profile and surface modification.

Chapter 4: Flow profile and surface modification.

4.1   Test channel and assessment of requirements

In chapter 3 examples of lubricated flows were given. The summary was reached that interfacial effects have an important role in determining the configuration adopted by the two phase immiscible flows. Since such flows are key to the proposed experiment and figure 3.3 assumed that the fluids would adopt a layered, stratified format under gravity, it is pertinent to evaluate what structure is actually adopted in real world flows.

To perform these tests, a "wedge" contraction channel was constructed by the author. Figure 4.1 shows the pertinent mechanical details. A linear contraction is used as this can be easily machined to produce a flat walls; and Perspex used for no other particular reason than it being a go-to choice as a general purpose transparent fabrication plastic. The channel tapers from ~16mm high to 1mm high across a length of 148mm, followed by a parallel wall outlet section of 30mm length. The channel is constructed in two symmetrical upper and lower halves, bolted together with through bolts and locating pins. Production of these two halves and the final results are shown in figure 4.2a and 4.2b. With the 16mm channel width, the 1mm high outlet of the contraction satisfies the "shallow" aspect ratio desired (as defined in chapter 3) certainly in the latter part of the channel. Flow is fed into the cell through a single port, modified into two separate channels for each phase via a "baffled" Y union (figure 4.2c). This channel was actually constructed with the intention of using it to test strain sensitive fins described in chapter 2, hence the single inlet port. Strain sensitive fins (initially optical-based fins were envisaged) would have been sandwiched between the two polished cell halves.
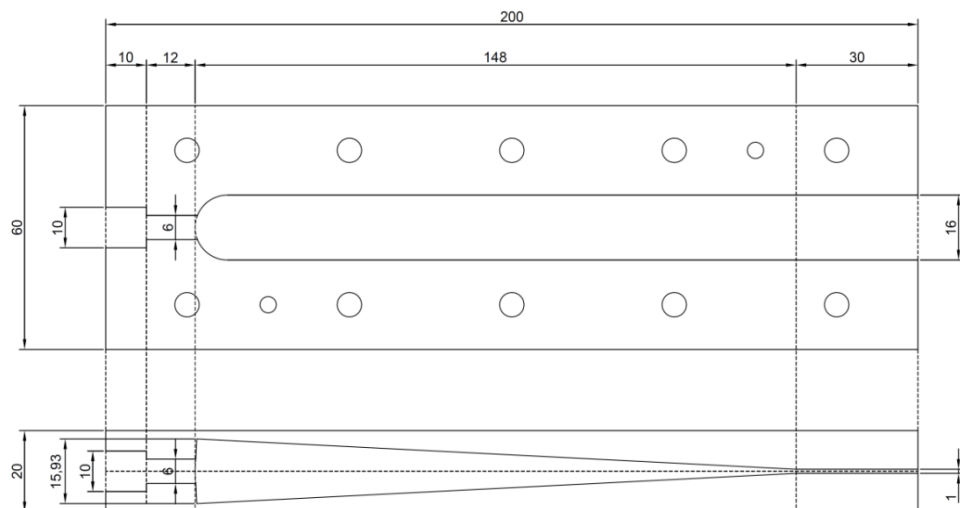
Figure 4.1: "Wedge" contraction channel key mechanical details. All dimensions in mm.

Top: View from above, bottom: side view of symmetrical sandwiched upper and lower halves

(through bolts and pins omitted for clarity)
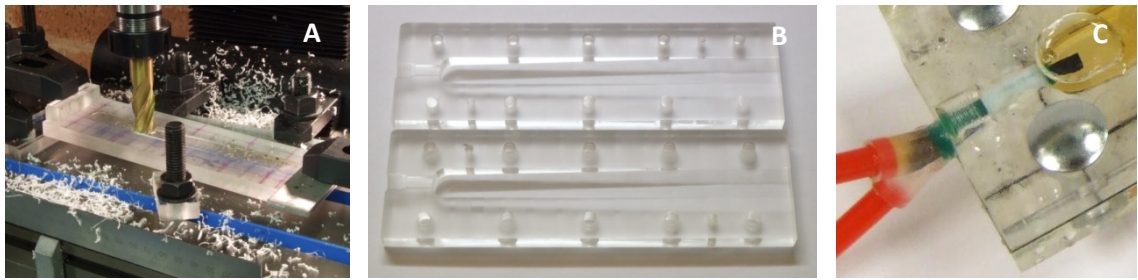
Figure 4.2: A: Cell production, B: Two halves of the flow cell, C: Detail of flow splitter

Flow was fed to the cell by means of a pair of syringe pumps, one for each phase, and the internal baffle of the union twisted to flow the oil phase on top of the aqueous phase irrespective of the upstream piping layout. A commercial automotive 15W/40 mineral oil (see Halfords (2017)) and a 8g/L guar gum aqueous solution were used as the two phases. The aqueous solution was prepared in deionised water (using product G4129, Sigma Aldrich, UK) and stirred overnight in a heated container. Concentration was chosen to give a viscosity similar to that of the oil – producing a zero shear viscosity around 2Pa.s and a corresponding Trouton ratio roughly around 3 from the data in Torres et al. (2014). Flow rates were approximately 630ml/hr for each phase. The fluids are allowed to drain into a collecting tray once they have passed through the cell and discarded. In all subsequent photographs, flow is directed left to right, with the cell gap reducing along the direction of flow.

If the cell is thoroughly cleaned and primed with the guar gum solution, the evolution of the flow structure is sporadic, as shown in figure 4.3. In the flow durations attainable with the syringe pumps, the flow structure did not readily reach a final developed state. Wherever the surface is wetted by water, if the oil is allowed to contact the surface the water tends to be displaced, resulting in the surface being oil wet. Taking the assumption that eventually surfaces would inevitably be wet by oil from flow disturbances, and to encourage an ordered flow structure to be developed, pre-wetting of the cell surfaces with oil was adopted. Two cases were tested: A cleaned cell prefilled with the oil phase, and this condition but subsequently irrigated with water to leave an oil film on the cell surfaces and prefilled with the aqueous phase. This is considered to be a fair test, as the very thin oil film remaining offers the least resistance to displacement through wetting of the aqueous phase, if it occurred.

Figure 4.3: Sporadic wetting of the oil phase with the cell cleaned and prefilled with the aqueous phase

Figure 4.4 shows stages in the evolution of the flow field for the oil prefilled case, viewed from above. Time is measured to the nearest second from the image data. Figure 4.5 shows the final flow profiles viewed from the side and outlet of the channel. Figure 4.6 and figure 4.7 show the same for the aqueous prefilled case, respectfully.
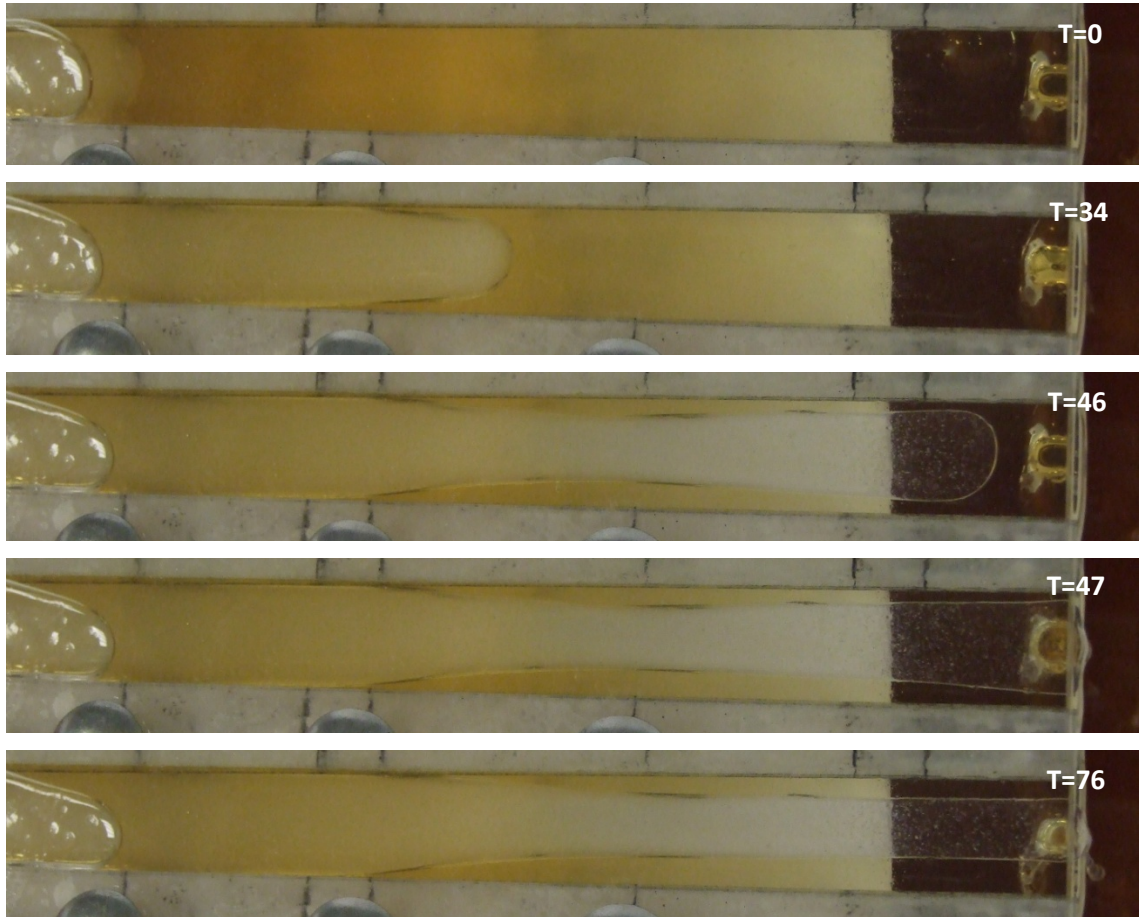
Figure 4.4: Evolution of the channel flow profile for the oil-prefilled case, viewed from above.
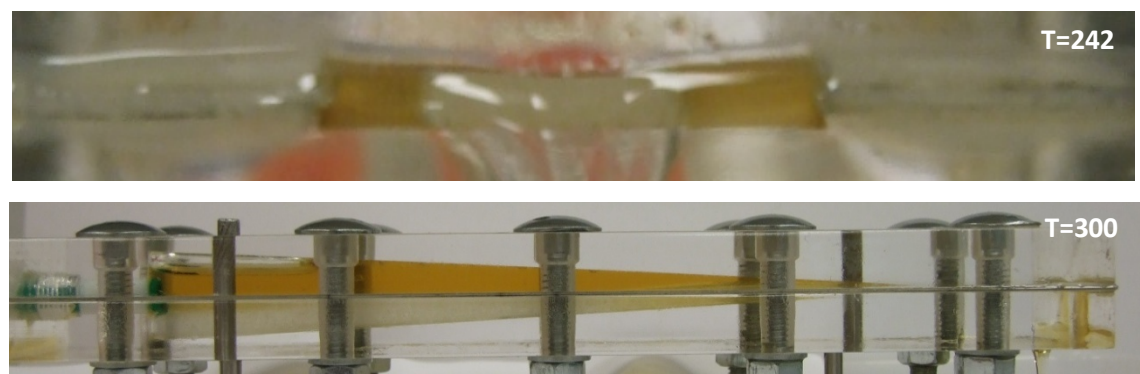
Figure 4.5: Oil prefilled - outlet view (top) and side view (bottom) at end of experiment

Figure 4.6: Evolution of the channel flow profile for the aqueous-prefilled case, viewed from above.
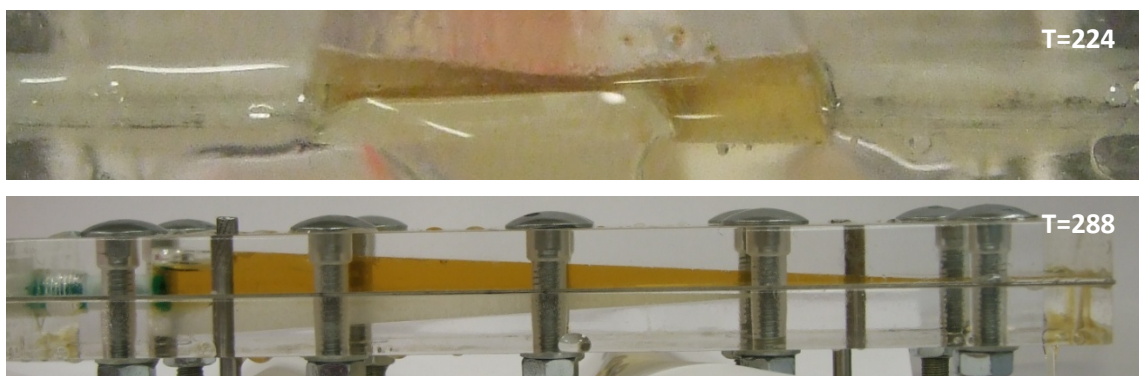
Figure 4.7: Aqueous prefilled - outlet view (top) and side view (bottom) at end of experiment

The situation exemplified by figures 4.4 – 4.7 is strikingly different to the stratified, layered two phase flow desired. From the above and side views in both cases, it appears that the oil phase does indeed flow on top of the aqueous phase at upstream locations, in a stable manner with respect to time. However, beyond about half way down the contraction channel (around the central pair of through bolts, or 8mm channel height at this location) we see structures that depart from that expected and/or evolve in time.

In the oil prefilled case of figure 4.4, we see that beyond this location, a different structure is almost immediately adopted. Stratification appears essentially perpendicular to that expected for a flow of two different density phases under the influence of gravity. This structure is clearly visible in the outlet flow of figure 4.5, and we can see the evolution towards this structure in the side view. The upper interface of the aqueous phase rises to fill the total channel height at the channel centreline, and we can see the orange colouration from the oil phase simultaneously becoming more intense and uniform as the oil phase moves to occupy the full height of the channel at the edges. Closer inspection of figure 4.5, and in particular the shape of the central aqueous phase suggests that the aqueous phase has been totally enveloped by the oil phase and has fully detached from the channel walls. Since pressure forces must balance between the interfaces of the two fluids, a specific cross sectional area is required for the central aqueous flow. Due to surface tension, this flow would preferentially adopt a circular cross section, i.e. a thread within a sheath of oil, minimising surface energy. However, due to the shallow channel height, this thread is compressed between the upper and lower walls; the most favourable resulting configuration being to occupy a segment of the overall channel width (hence the "stratified" appearance). The aqueous phase occupying the full channel height prevents shear rate measurements across an interface from being performed (at least on a vertical plane) in this geometry.

This shift in flow configuration can be explained by a change in dominance between gravity and surface tension effects as the channel height reduces down the channel length. Upstream, if surface tension attempted to adopt the stratification pattern found, hydrostatic forces from the difference in phase densities would be dominant, preventing this from occurring and keeping the aqueous phase stratified across the bottom of the channel. A characteristic interface radius of curvature would be present at the vertical channel walls. When the channel height reduces below the interface radius of curvature, it would be reasonable to say that surface tension effects have become dominant, and now the hydrostatic pressure of the aqueous phase, when extending the full height of the channel, could be fully supported by surface tension effects.

The ~8mm channel height at this transition location is somewhat large for a interfacial radius of curvature but lends credence to this explanation.

The asymmetry of the outlet in figure 4.5 (and also figure 4.7) may be due to the cell not being exactly level and a "spirit bubble" like positioning of the aqueous phase laterally across the channel. With a narrow height difference between the upper and lower plates, the flow is akin to a "Hele-Shaw" flow, and pressure drops determining the flow field arise essentially from the upper lower walls: The position of the central aqueous core has no effect on the pressure drop in the oil phase, and thus can adopt any location across the channel providing the cross sectional area of flow remains constant.

In the aqueous prefilled case the situation is similar; however the structure is not immediately adopted. Interpreting the exact height occupied from each phase is somewhat difficult from the images; however it seems the oil phase progressively wets the upper channel wall, before reaching an edge and progressing to "snap" to the lower channel wall. In figure 4.7, the aqueous phase has not been fully enveloped by the oil phase as the aqueous phase naturally resides on the lower wall, hindering wetting of this surface. As a particular cross sectional area is still required for the flow of the aqueous phase, this can be satisfied without requiring the full height of the channel of the outflow. However, given that wetting of the lower channel wall by the oil phase will no doubt continue with time and/or flow disturbances, this structure would not be stable and would likely evolve to that seen in figure 4.5.

Before the consequences of this surface tension dominated flow field on the experiment are discussed, we can ask why this enveloping of the aqueous phase by the oil phase occurs. The first reason for this is the preferential wetting of Perspex by oil compared to water. Contact angle, introduced shortly, is broadly used as a measure of "wettability" of a surface by a particular fluid. Table 4.1 shows contact angle images of water and oil droplets on Perspex (as well as glass referred to later) imaged with a First Ten Angstroms FTA200 instrument and analysed with the associated software. It can be seen that the oil used in these flow experiments (any other oil would behave similarly) has a much lower contact angle on the cell walls than water. As a result, once oil has wetted the channel surfaces a stable oil film and/or flow layer will be produced next to the wall, with the aqueous phase excluded away from the wall. The sporadic wetting in figure 4.3 for a clean channel is indicative of this preferential wetting occurring. Secondly, in the narrow channel region, if this wetting process did not continue to the bottom wall, a stable stratified two phase system might be attained. However, once the oil does inevitably contact the lower channel wall however (i.e. by virtue of the

interface radius of curvature, or flow disturbance) it will continue displacing the aqueous phase until inevitably all channel surfaces are oil-wetted.

Substrate:	Perspex	Glass
Deionised water	CA = 63.7° CA, θ	CA = 17.9°
15W/40 Mineral oil	CA = 12.7°	CA = 13.3°

Table 4.1: Comparison of contact angles for water and oil on ethanol cleaned Perspex and glass substrates. Average contact angles (labelled in the Perspex/DI water case) are shown for each case, based on at least 5 tests. Red / dashed lines are added for illustration to show the measurement of the contact angle.

At this point it is useful to highlight that Cubaud and Mason (2009) in fact present in figure 4 of their work a planar flow field that looks remarkably similar to that in the outlet view of figure 4.5. However no surface tension effects are present as their two fluid phases are miscible, and their inflow closely resembles that achieved at the outflow. It is however informative as the shallow channel produces Hele-Shaw flow dominated by the upper and lower walls. In the case of a single fluid phase would produce a plug, rather than (for Newtonian) parabolic velocity profile running across the width of the channel, i.e. free of shear. Their velocity profiles for two phase flow of differing viscosities shows sharp shear gradients across the boundary between the phases due to their differing velocities, with plug flow still present in the core of the phases.

The flow regimes exhibited in this experiment, arising from wall wetting by the oil phase, mean options for achieving the desired two phase flow field are very restrictive. It is also desirable to avoid generating transitions in interface configuration down the length of the channel, as experienced in figure 4.4, which could lead to instabilities or limit regions over which data could be taken. The three possible arrangements are shown on the following page in figure 4.8.

A: Large scale "shallow" aspect ratio channel

B: Square aspect ratio channel

C: "Tall" aspect ratio channel, with image of flow channel in early work
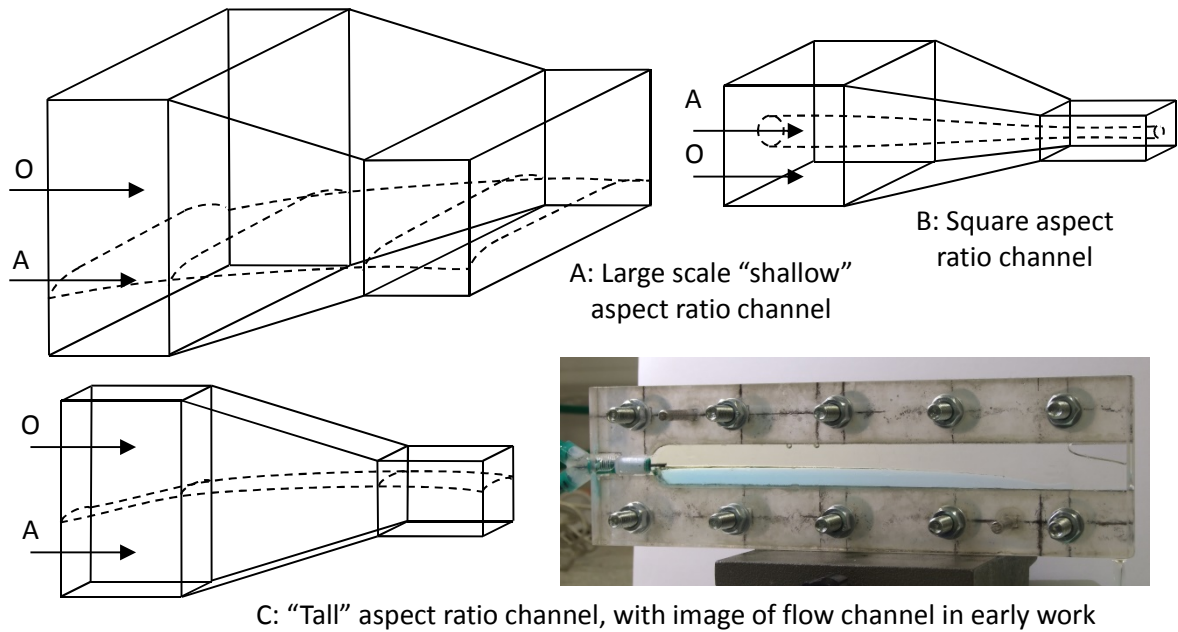
Figure 4.8: Configuration options for two phase flows in a converging channel. Dashed lines denote the two-phase interface edges and structure. O denotes the oil phase, and A the aqueous phase. Appreciation of associated scale is given by the interface radius of curvature shown. The inset image shows the flow channel in early work orientated producing the conditions of case C, if with different test phases to those shown previously and the contraction direction instead directed horizontally.

The first option, shown in figure 4.8a, is that of a "shallow" aspect ratio channel which features dimensions (specifically height) always in excess of the interface radius of curvature, i.e. such that gravity dominates over surface tension in producing a horizontal interface. The channel could reduce in either in height to generate extensional flow, as shown here, or alternatively in width. As an indication of size, we saw this condition being achieved previously in figure 4.4 earlier, in the upstream channel sections above 8mm in height. Similarly, the Bond number (equation 4.1) is also a useful quantity, defined as the ratio of gravity to surface tension forces:

$$Bo = \frac{\Delta \rho g L^2}{\sigma}$$
(4.1)

If we take a Bond number of 1, assume the surface tension (σ) of water, and a density difference (Δρ) of 200kg/m^3 between phases, we obtain a characteristic length scale (L) of 6mm. We thus see that for this configuration, the narrowest channel dimensions of a contraction would be on the order of 10mm - a very serious limitation. As described in later in section 5.1, large scale channels severely limit attainable extension rates and require high flowrates/pressure drops compared to smaller scale channels, amongst other factors.

The second option, shown in figure 4.8b, is to permit the central aqueous phase in figure 4.5 to adopt the core-thread configuration by using a square, rather than "shallow" aspect ratio contraction. This prevents the thread from being compressed by the upper and lower channel walls, and thereby permits regions of both phases which can be imaged across, based on a horizontal camera. This "thread" configuration is exactly that which Arratia et al. (2008) and Lee et al. (2011) used for immiscible lubricated capillary extensional rheometry highlighted in the previous chapter. Whilst it is conceivable to image across the interface such a thread, such a configuration is impractical. The position of the thread is not well defined in the channel which may again lead to issues of contribution from lateral shear. The thread would also fall towards the lower wall (the figure ignores gravity) and be distorted from a circular cross section if it came into contact with it. The stability of the thread would be paramount, as the thread must not break or oscillate in this experiment (a criteria that eliminates any verification tests with Newtonian fluids that are inherently susceptible to capillary breakup). The fully lubricated form of the thread, whilst it does keep shear induced rheological changes to a minimum, also greatly limits direct control over such shear rates compared to a system featuring a well-defined flat interface between an upper and lower bounding wall. There is also no simple way of separately extracting the two phases once they have passed through the experiment for recirculation or reuse.

The third and only potentially practical option is that of figure 4.8c, that of using a "tall" rather than "shallow" aspect ratio channel. This is akin to rotating the test channel in the previous figures by 90 degrees, allowing the aqueous phase to settle under gravity, and imaging across what used to be the vertical interfaces. Such an orientation is shown in the inset image during earlier work (if with different fluid phases to those used previously). The drawing in case C instead shows the contraction direction directed vertically which serves to always maintain this aspect ratio condition. Here the "thread" of the aqueous phase is in effect bounded on either side by the vertical walls and by resting on the lower horizontal channel wall. This produces a well-controlled two phase interface position for conducting measurements. However, now the cell aspect ratio is "tall", with lateral shear rates very much greater than those in the vertical direction. In theory this is not a problem as shear lateral shear rates should be zero along the exact cell centreline, however this creates high levels of sensitivity to any flow field or measurement misalignment. The same comments on velocity profiles in this Hele-Shaw like flow field made previously still apply.

The ideal case would be if the flow field in figure 4.7 could be reproduced in a more symmetric manner. As already stated however, this flow field could in no way be relied on to be stable or

symmetric, and it would only be a matter of time before the flow structure was disrupted by wetting of the channel walls by the oil phase. It was highlighted in chapter 3 that in the work by Wang et al. (2010), (2011) did in fact achieve what appears to be the ideal flow field for this experiment, with a "shallow" aspect ratio channel, and apparently verified the form of their flow field with confocal microscopy. All their walls had uniform wettability, and their use of perflurohexane rather than the more conventional oils used here (both have low surface tensions) does not offer any explanation as to how this was fortuitously achieved.

We can conclude what is ideally required is a proactive means to modify the wettability of specific areas of the channel walls to control the interface shape, and thus the stratification of the two phases. This will be investigated in the following section.

4.2   Literature review on routes to surface modification

We have just seen in the previous section that Perspex, an example flow cell construction material, satisfies the criteria of a material that is preferentially wetted by oil over water. The contact angles in table 4.1 were not >90° for water (the usual criteria for hydrophobicity), but comparatively speaking, Perspex is hydrophobic and oleophilic. To control the locations where the two phase interface contacts the walls, and thereby shape of the interface, a complementary "hydrophilic and oleophobic" surface is required. A channel constructed with a upper oleophilic and hydrophobic wall, and a lower oleophobic and hydrophilic wall, should prevent encapsulation of the aqueous phase and permit a stratified flow to be obtained in a small scale channel. The wettability of the side walls is less important, but will be commented on shortly.

To a first approximation, crude speculation suggests a minimally charged surface would be better wet by oils, and a surface featuring charged surface groups would be better wet by polar water molecules. Glass, when clean, has a concentration of polar hydroxyl groups at the surface (take for example, Liu et al. (2009). Contact angles for oil and water on an ethanol cleaned glass slide are also presented table 4.1; it is clearly evident that oil still preferentially wets the surface over water. Fortunately in recent years, there has been much work on developing hydrophilic-oleophobic materials and coatings, particularly in lieu of oil-water separation and anti-misting coatings on glass. In the former, hydrophilic and oleophobic meshes represent a significant advance on existing approaches with oleophilic, hydrophobic materials; in the latter case highly wettable surfaces to prevent beading of water are readily fouled by oils (Howarter and Youngblood, 2007). Pertinent reviews to date are those of Xue et al. (2014), Zhu et al. (2014), Chu et al. (2015), Kwon et al. (2015), Wang et al. (2015), Wang et

al. (2016), Yu et al. (2016), and Zhu and Guo (2016); and to a lesser extent Padaki et al. (2015). A short introduction on surface wetting is necessary: This is summarised from these sources.

The contact angle of a liquid droplet on a smooth, chemically homogeneous surface (figure 4.9) is defined by the Young's equation (equation 4.2). The contact angle is a result of resolving the surface tensions (or energies) between the solid and the vapour (γ_{SV}), the solid and the liquid (γ_{SL}), and the liquid and the vapour (γ_{LV}).
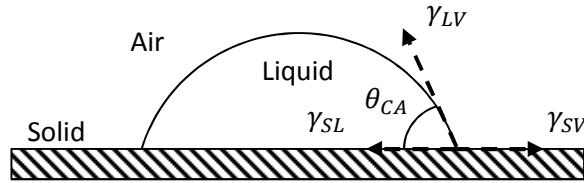
Figure 4.9: Contact angle and interface forces acting on a liquid droplet on a smooth, flat horizontal surface. The drop is small to render gravity negligible.

$$\cos \theta_{CA} = \frac{\gamma_{SV} - \gamma_{SL}}{\gamma_{LV}}$$

(4.2)

In addition to the above case with a smooth substrate, the substrate may also be rough. In this case, two different wetting situations are possible: The Cassie-Baxter and the Wenzel case, shown in figure 4.10.
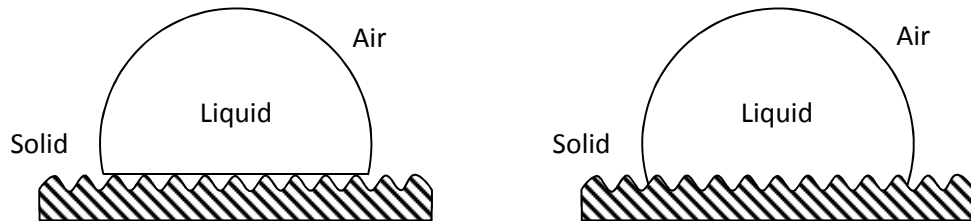
Figure 4.10: Wetting situations on rough substrates.

Left: Cassie-Baxter wetting, right: Wenzel wetting

In the Cassie-Baxter case, a droplet placed on a rough substrate does not permeate into the pores of the substrate. The droplet effectively sits on and traps a layer of air, making contact with only the very highest asperities of the surface. In contrast in the Wenzel case, the substrate is fully wetted by the liquid droplet. Both wetting regimes have the ability to produce a much greater range of contact angles than attainable with smooth substrates (i.e. super-hydrophobicity and super-hydrophilicity with contact angles typically >150° and approaching 0° respectfully). The Cassie-Baxer case tends to lead to very low contact angle hysteresis with droplets readily rolling off the substrate when tilted, and the Wenzel case in contrast tends to

pin droplets to the substrate, leading to high degrees of hysteresis between the leading and trailing edges of a droplet (e.g. Kwon et al. (2015)).

Young's equation indicates that the resulting contact angle of a liquid drop on a surface is dictated, for a particular substrate, purely by the solid-air and liquid-air interfacial tensions. Oils have a value of γ_{LV} between 20 to 30 mN/m, compared to water of 72 mN/m. Whilst the variability of γ_{SL} is not additionally commented on in the reviews, this leads to the situation highlighted in the references that it is extremely difficult (if not intrinsically impossible for normal substrates, see for example Zhu and Guo (2016)) to achieve a contact angle for water simultaneously lower than that for oil. In table 4.1 it can also be seen that the contact angle for oil increases when a Perspex substrate is replaced by glass, rather than decreasing, which would superficially indicate a preferential increase of γ_{SL} in this case. However, thoroughly cleaned glass substrates typically show near zero contact angles and are (similarly) readily contaminated on account of their high surface energies - the increase of contact angle could be explained by remaining adsorbed water on the glass surface.

There are two key methods, evident from the reviews highlighted, through which hydrophilic and oleophobic surfaces have been realised: firstly, via pre-wetted, rough hydrophilic surfaces; and secondly, by structurally responsive surfaces incorporating both hydrophilic and oleophobic constituents (that according to Kota et al. (2012) reviewed later, effectively respond by modifying γ_{SL}).

It can be shown by equation 4.3 (directly derived from equation 4.2) that a hydrophilic (and thus oleophilic) surface in air attains hydrophilic and oleophobic properties underwater (see for example, Zhu and Guo (2016)). OA signifies the oil-air surface tension and contact angle of oil droplet in air, with WA similarly for the water-air case and OW for the oil-water case. For a hydrophilic material with low oil and water contact angles, $\cos\theta$ in the OA and WA cases are near 1. With the difference in surface tensions between oil and water in air, $\cos\theta_{OW}$ is typically negative and thus θ_{OW} is greater than 90 degrees, or oleophobic.

$$\cos\theta_{OW} = \frac{\gamma_{OA}\cos\theta_{OA} - \gamma_{WA}\cos\theta_{WA}}{\gamma_{OW}} \qquad (4.3)$$

Though not explicitly stated in the review references, the above condition appears insufficient for achieving a practical hydrophilic, oleophobic surfaces. If the predictions of equation 4.3 held in isolation, oil on a glass surface would be readily displaced when placed underwater

which is clearly unphysical (and contrasts with the "ruining" of hydrophilic anti-mist surfaces highlighted earlier). It is energetically unfavourable to replace a low energy surface higher energy one, and as a result, when oil contacts a surface it cannot be subsequently displaced by water.

The key requirement to realise a underwater hydrophilic and oleophobic surface is a combination of both hydrophilicity and surface roughness (i.e. as clearly stated in Chu et al. (2015)). Firstly, when pre-wetted the surface roughness traps a layer of water in the pores of the surface (the Wenzel configuration, with respect to water), leading to high contact angles of oil in a Cassie-Baxter like state on this "composite water-solid interface and preventing it from penetrating into the textured substrate" (Xue et al., 2014). This trapped layer of water thus renders the surface both hydrophilic and oleophobic. Secondly, a "re-entrant" surface (i.e. as can be formed by the lower halves of spherical particles) is crucial (Kwon et al. (2015), Wang et al. (2015) and in particular Wang et al. (2016)) the increase in oil-water surface area for oil to fully wet this topology and transition to a Wenzel configuration is unfavourable (i.e. unlike the progressive wetting in figure 4.3 with the smooth channel walls). This creates a metastable energy minima that prevents oil progressively displacing the water from this pre-wetted surface.

Whilst re-entrant structures enable a stable Cassie-Baxter configuration to be attained, external effects can cause a transition to the Wenzel configuration. The simplest example of this is a pressure increase in an air-water situation Cassie-Baxter situation (E.g. Wang et al. (2016)). These hydrophilic and underwater oleophobic surfaces are thus not intrinsically stable. Furthermore, these surfaces must be thoroughly water wetted before use, which means in their dry state they are very sensitive to oil fouling (explicitly highlighted by He et al. (2015) more recently). These drawbacks are the main reason why hydrophilic and oleophobic surfaces in air have been sought. Kwon et al. (2015) highlights this in particular, for the separation of water-in-oil mixtures with hydrophilic-oleophobic approaches, where the "drying out" of the surface around pores is detrimental. In air hydrophilic and oleophobic surfaces have been achieved through "responsive" surfaces which present an oleophobic condition to oil, and rearrange to present a favourable condition to water. This may additionally be accompanied by trapping of a layer of water in a hydrophilic subsurface (in a similar manner to underwater oleophobic surfaces). Three examples will be given shortly.

Before examples of oleophobic and hydrophilic surfaces are considered for the lower channel wall, there are some advantages to considering the channel side wall wettability. The most

important (indirect) requirement of the channel side walls is that the interface attains a symmetric configuration across the channel width. This must also be stable in time and not subject to progressive changes in surface wetting configuration. We cannot aprioi specify symmetric interface contact point on the side walls (i.e. through partially coating them) as this location is unknown and affected by the flowrates and rheometry of the two liquid phases. Either wholly "conventional" (i.e. preferentially wetted by oil) or hydrophilic/oleophobic side walls could be used, but with the only difference being upward or downward curvature of the resulting interfaces, as discussed in chapter 6. With "conventional" side walls, the best that can be achieved is to ensure these walls are fully coated in oil before experiments. In "shallow" channel regions the oil-water interface surface would then be pinned at the lower hydrophilic oleophobic channel wall, and in "tall" channel regions where the aqueous phase contacts a fraction of the height of the side wall surfaces, the oil pre-wetting would be hoped to produce a stable and symmetric configuration.

In addition to a stable symmetric interface, it would also be preferable to have an interface with the minimum of curvature across the channel width for imaging purposes. Fortunately in the critical contraction region where the channel aspect ratio is shallow, the pinned interface to the lower channel wall would directly facilitate this. However, in the upstream and downstream regions where the aqueous phase would contact the side walls, interface curvature could be significant. Suitable choice of a channel side wall material to minimise this curvature would be pertinent, i.e. attempting to achieve a 90 degree contact angle of the oil-water interface when in contact with the channel side wall materials. Whilst both water and oil have superficially similar contact angles on glass, and thus what might be considered "similar" wettability. However this does not directly translate to a 90 degree contact in the oil-water case as the contact angle in the Young's equation is directly sensitive to the difference in the solid-liquid surface tensions between the two fluids. The oil pre-coating of a side wall would moreover limit the usefulness of any model predictions based on "clean" substrates. Despite this, consider figure 3.4 presented earlier for a real world channel with ample opportunity for pre-wetting by the hexadecane phase: The oil-water interface contact angle on the glass channel wall is clearly shallower than that against the PDMS wall, suggesting that the consideration of glass side walls may be useful. This is used in chapter 7.

An ideal surface modification/coating technique for a lower flow channel wall would be:

- Hydrophilic and oleophobic, stable against time, and resistant to direct contact by oil - be this through under water oleophobic/hydrophilic or stimuli-responsive in-air techniques

- Mechanically robust against shear forces and not stripped off the surface under flow

- In the form of a "thin" layer, or if rough, with an average roughness much less than the smallest channel dimension

- Readily applied to, and independent of, a substrate material - techniques dependent on modifying a specific substrate are limiting in terms of channel fabrication

- Fabricated using very simple chemistry and readily achievable processing techniques

- Not dependent on treatment or application steps that may impose size or shape limitations on components (e.g. plasma cleaners, spin coaters)

- Ideally optically clear – not essential, but superficially more flexible in terms of optical visualisation or injection (and removal of non-scattered) of PIV laser illumination

In perhaps the last 2 years or so, there has been a great increase in interest in this field, both in research and commercially. This issue of the channel wettability was addressed in 2014 for this application; attempting a full review of current literature is extensive (at least 60+ papers from a simple search). Instead, the review of Xue et al. (2014) conveniently summarises what proved to be some of the most promising techniques that were considered to address the problem and will be used as a select basis for examples, with additional detail added. There may well be more useful and applicable techniques in current literature than those shown here.

Howarter and Youngblood develop a stimuli-responsive hydrophilic/oleophobic surface coating based on perfluorinated end-capped polyethylene glycol surfactants: The fluorinated end caps are oleophobic, and with the remainder of the molecule hydrophilic. This was first applied as a grafted anti-fog coating on glass (2007) (2008) then subsequently used with glass membranes for efficient oil-water separation (2009). Robust, self-cleaning (undercutting) of oil droplets initially placed on dry glass slides by water with this coating have been clearly demonstrated (Howarter and Youngblood, 2007), where oil would otherwise preferentially remain adhered to an untreated glass surface (or, a dry hydrophilic surface used for underwater hydrophobicity). The most recent work using this system appears to be that of Howarter et al. (2011), investigating spun-cast films based on the same stimuli-responsive concept but using different co-monomers attached to the same flurosurfactant. There is some debate with regards the

mechanism that makes this surface hydrophilic and oleophobic, in their publications it is thought that oils are repelled by the fluorinated end groups, whilst water is able to penetrate through the relatively mobile surface groups, into the hydrophilic sub layer, and wick across the surface. In their initial paper, they also present an alternative explanation in that water may be bypassing the fluorinated surface and simply swelling the water soluble base PEG constituent. Whatever the case, stable hydrophilicity and oleophobicity, as well as self-cleaning were demonstrated. This work is furthermore promising as the grafting approach with silage enables a means to create covalently attached, solvent resistant robust coatings (if albeit to glass) and all of their coatings are optically transparent, achieving hydrophilicity and oleophobicity without the use of additional surface roughness. Alternative application methods than the spin coating technique used can also be envisaged. Regrettably, since this work the perfluoro compounds of lengths greater than C6 (i.e. the Zonyl FSN-100 molecule used in their work) has since been banned under environmental regulations. From personal communication, the authors tested shorter perfluoro molecules still on the market and concluded that "The pefluoro unit just wasn't long enough" (Youngblood, 2014), rendering this technique not an option. More recent works however, i.e. the widely reported work of Brown and Bhushan (2015) seem to have had luck using shorter fluorinated chain lengths that are still available (Capstone FS-50).

Following this Xue et al. (2011) created a superhydrophilic and underwater superoleophobic membrane, satisfying the rough hydrophilic surface requirement by using a hydrogel (PAM) dip coated onto a stainless steel mesh. Water fills and is retained by the interstitial spaces with within the hydrophilic gel rendering it oleophobic and droplets easily roll off the surface. This technique similarly displayed high efficiency in separating oil-water mixtures with fouling resistance. This is very similar to the work of Rohrbach et al. (2014) more recently, who used a cellulose filter paper modified with nanofibrillated cellulose (NFC) hydrogel to generate hydrophilic, oleophobic properties when hydrated through the same mechanisms. Similar performance was reported. In both cases the coatings could no doubt be applied to a solid surface rather a mesh or filter. However, in the former case an in-situ polymerisation reaction is required to produce the PAM hydrogel coating, and in the latter case the NFC also needs to be prepared.

Kota et al. (2012) describe another widely reported stimuli responsive surface for oil-water separation that is oleophobic and hydrophilic when dry and under water, this time using a polymer blend dip coated onto stainless steel mesh and polyester fabrics. Successful separation of stabilised oil-water emulsions was demonstrated. The dip coated responsive surface

consisted of a blend of 20 wt.% fluorodecyl polyhedral oligomeric silsesquioxane (POSS) and cross-linked poly(ethylene glycol) diacrylate (x-PEGDA). This coating was shown to be covered in crystalline domains of flurodecyl POSS on the surface (under air), with their segregation being expected due to their low surface energies. Under water, these domains were found to disappear (in a reversible manner) revealing a smooth surface, indicative of surface reconfiguration. It is believed that this reconfiguration increases the interfacial area of the PEGDA chains with water and facilitates favourable hydrogen bonding. Preferential wetting of this coating by water even when initially contacted with oil (with a water-in-oil emulsion) was similarly exhibited (though this time with the coated meshes tested). The chemistry behind this rather more involved than desired here – For example, flurodecyl POSS synthesis is required, as described in a separate reference, along with a range of other unusual materials that would require sourcing.

The most promising work for the purposes required here is that reported by Yang et al. (2012). They developed a stimuli responsive superhydrophilic-superoleophobic polymer coating with both hydrophilic and oleophobic constituents that, as per previous groups, displays the ability to rearrange to permit water wetting but avoid oil wetting, even when dry. Efficient water-oil separation using a stainless steel mesh was similarly demonstrated. Importantly however, the chemistry is relatively simple: reacting poly(diallyldimethylammonium chloride) (PDDA) with sodium perflurooctanoate (PFO) in aqueous solution. Although a fluorinated compound (perflourooctanoic acid) is used as a precursor material, the limited chain length renders it readily available. As per previous groups, the fluorinated end groups are said to give rise to oleophobicity and they postulate that they remain in a mobile state, permitting a surface rearrangement in the presence of water and subsequent penetration into the hydrophilic subsurface (carboxyl and quaternary ammonium groups). The responsiveness of spun coated (clear) films of this polymer is somewhat limited; however they amplify this effect by generating a rough surface hierarchy by the addition of fumed silica (SiO_2) nanoparticles. This nanocomposite coating can readily applied by airbrushing to any substrate.

Given the simple chemistry described for achieving a surface responsive coating, and the ease of application to non-specific substrates via airbrushing (the technique could of course be applied elsewhere, but here it has been demonstrated) the decision was made to take this technique forward.

4.3 Testing and progression based on Yang et al. (2012)

To test the coating developed by Yang et al. (2012) for this application, the following synthesis procedure was followed, elaborated from that described in the source. Perflurooctanoic acid (($CF_3(CF_2)_6COOH$, 414.07 M_w), poly(diallyldimethylammonium chloride) (PDDA) solution (200k – 350k M_w, 20wt% in water as supplied, 1.04g/ml), and fumed silica (specifically product S5130) were purchased from Sigma Aldrich, UK. The acid and PDDA solution are precisely identical to that used by the original authors. However due to local availability issues the fumed silica (particle size 0.007μm, featuring "… branched, three-dimensional chain-like aggregates" with many aggregates having "chains from 10 to 30 spheres in length, or from 0.1 to 0.2 microns (μm) in length", Sigma-Aldrich Co. LLC. (2012)) had to be used as a close substitute for the SiO_2 nanoparticles (average diameter 20nm) used in the original reference.

To make the 0.1M stock sodium perflurooctanoate solution required in the source, 100ml of 0.5M NaOH stock solution was first prepared. 4.14g (0.01 moles) of perflurooctanoic acid was reacted with ~ 20ml of the NaOH stock, monitored via litmus paper. The resulting sodium perflurooctanoate solution was diluted to a total volume of 100ml by deionised water. The required 1mg/ml poly(diallyldimethylammonium chloride) (PDDA) solution was prepared by diluting 2.40ml (2.5g) of PDDA solution with deionised water to a total volume of 500ml.

To prepare the complex, 1.5g of fumed silica was added to the 500ml of 1mg/ml PDDA solution (in the same ratio as the original reference) and sonicated. To this, the 100ml of the 0.1M sodium perflurooctanoate solution was added dropwise under stirring at ambient temperature, according to the reaction scheme reproduced in figure 4.11 below:
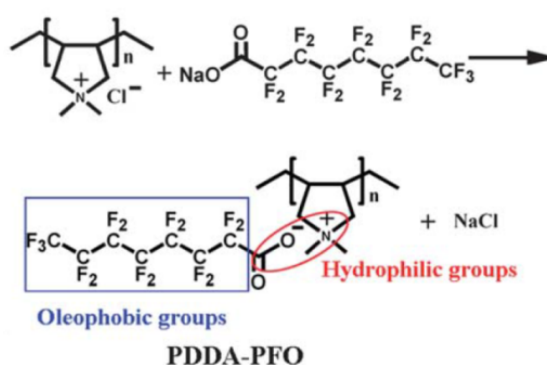
Figure 4.11: Reproduced excerpt of figure 1 from Yang et al. (2012) showing reaction scheme used to produce the PDDA-PFO material

Following this, the source indicates that "the product was rinsed with deionised water and dried", which requires interpretation – Presumably this is to remove the sodium chloride liberated by the coordination reaction. Here, the bulk of the product was reduced in volume

by centrifugation (15min, 4000rpm) before being rinsed three times via centrifugation with deionised water, then dried in a rotary evaporator. Foaming was found to be a significant issue during drying, ethanol was used to both supress this and facilitate water removal. 2.78g of solid dry product was recovered, which is now herein referred to as PDDA-PFO/SiO$_2$.

If we consider the mass of each PDDA sub unit (M_w = 133.5) on the PDDA chain, for the 0.5g of PDDA used, this corresponds to 3.74 x10^{-3} moles of sub-units, or assuming every sub unit reacted with no steric hindrance, a requirement of 1.55g of the original perflurooctanoic acid. The 4.14g thus used here represents a reasonable excess. The coordinated product has a sub-unit M_w = 511, thus with the addition of 1.5g of fumed silica a theoretical yield of 3.41g would be expected for full coordination. The ~80% yield achieved here is very satisfactory.

As per the reference, 0.2g of product was ultrasonically dispersed in 20ml of ethanol, airbrushed using a nitrogen fed spray gun onto cleaned glass slides and allowed to dry. High shear mixing was found to be required in addition to aid in breaking up large stubborn aggregates. Again due to sourcing restrictions, a generic airbrush was used here rather than the one reported in the reference. Any differences due to the exact airbrush used are however expected to be swamped by the airbrushing technique used, which was not described in the source and has been found by other fellow researchers to be a major reproducibility issue (Dunbar, 2014). Figure 4.12 exemplifies the situation with SEM (JEOL JSM-6010LA Analytical Scanning Electron Microscope, 20kV, 600x magnification, gold sputter coated samples) and visual images of two different coated films prepared by slightly different methods. A range of sites were imaged at different magnifications, the morphologies presented are typical. With the airbrush held a significant distance from the substrate, a fogged, apparently "dry" film of deposit is gradually accumulated on the surface. Holding the airbrush closer than some critical distance does not allow sufficient time for the bulk of the ethanol to evaporate before it hits the substrate however, creating a "wet" deposit that has the tendency to run and create non-uniform coatings. The substrate can equally become saturated if the jet is directed at a fixed area for a period of time. As no "coated density" is reported in the reference, this spray coating process is an arbitrary exercise. Furthermore, whilst SEM images are presented in the reference, the lowest is at x5000 magnification (i.e. equating to the surface of some of the clusters visible here) which compared to the 600x used here provides no coating density information. Note the ~10µm clusters visible on the samples prepared here are much larger than the tenths of a micron long aggregates reported for the supplied fumed silica, indicating an additional agglomeration process has taken place.
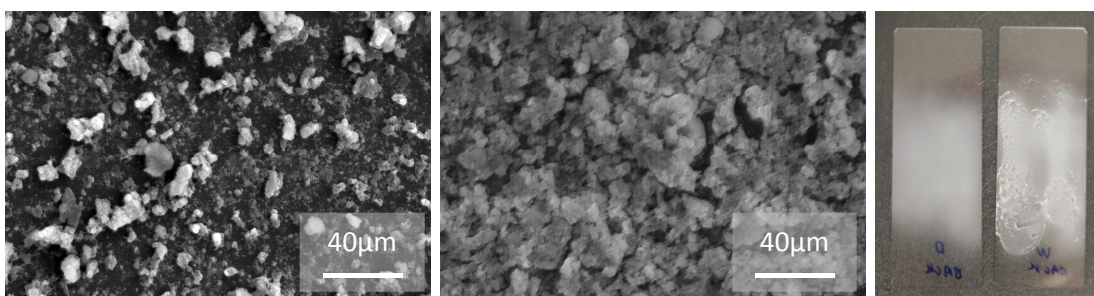
Figure 4.12: SEM comparison between "dry" and "wet" air brushed substrates. Left SEM image and left slide: "dry" air brushed, right SEM image and right slide: "wet" air brushed.

Variables such as this "dry" or "wet" coating approach, together with the coating density, will no doubt strongly influence the surface morphology, adherence, and wettability. Some authors who have conducted spray coating in literature report holding an airbrush at a specific distance from the substrate, but without many more details of the characterising parameters of the process (jet rate, flux, area spread, droplet size etc) it is pointless to report or attempt to reproduce this isolated condition. Here, all airbrushing has been conducted in such a way as to deposit an apparently "dry" uniform film on the substrates to a "medium" level of transparency as this visually best resembles those in the source and is free of runs and generally uniform in appearance.

A common artefact reported between all three stimuli responsive techniques highlighted previously (including the system under study here) is that immediately after droplet placement on the surfaces, both water and the appropriate oil phase used initially exhibit high contact angles. After a period of time, as required for surface rearrangement (typically 10 or 20 minutes) the contact angle of water falls, however the contact angle of the oil remains more or less static at a high level – i.e. hydrophilicity is not immediately apparent on dry surfaces. Yang et al. (2012) did further modify their PDDA-PFO/SiO$_2$ coatings with air plasma treatment to form additional hydrophilic polar groups and thus accelerate wettability, this was not performed here in respect of the size restrictions of the plasma cleaner available. To examine whether the coatings prepared here exhibited similar time dependent wetting to that presented in the original reference, glass microscope slides were cleaned and airbrushed with the prepared coating. Contact angle images of droplets deposited on the modified surfaces straight after deposition, and of the same droplet after 10 minutes, are shown in table 4.2 below. The same 15W/40 oil used in the channel tests was used here (and in following figures in this chapter) instead of hexadecane as per the original authors for applicability to the problem under investigation. Contact angles are measured roughly by eye for indication only – the optically rough substrates prevented use of the standard contact angle analysis software.

Time:	0 Min	10 Min
Deionised water	CA = ~149°	CA = ~139°
15W/40 Mineral oil	CA = ~126°	CA = ~121°
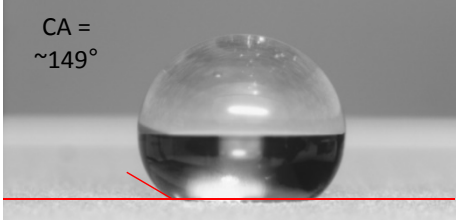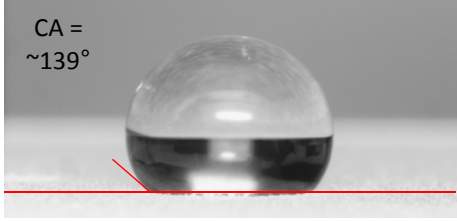
Table 4.2: Time evolution of contact angles for water and oil on a glass slide coated with the PDDA+PFO/SiO$_2$ coating. Red lines are approximate contact lines.

The results shown in table 4.2 contrast with those reported by the authors. They reported contact angles for water decreasing from 165° to 0° (i.e. complete water wetting) within 9 minutes on the PDDA-PFO/SiO$_2$ surface, whereas here, we see only a very slight decrease in contact angles for either water or oil for an equivalent time period. Water droplets in several locations on the same slide showed similar continuously hydrophobic behaviour. Assuming that the basic synthesis chemistry was successful, and noting that this same coating has been used by Yoon et al. (2014) successfully (if with a dip-coating approach), we can postulate that this lack of responsiveness is down to the surface structure and/or airbrushing technique employed. In particular with regards the particles used, Yoon et al. (2014) in fact source silica nanoparticles from Sigma-Aldrich in Korea but give no other information than a size of 10-25nm from their TEM images. Howarter and Youngblood (2008) report a situation where their films showed hydrophobic/oleophobic properties if produced differently, however their comments relating to this being through fluorinated constituents being distributed throughout the film, rather than solely at the surface, are incompatible with the disordered spray or drip coating processes used here.

Despite the preliminary non-responsiveness found here, the spray coated PDDA/PFO-SiO$_2$ film did show some potential and suggestions. When water was aggressively flowed onto the surface, water did completely wet the coating, and oil would also wet the dry coating similarly. Figure 4.13 shows water and oil droplets "pressed" (wetted) onto the otherwise dry coating.
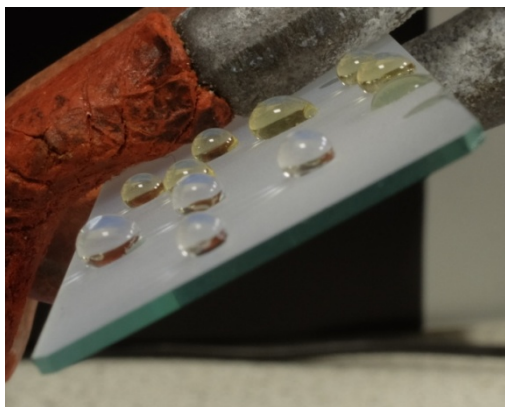
Figure 4.13: Hysteresis effects of oil and water droplets previously "pressed" on a tilted glass slide coated with the PDDA-PFO/SiO$_2$ coating.

What is quite clear from this is that for whatever reason, this coating is producing apparently stable Cassie-Baxter wetting scenario: The droplets only wet the rough surface and displace air when the air-layer stability is broken via an external influence (i.e. forcing the droplet onto the surface). The strong contact angle hysteresis of the droplets visible in the figure is indicative of this process, with a wetted zone under the droplets and dry regions immediately adjacent. The wettability of the oil droplets is also indicative of a lack of hydrophilic-oleophobic discrimination. Despite the unsuccessful responsive nature, it was found that so long as this coating was pre-wetted by water, oil droplets would be repelled or otherwise washed off the surface: In hindsight, the rough structured surface was performing exactly as a (mildly) hydrophilic and underwater oleophobic surface. This behaviour when pre-wetted would be expected to be produced by fumed silica alone given it is highly hydrophilic and features an enormous surface area per unit mass. The circular aggregates additionally satisfy the re-entrant structure requirement, and the presence of pores in the interstitial structure provides an opportunity to trap water (indeed, if the fumed silica trapped the initial PDDA into pores and prevented it from reacting, which may not of been present in "nanoparticle" silica, this may explain the lack of surface responsiveness).

In light of the findings working with the PDDA-PFO/SiO$_2$ system, it was thus decided to see what could be achieved with a simple coating of pre-wetted, fumed silica. The pre-wetting requirement means additional care is necessary to ensure the coating does not dry out before an experimental geometry is filled, but this can be managed. To begin with and primarily as a reference, figure 4.14 below shows the wetting behaviour of water (4.14a) and oil (15W/40 as previously, 4.14b) on a cleaned Perspex surface (emulating the flow channel), spray coated solely with fumed silica dispersed in ethanol at 0.2g/20ml. In these images, the "mixing needle" (90 degree bluff tip, diameter 0.9mm) is placed just above the surface of the substrate

without touching it. A liquid droplet is carefully advanced from the end of the needle until it touches the substrate and wetting commences. At this moment pumping is stopped and the liquid allowed to wet the surface under its own processes. These images are extracted when little further wetting progression is observed (in figure 4.14a, the water eventually evaporates from the surface).
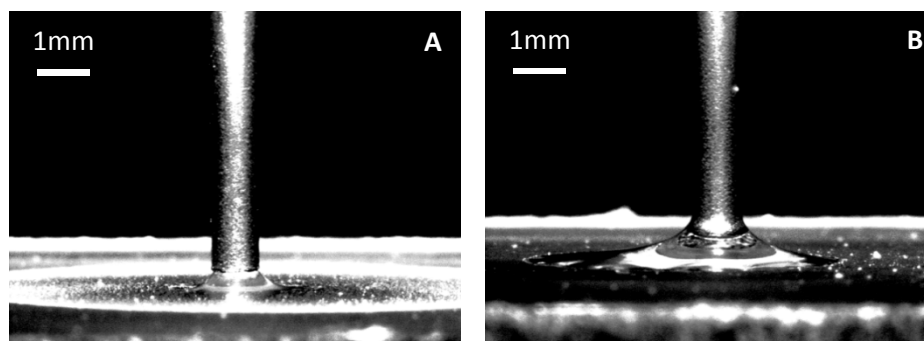
Figure 4.14: Wetting of water (A) and oil (B) on fumed silica sprayed on Perspex. Flow is stopped the moment contact is made with the surface. Images are taken when surface coverage propagation has slowed significantly.

We can see in both cases, but most strongly in case A with water, that the surface is very easily wetted by both water and oil. In fact, the wetting process is so strong with water that the moment a droplet touches the surface, it completely wets the surface, and proceeds wick across the substrate. This is less so with the oil, most likely due to the increased viscosity. When this fumed silica surface was pre-wetted with water, the oleophobic behaviour appeared equivalent to that of the prewetted PDDA/PFO-SiO$_2$ material. The problem with this coating, and equally with the PDDA/PFO-SiO$_2$ material, is that it is rubbed off with a single stroke from a base material. As a result it was considered likely that the coating may be washed away in a practical application, and a means to anchor it onto a surface was prudent (how wall shear rates in this application compare to that through separation meshes prepared in literature could be asked). This was achieved, quite successfully, by dispersing the particles in acetone, rather than ethanol, and airbrushing them onto a coating of household nail varnish previously applied to a Perspex substrate. Acetone is a well-known (if quite aggressive) solvent for nail varnish, and as a result the remaining acetone adsorbed on the silica particles solvates the surface and adheres them in place. The aim of this process is, rather than mixing the particles with an adhesive material which would completely cover the particles, is to anchor only one side and ideally leave the other side of the particles clean for maximum wettability. It is especially important in this case to "dry" coat the sample in-lieu of the previous discussion on airbrushing practice. Table 4.3 below compares the wetting behaviours with water on both a

Perspex sample coated with nail varnish, and the same such sample sprayed with fumed silica dispersed in acetone. Again, the needle is placed just above the substrate. Water is slowly pumped onto the substrate and the droplet allowed to grow in size, before being retracted back into the syringe to illustrate the advancing and receding contact angles.

Substrate coating	Advancing droplet	Maximum size	Receding droplet
Nail varnish	CA = ~82°	CA = ~64°	CA = ~50°
Nail varnish + fumed silica	CA = ~67°	CA = ~60°	CA = ~0°
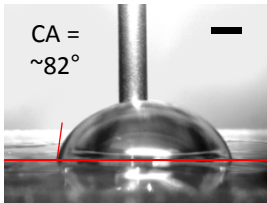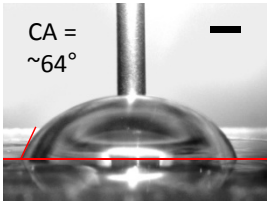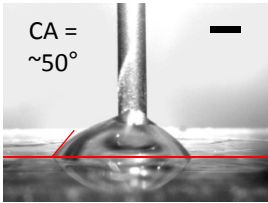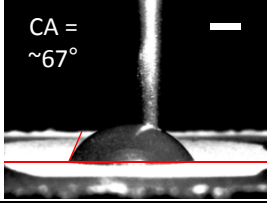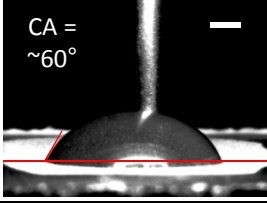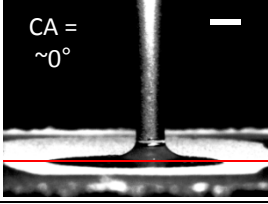
Table 4.3: Comparison of advancing and receding water contact angles (at similar areas of the substrate as figure 4.14) for nail varnish and nail varnish/fumed silica coatings applied to Perspex substrates. Scale bars are 1mm. Red lines are approximate contact lines.

In the case of the nail varnish layer, we can see that an advancing contact angle of about ~82° and a lower receding angle around ~50° is achieved, the hysteresis being most likely through brush strokes and imperfections in the surface from drying processes. For the fumed silica coated sample the advancing contact angle is quite high (~67°), as opposed to the self-wetting behaviour seen previously. Even with the care taken to adhere the fumed silica particles only partially into the surface, the advancing contact angle is shallower, but nonetheless comparable to that for plain varnish (~82°), suggesting either the particles have been wet significantly by varnish, or the substrate layer is having some important effect through the silica coating. Either way, once the fluid droplet is receded, a 0° contact angle is clearly evident, with water remaining wetted in the Wenzel state in the coating, as desired. Figure 4.15 below shows a simple test to demonstrate the mechanical robustness of this coating. Three areas on a Perspex sample are painted with varnish (as marked) and the entire sample spray coated with fumed silica. A damp tissue is then dragged over the lower half of the sample, here from right to left.
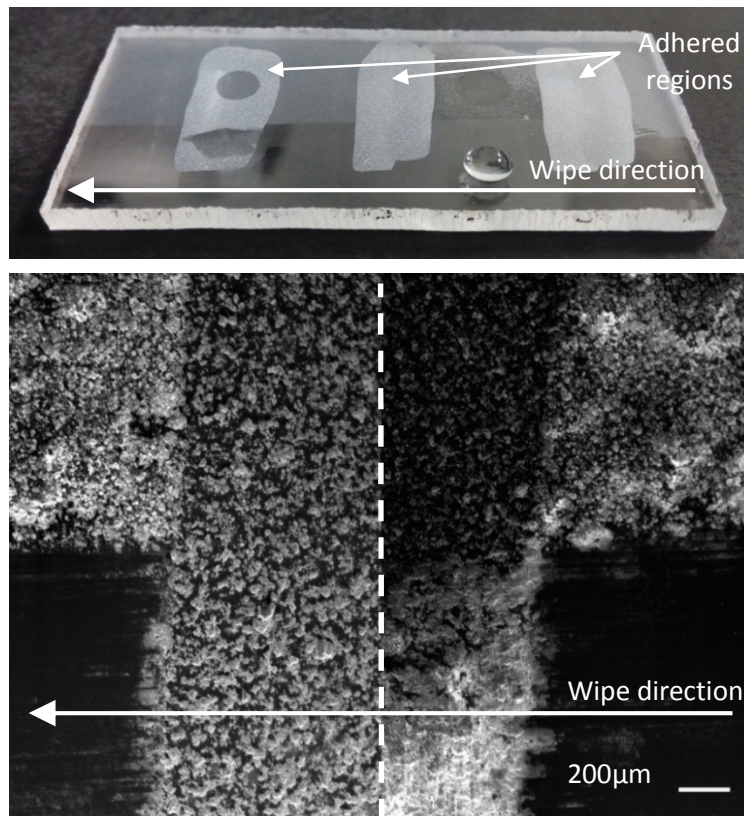
Figure 4.15: Robustness "wipe" test of adhered fumed silica coating. Top: photograph of sample with droplets to compare wetting characteristics, bottom: split x60 SEM images at intersections between an adhered region and wiped areas

It is quite clear that the coating (and surface wetting properties from the water droplets) has been completely lost in the unadhered regions. In the adhered regions, the wettability remains seemingly unaltered. The split SEM image shows detail at the intersections of the wiped-unwiped and adhered-unadhered regions of one of the painted segments. Evidently the coating is completely removed from the unadhered regions, but surprisingly in the adhered areas the coating is negligibly affected, apart from accumulating removed material. A definite difference can also be seen in the morphology between the adhered and adhered regions, suggesting that some coating of the particles with varnish could well of occurred and an even lighter coating technique may be preferable.

In order to demonstrate the effectiveness and stability of this adhered coating at defining the points of interface contact on channel walls, even with deliberate oil contact, a simple test was devised. A strip of Perspex sheet was cut, around 1cm wide by several centimetres in length. Both of the smooth faces of this sheet were cleaned with ethanol, and to only one face, and only over part of the strip length, was an adhered fumed silica coating applied. The end of this region was marked on the side of the strip with a red line. The fumed silica coating was

prewetted, then immersed into a tank containing only water to a depth beyond the end of the coating. A layer of oil was then carefully run onto the top of the water surface. The test sample was then drawn up, through this oil layer, to a height that placed a large section of the coated surface in direct contact with the oil layer, and left in this location for 20 minutes (the motorised contact angle syringe pump was adapted for this purpose). After this time had elapsed, the sample was then lowered back to the original location. Figure 4.16 overleaf shows this process. The entire coated surface has been marked with a red dashed line in these images for clarity, the sample being viewed edge-on.

In image 1, we can see the static contact angle between the oil and water phase indicating the usual preferential wetting of the clean Perspex by oil (oil contact angle <90°). In image 2, once motion starts, the oil contact angle becomes >90° as it is now an advancing contact angle. Both sides of the sample in contact with the oil layer are still native Perspex at this point. Image 3 shows that the situation remains essentially similar as the modified surface passes into the oil phase, and image 4 shows the situation at the moment motion ceases, with approximately the middle third of the coated region directly situated in the oil phase. After 20 minutes, image 5 shows that the contact angle has recovered slightly on the native Perspex side of the sample, but failed to do so on the coated surface. The most important image is image 6, when the sample is being lowered back towards the original position. We can clearly see on the native Perspex side of the sample oil that has now wetted this surface and is being dragged down with the sample into the water layer. On the coated side of the sample, the oil contact angle is still somewhere well above 90°, due to the layer of water contained in the coating having acted as a barrier. This behaviour is continuous across the full length of the coated surface, including the region that was held in the oil phase. Only in image 7, when the end point of the coated region passes the water-oil interface, do we see the oil phase contact angle start to transition to a more familiar situation for Perspex. The final image, image 8, shows the sample lowered back to the original location. The uncoated native Perspex on both sides of the sample have been clearly wetted with oil as normal.

This test clearly shows that despite the coated surface being fully immersed in oil for an extended period of time, it has resisted movement of the oil contact line onto the surface. In this way, the two phase interface is successfully pinned at the edges of this area, as clearly seen in image 7.

Raise sample from tank:
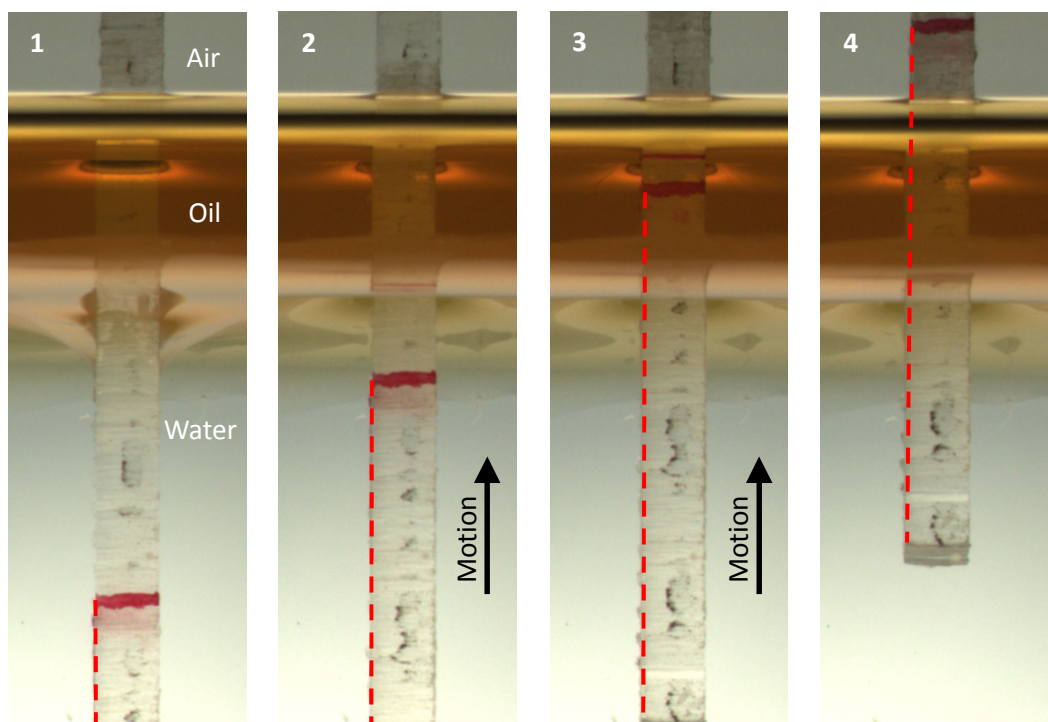
Lower sample into tank after 20 minutes:
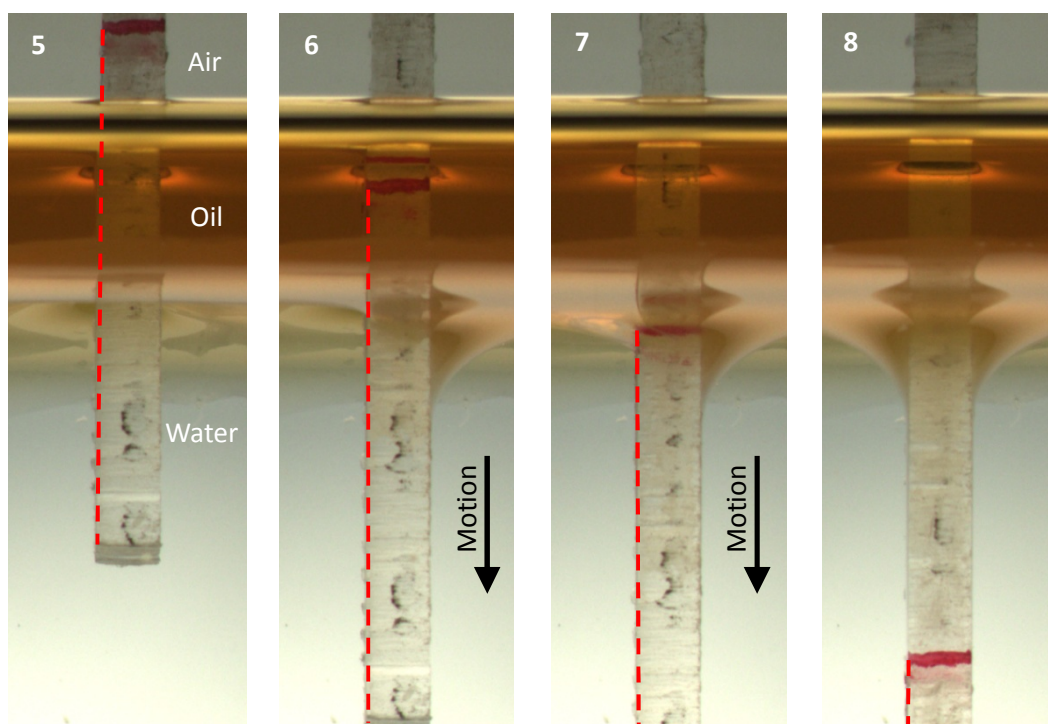
Figure 4.16: Images from "Dip tests" of Perspex substrate partially coated in water wetted, nail varnish-adhered fumed silica. Coated surface is shown by the red dashed line. The sample is raised through the oil layer, held for 20 minutes, then lowered back. The Perspex sample is 3mm thick.

4.4 Practical application of adhered fumed silica coating

To conclude this work, it is now prudent to demonstrate the functioning of this adhered fumed silica coating in the original flow channel. The air brushing process is versatile as it can be used to apply the nail varnish as well as subsequently the fumed silica, and achieves a thin layer over large surfaces, something difficult to achieve via brush application used herein. The channel was prepared by thorough cleaning and masking of the channel side walls to prevent coating. The lower channel wall was airbrushed with a black nail varnish thinned with 50:50wt% ethyl acetate (acetone is widely not recommended as a thinning agent). After a short drying period, this surface was then airbrushed with a coating of fumed silica in the same manner as described previously. The fumed silica surface was fully water wetted, then the entire channel assembled and flooded with oil to pre-wet all salient surfaces, in accordance with the conditions of figure 4.5, and ensured level with respect to gravity. The same oil and the same aqueous solutions as previously have been used, but at a higher flowrate of 2000ml/hr to look for flow instabilities, restricted by the stall limit of the syringe pumps.

The figures presented next show the fully developed flow configurations towards the end of the achievable flow duration. Figure 4.17 shows the channel outflow and complements that shown earlier in figure 4.5. It can be seen in figure 4.17 that unlike figure 4.5, where the oil phase envelope the aqueous phase, the surface coating has caused the two fluids to flow in the desired stratified manner despite the shallow aspect ratio channel. We can also demonstrate that this is the case throughout the entire channel length, in a more rigorous manner to that achieved previously, by moving an illumination source and watching the reflection off the meniscus. A strip light was rotated in a cone, the axis of which was approximately in line with the cell, and five frames from the resulting video are reproduced in figure 4.18. The reflection lines suggest the stratified structure is achieved throughout the channel length, with a high radius of curvature upstream where the channel is tall (i.e. tending towards the natural meniscus radius of curvature) and an essentially flat interface downstream where the channel is shallow. This corroborates with the flow structure at the outlet in figure 4.17.
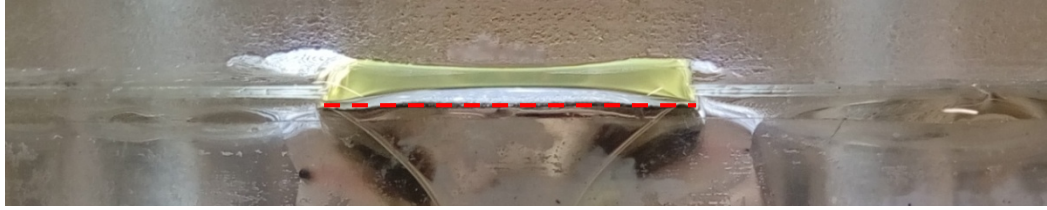
Figure 4.17: Outlet view of the adhered fumed silica coated channel under two phase flow (compare to the uncoated channel in figure 4.5 previously). The coated surface is highlighted by the red dashed line.
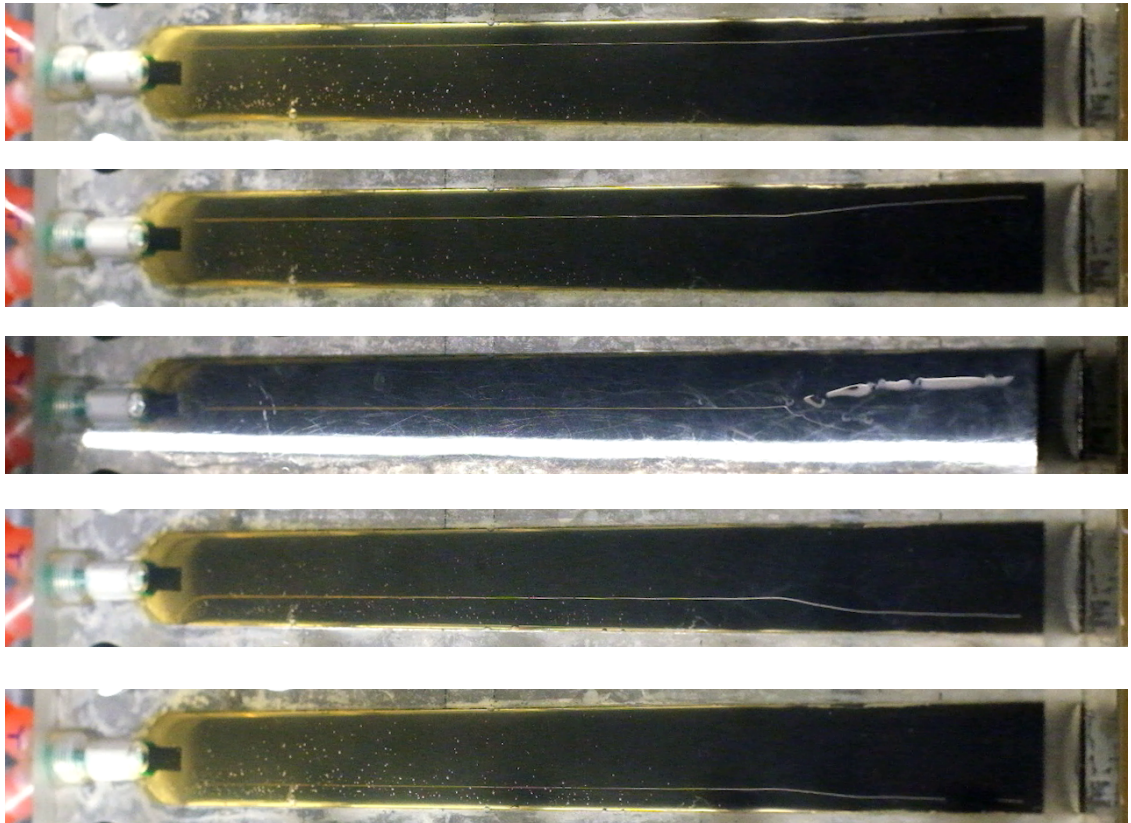
Figure 4.18: Above view of the adhered fumed silica coated channel under two phase flow. A strip lamp is rotated in a cone roughly about the axis of the channel to provide information on the two phase meniscus shape.

Further to the ideal requirement for an optically clear coating, both the PDDA/PFO system originally tested, as well as both the adhered and un-adhered versions of the fumed silica coating, take on a frosted appearance when dry, as visible in figure 4.15. When wet, the white appearance disappears, but a rough surface is still clearly visible. This means that the surface cannot be optically viewed through and similarly a laser beam cannot be injected through it (key factors in experimental design in chapter 6). When laser illumination impinges on this

surface, attempting to exit a cell, it will also scatter excess light back into a flow geometry, and more importantly, directly back to a viewing camera.

In figure 4.18 a black nail varnish, rather than clear varnish, was used assuming it would minimise light scattering in this regard. However, whilst the clear varnish would allow the majority of the incident illumination to pass out of the cell, the black varnish would need to absorb all the excess illumination. A simple comparison was conducted to compare these different approaches. Two fumed silica coated Perspex substrates were prepared, one using clear and one using black air brushed nail varnish. A third substrate was prepared by replacing fumed silica for acetylene black at the same airbrushing concentration. AB 50%-01, kindly donated from Soltex Inc. was used, composed of particles of mean size 25-45nm (Soltex Inc., 2016) with a high specified absorptivity (thus a possible candidate for trapping a water layer at a surface, even if not evidently re-entrant) and inherently low reflectivity. The experimental setup is shown in figure 4.19. These substrates are held in a tank of water, on a support that allows a clear aperture at the rear of the substrate for transmitted light to pass. Laser illumination from a 532nm laser pointer is directed at 90 degrees to the substrate, and microscope system used to image the scattered light from the surface at an inclination of 30 degrees relative to the plane of the coated surface, emulating the oblique imaging technique detailed in chapter 6. A PixeLINK B741 camera and Navitar Zoom 6000 system (1-60135 zoom lens equipped with 1x adaptor and no additional lens attachment) is used. The tank is arranged to provide a wall at 90 degrees for the microscope to image through. Images are recorded with camera settings set to manual and after a period of sensor warm up, and the sample is gently tapped to average out interference patterns. Pixel intensities are subtracted from a background level (nominally 12 counts in a 8-bit image) and summed across a standardised cropped area of the resulting images and averaged over 8 repeats (two sets, each at 4 different incident locations). Figure 4.20 presents the average results, normalised against the brightest sample.
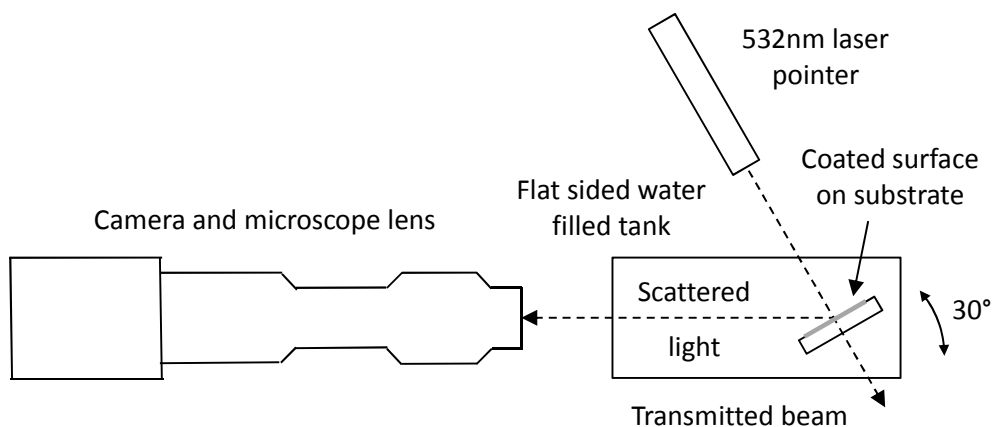
Figure 4.19: Experimental setup for characterising reflectivity of coated substrates
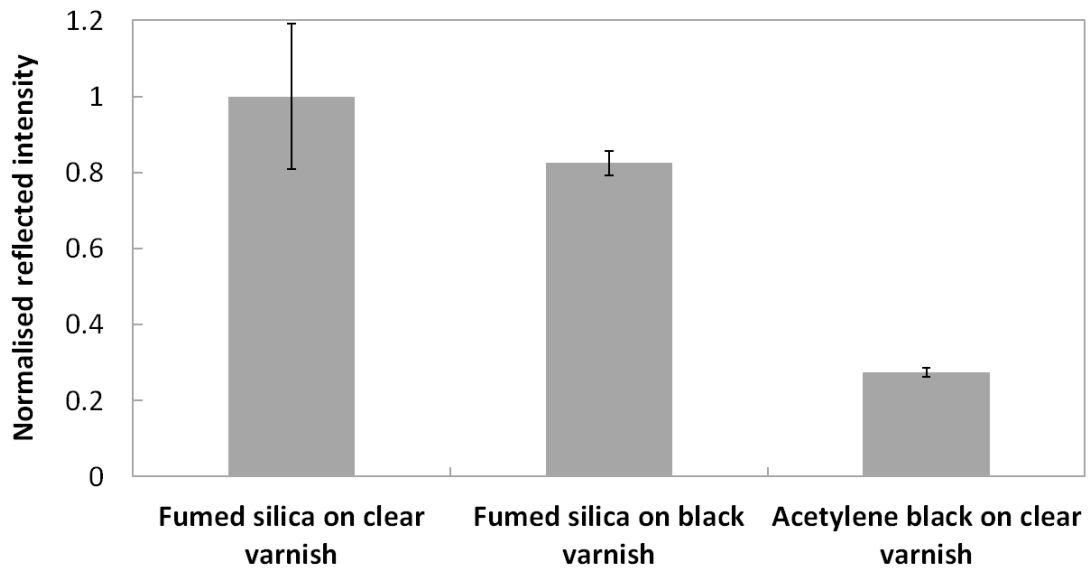
Figure 4.20: Reflected light intensity comparison for the three different substrates. Averaged results normalised to the brightest sample are presented. Error bars are to 1 standard deviation.

From figure 4.20 we can see despite the variability in results that the use of black as opposed to clear nail varnish is successful at minimising reflected light, but only marginally, whereas the acetylene black significantly reduced the reflected light intensity. This marginal change in reflectivity can be explained by the majority of the scattering being caused by the fumed silica layer (noting the coated black varnish has a white frosted appearance when dry, if not when wet), thus the varnish layer underneath has limited overall impact. Although successful at minimising scattered light, the freshly airbrushed acetylene back when sat in air proved not impossible but quite reluctant to wet with water, suggesting limited usefulness for this application.

4.5 Conclusions

From this superficial study and the tests performed it was deemed that the adhered fumed silica coating was sufficient for the purposes desired. Following the requirements presented earlier, in section 4.2, this coating achieves the desired functionality and is stable against time (so long as drying out is prevented), has been made mechanically robust, is simple to prepare and can be easily applied in a thin layer to any size substrate without specialist equipment. The coating does impose optical restrictions, but there are very few systems in literature that enable this shortcoming to be overcome.

The following points of investigation are acknowledged for future work:

- Well controlled long term stability tests (though general use to date suggests this coating is quite stable even when water wetted but covered in a layer of oil)
- Optimisation and investigation into airbrushing practices and improved achievement of "partially embedded" fumed silica particles, together with quantification of associated contact angles in different test scenarios
- Closer investigation into the reasons why the PDDA/PFO-SiO$_2$ proved unresponsive, in particular focused on the airbrushing technique and the type of silica particles used

It is acknowledged in retrospect that this fumed silica coating technique shows quite similar characteristics to at least two other works recently identified. Firstly, Chen et al. (2014) use silica gel, arguably similar to the fumed silica as used here, to create an underwater hydrophobic coating. Secondly, Li et al. (2015) also use the airbrushing technique for deposition of a simple rough surface modification agent (i.e. the airbrushing is not limited to a complex PDDA/PFO-SiO$_2$ blend), in their case zinc oxide.

The sequential deposition of a binding substrate followed by particles, used here however differs from the work of these two groups who both mix binding/adhesion agents directly with their particles. If this process two-step did indeed successfully only partially cover the particles, rather than inevitably coating them with a layer of binding agent, this might represent an improved coating approach, if no longer a single step or dip-coatable process. As the work of these two groups is with meshes, rather than flat surfaces, it is not immediately apparent if they also feature the same resistance to initial wetting as seen here, with their adhered particles, over un-adhered systems.

Chapter 5.

Profiled channels for extensional flow.

Chapter 5: Profiled channels for extensional flow.

5.1   Examples of profiled extensional channels in literature

In section 1.5 it was highlighted that the key requirements for meaningful measurements based on extensional flows, due to the time sensitivity of materials under study, is that a. the extension rate is held constant along a streamline, and that b. measurements are conducted at steady state (or $t = \infty$). To this end, appropriate profiling of a converging channel is necessary to attain a constant (or as close as possible to constant) extension rate in the Lagrangian sense, and critical consideration of channel design variables are necessary to allow as long extensional durations as practicable.

In almost all work attempting to produce constant extension rates a hyperbolic profile is adopted; of the form $r^2.z = constant$ for axisymmetric geometries (extension directed along the z axis) and $y.x = constant$ for planar geometries (extension directed along the x axis). Table 5.1 overleaf summarises examples where hyperbolically profiled channels have been derived, constructed or simulated, all featuring these forms (or modifications thereof). Pipe and McKinley (2009) was used as a starting reference. This list is neither complete nor a strictly representative cross section. A third important criteria for meaningful extensional measurements, also highlighted previously, is that the elongation rates are constant not only along, but between streamlines - viz, fluid shearing is minimised as well as appropriate channel profiling used. In the examples of table 5.1, either mixed flow is allowed, a lubricated flow is attempted, or moderate Reynolds values used to produce a core flow of approximately homogeneous elongation. In the latter two cases, even when design of the channels have taken these factors into account, the resulting channel profiles used still take the above hyperbolic forms. For the rest of this chapter, we will be assuming pure wall slip flows, and working with planar extension, though analogous results could no doubt be reached based on axisymmetric geometries too. "Area" based flow rates will thus be referred to, and "shear rates" will still be commented on in-lieu of real-world mixed flows.

From the survey, hyperbolic profiling often appears to be taken as read (indeed being "known from literature" (Schuberth and Münstedt, 2008)) without assessing underlying assumptions. However Feigl et al. (2003), Winter et al. (1979), James (1991), and Collier et al. (1998) derive the hyperbolic profiling in varying degrees. There are two complementary derivation routes that lead to the hyperbolic profile: A 1D analysis, and inviscid flow in a cross-slot type geometry. Both assume the fluid to be "shear free" (i.e. referred to as having zero vorticity), assuming that such conditions can be achieved via wall lubrication. The fluid is also incompressible and under steady flow.

Reference(s)	Extension and channel type	Hyperbolic contraction dimensions (for largest total strain channel) R = Radius W = Width L = Flow length D = Planar depth (constant)	Shear conditions	Highest flow parameters reported for a complex fluid test Re = Reynolds number (when given) Q = Flowrate E = Extension rate	Hyperbolic profiling form	Channel entrance adaption to hyperbolic section	Complex fluids under study and additional notes
Williams and Williams (1985)	Planar, stagnation	W: 5 – 205mm L: (Not apparent) D: 50mm	Lubricated	Q: 18cm^3/s (+ 2.4cm^3/s lubricant) E: 12s^{-1}	y.x = C (incorporates lubricant layer)	(Stagnation flow)	Maltose syrup, polyacrylamide and water mixture. Appreciable scale experiment. Limited by flow instabilities above 20cm^3/s.
James et al. (1990)	Axisymmetric, converging	R: 25 – 5.23mm L: ~50mm (inc. conical section)	Moderate / high Re	Re: 334 Q: 534cm^3/s E: 177s^{-1}	R^2.z = C	Cylindrical – conical – converging	Copolymer solution of polymethylmethacrylate in dipropylene glycol monomethyl ether. Note existence of shearing boundary layer.
Everage and Ballman (1978)	Axisymmetric, converging	Not stated, assumed cm scale	Lubricated	Q: Not stated E: ~1.2s^{-1}	Not stated, however corrected for lubricant layer	Cylindrical – corner – converging	Polystyrene melt. Detailed report "to be presented elsewhere" could not be located. Setup stated to of been used up to extension rates of 200s^{-1}.
Ober et al. (2013)	Planar, converging (- diverging)	W: 2920 – 400µm L: 200µm D: 200µm	Mixed flow	Re: O(<1) Q: 50µl/s E: O(1000s^{-1})	y.x = C	Parallel – corner – converging	Range of fluids studied. Work towards a practical extensional rheometer.
Oliveira et al. (2007)	Planar, converging	W: 400µm – 10µm L: 780µm D: 46µm	Mixed flow	Re: 9.62 Q: 0.83µl/s E: 4000s^{-1}	y.x = C	Parallel – corner – converging	4 geometries studied. Study of Newtonian fluid (DI water) as design work for Ober et al. (2013).
Winter et al. (1979)	Planar / axisymmetric, aimed at	Not stated, assumed cm scale for physical channel	Zero vorticity (shear free) assumption.	Q: 6.85cm^3/s (+ 3.42cm^3/s lubricant) E: Not stated	y.x = C and R^2.z = C (shown).	(Stagnation flows). Not visible in	Framework for extensional rheometry, various concepts presented. Polyacrylamide solution in water used

	stagnation flows. Figure 8 / 9: axisymmetric channel		With / without lubrication for physical channel		$R^2.z = C$ for physical channel.	figure 8 or 9 of reference	with lubricated axisymmetric converging channel in figures 8 and 9 of reference (under development).
van Aken and Janeschitz-Kriegl (1980), (1981)	Axisymmetric, stagnation	R: 3 – 10mm L: 5.5mm	With/without pre-coated lubrication	Q: Not stated E: ~0.1s⁻¹	$R^2.z = C$	(Stagnation flow)	Polystyrene melt biaxial stagnation flow.
Macosko et al. (1980), (1982)	Planar, stagnation	W: 3.7 – 76mm L: 34.9mm D: 100mm	Lubricated	Q: 0.9cm³/s (+ 2.4cm³/s lubricant) estimated via fig 5. E: 0.08s⁻¹	y.x = C	(Stagnation flow)	Polystyrene melt. After Winter et al. (1979).
James (1991)	Axisymmetric, converging	R: 25 – 5.23mm L: ~50mm (inc. conical section)	Moderate / high Re	Re: 200 Q: < 600cm³/s E: Perhaps ~230s⁻¹ (fig. 5 and table. 1)	$R^2.z = C$ (+ boundary layer) (shown)	Cylindrical – conical – converging	Newtonian water glycerol mixture. Flowrates not directly reported. Same program of work as James et al. (1990).
Feigl et al. (2003)	Axisymmetric, converging	R: 10 – 0.3mm (calculated) L: 25mm	Wall slip assumed	Q: 0.4921cm³/s E: 25s⁻¹	$R^2.z = C$ (shown)	Cylindrical – corner – converging	Two geometries. Simulation study of a low density polyethylene melt. Detailed theoretical background information.
Pandey and Lele (2007)	Axisymmetric, converging	R: 10 – 0.3mm L: 25mm	Mixed flow (no-slip)	Q: 0.02cm³/s E: 12.48s⁻¹	$R^2.z = C$	Cylindrical – corner – converging	Low density polyethylene melt. Simulation linked with experimental work.
Nyström et al. (2012)	Axisymmetric, converging	Non-dimensional	Mixed flow (no-slip)	Re: O(10⁻²) assumed Q and E: Non-dimensional	$R^2.z = C$	Cylindrical – corner / radiused corner – converging	Simulated Newtonian and Boger fluids. Simulation study of various contraction forms.
Wang et al. (2010) Wang and	Planar, converging	W: 500 – 26µm L: 422µm D: 46µm	Lubricated	Re << 1 for core fluid Q: 0.28µl/s core	y.x = C	Parallel – corner – converging	High molecular weight PEO in water/PEG solution. Lubricant significantly affects profile of core

James (2011)				fluid (+ 0.28 µl/s lubricant) E: 200s^{-1} (depending on position)			flow.
Schuberth and Münstedt (2008)	Planar, converging	W: 14 – 0.5mm (calculated) L: 50mm D: 14mm	Mixed flow	Q: 47cm^3/s E: 60s^{-1}	y.x = C	Parallel – corner – converging	Aqueous polyacrylamide solution
Collier et al. (1998)	Axisymmetric, converging	Not stated, but two dies of Hencky strains 6 and 7	Lubricated	Q: Not stated E: 136s^{-1}	R^2.z = C	Cylindrical – corner – converging	Polypropylene melts and lyocell solutions. Core-skin polymer samples achieve lubrication. After Kim et al. (1994). Strain rates achieved up to 533s^{-1} with this setup.
Shirakashi et al. (1998)	Axisymmetric, converging	R: 24.7 – 4.99mm L: 127.03mm	Mixed flow	Re: 494 Q: 94.1cm^3/s E: 8.7s^{-1} (calculated)	R^2.z = C	Cylindrical – corner – converging	Polyacrylamide aqueous solution
Kim et al. (1994)	Planar, converging	W: 16 – 2.29mm (calculated) L: 31mm D: 25.4mm	Lubricated	Q: 0.35cm^3/s (calculated assuming both core and lubricant) E: 0.19s^{-1}	y.x = C (shown)	Not shown	Polypropylene melt. Core-skin polymer samples achieve lubrication

Table 5.1: Non-exhaustive examples of profiled hyperbolic channels in literature. Channel dimensions are interpreted from the information in the references (particularly for stagnation flows). Flow rates, extension rates and Reynolds values are intended as examples of the maximum conditions in the experiments: these values do not necessarily correlate to the same test conditions and the reference should be consulted directly for more detailed information. Note "corners" for inlet adaptions vary from relatively modest to almost 90 degrees in some cases. Lubrication for planar channels is usually only applied to two of the four channel walls.

When designing a hyperbolic planar contraction based on a curve of $y = 1/x$, there are essentially three design parameters that can be adjusted: these are the overall channel scale, the desired Hencky strain, and the start and end points of the hyperbola to use for the physical channel, illustrated in figures 5.1 to 5.3. An initial hyperbola of $y = 1/(x + 1.7)$ has been used here for illustrative purposes. These three factors have important design consequences and are essentially independent in nature. In these examples the coordinate points have been transformed geometrically from the initial hyperbola, rather than via modifying the defining equation.
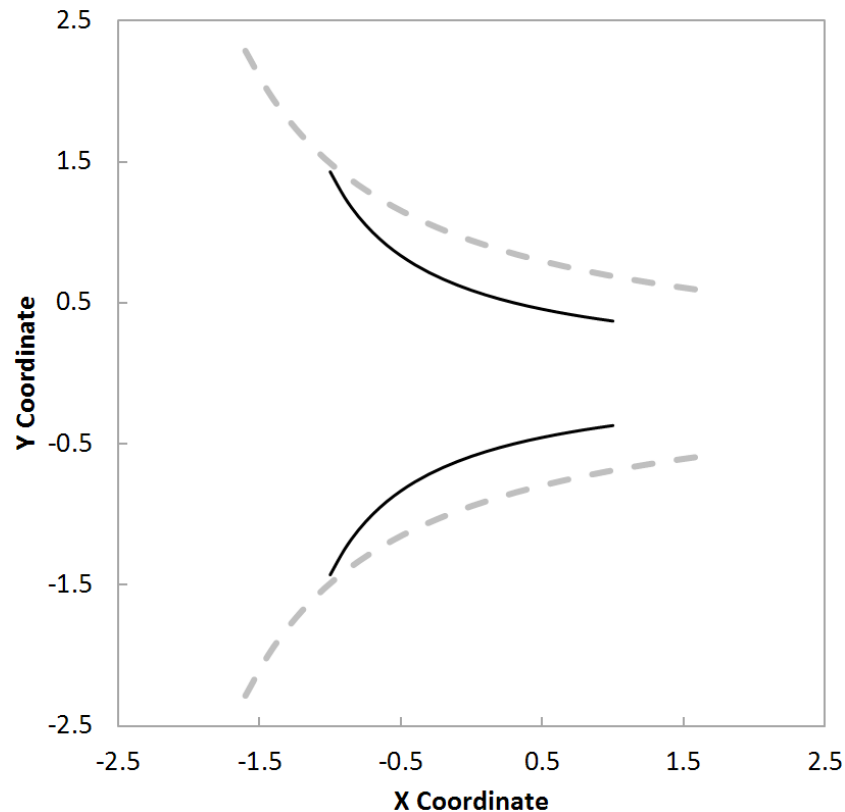
Figure 5.1: Scaling of hyperbolic channels. The initial hyperbolic channel (black line) is scaled by a factor of 1.6 in both the X and Y directions, centred about the plot origin, to yield a new hyperbolic channel of larger physical scale (dashed grey line).

In figure 5.1, the original hyperbola has been scaled by a factor of 1.6, from a 2 unit long contraction to a 3.2 unit long contraction. The original hyperbola can similarly be shrunk. Irrespective of scale, the final Hencky strain achieved (based on the ratio between the start and end channel heights) remains the same, and constant extension rates are still produced through the channel. There are significant advantages in tending towards a smaller channel as briefly noted section 4.1 previously. If the same extension rate is to be attained in two hyperbolic channels of different scales, the transit time of a fluid particle from the start to the end of the channel are identical. The narrower, but also shorter channel means shear rates

125

remain identical; however shear induced pressure drops, which scale with shear rates and channel length, are subsequently reduced in small scale channels. This reduces their contribution relative to pressure drops from extensional flow which are usually of interest. With the smaller channel, reduced flow rates of test fluid for the same extension rate are also required, permitting smaller sample volumes. The most significant benefit however is the dramatic reduction in Reynolds values with decreasing scale for the same required extension rate and Hencky strain. This occurs though the simultaneous reduction in both velocities and channel dimensions. Inertial contributions to pressure drops also fall, in addition to those from shear flow. Dilute, low viscosity samples usually feature relatively rapid relaxation timescales, which thus demand high extension rates to show phenomena of interest. Both the viscosity and strain rate factors with these fluids make the use of small scale channels the only way to study such flows whilst maintaining stable laminar conditions.
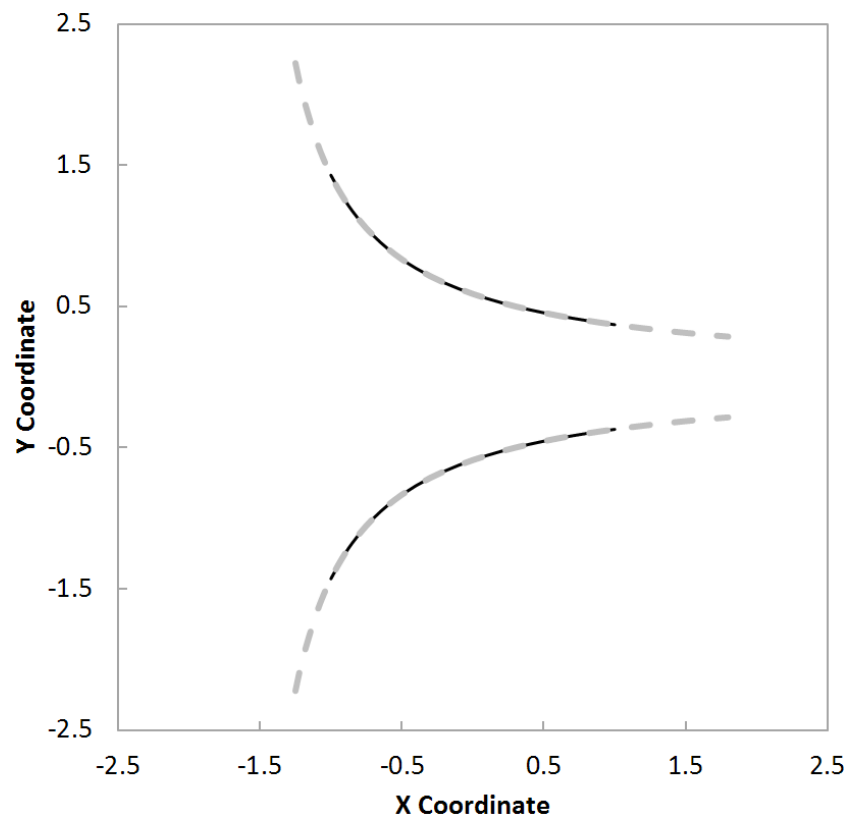
Figure 5.2: Variation of Hencky strain through choice of hyperbolic channel extents. The initial hyperbolic channel (black line) has a Hencky strain of 1.35. This is extended upstream and downstream to yield a Hencky strain of 2.05 (dashed grey line).

In figure 5.2, the original hyperbola has been extended to locations further upstream and downstream than the initial hyperbola, increasing the Hencky strain from 1.35 to 2.05. The original hyperbola can similarly be extended solely in an upstream or downstream direction as desired. The extension rate between the two cases, for the same area flow rate, remains

identical. The Hencky strain, or total extension experienced by a fluid packet as it propagates down the channel, is important, and is directly analogous to the time period for which a fluid packet is undergoing extension. Authors such as Ting and Hunston (1977) underline the need for sufficiently long timescales and sufficiently high rates of strain (e.g. relative to the relaxation timescales of the system under test) for meaningful data to be obtained. In an idealised situation, sufficient total strain would occur to reach some form of steady state with respect to fluid stresses. As Hencky strain is increased however, pressure drops rise and channel dimensions increase. This is particularly so if the channel is extended in a downstream direction. Hencky strains typically around 3-4 are as high as normally attempted, as channel lengths, shear rates, and thus pressure drops increase very rapidly beyond this point for even slight increases in total strain.
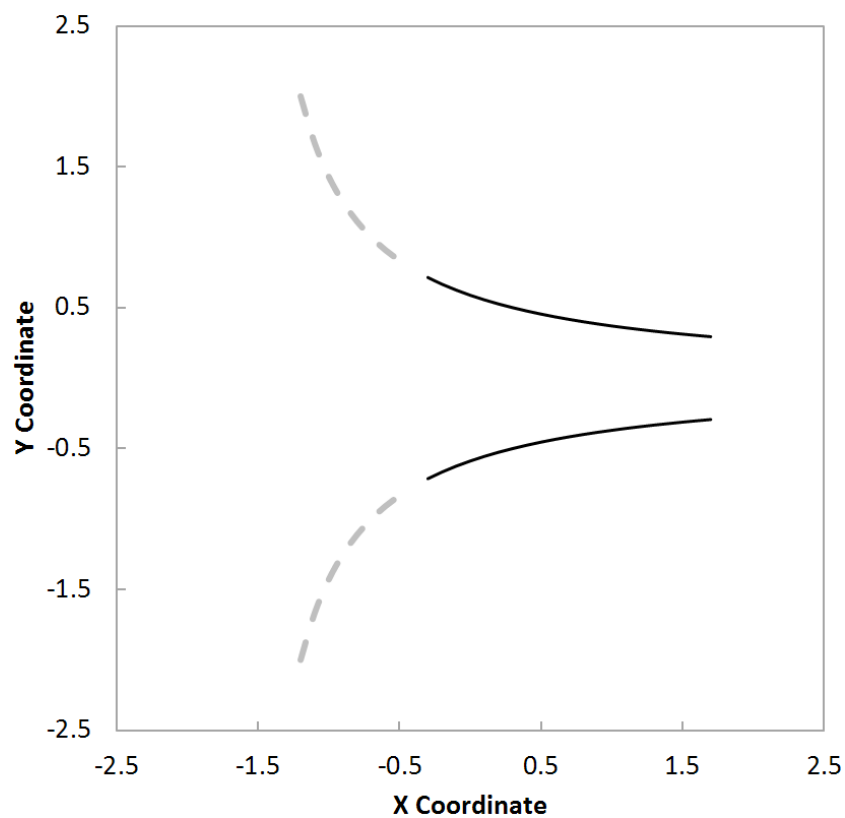
Figure 5.3: Choice of start and end points of a hyperbolic channel. Two choices are shown, one dominated by shallow wall angles (black line) and one dominated by steep wall angles (grey dashed line). Both channels have identical Hencky strains of 2.4 and identical extension rates for a given flow rate.

Figure 5.3 shows two hyperbolic channels, with the same Hencky strain and extension rate, but with different start and end points on the initial hyperbola. The choice of the starting point, or in effect the wall angle range used, is evidently a useful criteria – At locations further "upstream" (at higher wall angles) in a hyperbolic channel, velocities and shear rates would be

greatly reduced, and significant changes in Hencky strain area achieved for only modest increases in channel length and associated pressure drops. Thus, it is evidently beneficial to use this upstream region (or otherwise extend a channel in an upstream direction), something which will be considered further in the next section.

There is one further parameter that might be considered, and that is the "rate" of the hyperbolic contraction, by taking an initial hyperbola and stretching it in only one direction – For example, the X axis. It can be readily shown with a basic spreadsheet test that shrinking a channel by half in the X direction produces a doubling in the extension rate for a given area flow rate, and constant extension rates down the channel length area still attained. Thus, this would superficially appear as an additional method to control extension rates, in addition to that through the ratio of flow rate to length scale squared. Consider figure 5.4 below however.
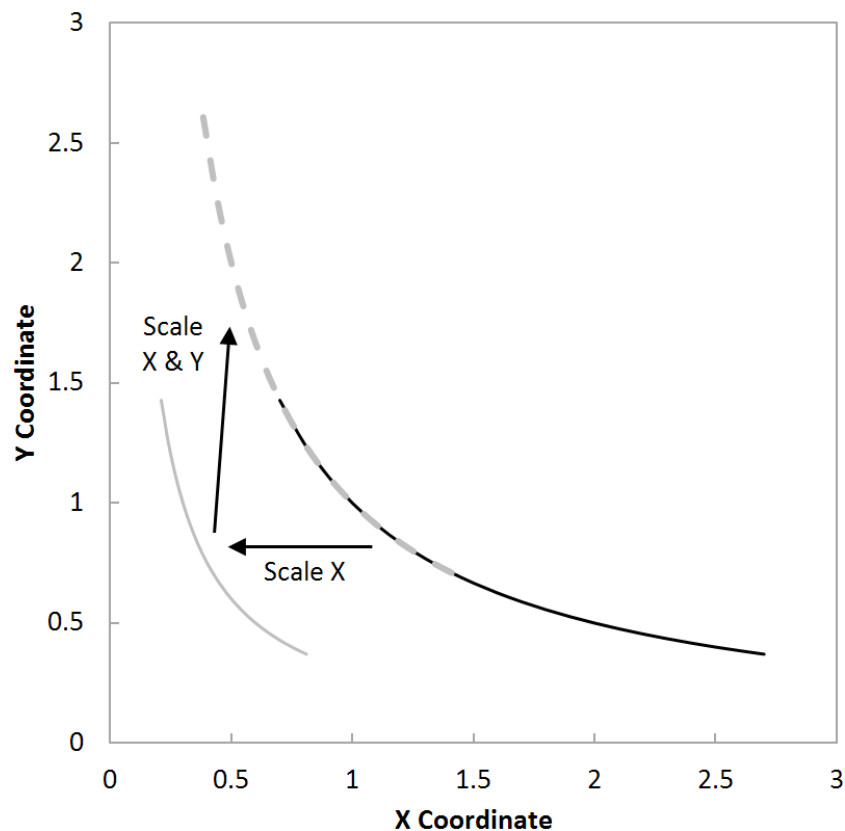
Figure 5.4: Equivalence of a hyperbola scaled in only one dimension. The initial hyperbola, $y = 1/x$, (black line) is scaled in the X direction only by a factor of 0.3 relative to the origin to yield the grey line; followed by a stretch in both X and Y of factor $\sqrt{1/0.3}$ relative to the origin to produce the dashed grey line. The resulting hyperbola maps directly back onto a different section of the original hyperbola.

In figure 5.4, an initial hyperbola of $y = 1/x$ is first scaled by a factor of 0.3 in the X direction, which would give an increase in extension rates of 3.33x. If this curve is then stretched in both X and Y by $\sqrt{1/0.3}$, it then maps back onto the original hyperbola for a region of the channel "further upstream". We thus realise that by scaling only one dimension, a new hyperbolic channel has been created which is simply on a smaller scale, and uses a region further "upstream" of the original; and is not an independent design choice. This ability to "map" the hyperbola back onto the original is supported by scaling X or Y in the numerical definition of a hyperbola being equivalent.

Choice of the extension rate, as dictated by the channel area and imposed flowrate, simply becomes a trade-off between it being sufficiently high for useful measurements against resulting shear rates and pressure drops, and any flow instabilities incurred. Extension rates in excess of one half of the relaxation rate $\dot{\varepsilon} > (1/2\lambda)$, are required for significant accumulation of macromolecular strain (or, that the Weissenberg number $Wi = \dot{\varepsilon}\lambda > 0.5$) (Haward et al., 2012).

5.2   Choice of hyperbola starting location for converging flow

In the previous section the significant apparent advantages of extending a hyperbolic channel in a direction "upstream" were noted. Following the definition that a hyperbolic channel produces constant rates of extension aprioi, and noting that such a channel extends to infinity at X = 0, channels taking the appearance of figure 5.5 could then be considered. Within these considerations such a channel would allow very high overall Hencky strains to be attained with minimal pressure drops. Despite the advantages apparently offered by designing channels in this regime, no critical consideration of the "start point" of a hyperbolic channel has been found in literature even though factors such as scale, Hencky strain, and profile are at least specified with regards to channels used. Conical sections, corner, and radiused corner adaptions to upstream sections are all present in the references of table 5.1, with varying terminating angles of the hyperbolic sections chosen.
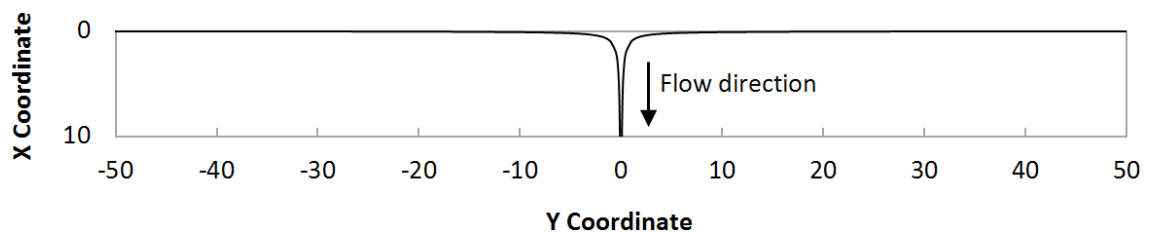
Figure 5.5: Notional hyperbolic channel with large, steep wall angle upstream region to minimise wall shear rates whilst maximising total Hencky strain (rotated view)

129

In this limit, we realise that there is something quite unphysical occurring. The hyperbolic profile suggests that all fluid immediately after the X=0 plane is undergoing constant extension, in an apparently thin plane immediately adjacent to the channel wall, despite the majority of the fluid being located a large distance from, and thus only moving slowly towards the X axis. Additionally, what is occurring before the X=0 plane is not evident.

The reason for this discrepancy is that hyperbolic profile only makes logical sense when applied to a symmetric geometry (i.e. a stagnation flow), and again only one with slip walls, a situation that greatly differs from the "one sided" converging flow we have here. Consider, as a crude example, a fluid packet approaching the stagnation point in figure 5.6, travelling along the Y axis. The packet slows as it approaches the stagnation point as the area normal to the flow direction increases. This is in a controlled manner, by virtue of the hyperbolic walls, which satisfies a constant velocity gradient along the streamline, or constant extension rate: $\dot{\varepsilon}_{xx} = -\dot{\varepsilon}_{yy} = \partial u_x/\partial x = -\partial u_y/\partial y$. Conversely, without the symmetric walls the changing area over which the fluid is flowing, and indeed the direction in which it is travelling, are quite different. Thus in this region of "high" wall angles, it would seem that constant elongation rate may no longer be satisfied by such a channel profile, and the ability to create channels of the form of figure 5.5 is doubtful. Downstream in a converging channel (i.e. where the wall angles are shallow) the area over which flow is passing is more obvious, essentially perpendicular to the channel walls, and it is likely the hyperbolic profiling would remain valid in this region.
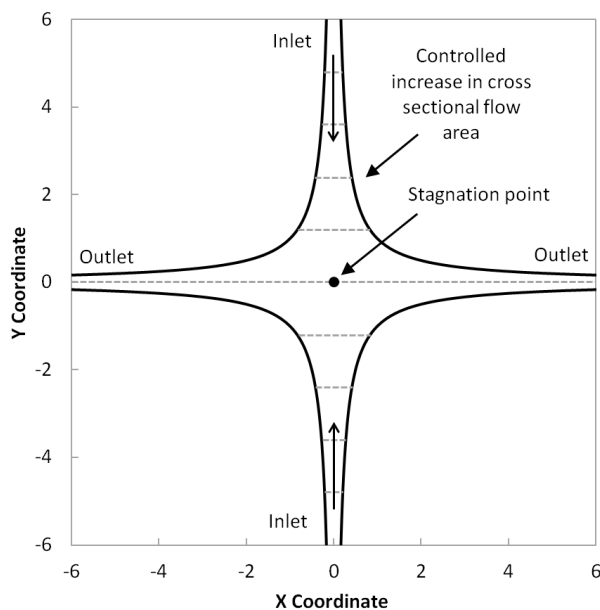
Figure 5.6: Rudimentary depiction of the controlled increase in flow cross sectional area (shown by the dashed grey lines) towards a stagnation point in a hyperbolically profiled "cross slot" geometry

130

To allow design optimization, an improved description of both channel wall shape and extension rates for those attempting to use "one sided" converging channels is thus sought, particularly in regions of high wall angles. Whilst authors such as Oliveira et al. (2007) have previously attributed deviations from the constant elongation rates expected in hyperbolic channels in this region simply to "entrance effects" (and legitimately so where abrupt transitions between parallel and hyperbolic sections have been used), better understanding what is happening in this entrance region will inform the situation. Note in passing that variations in extension rate have been illustrated by plotting velocity against centreline coordinate, this process underestimates the importance that a large majority of the total extensional strain is accrued in this region (calculating elongation rate directly and plotting against integrated time or total Hencky strain accrued would be a better representation).

5.3   Development of iterative flow front model for converging channel design

The first step in developing this improved description is to recognise that the flow field in figure 5.5 at negative X axis locations, and an infinitely small "contraction", would be very similar to that of radial sink flow, with fluid motion directed directly towards the contraction. The consequence of this is that extension rates will increase as fluid approaches the channel entrance, rising from zero at an infinite distance and reaching the desired value at some finite point. This would be a valuable parameter to find for channel design, as this places a limit on extrapolating to channels of the form of figure 5.5, essentially leaving inlet angle (if not 180 degrees, i.e. to mitigate free convergence, for example – see Binding (1988)), scale and Hencky strain to be decided on. Secondly, with wall slip, but with a finite fluid viscosity, there will be a resulting tendency for fluid to travel in semi-circular "fronts": Adjacent fluid packets would constrained to flow next to one another, i.e. in a direction perpendicular to such a front. Fluid packet rotation will additionally be induced by curvature of the bounding walls as the front (perpendicular to the bounding walls) tracks around them.

In literature, and particularly concerning lubricated extensional channels as previously highlighted, wall slip is commonly used as an approximation, or assumed analogy, to inviscid flow: flow free from the effects of viscosity and of zero vorticity (or irrotational in nature). Conversely here, whilst we are using the wall slip condition, inviscid flow is not being assumed: indeed we are using the notion of viscous effects to inform how the fluid is flowing, and recognising through these flow "fronts" that fluid packets are in fact being reoriented. This addresses some concerns relating to the stream wise orientation of fluid packets and the relative direction of extension raised in Williams and Williams (1985); an important consideration when those streamlines nearer to the walls in stagnation flows are considered

(are the fluid packets being rotated relative to the extension direction by the wall presence, as they pass through the channel?).

If one attempts to simply attach a region of sink flow, at the point where the desired extension rate is first achieved, to a hyperbolic channel designed for this extension rate, we find there is a problem. In the radial sink flow, extension rates are dictated by the area of the semi-circular flow fronts, whereas in the hyperbolic description a planar flow front is essentially being assumed, and the two channels are different physical sizes at this point. What is desired is a single description of extensional flow, that is usable and continuous both in and between a region of pure sink flow with semi-circular flow areas, and far downstream in a contraction, where flow fronts are approximately planar. To achieve this, flow fronts need to be considered in a situation where the wall angle is changing. This notion of flow "fronts", in conjunction with extensional flows, has in fact already been suggested. James and Saringer (1982) used such an analysis to estimate the extension rates of fluids propagating into a radiused axisymmetric hole, and equally assumed a viscous fluid and conditions of wall slip. In their work, a spherical flow front was used to dictate the area over which flow occurred, and from this the flow velocity could be found from a specified flow rate. As this flow front has a corresponding position on the channel axial centreline, by finding the rate of change of velocity with respect to position along this axis, the elongation rate could then be determined.

When the model is considered, an issue is however apparent with their determination of velocity from flow over area. This implies uniform velocity across the front. As a fluid rounds a corner however, elements on the inside of the curve travel slower than those on the outside due to the assumption of viscosity, and reach the next flow front simultaneously. Assuming that flow moves in pure fronts, their calculation approach therefore misestimates the actual elongation rate attained. We propose an alternative approach to avoid the requirement to determine velocity. From the definition of extension rate, two parameters are required to determine elongation rate, a fluid element dimension before and after elongation, and a timescale. The first can be provided by the arc length of two successive fronts – representative of fluid elements being compressed across this span. For the latter, consider the movement of such a front in a 2D channel, from an upstream to downstream location. All fluid elements across the front remain fixed alongside each other, sweeping out an area between the two fronts. This area must be filled according to the flow rate. From the modelling detailed later, calculating elongation by both this approach and that of James and Saringer in the inlet region of a converging channel shows James and Saringer's approach to produce a value similar to, but systematically lower than, that computed by considering successive fronts. Despite this

adjustment, there is a second more subtle shortcoming present, specifically when flow proceeds around a corner of varying, rather than constant radius (i.e. as would occur when flow enters a hyperbolic channel). This is investigated separately in section 5.6 later.

In summary, both of these approaches using flow fronts, irrespective of how the extension rate is determined, have the ability to determine extension rates continuously through the sink flow region and straight through to regions far downstream: the issue of discontinuously considering spherical, followed by planar flow areas is simply replaced by spherical flow fronts that change in radius. The use of flow fronts also inherently caters for rotation of fluid particles on entrance to a contraction, and correctly directs extension. Compared to the approach of James and Saringer that derived extension rates analytically for a spherical contraction, the revised approach of using two successive flow fronts lends itself readily to discretising a channel wall into multiple segments. This instead then permits a iterative computational approach to be applied, which is performed next, and the shape of a channel computed where the angle of each wall segment has been adjusted to produce a constant rate of extension.

The computational optimisation of channels for constant extension rates is something that has gained interest in recent years for stagnation flows (e.g. the work by Haward et al. (2012) and Galindo-Rosales et al. (2014)). Whilst the approach here is a relatively primitive geometric approach rather than the iterative CFD approaches usually employed, it is believed this is the first attempt an optimisation has been conducted for converging channel geometries in contrast to the common use of hyperbolic profiles.

5.4   Iterative flow front model computational setup

In order to perform an iterative computational study, the flow front model and a solution procedure was set up in the LabVIEW programming environment (National Instruments (2012)), based on constructing the channel wall from a series of small segments. Two closely spaced semi-circular flow fronts are considered, one attached to the end of the previous wall segment, and one to the end of the new segment, shown in figure 5.7 and described overleaf. The area between fronts and the change of front arc length is used to calculate the elongation rate as previously suggested. The angle of successive wall segments are then adjusted to produce a constant rate of elongation as flow propagates down the channel. The assumptions as previously stated are taken: 2D flow (flow rate in units of m^2/s), low Reynolds value flow, perfect wall slip, and that shear viscosity forces fluid packets to remain adjacent to one another to form "fronts", neglecting the factors detailed later in section 5.6. The channel and flow field are symmetrical either side of the x axis and calculations are performed accordingly. Here, the

term "full angle" refers to the angle between the two symmetrical walls, and "half angle" to that between a wall and the x axis.
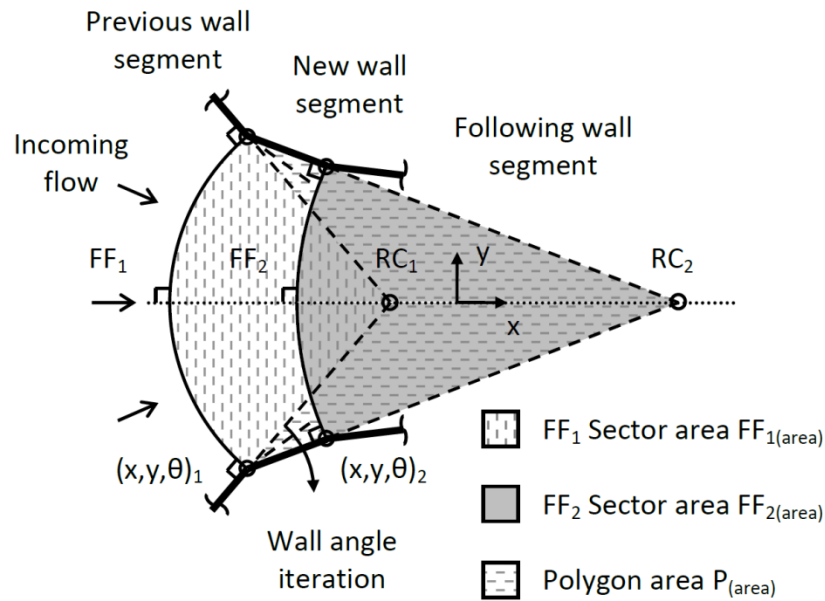
Figure 5.7: Geometric construction of radial flow fronts for channel profile design. Flow is 2D and proceeds perpendicularly across flow front FF$_1$, followed by FF$_2$. These flow fronts are defined by the end points of the previous and new wall segments, respectfully. See text for details.

The flow is constructed geometrically as follows:

1. The coordinate of the previous wall segment end point is provided, together with angle of the previous wall segment. This point, $(x,y,\theta)_1$, then defines the end of the first circular flow front, FF$_1$, orientated perpendicular to the wall at this point, and passing at 90 degrees through the X axis. This corresponds to the channel inlet half angle and start coordinate for the first iteration.

2. The first flow front is constructed by extending from $(x,y,\theta)_1$ to the X axis to locate the radial centre of the front, at RC$_1$. The sector area, FF$_{1(area)}$, and flow front arc length FF$_{1(length)}$, are then calculated via angular fractions of a 360 degree flow front.

3. The (x,y) coordinate end point of the new wall segment is defined through the iteration procedure. The angle of the new wall segment between these two points is thus calculated, and point $(x,y,\theta)_2$ determined for the end of the second flow front, FF$_2$. RC$_2$, the sector area, FF$_{2(area)}$, and flow front arc length, FF$_{2(length)}$, are determined accordingly.

4. The X axis coordinates of RC$_1$ and RC$_2$ and the end point of the previous wall segment at point $(x,y,\theta)_1$ define a triangular polygon (see key). The area of this polygon, P$_{(area)}$, is calculated.

5. Adding $FF_{1(area)}$ and $P_{(area)}$ corresponds to the area of the entire construction depicted in fig. 5. Subtracting $FF_{2(area)}$ provides the area between the two flow fronts, over which flow occurs. The timescale, dt, is then determined via the area flowrate entering the channel.

6. $FF_{1(length)}$ and $FF_{2(length)}$ are used, together with dt, in equation 1.10 and 1.11 (introduced in chapter 1) to determine the extension rate. Since the flow is planar, the result is negated to represent elongation in the direction perpendicular to the fronts.

The results of these computations in LabVIEW were verified against sample area and perimeter calculations performed in CAD software (Pro/DESKTOP, Parametric Technology Corp. (2000)).

The above sequence is iterated, redefining the end point coordinate of the new wall segment to achieve the target elongation rate. The wall segment step length is kept fixed (10^{-5}m) and rotated about the end of the previous wall segment. The solution region is bounded by orientating the new wall segment parallel to the previous segment (sink flow, where the elongation rate increases), and orientated parallel to the x axis ($\theta = 0°$). This region is divided into 10^7 angle steps for each wall step. We use an initial wall angle equal to that of the previous wall segment, corresponding to sink flow, and reduce the wall angle until the elongation rate is equal to or below the target value. This therefore enables radial sink flow to be automatically produced upstream where the target elongation rate has yet to be attained. Starting from this point and decreasing the wall angle, and checking that the coordinate of $RC_2 \geq RC_1$, ensures flow fronts can never intersect during iteration. The whole process is then performed at each wall segment, starting from an initially specified coordinate and wall angle, to yield the final channel shape. The front panel of the program written is shown in figure 5.8 overleaf for illustrative purposes (due to the graphical nature of LabVIEW code reproducing it on paper is restrictive). With regards accuracy, approximately 10,000 angle iterations per wall step occur in the inlet region, and ~1,000 angle iterations per wall step with near parallel walls downstream. Decreasing the wall step length to 10^{-6}m was shown to produce negligible change in the resulting profile and extended precision calculations were used throughout. Elongation rates were achieved within 0.000001s^{-1} of the target value.

It was found that specifying relatively wide inlet angles much in excess of $\theta = 60°$ (120° full angle) produced sink flow in the iterative procedure, followed by a relatively sharp change in wall angle – comprised of a very large number of wall angle iterations over a few wall segments – down to a significantly lower wall angle. This change is visible in the program output image in figure 5.8 where an initial full wall angle of 170 degrees was used.
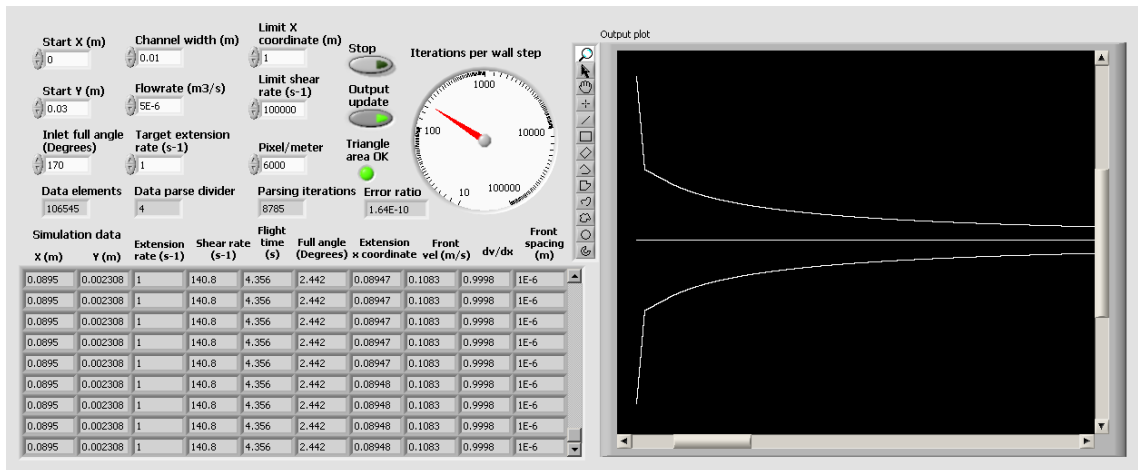
Figure 5.8: Front panel of LabVIEW iterative channel design program during calculations. A initial wall angle of 170° full angle has been used and the resulting characteristic "step" in the computed wall profile can be seen in the output plot.

Since a large number of iterations are being taken in this situation before the target elongation rate is reached, the cause must lie in the manner in which the the extension rate varies, at high wall angles, as the segment angle is progressivly reduced (in the model, it is assumed that reducing the wall angle results in a reduction in elongation rate). To address this, and determine wether this sudden drop in wall angle is a computational error, we can analytically model the progression of flow fronts around a sharp corner. The problem is set up in figure 5.9 below, and the geometrical considerations are similar to those previously described.
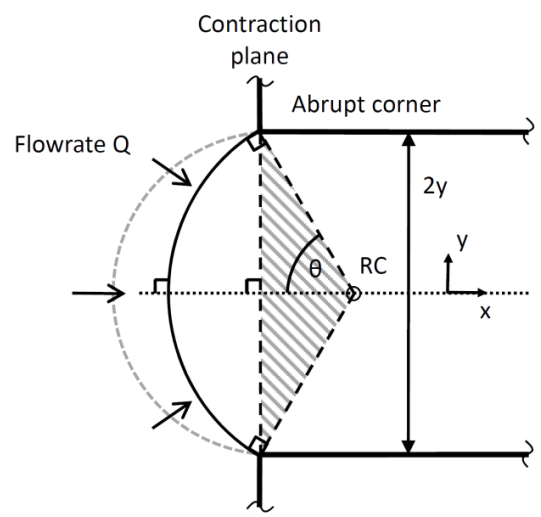
Figure 5.9: Geometry used for analytical analysis of radial flow fronts around a sharp, abrupt corner to a channel of width 2y. Flow fronts proceed in the manner depicted by the dashed grey flow front followed by the solid black flow front. The hatched area is subtracted from the area of the flow "sector" such that the area of each successive flow sector is normalised against the contraction plane.

Starting with a defined flow front angle (2θ) and channel width (2y), the radius of the flow front can be found by trigonometry with the centre located at RC. Subsequently, the length of the front over which is flow is travelling, denoted $f(\theta)$, can be calculated as a fraction of a full circle, yielding equation 5.1. This is exactly the same process as used in the iterative computation previously.

$$f(\theta) = \left(\frac{2\theta}{2\pi}\right) 2\pi \left(\frac{y}{\sin\theta}\right) = \frac{2\theta y}{\sin\theta} \qquad (5.1)$$

In order to determine the area over which flow occurs, a slightly different process to that used in the iterative model is instead adopted, which avoids the issue of determining the polygonal area in figure 5.7. The area over which flow is occurring between two successive flow fronts is the difference in sector areas lying on the left hand side of the contraction plane, as there is now no wall segment separating the fronts. If we thus subtract the hatched area in figure 5.9 from the overall area of a sector described by a flow front, the areas of two successive flow fronts are made directly comparable, and calculating the change in areas between two successive fronts is straightforward. This area for one flow front, denoted $g(\theta)$, is given by equation 5.2:

$$g(\theta) = \left(\frac{2\theta}{2\pi}\right) \pi \left(\frac{y}{\sin\theta}\right)^2 - \frac{2}{2}\frac{y^2}{\tan\theta} = \theta \left(\frac{y}{\sin\theta}\right)^2 - \frac{y^2}{\tan\theta} \qquad (5.2)$$

Considering equations 1.9 and 1.11 in chapter 1 (as we are now considering an infinitesimal extension, rather than a finite extension in the iterative model) and incorporating the flow rate Q gives equation 5.3. Here, dL is the infinitesimal change in flow front length (which causes extension) and dA is the infinitesimal area over which flow has passed, which dictates the timescale for such extension:

$$\dot{\varepsilon} = \frac{dL}{L}\frac{Q}{dA} \qquad (5.3)$$

Writing equation 5.3 in terms of $f(\theta)$ and $g(\theta)$ and a infinitesimal (here, negative) change in flow front angle, Δ, between two closely spaced flow fronts gives equation 5.4:

$$\dot{\varepsilon} = \frac{f(\theta) - f(\theta + \Delta)}{f(\theta)} \frac{Q}{g(\theta) - g(\theta + \Delta)} \qquad (5.4)$$

Considering the elementary definition of differentiation, then finding of $f'(\theta)$ and $g'(\theta)$ for equations 5.2 and 5.3 accordingly gives:

$$f(\theta) - f(\theta + \Delta) \approx -f'(\theta) \cdot \Delta \approx -2y \frac{\sin\theta - \theta\cos\theta}{\sin^2\theta} \cdot \Delta \qquad (5.5)$$

$$g(\theta) - g(\theta + \Delta) \approx -g'(\theta) \cdot \Delta \approx -2y^2 \frac{\sin\theta - \theta\cos\theta}{\sin^3\theta} \cdot \Delta \qquad (5.6)$$

Substituting equations (5.5) and (5.6) into (5.4) and simplifying gives:

$$\dot{\varepsilon} = \frac{Q}{2y^2} \cdot \frac{\sin^2\theta}{\theta} \qquad (5.7)$$

Evaluating equation 5.7 for 0° < θ < 90° (Full inlet angle form 0 to 180°) and normalising against the maximum elongation rate gives the black curve in figure 5.10. Spreadsheet computation with small Δ values (using infinitesimal or Hencky strain rate), verifies this. This plot depicts the change in elongation rate; based on the flow front model, of fluid element from the moment radial sink flow ceases (i.e. forming a semi-circular 180 degree flow front, located at distance y from the contraction plane), through the transition region, and finally till when a parallel channel with a flat (i.e. infinite radius) flow front is adopted. The form of the result is independent of the channel width (2y) or area flow rate (Q).
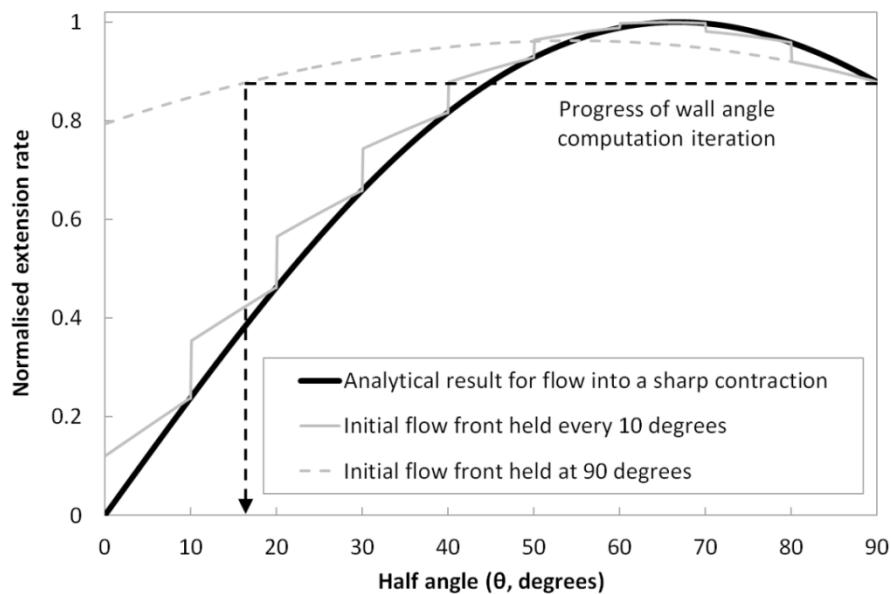
Figure 5.10: Comparison of extension rates into a sharp contraction from both the analytical solution and the computational procedure with finite separation between successive flow fronts. The dashed black line shows how a calculation would progress in the case of the computational procedure if started with a 180 degree inlet, as detailed in the text.

Whilst equation 5.7 cannot be readily differentiated, we can see that a clear maximum in elongation rate (black line) occurs at θ values around 67 degrees (i.e. 134 degrees full angle in the iterative channel design). In the iterative procedure, sink flow increases the elongation rate to the target value. At the next wall segment of sink flow, the elongation rate exceeds the

target and the wall angle begins to iterate. Below this critical angle, a solution is found in a modest number of steps. However, above this critical angle, the elongation rate increases further, rather than decreases as the iterative process assumes. Thus, for inlets above this critical angle, a large number of iterations and sharp wall step occur in the profiles produced. It is therefore necessary to start the computation at or below this critical angle.

The situation is exaggerated since the iterative procedure holds the previous flow front at the same location as θ is reduced, until the elongation rate is reduced back to the target value. The elongation rate determined (based on Hencky strain) is shown by the dashed grey line for inlet of θ = 90° (where the first front is held i.e. from prior sink flow) to the new front at θ. This would cause the solution to dramatically overshoot the optimum inlet angle, down to a θ angle of approximately 18 degrees, with the target elongation rate being re-attained as shown by the dashed black line. This verified by a θ angle of 89 degrees (i.e. <90) in the simulations overshooting to a wall angle of 19 degrees. The overshoot is further compounded by the fact that rapid changes in flow front length and flow area are most significant at high values of θ, and correspondingly a large change θ is necessary at low angles to re-attain the target elongation rate.

An important additional observation can also be made from figure 5.10, in that even in the limit of very small angle differences between flow fronts (i.e. when the iterative model is working correctly), whilst the extension rates predicted by the analytical and discrete front solutions are essentially the same, their gradients with respect to θ are rather different. The solid grey line (also based on Hencky strain) shows this by holding the first flow front at increments of 10 degrees. This gradient difference is evident at high θ angles where the extension rate is rising with respect to θ, and also at lower θ angles where extension rates are falling: In both cases the iterative approach would overestimate the change in wall angle needed to reach a desired elongation rate. This is a direct result of the averaging effect of the finite area between two successive flow fronts. No matter how small a wall segment is thus made, the iterative changes in wall angle will be significantly larger than that required to attain the desired elongation rate of interest. The counterargument to this is that at the next wall segment, the previous overshoot should cause a much lower change in wall angle of this segment, and the solution may oscillate around the profile of the ideal wall. This underlines the requirement for very fine iteration steps, as used here: In the data of which (when exported at high precision) no oscillation in the profile is apparent.

5.5   Calculated channel profiles and discussion

Figure 5.11 below compares a hyperbolic channel profile (y=0.001/x) and the computed profiles based on an area flowrate of 0.001m^2/s and a design elongation rate of 1s^{-1} (based on a 1D flow being forced to accelerate). In the calculation procedure, the computed profiles start from the coordinate (0,0.03) with sink flow at a range of convergence angles between 50 and 130 degrees full angle. In their raw form, they do not align for profile comparison with either the hyperbolic profile or themselves (the change in inlet angle causes the resulting profile form to shift along the x-axis). No obvious alignment feature exists (for example, in the models the target elongation rate is reached at x=0 for the hyperbolic channel, but well in front of the inlet of the computed channel). The x coordinates are, in this case, arbitrarily normalised by arranging for the computed channels to pass through the point (0.2,0.025), lying far downstream on the hyperbolic profile.
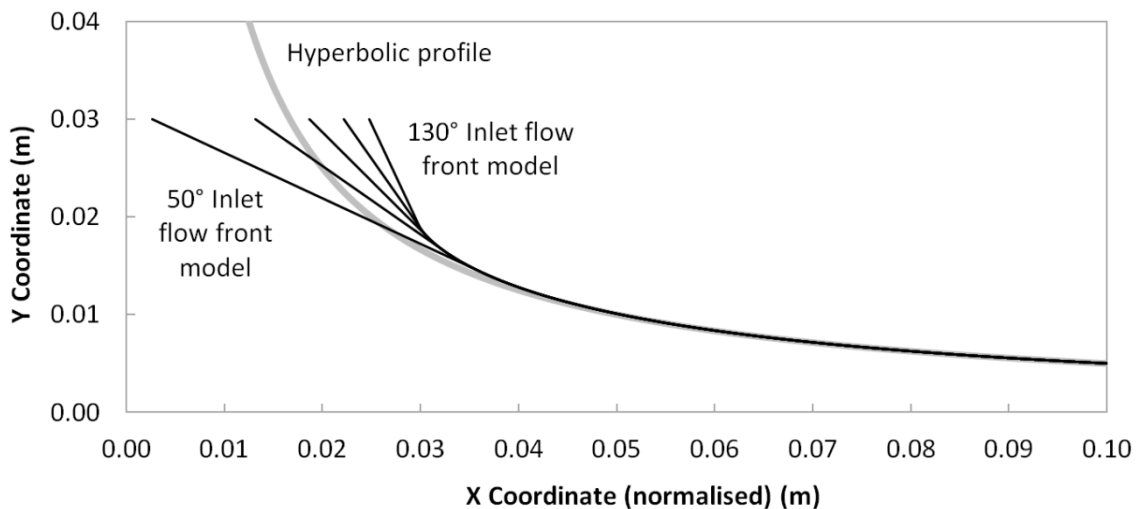
Figure 5.11: Comparison of computed channel profiles for different inlet angles (black lines) to a hyperbolic channel profile (grey line) for a flowrate of 0.001m^2/s and an extension rate of 1s^{-1}, plotted against normalised X coordinates.

As shown by figure 5.11, the computed profiles (black lines) and the hyperbolic profile (grey line) are very similar in form, except for a region in close proximity to the inlet where the computed profile increases at a higher order rate than x^{-1}. We would expect this similarity downstream since the flow fronts become essentially parallel. We also see that the computed profiles for different inlet angles are self-similar, except the lower inlet angle profiles are simply cropped forms of the higher inlet angle result. This is also reasonable, as exactly the same form of flow is being created in each case, except simply iterated from a different starting point. The computed profiles do not show indefinite elongation, unlike the hyperbolic case, with the

target elongation rate being first attained where the straight sink flow sections begin to curve (i.e. the tangential intersects). This is the limiting point of sink flow, sought in section 5.3.

As one fundamental profile form exists independent of inlet angle, we now explore the effects of changes in elongation and flowrates for a 130 degree inlet channel in figure 5.12. Computed profiles have been normalised with respect to their X axis positions against the location where the channel first starts to taper as a basis for comparison.
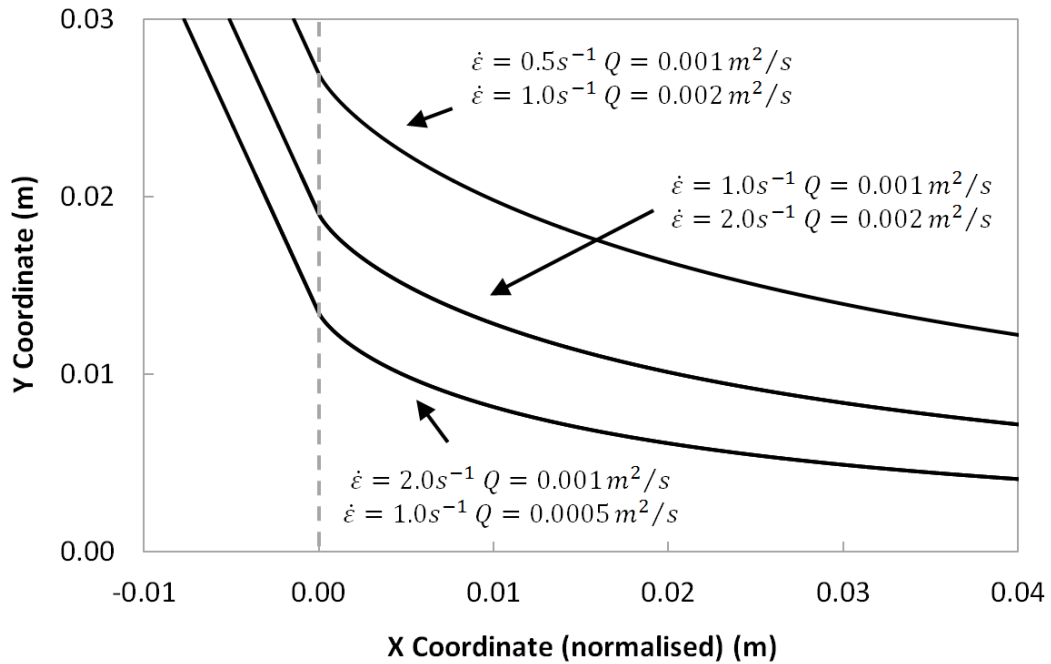
Figure 5.12: Computed profiles for 130-degree full angle inlets at a range of flowrate and design extension rates. X Coordinates are normalised relative the first wall segment at which the target elongation rate is achieved and thus starts to taper (grey dashed line).

As can be seen in figure 5.12, reducing the flowrate has the same form of effect as increasing the design extension rate and the profiles produced are identical. Furthermore, for a factor of 2 increase in flowrate, or decrease in extension rate, the X and Y coordinates scale by $\sqrt{2}$. Thus, one fundamental profile exists that simply scales in size with imposed flowrate and extension rate, cropped upstream for the choice of inlet angle within the limiting factor of 134 degrees full inlet angle, and cropped downstream for the choice of total Hencky strain.

The maximum Y extends of the channel, for design estimation, can be described by the useful dimensionless group:

$$y^2 \frac{\dot{\varepsilon}}{Q} = K \qquad\qquad (5.8)$$

Where K=0.3623 for a 134 degree inlet from the computational procedure. K decreases for lower angle channel inlets.

5.6   Assessment of flow front model validity and evaluation of new profile

In section 5.3, it was noted that an additional issue existed with the flow front model when flow around a changing channel wall radius, rather than one of a constant radius, is considered. The revised form of the flow front model proposed had the advantage that it took into account for a fluid entering a radial contraction, a distribution of velocities exists for fluid travelling in the form of "fronts". Those fluid packets nearer to the wall have a lower streamline velocity than those on the centreline of the contraction, and in the case of a radial contraction at least, extension is caused solely by the compression of these flow fronts between the bounding walls. However, when a change in wall radius occurs, i.e. to a smaller radius, those fluid packets travelling near the wall must decelerate, and those at the channel centreline must accelerate if these flow fronts are to be preserved. Firstly, this imposes an additional distribution of extension rates in addition to that sought by profiling the channel, of which very little can be done about. Secondly, this acceleration or deceleration would be resisted by the fluid extensional viscosity, however it is being caused by the fluid shear viscosity attempting to maintain flow fronts. Thus there would be a competition between the two modes of deformation, and shear (even in a wall slip environment) and distortions from the hypothesised flow fronts might be expected.

Figure 5.13 presents a CFD analysis of a simple wall-slip flow around a 180 degree corner bend to elaborate this issue. The analysis is conducted in the commercial Fluent (SAS IP. Inc, 2011) package with a viscous, low Re value flow. An arbitrary $1000 kgm^{-3}$, 100Pa.s Newtonian fluid is simulated with an inlet velocity of $0.001 ms^{-1}$. An outer wall radius of 4mm, inner wall radius of 1mm and upstream/downstream parallel channels of 10mm length are used. Strong sensitivity to solution residuals was noted due to the slip walls, with a variety of different plausible results during the calculation progression. A modest ~69,000 cell triangular mesh (~60 cells across channel width) was therefore used with iteration to low continuity and velocity residuals < O 10^{-12}. Generalised strain rate is plotted, here defined as $\sqrt{2(D:D)}$, depicting contribution from both shear and elongation. Particle track lines depict elongation through variation in spacings.

To indicate shear, the progression of massless, point tracer particles along the path lines are shown at different time intervals from injection at the inlet boundary. A spatially curved distribution of such point tracers may also result from diverging or converging aspects of the flow field, thus to provide an indication of orientation, these particles are shown as point velocity vectors, elongated perpendicular to streamlines. Reduction in flow rate by 1 order of magnitude shows the solution to be insensitive to flow rate.
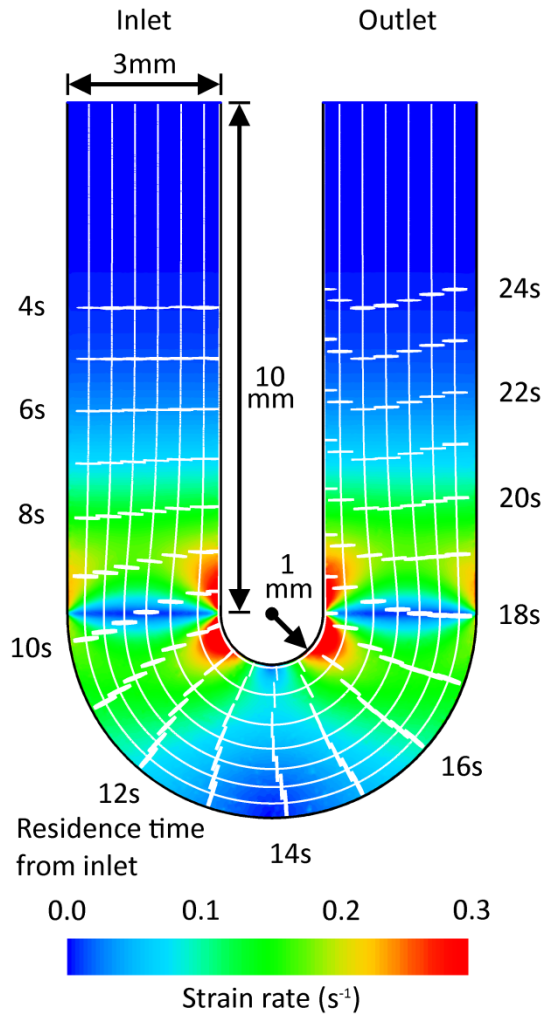
Figure 5.13: Viscous flow with slip walls around a 180 degree bend. Contours depict streamlines, with point tracer particles (depicted as lines perpendicular to the streamlines) released from the inlet at t=0. Shading indicates the generalised strain rate experienced by the fluid, defined as $\sqrt{2(D:D)}$.

From considering figure 5.13, we can see the consequence of the interplay between shear and extensional deformation. Rather than having zero shear and infinite extension at the point of transition between the straight and radial sections, or zero extension and only internal shear, a combination of these two deformation modes is preferred, straddled about the channel transition points.

As can be seen from the figure, 4 seconds after tracer injection the flow is following pure plug, slip wall flow with no strain occurring and an un-sheared, un-curved flow front present. Prior to the flow reaching the channel bend, at around 7 seconds, streamline spacing indicates elongation "in anticipation" occurring to reduce fluid velocity at the inner radius, and increase the velocity at the outer radius. Simultaneously, internal fluid shear can also be seen by tracer particle "line" becoming disjointed, with fluid packets attempting to accelerate or decelerate as appropriate, before reaching the channel transition point. Total shear deformation reaches a maximum around the interface between the parallel and curved channel sections (at approximately 10 seconds transit time), with the highest shear deformation in the vicinity of the inside wall as might be expected (fluid would have to come to a stop for a radius of 0). Somewhat unexpectedly, we also see zero strain rate across the transition plane between the parallel and curved channel sections despite that we can see extension occurring from the streamline spacing, how this relates to equation 3.10 is currently unclear. As the fluid propagates around the channel curve, shear now appears to occur in the opposite direction: Following a tracer on the inside of the curve, before entering the bend it was travelling slower than expected for the flow field, and thus shearing backwards. On entering the bend, it is now travelling faster than expected, and thus shears forwards, together with continuing to experience extension perpendicular to the streamlines. About halfway around the bend, the tracers return back to an approximately flat flow front half way around the curve, accompanied by a minimum in the strain rate. The reverse process now occurs for the transition from a curved channel to the downstream parallel section, though non-flat tracer profile eventually results at 24 seconds, rather than a flat one, indicating shear-extension process is not geometrically reversible, at least in the case studied here.

In summary, from this simplified geometry, we can see that firstly, despite the wall slip flow, shear is not eliminated within the flow field; and secondly, there is cause to suspect that even with perfect wall slip, uniform extension rates between streamlines may not be achievable in a profiled channel. Both of these observations contrast with the generally held view that wall slip (i.e. the use of wall lubrication) is a means to produce uniform extensional flows entirely devoid of shear. Such comments could be directly extended to practical fibre spinning operations which in effect employ perfect wall slip and are assumed to be entirely shear free. Fano flow (tubeless siphon) flow is an ideal example, as this follows a geometric form rather comparable to that of a hyperbolic channel with a 180 degree inlet region.

Given the behaviour identified in this simple geometry at a change in wall radius, we can now use CFD to evaluate the actual profile of "flow fronts" and extension rates in a profiled channel,

where the wall radius is continuously changing. Both a hyperbolic and a computed channel profiles are simulated here, with the pertinent geometrical features shown below in figure 5.14. A channel inlet angle of 70 degrees is used, chosen as a compromise between exaggerating effects from channel curvature radius changes and the rather sharp corner at higher inlet angles in the computed channel profiles. Inlet flow is directed tangentially to an upstream radial boundary of 80mm radius. With the chosen inlet velocity and design extension rates of $0.01023ms^{-1}$ and $1s^{-1}$ respectively, this gives a wall length of approximately 50mm before the channel profile begins to significantly curve. Fluid properties of $1000kgm^{-3}$, 100Pa.s; and triangular meshes of uniform density across the whole channel (both in excess of 75,000 cells) are again used - approaching the limit of the educational licence. Simulations are conducted in double precision and iterated until the computational scaled residuals flat lined (order $1x10^{-15}$).
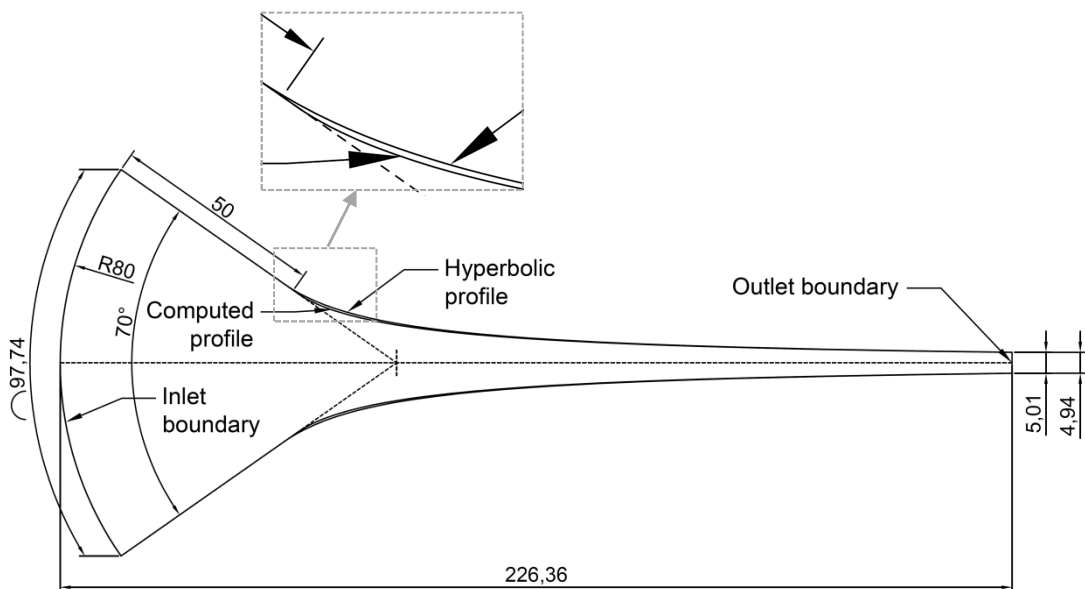
Figure 5.14: Geometry of the hyperbolic and computed wall profile extensional channels simulated using CFD. Both channels have an inlet full wall angle of 70 degrees. Inset image shows enlarged view of radial-profiled transition region and difference in wall profiles.

To begin with, the hyperbolically profiled channel is considered due to the smoother wall profile. Inviscid flow is initially simulated, followed by viscous wall slip flow, as shown in figure 5.15. In both these scenarios contours of velocity and lines of tracer particles released from the inlet at 0.5 second intervals are shown. Figure 5.16 then shows extension rates evaluated for three streamlines in the viscous, wall slip case, positioned as depicted by the inset diagram. Despite the fine mesh and solving to such high precision, evaluating the extension rate as the rate of change in velocity magnitude along a streamline proved difficult due to apparent computational noise. Extensive averaging and smoothing has been used to generate the plots

in figures 5.16 and 5.17 shortly. This consisted of grouping and sorting data for four neighbouring streamlines, applying a 50 point moving average, evaluating the derivative over an 800 data point span, and then applying a 300 point moving average on the extension rates calculated. The data points for which values are presented are based on data up to 1148 points apart. This correlates to a maximum span up to about 0.008m path length either side of a data point. The lack of data at very short path lengths in figure 5.16 is a direct result of this process.

It is postulated that this issue of "noise" in the velocities may be a result of how velocities were interpolated in between mesh cells: given the evaluation of a velocity gradient, it would make sense that increasing the mesh density might only provide limited benefit. This shortcoming is something that more detailed setup of Fluent or use of a different customisable CFD package in future work may solve.
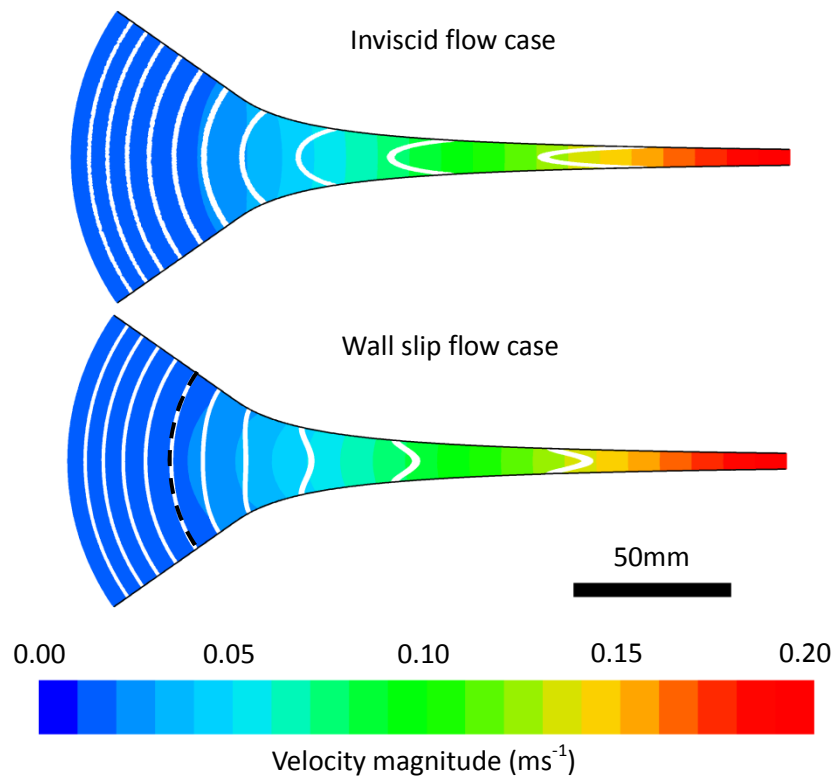
Figure 5.15: CFD simulation of flow into a 70-degree inlet angle hyperbolic contraction for inviscid (top) and wall slip viscous flow (bottom). Fluid inflow is directed normal to the semi-circular upstream boundary. Contours of velocity magnitude are plotted, together with a line of tracer particles every 0.5 seconds, released from the inlet at t=0. The black dashed line in the wall slip flow case is orientated perpendicular to the channel walls to highlight departure from radial flow fronts.
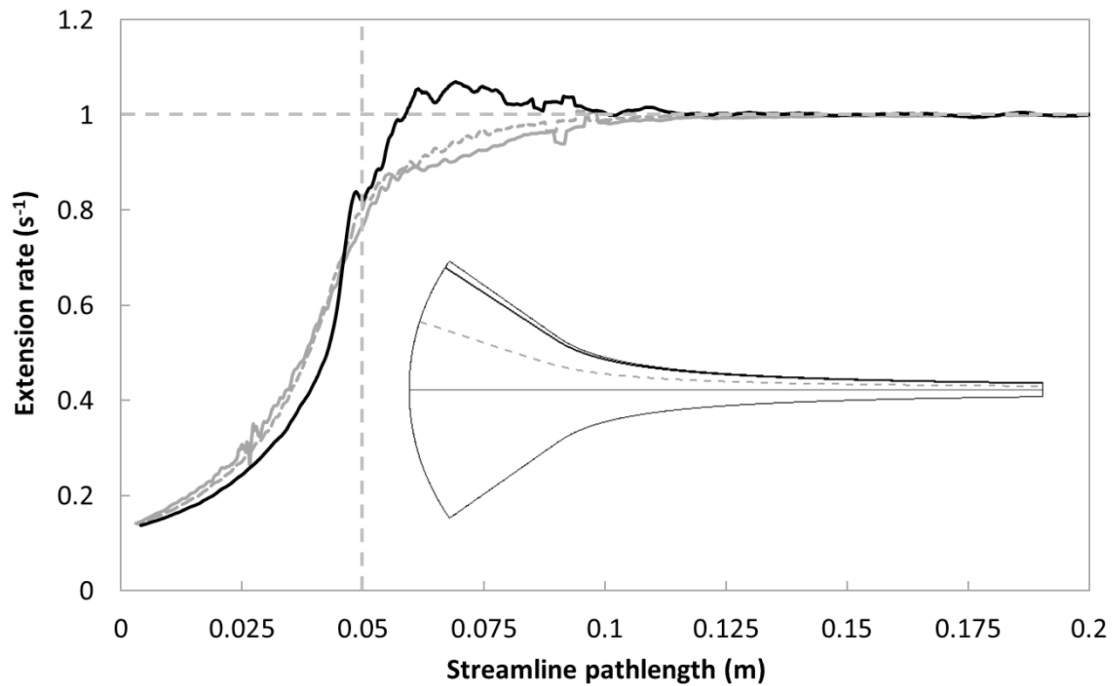
Figure 5.16: Evaluation of extension rates along three streamline locations (shown by the inset diagram) in the wall slip case of figure 5.15.

The inviscid simulation in figure 5.15 is included here simply to demonstrate that the flow fields in an inviscid case are very much different than those from viscous, wall slip flow, underlining the comment in section 5.2 that wall slip cannot be used as an approximation of inviscid flow, or vice-versa.

In figure 5.15 for the wall slip case, from the tracer plots we can see that upstream flow is in the form of radial fronts (if albeit this is also presupposed by the boundary condition) and extension rates rise geometrically in figure 5.16, as would be expected for sink flow. Around 30mm from the inlet, distortion from the circular flow front form assumed by the iterative channel design model starts to become apparent (a dashed circular front, centred on the convergence point of the linear walls, is overlaid to aid in identifying the distortion). Both this flow front distortion and the velocity contour slightly downstream shows the flow near the walls to be decelerating (observe the contour does not meet perpendicularly to the channel wall), and the flow in the core to be comparatively accelerating, even though at the location where the flow front contacts the channel walls a change in radius is not yet taking place. This is directly in accordance with the behaviour seen earlier in figure 5.13, with the flow "anticipating" the change in channel radius. We can similarly see from figure 5.16 that before particles near the walls reach the region where the wall radius changes, they have an extension rate below that of streamlines in the channel centre as they are slowing down and compressing

147

to cover the reduced path length nearer to the curvature radial centre. Compared to the previous simulation, the length over which the channel curvature radius is small is quite short, and almost as soon as the radius falls it rises again. We correspondingly see in figure 5.16 extension rates of particles travelling near the walls to be in excess of those along the centreline as they attempt to accelerate back up the velocities dictated by plug flow downstream (and/or cause the core fluid to decelerate by virtue of drag, if difficult to see in the contour plots). As with the previous simulations, we find a flat tracer profile is not restored downstream of which the origin is not readily apparent (path track lengths at the wall and centreline are similar, differing only by 3mm, and arguments of the accelerated core flow "overshooting" the streamlines at the edges are quite approximate); however in this region of high wall curvature radius the extension rates across the channel are approximately uniform and equal to ~$1s^{-1}$ as would be expected.

The variation of extension rates between streamlines in the core of the flow and near the walls demonstrated here confirms that this change of channel radius does overlay an extension rate distribution across the channel width, as hypothesised earlier: vis, the very profiling intended to produce constant extension rates also serves to generate a distribution of extension rates. The variation in extension rates between streamlines at the core and walls would be much greater for situations with rapid changes in radius, i.e. abrupt and radiused orifices (if they were successfully lubricated in practice). As far as the validity of the flow front geometric design approach is concerned, a relaxed viewpoint can be taken. It may be argued that the assumption of fluid travelling in pure flow fronts is broken in reality, but on the other hand, if this assumption were not broken, this would not damp the much more severe extension rate distributions would otherwise be seen across the channel. The use of tracer particles also accentuates deviations from a flow front as they are referenced right back to the channel inlet. Either way, geometric shape adjustments can offer no further recourse to this dilemma of radius-variation induced extensional flow.

Now that a spatial variation in extension rate has been identified in a converging channel, we can proceed to compare the extension rates produced by the traditional hyperbolic channel and the computed profile. Rather than plotting against streamline path length, in figure 5.17 data is plotted against total Hencky strain accumulated, as per the previous comment in section 5.2. This also serves to improve the comparability of the simulated hyperbolic and computed channel profiles as they terminate at slightly different widths, as indicated in figure 5.14.

From figure 5.17 on the following page we see that the new computed channel profile, although geometrically very slight, has made a definite difference to the extension rates. For streamlines travelling down the channel centreline, or spaced mid-way between the walls and centreline, we can see that around a total Hencky strain of 1 extension rates closer to the design value of $1s^{-1}$ are being attained. However, in the case of streamlines near the channel walls, we find that extension rates, which already overshoot the design value in the case of the hyperbolic channel, overshoot more severely in the case of the new computed channel profile. This would be expected, as the sharper corner of the computed channel profile, compared to the hyperbolic profile, forces higher extension rates as fluid packets accelerate away from this smaller radius. We can argue to some extent that limited overshoots are in fact preferential to undershoots, as they would permit a more rapid accumulation of molecular strain towards the steady state value desired.
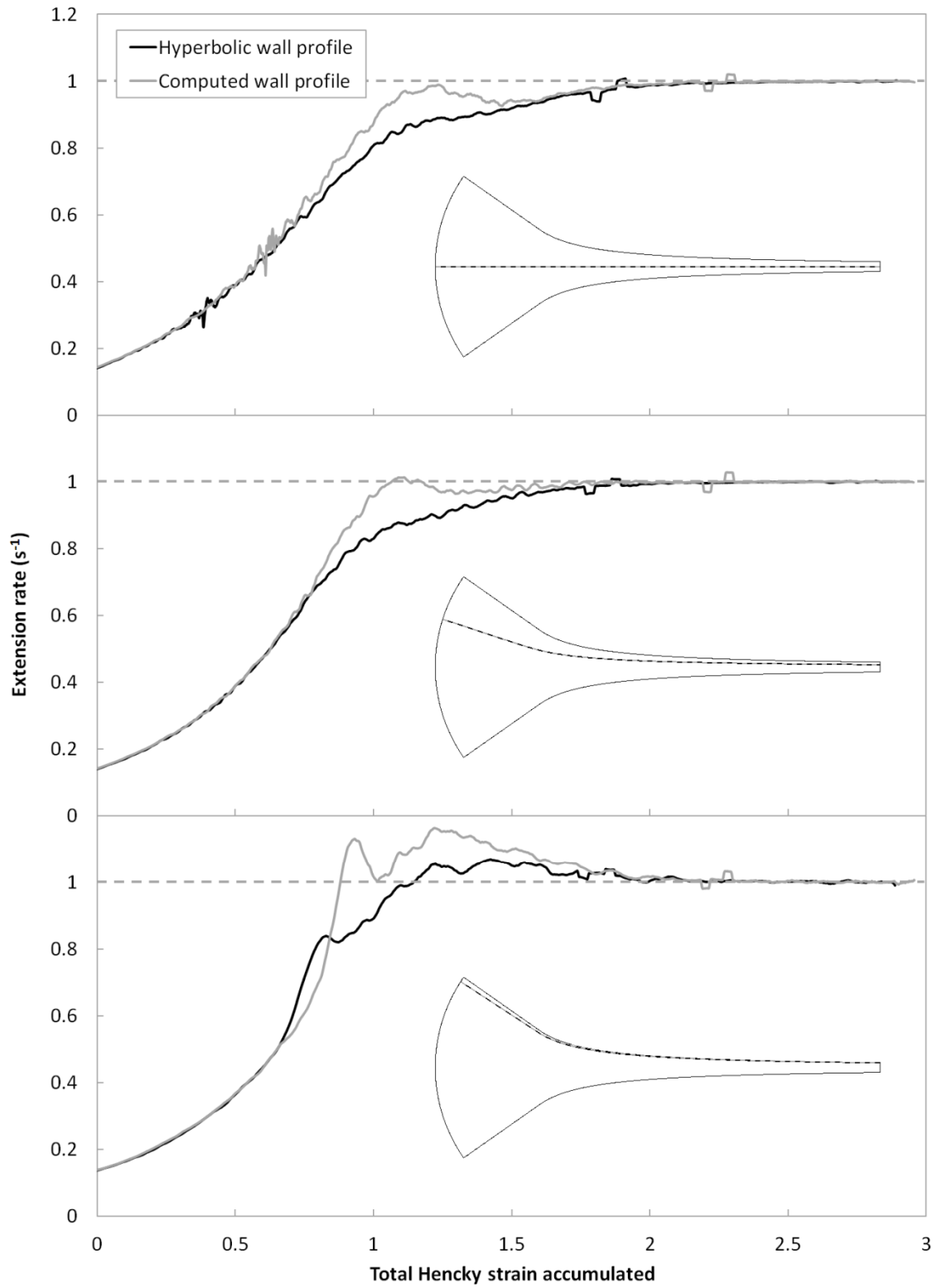
Figure 5.17: Evaluation of extension rates generated for wall slip flow with both the hyperbolic channel (black line) and computed profile (grey line), the geometry being shown earlier in figure 5.14. Extension rates are compared for three different locations, as shown by the inset diagrams.

5.7   Conclusions

The main finding from this chapter has been that there exists a finite limit on the inlet extents of a profiled converging channel; in contradiction to that supposed by a hyperbolic form, and that this limit is governed by sink flow at the channel inlet. There is also probably little to be practically gained by channel inlet angles greater than 130 degrees. As previously stated such a limit facilities meaningful and informed channel design. Despite the shortcomings of the modelling approach highlighted, this region of sink flow, the most important new feature of the model, has been captured entirely accurately, with no caveats with regards extension rate distributions or flow front distortions in this region.

From this modelling, a new channel profile for generating extensional flow has also been presented, and as part of this, important factors noted: even with perfect, full wall slip, extension rates are not constant between streamlines, and the flow is not completely devoid of shear, contrary to the usual assumptions. Due to these factors, it is impossible to design a channel shape that produces constant and uniform extension rates both along and between streamlines. Despite these limitations, the new channel profile proposed offers improved extension rate homogeneity along streamlines at a distance from the channel walls (typically of interest for most experiments). However, for practical purposes the improvements are rather modest, and given factors such as non-lubricated or imperfectly-lubricated flow fields, a hyperbolic channel remains a reasonable option.

As stated previously, the comparisons of extension rates between the hyperbolic and the computed profile channels are restricted by the amount of noise in the simulation data obtained. It would be valuable to repeat the simulations in this chapter with a different CFD package in the future. It may also prove interesting to conduct a study to see if a peak in extension rates, as predicted in figure 5.10, did exist for a simulated wall slip flow into such a geometry. Finally, it may be valuable to recode the channel shape computation based on an axisymmetric rather than planar contraction. Axisymmetric extensional channels in nature (e.g. silk spinning ducts) show deviations in shape to that of a hyperbolic form (Davies et al. (2013) and associated discussion with Holland (2016)), though at much lower inlet angles than the deviations seen in this work with planar channels.

Chapter 6.

Optical configurations. Choice and refractive index matching thereof of test and reference phases.

Chapter 6: Optical configurations. Choice and refractive index matching thereof of test and reference phases.

6.1   Choice of experimental scale

In previous chapters, it was commented that it is beneficial to minimise the scale of extensional flow experiments. Before design considerations are discussed, it is first necessary to set the scene why, for the experiment considered here, a "meso" scale extensional flow channel was decided upon as this affects many other considerations. More details of this channel will follow in chapter 7. The final channel width used is 8.36mm, and contracts to a minimum gap of 2.61mm (satisfying the "shallow" aspect ratio requirement – as defined in chapter 3 – at the narrowest regions). Many extensional flow experiments in recent years, with the advent of microfluidics, typically have channel dimensions on the sub-millimetre scale.

There are three key reasons: The necessity for a surface coating, materials and manufacturing restrictions, and the size of the imaging region of interest.

Typically for microfluidic work, channels are made using some form of soft-lithography (e.g. PDMS based) or etching processes and usually irreversibly sealed once completed. Here, a special requirement exists that one surface of the channel needs to have a coating applied, and in particular, this coating may need to be re-applied if it accidentally became oil-wetted. Firstly, it is clearly impractical to airbrush one wall of a narrow, deep etched channel, a process much easier if the channel can be somehow (practically, on the length scale of choice) "disassembled" into separate walls for access and "reassembled" afterwards; a design which is detailed further later. Secondly, the surface coating developed does have a degree of surface roughness which would affect a microfluidic channel to a greater degree than one on the scale developed here. In terms of materials and manufacturing routes, lithographic and etching processes have limitations in that only a small number of fabrication materials can be chosen from, and that control of the parallelism and shape of channel walls can be restricted (a key factor in generating the desired 2D flow field). By using traditional machining routes, sub-millimetre features become impractical, but channel features are much more precisely controlled and many more materials can be chosen from (a factor especially useful in the optics considerations shortly). Lastly, the imaging region of interest is not the entire channel width (as usually of interest) but rather a small region either side of the two phase interface. With a 10x LWD microscope objective (as used later) this provides a vertical field of view of about a millimetre. It is therefore sensible to keep the minimum channel height above this level.

6.2   Requirement for optical access

In section 3.9, it was mentioned that the shear rates in the reference and test fluid phases could be obtained optically via a PIV (particle image velocimetry) type technique. Variations of this technique exist, but the basic concept is that tracer particles are added to the liquid (or also often gas), and two images are taken, one before and one after specific time delay. From this information, the velocity profile can be deduced. Implicit in this is that some means of getting illumination (typically a pulsed Nd:YAG laser source in most cases) into the flow geometry is required, together with some means of recording high quality, distortion free images from the flow geometry. Usually this is a relatively straightforward to implement. For example, in what can be referred to as "conventional" PIV, a Nd:YAG laser beam is spread into a laser sheet and projected across a tank or wind tunnel, being imaged with a camera and conventional photographic lens. The relatively thin laser sheet serves to select the plane of interest. In μPIV, an entire microfluidic chip is illuminated, and the focal plane of a microscope objective selects the plane of interest. Here however, the two-phase flow used demands special consideration on account of refraction across the associated interface. Imagery is also required at several locations down a geometry, which necessitates a convenient method to relocate both the imaging camera and illumination source.

The use of optical techniques has a number of complications that will be discussed in this chapter, of which the issues could be completely avoided by using NMR velocity imaging as introduced in section 2.1. However, firstly high resolution systems are complex and expensive instruments. Secondly, the magnet bores are typically orientated vertically, rather than horizontally as required here, and over the bore height, surface tension and pressure drops could not be expected to overcome the hydrostatic head differences between the two fluid phases. Furthermore, there is no ready optical access by which to keep check on the interface behaviour during an experiment. Finally, and most significantly, the entire extensional channel must fit within the restricted bore diameter, and NMR/MRI velocity imaging has limited spatial resolution, which is only useful across a very small region either side of the interface, and predominantly at the narrowest channel locations. Britton (2010) presents a review of NMR/MRI velocity imaging, highlighting sample sizes generally ranging from 5 – 60mm and spatial resolutions from 10 – 200 μm, two factors which are probably mutually exclusive. The optical system culminated in in chapter 8 has a maximum flow height of 85.9mm (excluding walls, etc.), a minimum of 2.61mm, and once analysed a resolution perpendicular to the interface of 7μm. Decades into the future it may be possible to use NMR velocity imaging at comparable performance, horizontally, with integrated viewing access. Axisymmetric, as well as planar contractions could also be studied, as well as opaque systems (e.g. such as polymer

melts used in industrial extrusion processes). For the moment however, the use of NMR velocity imaging in this application is neither practical nor technically feasible to achieve.

Before the issue of the interface is addressed, we shall consider the cell configuration and illumination source, which is illustrated in figure 6.1 below. Since it is preferable to keep the depth to the imaging plane in a flow geometry constant and look through a flat wall, the cell width is held constant, and a planar hyperbolic contraction applied in the height direction only. On the bottom wall of this channel is applied the black surface coating from chapter 4. Illumination is directed through the top wall of the channel, fabricated from a clear material, passing through the two fluid phases, before impinging on the black coating. This arrangement means the entire channel can be easily illuminated along the centreline, through the upper wall. Initially using a laser sheet was considered, but this necessitates illuminating the full length of the channel, some 130mm. An approach was then arranged where the laser output is kept in a beam configuration and swept down the channel length to the imaging location, which has a field of view on the order of a millimetre or so, comparable to the beam width. Although the channel is only being illuminated along the centreline, as a microscope objective is being used the focal plane of the objective (μm thick, compared to the beam width) thus serves to define the plane of interest. Additionally, in this manner (noting the cm channel scale, but mm field of view) this experiment has elements in common from conventional and μPIV setups, respectfully.
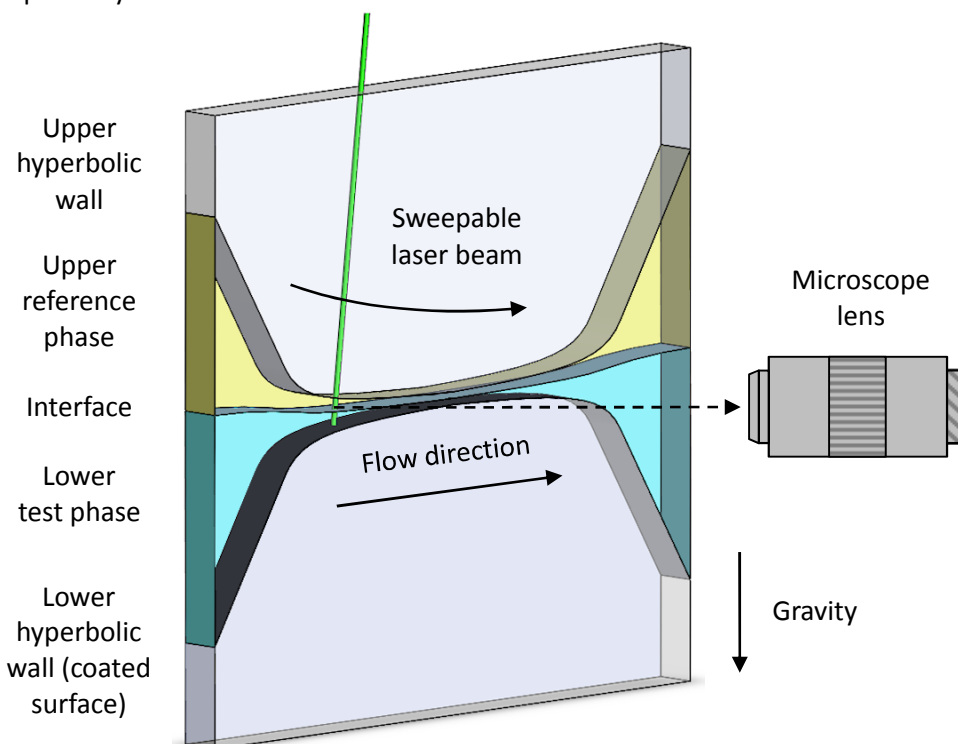
Figure 6.1: Illustration of illumination geometry and the orientation of the planar contraction, front and rear walls are omitted for clarity.

Given the cell and illumination configuration, we will now consider how to image the flow field with a few examples. The first of these, shown in cross section in figure 6.2 below, has the lens viewing in a simple horizontal configuration (also as per figure 6.1). Two phase flow in the cell is now directed into the plane of the page. Although the interface is for the most part flat, the interface must curve at some point to reach the lower wall. This means that whilst imaging in the upper oil phase is unimpeded, imaging in the lower phase is prevented by refraction of the imagery occurring across the interface, rendering it unobtainable. Aside from considering some form of moveable dissimilar wettability on the side walls to artificially generate a flat interface (highly impractical especially with multiple imaging points, and something that demands a optically clear surface coating), the only way imagery can be obtained in this situation is if the refractive index of both phases were exactly matched, which is possible to achieve. This will be now referred to as the "liquid-liquid" matching approach.
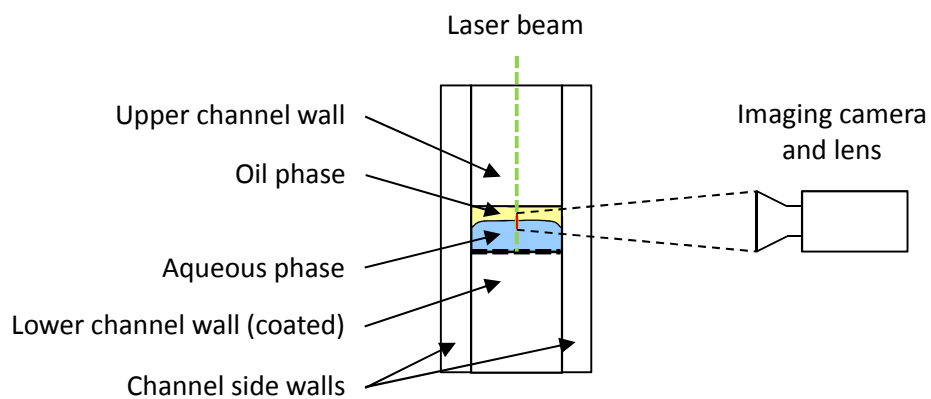
Figure 6.2: Two phase flow channel with an imaging camera looking horizontally into the cell. The surface coating is denoted by the thick black dashed line. The thin dashed black lines denote the cone of light transmitted to the imaging lens. The focal plane / field of view are shown by the red line, the laser beam by the green dashed line.

The second route by which imagery could be obtained is to image through the meniscus, but to avoid regions where the meniscus is strongly curved. This can be achieved by orienting the lens to image obliquely trough the central flat region of the meniscus, from the oil phase, into the aqueous test phase beneath. Assuming a flat interface is a modestly reasonable assumption with the small field of view and footprint through the interface compared to the channel width and length (both causing curvature), the short ray lengths below the interface, what should be a symmetric interface shape, and in particular the shallower aspect ratio sections of the channel. This is illustrated in figure 6.3. Since the channel is wide however, imaging obliquely necessitates that the imaging path must pass through the upper channel wall, certainly in narrower regions of the channel. One solution might be to use a "half hyperbolic" channel with

the lower wall curved, and the upper wall flat to provide a flat surface to look through. However, this raises complications depending on how much of the upper wall is being viewed through, as the lens is tracked vertically, and how this would affect or shift resulting imagery. A more practical solution is to match the refractive index of the upper oil phase to that of the upper channel wall material, essentially making the wall and the associated curvature and lensing artefacts disappear. This is also possible to achieve, and is now referred to as the "wall-oil" matching approach.
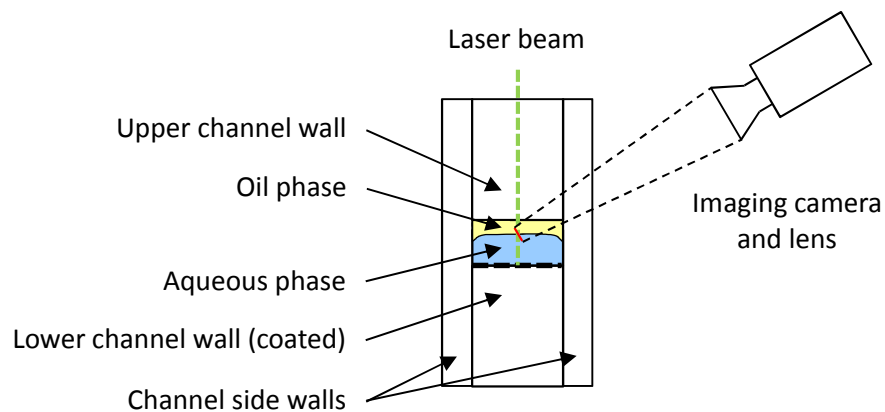
Figure 6.3: Two phase flow channel with an imaging camera looking obliquely into the cell, via the upper channel wall. The surface coating is denoted by the thick black dashed line. The thin dashed black lines denote the cone of light transmitted to the imaging lens. The focal plane / field of view are shown by the red line, the laser beam by the green dashed line.

The third option is, rather than making the interface disappear, or looking through the interface in a flat region, is to arrange the imaging camera to avoid looking through the interface at all. As illustrated in figure 6.4, this is unfortunately essentially impossible to achieve here on a number of grounds (or one, on complex mountings). In order to avoid looking through the interface, two imaging cameras would now be required. The optimum configuration with a surface coating on the lower wall (figure 6.4a) would be to arrange one camera horizontally to image the oil phase, as previously discussed. A second camera would then be required, looking up obliquely through the lower channel wall, thus avoiding the interface pinned at the edges of the lower channel wall by the surface coating. Firstly, the lower channel wall would now need to be flat and the upper channel wall hyperbolic (on account of avoiding imaging through a curved channel wall), which could be achieved but with the previous reservations about different path lengths through this surface. More importantly however, an optically clear surface coating would be required to look through, which the surface coating prepared in chapter 4 is not. A slight permutation is also possible assuming an optically clear surface coating - the lower and side walls of the channel could instead be coated, pinning the interface

at the edges of the upper channel wall (figure 6.4b). Instead the aqueous phase could now be imaged horizontally and the oil phase obliquely through the upper channel wall, which offers the advantageous ability to match the refractive index of the oil to the upper channel wall material as previously. Either way, tracking two cameras is both difficult (and only one camera was available) and optically clear coating is of course still necessary.
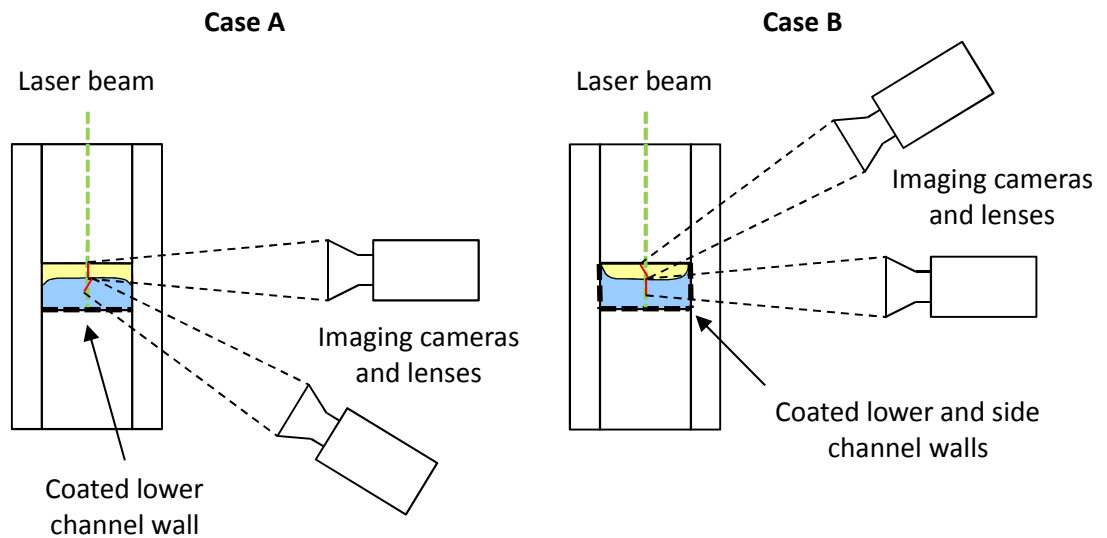
Figure 6.4: Two phase flow channel with a pair of imaging cameras to avoid looking through the two-phase meniscus (omitted labels would be the same as figures 6.2 and 6.3). Figure A has the lower channel wall coated in the surface coating (denoted by the thick black dashed line), figure B has everything except the upper channel wall coated. The thin dashed black lines denote the cone of light transmitted to the imaging lens. The focal plane / field of view are shown by the red line, the laser beam by the green dashed line.

The concepts of the liquid-liquid and the oil-wall index matching approaches have relative merits and disadvantages. In terms of achieving the required index matches, as will be shown in the next section, this is fairly straightforward for matching an oil to the upper wall as oils typically have high refractive indexes close to that of solid materials. Matching the refractive index of the two fluids to one another is much more restrictive. Matching the oil index to the upper wall will only be modestly sensitive to mismatches as the upper wall is only slowly curving and distortions from this interface would tend to affect length scales in both phases. Conversely, matching the index of the two fluids involves imaging through a strongly curved meniscus at the cell edges (and at other locations, forming a shallow angle to light rays) and at a substantial distance from the imaging zone, which would strongly affect length scales (and shear rates) if mismatched only in the lower phase. These effects would also change with the changing interface curvature radius at measurement sites down the channel. Due to refraction

(assuming perfect matches are achieved), the liquid-liquid matching approach is useful, as the same length scales would be present in the upper and lower phases. In the wall matching approach, different length scales are present above and below the interface. The length scales in the aqueous phase are a function of the difference in refractive indexes. This change in length scale could be calculated. However, even if the interface is flat, tilt of the interface will affect length scales, so an in-situ methodology of judging reference length scales in both phases is required. More specifically in the lower phase, this would ideally be performed under flow conditions, when the exact interface configuration thus adopted. This is attempted in section 8.1 later.

Considerations are also pertinent with regards capturing light from tracer particles and transmitting this to the camera, and also, the efficiency of coupling light into the channel through the upper wall. The wall-oil approach is useful, as even with a very narrow contraction in a shallow aspect ratio channel, a wide aperture exists from the imaging zone (predominantly though the upper channel wall) through which the lens can gather light. It is also permits the incoming laser beam will remain in a beam despite passing through the curved upper wall. Conversely in the liquid-liquid approach, light can only be gathered through a narrow slit, and some spreading of the laser beam will occur due to the curved upper wall (assuming a half-hyperbolic design is not used). Furthermore, aqueous polymer solutions have a tendency to be translucent, rather than transparent. The wall-oil approach greatly minimises path lengths through this translucent lower phase. The liquid-liquid approach (and the approach avoiding imaging through the interface) requires a significant proportion of the light rays to travel a substantial distance through this lower phase. This is especially so if the interface resides close to the upper channel wall. Note this suggests a small scale/reduced width is preferential, whereas the wall-oil approach in fact needs a wide/large channel to minimise interface curvature. Concurrent with the imaging "aperture" with this the influence of a focal plane depth in the two different approaches. With the liquid-liquid approach, as the lens is horizontal, particles at different depths in the focal plane all have the same velocities, so a lens with a relatively narrow aperture lens is acceptable (this differs from a wide aperture lens being restricted by the channel walls, horizontal rays would still permit a shallow focal plane). However, in the wall-oil approach, due to the oblique angle particles at different depths in the focal plane have different velocities. There is no way to differentiate between these particles, and as a result as shallow a focal plane as possible is critical, demanding a high numerical aperture lens. This has the side effects of maximising image brightness, but also requiring a high seeding density.

With regards the oblique imaging approaches, a note should finally be made in relation to "lens tilt". Specifically lens "tilt" (that is, tilting a lens relative to a sensor or film plane) is a technique normally used in photography, governed by the Scheimpflug principle, which reorients a focal plane of a camera/lens system (see for example Merklinger (2010). This is used, for example, to put an entire landscape or a tall building into focus. It is also used in stereo PIV setups where two cameras image a plane (illuminated by a laser sheet) from oblique angles for the same reason, and could conceivably be used here in a similar manner. However, firstly, lens tilt is only suited to situations where the lens-object distance is much longer than the lens-sensor distance, where only a small tilt is necessary to produce a significant tilt of the focal plane. With short working distance lenses (and their long lens-sensor distances) here, this situation is the converse and no useful degree of tilt can be obtained. Secondly, with a small field of view even a relatively thin (e.g. 1mm) laser beam can still illuminate the entire focal plane. Lens tilt also offers no advantage with regards to the depth of focus issue previously detailed.

From this point, both the wall-oil and liquid-liquid refractive matching approaches are taken forward. The following section details consideration of the liquid phases to attain these refractive index matches, and the limitations this matching requirement imposes.

6.3 Wall-oil system refractive index matching and methodology

To begin with, the simplest optical system to satisfy the refractive index matching requirement is that of the wall-oil configuration. Standard engineering oils tend to have refractive indexes quite close to that of Perspex, which makes matching the oil index to that of a optically clear upper channel wall relatively straightforward (hence the interest in not being restricted in material choice through lithographic or etching techniques). Refractive index values for Perspex at 532nm (the wavelength of the laser system) include 1.4953 (20.1°C), 1.4934 (23°C) and 1.4937 (20°C) for an initial estimate (average of 1.4941). These three values are sourced from the database of Polyanskiy (2016), with the first and last originating from Beadie et al. (2015) and Sultanova et al. (2009) respectfully. As highlighted in chapter 1, commercial off the shelf oils tend to contain polymeric viscosity modifier additives which may influence the rheology (potentially including the 15W/40 mineral oil used up to this point). These oils may also contain surfactants, two factors that render them unsuitable for detailed work. A "simple" oil is thus required, and here attention is focussed on untreated "base oils", intermediates which are blended to form final commercial products. These oils may be mineral and/or synthetic in origin.

Since a precise refractive index match is required, this can only be achieved through a blending approach of two different oils with refractive indexes either side that of a target value. It also permits the refractive index to be precisely adjusted to that of a sample of the cell wall material (designed in chapter 7), rather than a literature value, both at the correct wavelength and typical temperature conditions of which refractive index is a function of both (the previous literature values differ by some 8wt% of a prospective blend mix ratio). An individual mineral oil (Exol Lubricants E1600, sample kindly supplied by Exol lubricants via Chemodex, Worksop, free of charge), was initially identified with a refractive index quite close to that desired: n=1.4875 based on the product datasheet (Arnold, 2015) and converting the refractive intercept data (see Kurtz and Ward (1936) and ASTM D2159-93 (ASTM International, 1993)), but this leaves scope for improvement. To this end, two synthetic base oils were identified, SpectraSyn Elite 65 with an index below Perspex, and Synesstic 5 with an index above. 25L pails of each were kindly donated by Exxon Mobil free of charge, and key parameters are summarised in table 6.1 below from the manufacturer data and using ASTM D341-09 (ASTM International, 2015) accordingly.

Oil name	SpectraSyn 2	SpectraSyn Elite 65	Synesstic 5	Synesstic 12
Data source	ExxonMobil (2015a)	ExxonMobil (2015b)	ExxonMobil (2015c)	ExxonMobil (2015d)
Composition	PAO (polyalphaolefin)	mPAO (Metallocene polyalphaolefin)	Akylated naphthalene	Akylated naphthalene
Colour (ASTM D1500)	<0.5	<0.5	<0.5	<4
Kinematic viscosity at 40°C (cSt)	5.0	614	29	109
Kinematic viscosity at 100°C (cSt)	1.7	65	4.7	12.4
Kinematic viscosity calculated at 20°C (cSt)	8.8	1889	82	362
Refractive index	1.4418	1.4667*	1.522	1.506

Table 6.1: Characteristics of selected synthetic oils from Exxon Mobil. Data reproduced from the relevant product datasheets or provided directly from Exxon Mobil (*). Kinematic viscosities are calculated at 20°C via ASTM D341-09.

The Elite 65 and Synesstic 5 oils are miscible with each other, feature high demulsibiltiy according to the suppliers, and the Elite 65 oil is completely colourless and the Synesstic 5 is

only slightly coloured. The combination of the Elite 65 and Synesstic 5 oils thus produces a near-colourless oil as elaborated shortly. Assuming a linear change in refractive index with blend wt% (a good approximation) and a required index of 1.4941 gives an initial blend of 49.6wt% Synesstic 5, and the commonly used empirical mixing equations of Refutas and of Kendall and Monroe (Zhmud, 2014) give blend viscosity estimates of 284mPa.s and 516mPa.s respectfully at 20°C (approximate blend specific gravity of 0.88). Choosing the viscosity of the reference oil compared to that of a shear thinning, but viscoelastic, test phase is difficult. It is desirable to have a similar layer thicknesses of the two phases at similar flow rates, however it is impossible to rationalise a priori whether such a test phase would be thick (on account of a high extensional viscosity, resisting compression) or thin (on account of a greatly decreased shear viscosity under flow). This order of magnitude of viscosity, compared to zero shear viscosities of test solutions on the order of several Pa.s, was deemed a reasonable starting point.

In order to accurately determine the oil blend composition, two different methods were attempted. The use of a modern digital refractometer (e.g. a Bellingham and Stanley RFM 390) is not practical since firstly, it operates at the 589nm Sodium D lines using an integral light source, not the 532nm required; and secondly, it is not designed to handle solid samples.

The first approach attempted is that described by Budwig (1994). The light reflected from a dielectric interface (here between a solid sample and a surrounding liquid) varies according to equation 6.1 below "where R is the ratio of reflected beam power to incident beam power, n_1 is the refractive index of the liquid, and n_2 is the refractive index of the dielectric solid" (Budwig, 1994).

$$R = [(1 - n_1/n_2)/(1 + n_1/n_2)]^2 \qquad \textbf{(6.1)}$$

When the refractive index of the liquid and the solid are exactly matched (n_1=n_2) the reflected beam disappears as the solid sample and surrounding liquid are electromagnetically homogeneous. Studying a reflected beam makes using a low power 532nm laser pointer as the light source convenient. Whilst simple, despite modifications this approach proved in the end impractical. The authors describe the use of a flat sided tank with a few degrees separation between the incident and reflected beams and suggest the use of a photodiode for monitoring reflected beam intensity. Due to the possibility for beam alignment changing through refraction and the small area of photodiodes, this was replaced with a right angled geometry and large area (thermally equilibrated) camera sensor, shown in figure 6.5a. A more significant problem

with the method is ensuring a homogeneous sample between adjusting the composition, the authors suggesting a magnetically stirred tank. Figure 6.5a shows a revision with a minimal volume tank and stirrer paddle. No useful changes in intensity on composition modification were subsequently recorded, attributable to an unmixed boundary layer residing at the surface of the Perspex sample. Figure 6.5b shows a shallow tank for ready interchange of pre-mixed samples, however thorough cleaning was impractical and remnants of previous samples could still be seen moving through the laser beam. Although the system here is admittedly high in viscosity, no raw results are presented in the reference to substantiate that this technique is actually practical, given the boundary layer shortcoming. Techniques based on light intensity are also quite "fragile" in nature and easily disrupted (by dust, bubbles, stray scattering, interference patterns, and to an extent, oil absorption for example).
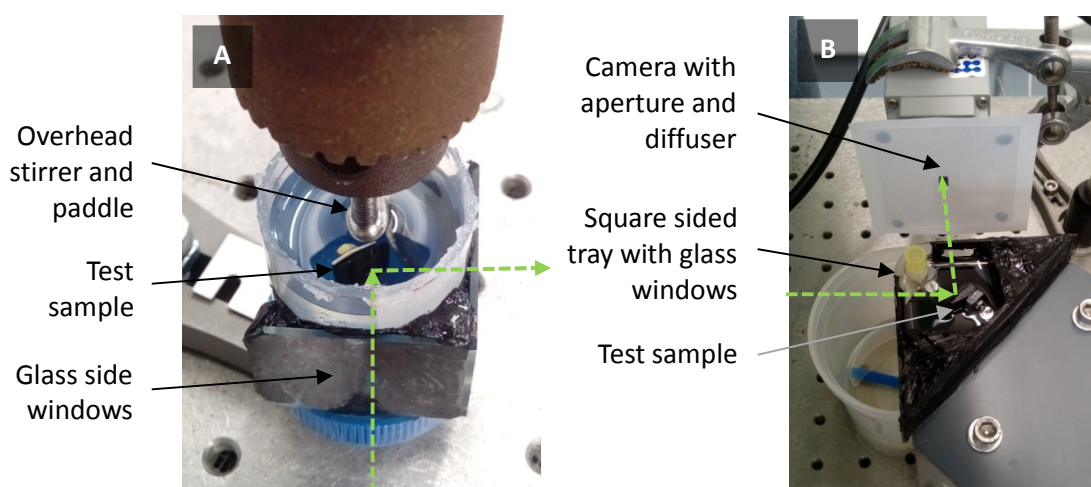
Figure 6.5: Refractive index matching to a solid sample by reflection intensity. The laser beam is shown by the dashed green line. Figure A shows a low volume stirred geometry. Figure B shows a shallow tray geometry to permit access to side walls and samples for cleaning between samples.

The second route, and the route used for all subsequent work, is to use an old manual Abbe refractometer (Bellingham and Stanley high accuracy model Abbe 60/ED). This instrument can accept both solid and liquid samples, is very simple to clean between samples, and can have the external sodium light source replaced by a 532nm source. This was initially a torch and 532nm filter, but was subsequently replaced by the 532nm laser pointer, providing improved monochromacity and brightness for more accurate work with the liquid-liquid matched system. The arrangement used is shown in figure 6.6, together with a spinning "despeckler" diffuser. Two levels of diffusion renders the laser pointer safe as a illumination source.

532nm low power laser pointer

Illumination prism of Abbe refractometer cell

Spinning diffuser sheet
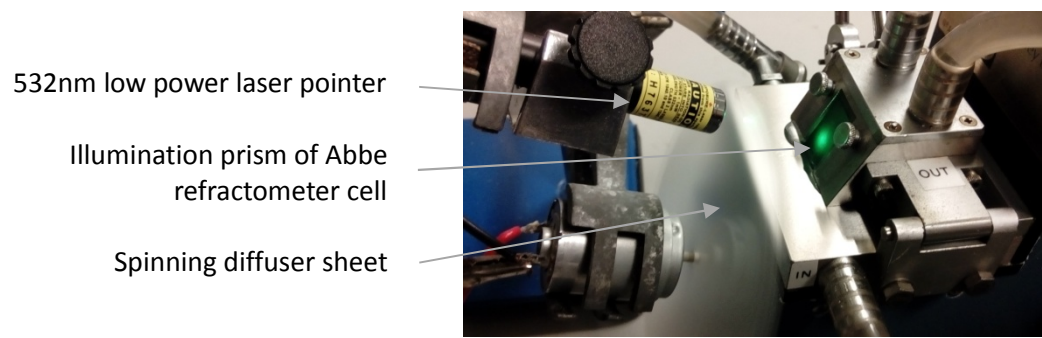
Figure 6.6: Laser illumination setup used with the Abbe refractometer. The spinning diffuser and diffuse surface of the illumination prism provide two levels of safety in this setup.

The instrument features an arbitrary scale that is converted to refractive index (at a specific wavelength) via a calibration table in normal use. For this work, operating in arbitrary units is practical, as only a match in refractive index is desired. For approximate indication however, water, n = 1.333 gives an average reading of 2.497; and glycerol n = 1.474 gives 17.117 (both at 20.5°C). Whilst an inherently high precision instrument, the main shortcoming in accuracy is due to the need to manually (by eye) line a crosshair with the bright-dark boundary generated via refraction in the instrument. This must be done accurately and reproducibly, which is limited by the low magnification of the ocular and eye strain caused by aberrations in the simplistic optics (reduced by maximising illumination intensity), with typical maximum scatter of 10 in the last readout digit being the best achievable. Replacing the ocular with a camera sensor for future work is recommended in chapter 9.

In order to determine the oil blend ratio to match to that of Perspex, a sample of the actual cell wall material used (as designed in chapter 7) was precision cut and one face polished to a high finish. Both the cut sample and the overall cell wall were checked for residual cutting/machining stresses which can cause birefringence, a phenomenon where the material exhibits more than one refractive index. The Synesstic 5 oil, being above the refractive index of Perspex, replaced the usual 1-Bromonaphthalene high-index coupling liquid used for solid samples in refractive index measurements. For this wall-oil matching work, the instrument was operated at ambient temperature (23.0±0.5 °C as indicated on the instrument), in a lab within about 2 degrees of that where the experiment is located which, as evident later, was sufficient for the scope of work conducted in section 8.1. 24 Measurements of the Perspex sample were performed, moving the sample around revolving the sample to minimise effects of excess contact fluid and incident light coupling effects. An average value of 19.110 with a standard deviation of 0.0099 was deduced. Samples of pre-mixed Elite 65 and Synesstic 5 oils were

prepared at approximate intervals of 0, 30, 40, 50, 60, 70, and 100wt% Synesstic 5, with the actual masses used (order of magnitude 10g) being recorded on a 4 d.p. balance. These samples were thoroughly mixed in sealed tubes under heating, before being allowed to return to room temperature. Additional data points at 45 and 55wt% were added subsequently. 4 Index measurements of each fluid blend were conducted. The data is presented in figure 6.7, with the second order polynomial trend line being fitted to the 4 data points visible. Error bars are 1 standard deviation. From this data, a blend ratio of 44.30wt% Synesstic 5 was determined, compared to the initial estimate of 49.6wt%. As stated in the preface, given commissioning of the DHR2 rheometer, accurate determination of the viscosity of this blend is intended, but for the moment the blending viscosity estimate is instead relied on as a guide.

$$y = -0.3828x^2 + 6.6816x + 16.225$$
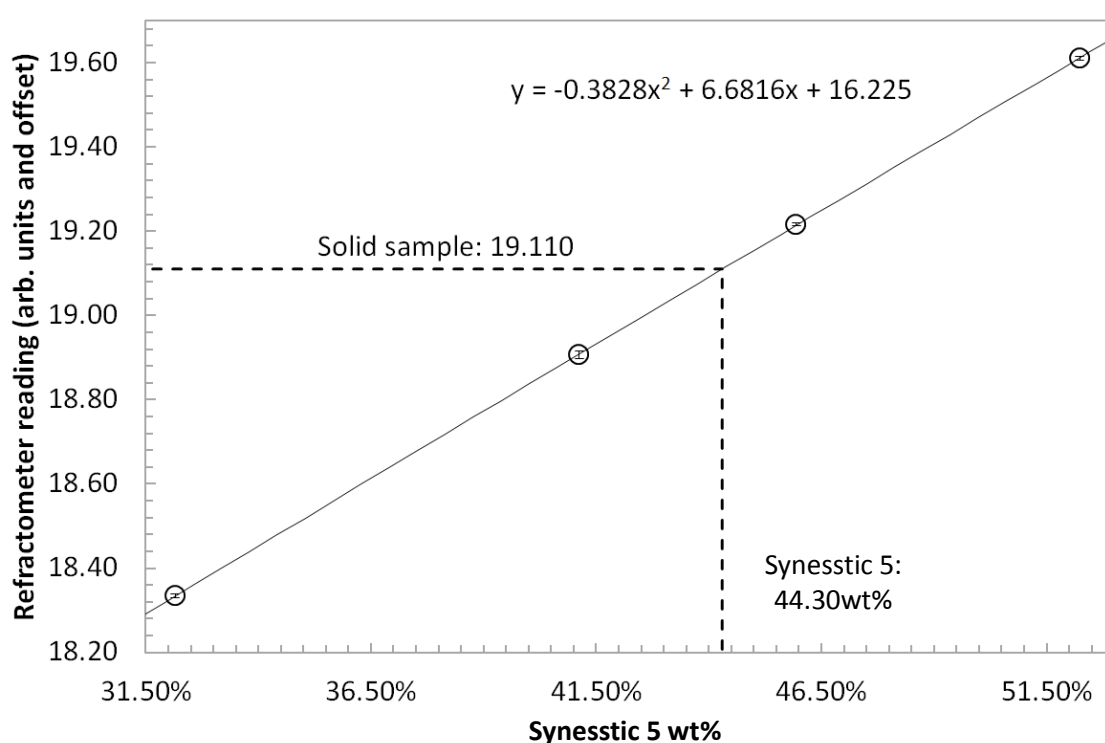
Figure 6.7: RI matching of a blend of Synesstic 5 / Elite 65 oils to a solid Perspex sample from the flow cell at 23.0 °C. Circular markers are centred on average values, error bars are 1 standard deviation, and the solid line is a polynomial fit to the data points shown.

With an index matched blend identified, we briefly return to the impact of oil colouration on light transmission and oil choice. ASTM D1500-12 (ASTM International, 2012) defines a scale of incremental oil colouration. Compared to the colourless Elite 65 and near colourless (ASTM D1500 <0.5) Synesstic 5 oils, the E1600 and a similar high refractive index Synesstic 12 oil, listed in table 6.1 as an alternative candidate, have colouration indexes of <4. A test of the E1600 oil was conducted with a UV-VIS spectrometer (Ocean Optics USB2000+UV+VIS+ES, equipped with an Ocean Optics DT-MINI-2-GS halogen / deuterium light source) at 532nm,

10mm path length, and relative to a similar refractive index glycerol reference sample. This showed a transmission of only 61% of the incident light. Supposing an incident beam length (with the illumination arrangement described) of 3cm in upstream or downstream channel sections, this corresponds to only 22% transmission. The E1600 also, interestingly, fluoresces with 532nm laser illumination. The refractive index matched blend of Elite 65 and Synesstic 5 transmits close to 100% of the incident light at 532nm.

For the oblique imaging approach, we can furthermore make a rough estimate of the required angle of tilt based on the difference in refractive indexes across the liquid-liquid interface. The value of n = 1.494 for Perspex as previously is taken, corresponding to an average measured value for the Perspex sample of 19.110 on the arbitrary instrument scale. For a typical test fluid, 1.2wt% 4×10^6MW PEO in water, the average reading is 2.720. Comparing this to the value given for water previously (2.497) shows little shift from this value and unfortunately does little to alleviate the refractive index step. Though this solution is concentrated, the finding corroborates with example references in table 6.2 which also predict inconsequentially small shifts for the purposes of this experiment. dn/dc, the specific refractive index increment, can be converted to refractive index by equation 6.2 below: n_m is the refractive index of the solution, n_w that of the solvent (water = 1.333), and c the solution concentration (usually g/ml). This equation is often stated as only being applicable at "low concentrations".

$$n_m = n_w + \left(\frac{dn}{dc}\right)c \qquad\qquad \textbf{(6.2)}$$

Reference	MW	Concentration regime in reference (units as shown)	Temp'	Wavelength	dn/dc or index n
Israelachvili et al. (1979)	1.5×10^5	0.01%	20.5°C	546nm	dn/dc = 0.137 ± 0.002 ml/g (Secondary reference)
Venohr et al. (1998)	1×10^4	Up to 15wt%	20°C	514.5nm	Values between 0.133 and 0.136 ml/g
Basavaraju et al. (2007)	Not stated	0.2% v/w Xanthan/PEO blends of various ratios	30°C	Not stated	n values all fall within the range of 1.339 and 1.345
Jayaprakash et al. (2013)	1×10^5	2% w/v HPMC/PEO blends of various ratios	30°C	Not stated	n values all fall within the range of 1.341 and 1.342

Table 6.2: Literature relations for the refractive index of PEO (and similar) aqueous solutions.

For light rays passing from the aqueous to the oil phase and entering the interface at 90 degrees to the normal (i.e. the situation for total internal reflection), they would therefore exit at a normal angle of 62.9 degrees, or a lens inclination from the horizontal of 27.1 degrees. No light rays can reach the lens below this angle, but continuing to increase it worsens the issue of the focal plane depth. Note that Perspex has a fairly low refractive index compared to other wall materials, so changing the initial choice of wall material to something with a lower index has no merit. Increasing the lens inclination to 30 degrees permits light rays to travel at 15.5 degrees to the horizontal under the interface. Figure 6.8 illustrates the problem.
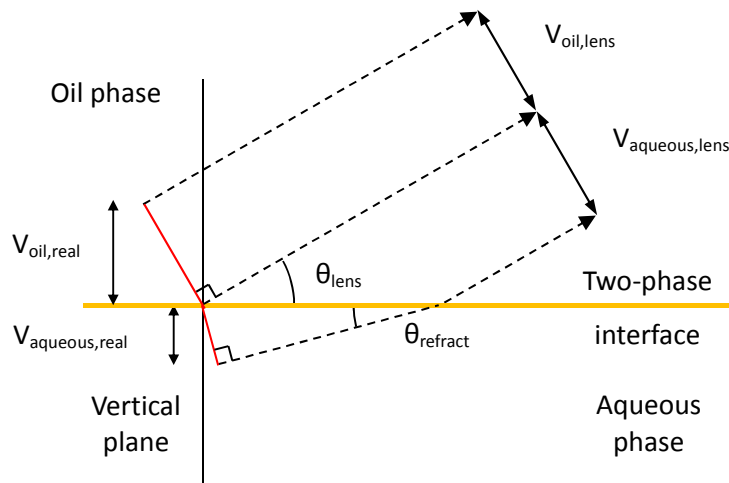
Figure 6.8: Vertical field of view rough estimate for an inclined lens looking through a two phase interface. Parallel light rays (dashed lines) propagating to the lens are assumed (infinite focal distance / infinitely small aperture), however it is still assumed to feature a focal plane. Focal planes (red lines) for the oil and aqueous phases are assumed to still be flat, and to be essentially at the same focal distance from the lens.

We assume parallel light rays to the lens (at infinite distance, or infinitely small aperture), but that the lens still features a focal plane. We also assume, for an approximation, that it remains flat above or below the interface, and that the focal distance is essentially analogous in both cases. We are also interested in vertical length scales for shear rate determination, not those aligned with the focal plane. With some trigonometry (θ_{lens} = 30 degrees, $\theta_{refract}$ = 15.5 degrees) estimates can be made. Assume a 1mm diameter particle covers 1mm across the front of the lens (e.g. being projected straight onto the lens front) and an analogous number of sensor pixels. In the oil phase ($V_{oil,real}$ = 1mm), the particle would cover 0.866mm of "lens height" ($V_{oil,lens}$), or exhibit an apparent aspect ratio (defined as the horizontal pixel size / vertical pixel size) of 1.15 in imagery. In the aqueous phase ($V_{aqueous,real}$ = 1mm), it would cover 1.803mm of "lens height" ($V_{aqueous,lens}$), or exhibit an apparent aspect ratio of 0.55. Imaged vertical distances

in the upper oil phase would thus be in real space 2.1 times those in the lower phase aqueous phase, and thus 2.1 times lower in real-world shear rate.

Finally, aside from considering viscous test fluids, an aqueous Newtonian system is also necessary by which to validate the experiment. Using water, which closely emulates the refractive index step, is impractical given the viscosity of the oils chosen, and as a result verifying against glycerol (about 1.4Pa.s at room temperature) could be considered. This, however, does not satisfactorily emulate the refractive index step expected in test situations (n = 1.474). A much lower viscosity oil than the Elite 65 for blending with Synesstic 5 would be desirable for such tests. The SpectraSyn 2 (also shown in table 6.1) is the lowest viscosity and incidentally the lowest refractive index oil offered by Exxon Mobil. Hexane has a lower still viscosity (and a refractive index of 1.375), but is highly volatile and no use on this basis. A compromise is necessary between emulating the refractive index step and having similar viscosities between the oil and aqueous (water-glycerol) phase.

6.4   Liquid-liquid system refractive index matching

We can now move onto considering how the liquid-liquid refractive index might be achieved. Clearly with the refractive index of standard oils around 1.5 and that of typical test solutions around 1.33, an alternative approach needs to be sought. The first route is to locate another fluid that is still immiscible with water, but which features a lower refractive index. Silicone oils have lower refractive indexes, nominally around 1.4 for anything except the lowest of oil viscosities where indexes decrease very slightly. Fluorinated oils such as Krytox from DuPont (Chemours, 2015b), and Demnum from Daikin (Daikin Industries, 2015) have very low refractive indexes around 1.3. Fluorinated substances are also listed in refractive index matching fluids from Cargille for microscopy (Cargille Labs, 2016) for fluids around n = 1.33, showing this to be a sensible course of inquiry. A second fluid miscible with the oil is now required to raise the refractive index. Since the low refractive index of such oils arises from the low electronegativity of the fluorine atoms (Sasaki and Nishi, 1996), the obvious option is to find similar oil but with chlorine replacing some of the fluorine atoms to blend with. Since Krytox is a perfluropolyether, this is satisfied by the PCFTE (polychlorotrifluoroethylene) oils with indexes around n = 1.4 offered by the Halocarbon Products Corporation (Halocarbon Products Corporation, 2016). However, fluorinated oils such as Krytox are immiscible in almost all liquids, including the PCTFE oils as well as silicone and alkane oils as informed by the suppliers (Johnston, 2016). Krytox is indicated as being soluble in some highly fluorinated solvents (Chemours, 2015a), hexaflurobenzene and 1,1 dichloro-1-fluoroethane being two with high enough refractive indices and the only evident route to achieve n = 1.33. However, these

are not inexpensive, and volatility, amongst other factors, must be considered. Note also the density of such a resulting blend dictates that it would sit underneath an aqueous test phase, requiring rearrangement of the illumination provision compared to the wall-oil case.

Based on using silicone oils, a method must therefore be found to increase the refractive index of a test solution to match that of the oil. Glycerol (and other glycols potentially, e.g. ethylene glycol) can be used to satisfy this, in virtue of the same way it is not ideal for validating experiments based on the wall-oil index matched system. To reach a refractive index of about 1.4, a glycerol-water blend around 50wt% is required. Despite being 1.4Pa.s at room temperature, a 50wt% solution has a viscosity on the order of 6mPa.s due to the highly non-linear relationship in viscosity with composition (Glycerine Producers' Association, 1963). As a result, such a mixture is not too dissimilar – in a crude rheometric context - to using water as a solvent.

Requiring such blended test solutions greatly restricts what can test systems can be analysed, precluding purely aqueous solutions commonly analysed in literature. Furthermore, at one end of the concentration scale, dilute PEO systems in a glycerol/water solvent are often used as model Boger fluids: table 6.3 summarises some of the higher polymer (opposed to ppm) concentration examples from literature. Solvent systems using PEG can also be used, for example (Wang and James, 2011). This means that whilst such solutions can be prepared, their shear rheology dependence is minimal, and thus the compositions in table 6.3 represent a lower bound on usable test fluid compositions.

Reference	PEO MW	PEO wt%	Glycerol wt% (of solvent mixture)	(Zero) shear viscosity mPa.s (power law parameter)	Crossover concentration (in a defined solution) g/cm^3
Steinhaus et al. (2007). See also Cooper-White et al. (2002).	3×10^5	0.21	36	5.7	3.9×10^{-3}
	6×10^5	0.17	34	5.8	2.4×10^{-3}
	1×10^6	0.10	37	5.6	1.7×10^{-3}
Lee et al. (2011). See also Christanti and Walker (2001)*	1×10^5	0.3	40.7	4.4	8.74×10^{-3}
	3×10^5	0.2	41.9	4.6	2.69×10^{-3}
	1×10^6	0.05	40	4.3	1.29×10^{-3}
	5×10^6	0.043	34	4.5	N/A
Mun et al. (1998)*	1×10^5	0.3	40.6	5.19	N/A
	3×10^5	0.2	36.2	5.40	N/A
	6×10^5	0.17	33.9	6.40	N/A
	1×10^6	0.075	38.0	4.94	N/A
Crooks and Boger	8×10^3	5	26	5.98	N/A

(2000)	3x10^5	0.2	36.3	5.65	N/A
	6x10^5	0.17	34	5.77	N/A
	1x10^6	0.1	37	5.63	N/A
Crooks et al. (2001)*	3x10^5	0.1	26.5	3.2	N/A
Rodd et al. (2007)*	2x10^6	0.075	45	9.03	N/A
		0.075	60	17.3	N/A
Sousa et al. (2010)*	8x10^6	0.1	40	10.5	3.48x10^{-4}
Negri et al. (2013)	1x10^5	1.1	22.9**	5.25	N/A
	3x10^5	0.27	31.1	5.20	N/A
	1x10^6	0.125	30.0	4.75	N/A
Rodd et al. (2005)	2x10^6	0.1	55	18.2	8.6x10^{-4}
Casanellas et al. (2016)	4x10^6	0.0125	25	0.3	5.5x10^{-4}
		0.05		1.7	
		0.1		4.8 (n=0.88)	
		0.2		15 (n=0.81)	
		0.35		56 (n=0.75)	
		0.5		158 (n=0.66)	
		0.75		498 (n=0.60)	

Table 6.3: Examples of PEO glycerol/water Boger (and very similar) fluid compositions used in literature: final reference includes shear thinning behaviour. Glycerol wt% is assumed to be that of the solvents only, and ppm polymer to be weight based, unless stated in the reference and/or converted if applicable. * = High MW values in source vary between low polymer wt% and low glycerol wt%: appropriate composition(s) selected. ** = Reference composition does not total 100wt%. N/A = data not presented.

At the other end of the scale with more concentrated systems, we recognise that whilst PEO is soluble in water "it is almost insoluble in pure glycols" (Dai and Tam, 2006). This means that more may occur than a simple change in solvent viscosity. In an extreme case, phase separation is possible (but not observed in the following chapters). We are however forced to consider relatively high concentration and molecular weights systems to both maximise viscosity (in-lieu channel scale and flow Reynolds value) and keep the required extension rates to a practical level. In their work on studying binding interactions, Dai and Tam (2006) comment on the issue of changing the solvent from water to water-glycol mixtures for PEO:

"Since the solubility of poly(ethylene oxide) (PEO) in water is due to the formation of hydrogen bonding with water molecules, the solution behaviour of PEO in glycol solution should be very interesting. Not only are glycols less polar solvents than water, but they are also strong hydrogen-bonding agents. Both glycols and water can act as hydrogen donor in the H-bond, while PEO, glycols, and water can act as the hydrogen acceptor. Competition for the establishment of hydrogen bonds with PEO occurs when glycols are added to water."

(Dai and Tam, 2006)

On the other hand, the work of Ortiz et al. (1994) is important. Firstly, they studied high concentration PEO solutions, in some cases as high as 7wt%, of various molecular weights, in both water and 50wt% water/glycerol solutions as solvents (5.24mPa.s viscosity). Both the water/glycerol solvent is very nearly that required here, and furthermore, most of their polymers are from the same supplier (Union Carbide, now part of Dow Corning) and the same family of products as the WSR-301 used in chapter 8. The highest viscosity system studied was ~5x10^{6}MW (two values from different sources) at 3wt%. Whilst preparing such concentrated and high molecular weight solutions are reported not to be easy, no comments are made as to any solution preparations to be "unsuccessful" in light of the previous comments here. Their ~5x10^{6}MW, 3wt% PEO solution in a glycerol/water solvent represents a upper bound on usable test solution composition and is shown to be highly shear thinning (fig. 2a of reference). Secondly, they report shear, normal force, and complex (oscillatory) viscosity data, and found that the glycerol/water solvent systems exhibit higher viscosities and normal forces than their water solvent counterparts. However, with only a few discrepancies, the data for the water and glycerol/water systems collapsed onto master curves for shear (being scaled by zero shear viscosity and a characteristic time, $(\eta - \eta_s)/(\eta_0 - \eta_s)$ plotted against $\lambda_E \dot{\gamma}$ in the reference) and primary normal force, "almost independent of concentration, solvent, and molecular weight" (Ortiz et al., 1994). Similar curves were also produced for complex viscosity data. This collapsibility of data therefore suggests no dramatic changes in rheology are occurring despite the substantial change in solvent conditions for these concentrated systems.

The companion reference listed in Ortiz et al. (1994) "Rheology of Dilute Poly(ethylene oxide) Solutions" was never published – However it was summarised in Carreau et al. (1997). For 2.89x10^6 MW PEO solutions between 10^2 and 10^3 ppm, both the intrinsic viscosity [η] and radius of gyration (R$_g$) of molecules were found to decrease (1.37 to 0.99 m^3/kg, and 266 to 243nm respectfully) on using the 50wt% water glycerol mixture over pure water as the solvent, concurrent with it being a poorer solvent (Mun et al. (1998) found the same effect on intrinsic viscosity). They also show (figure 3.1-12 of reference) that solutions of PEO in water satisfy the critical concentration (c*) relation of Gennes (1979), $[\eta]c^* \cong 1$, the concentration at which polymer-polymer interactions dominate over polymer-solvent interactions. The "crossover concentration" in table 6.3 (as defined in most references) is c*. For $[\eta]c < 1$, specific viscosity increased as defined by intrinsic viscosity. For $[\eta]c > 1$, i.e. predominantly concentrated systems, a marked increase in the viscosity gradient against concentration behaviour occurred as expected on account of entanglements. The data for the water-glycerol system (c* is a function of the solvent used for a given MW polymer) is stated to fall closely to that for the water solvent case. From this information, operating at polymer concentrations above 0.1wt%

(critical concentrations stated as being conservative) in a 50wt% water-glycerol solvent is therefore necessary for chain entanglements to be important (desirable here for shear dependent rheology). The Boger fluids in table 6.3 are accordingly prepared at concentrations below the critical contraction values, the last reference in the table conversely features both constant viscosity and shear-thinning behaviours at higher concentrations.

To summarise, from the data in table 6.3, Ortiz et al. (1994) and Carreau et al. (1997) we can conclude a sensible operating regime is in the region of 0.3-3wt% $4x10^6$MW PEO in the required water/glycerol solvent mixture for this liquid – liquid matched approach. Whilst the concentration range is limited and we are restricted to a custom solvent, the shortcomings are modest. Furthermore the use of glycerol/water solutions to achieve the refractive index match is simpler and less expensive route compared to tuning a fluorinated oil blend for each test solution. A second benefit is also apparent with raising the solvent refractive index: given the concern over test fluid translucency noted previously, in chapter 8 appropriately index matched solutions prove in fact virtually transparent. Supplier data such as Polysciences Inc. (2016) and Sigma-Aldrich Co. LLC. (2017) give native refractive index (n20/D) values for $1x10^5$ MW PEO of 1.510-1.540 and 1.4539 respectfully, i.e. raising the solvent index better matches that of the native polymer. In passing, whilst we have identified that the experiment must use two phase flow, and identified all the necessary information to use PEO as a test subject in both optical arrangements, we should also note that PEO is known to be a stabilising agent for oil-in-water emulsions (for example S.Różańska et al. (2012)), a fact that will necessitate very careful control of the two-phase flow experiment.

For this liquid – liquid matched system, a silicone oil, Allcosil 200/50, was obtained from J. Allcock & Sons Ltd., with a indicated refractive index of 1.402 and a certificate of analysis viscosity of 50.00 centistokes (J. Allcock & Sons Ltd., 2012) at 25°C, or 47.95mPa.s. The viscosity has been revised down from that of the Elite 65 / Synesstic 5 blend, firstly given the layer thicknesses commented on in section 8.1, but also as a viscosity remotely similar to that of the index matched glycerol – water system is required for validation work. Cost also increases significantly for oils below 50 centistokes, as well as the flow Reynolds value. Similarly to the oils previously used, this oil is colourless and readily demulsifies as found from practical use - any droplets formed easily re-incorporate themselves into their associated bulk phases.

Similarly to that conducted for the wall/oil system, the oil refractive index was measured (9.6894, standard deviation of 0.00284 over 20 measurements), and glycerol-water samples made up at approximately 52.5, 53.5, 54.5 and 55.5wt% to the same accuracy as previously.

Measurements for the glycerol-water solutions are also averaged over 20 measurements, and are plotted in figure 6.9 below with error bars to 1 standard deviation. This serves as an initial guide for a glycerol-water system at a temperature of 20.5 ±0.5°C as indicated on the instrument – the match is further refined at the lab temperature and for the test fluid compositions as detailed in section 8.2. The linear trend line shown gives a required composition of 53.553wt% glycerol, a second order polynomial gives essentially the same value. Again as per the comments in the preface, we rely on the manufacturer viscosity for the silicone oil. For the glycerol water blend, interpolation from the data in Glycerine Producers' Association (1963), firstly curve fitting at constant composition against temperature, then interpolating to the composition, gives an estimate of 6.3mPa.s at 25°C, the temperature at which the oil viscosity is specified. This provides a viscosity ratio estimate of 7.6 at 25°C, as used in section 8.2.
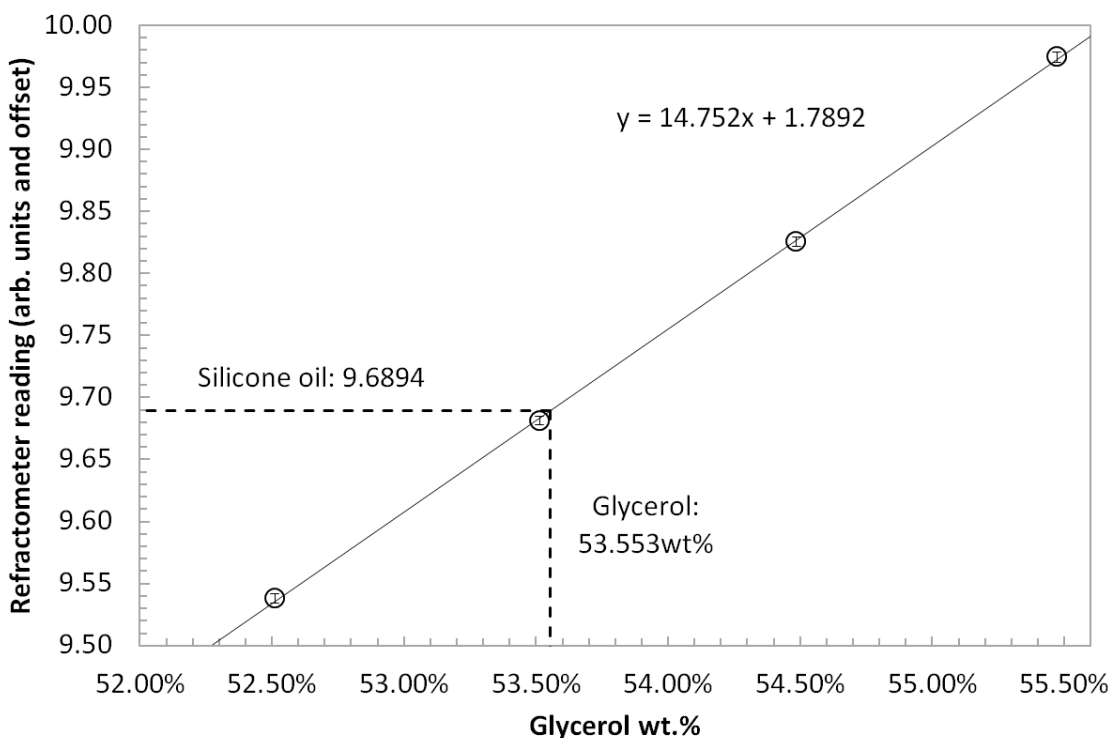
Figure 6.9: RI matching of a blend of glycerol / water to the Allcosil 200/50 silicone oil at 20.5 °C. Circular markers are centred on average values, error bars are 1 standard deviation, and the solid line is a linear fit to the data points shown.

We should note finally that for this liquid-liquid matching approach, aside from the ability for lab temperature variations to cause an index mismatch, many test fluids are also modestly birefringent. Simply, birefringence is a phenomenon where stresses cause two different refractive indexes to be exhibited by a test subject for light waves travelling in mutually

orthogonal polarisations, and the interference fringes ultimately result. Such fringes are commonly used to provide information on stresses in extensional rheological experiments, however in this case birefringence would serve to alter the effective refractive index of the fluid. Fortunately, this effect is quite small. For example, Talbott and Goddard (1979) studied birefringence in extensional flows of polyacrylamide (samples >$2x10^6$MW, 1.5 to 2.5wt% in 1:1wt glycerol water solutions) and reported birefringence values (the difference in refractive indexes caused by stress) not exceeding $2x10^{-5}$ with extension rates in their work around $1s^{-1}$. Haward et al. (2010) studied an aqueous $4.82x10^6$MW, 0.3wt% aqueous solution of PEO at extension rates $1500s^{-1}$ (much higher than attainable in this work) and report birefringence values also not exceeding $2x10^{-5}$. Performing an approximate linear conversion of the refractometer scale and assuming a birefringence of $2x10^{-5}$ gives a shift in indicated readings of the instrument of 0.002. This corresponds to a level of error at or below that attainable in the index match between the two liquid phases due to composition adjustment. If an error did occur, duplicate images of tracer particles would be expected in PIV image frames, this was not evident in experimental work in chapter 8. Similar considerations apply to the toughened glass walls used in chapter 7: when viewed under crossed polarisers they exhibited only one or two fringes in the channel viewing region.

Chapter 7.

Flow cell design, flow loop design, and optics

implementation.

Chapter 7: Flow cell design, flow loop design, and optics implementation.

7.1   Flow cell design

It was outlined in section 6.1, for the purposes of optics design, that a flow cell on a "meso" scale was desired, that could be readily sub-divided and reassembled to satisfy the need to coat the lower wall of the channel. At least the upper channel wall, to permit refractive index matching to oils, must be made from Perspex (section 6.3) and permit laser beam injection through it. In section 4.2 (vis figure 3.4 in chapter 3) it was highlighted that the use of glass sidewalls tends to produce a flatter meniscus, as a result the use of glass sidewalls would be preferable. Several modifications were made: for brevity figure 7.1 below shows the final variation of the design as used for experimental work in a partially assembled state, prior to capping, with coated surfaces flooded with water. Figure 7.2 and 7.3 show additional detail. Figure 7.4 shows a mechanical drawing (intended for indication only) of the salient dimensions.

The entire experimental setup has been designed and built by the author (with the exception of CNC cutting of the steel plates and the hyperbolic parts, and preparation of the glass plates). The liberty is taken here in briefly highlighting some of the more novel, interesting and unusual parts of the build and development process.
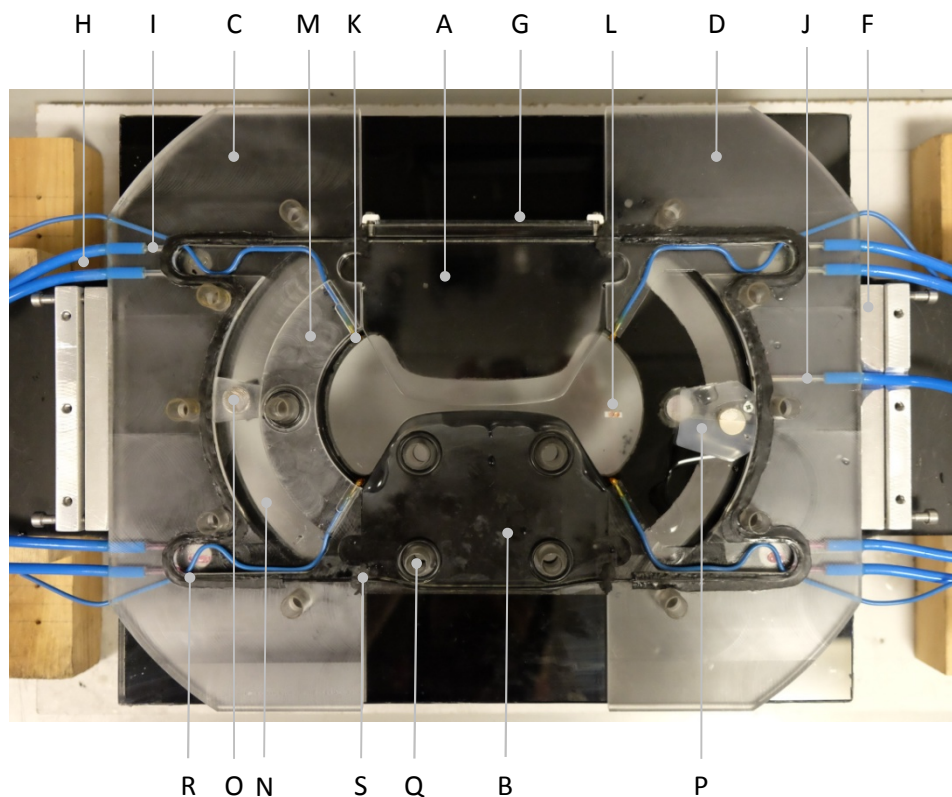
Figure 7.1: Partially assembled flow cell: see text for label descriptions.
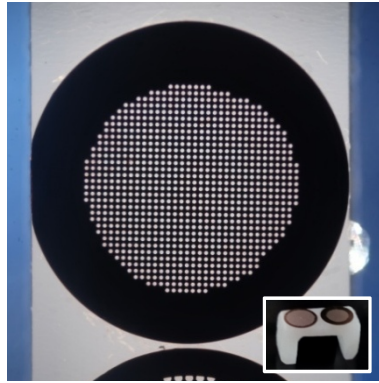
Figure 7.2 (left): AEI Calibration grid detail (inset: support)

Figure 7.3 (right): Outlet flow splitter detail (during manufacture)
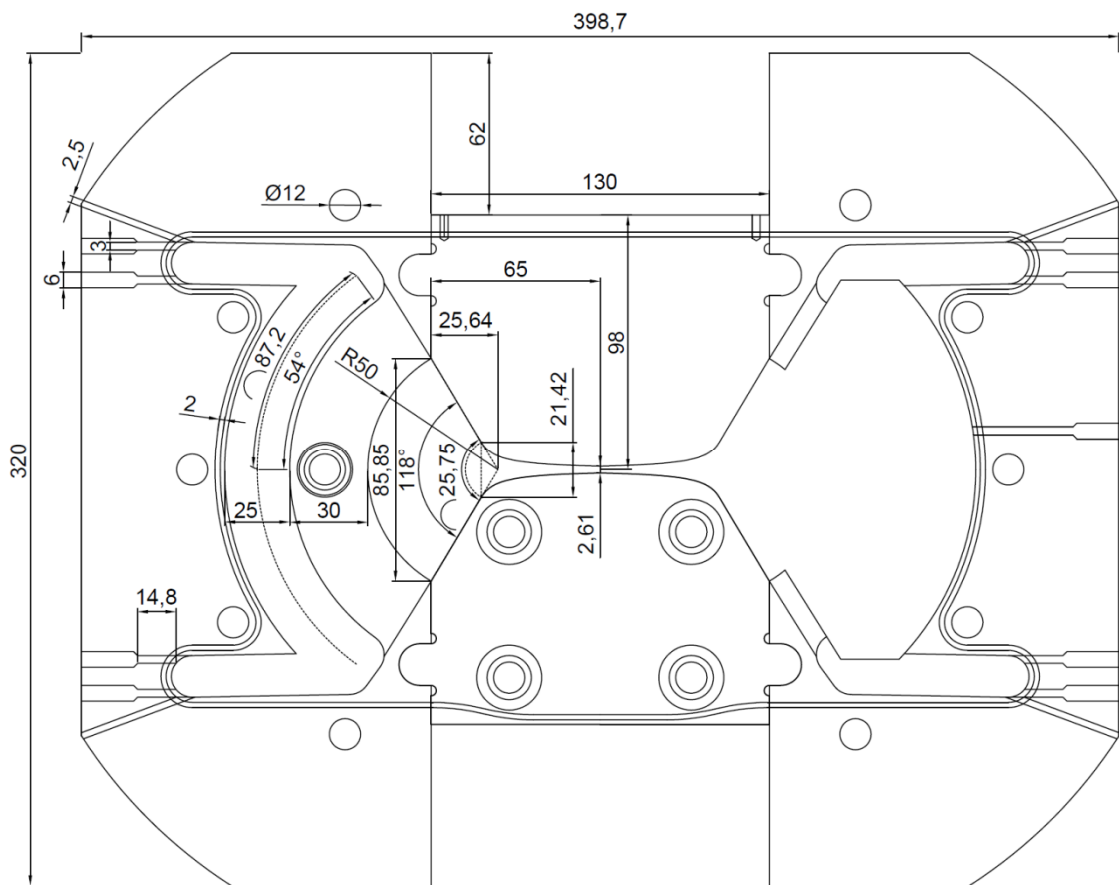
Figure 7.4: Key dimensions of flow cell (only the upper and lower channel walls and the inlet and outlet manifolds are shown, all other components are omitted). The four dashed lines show points of interest: the assumed length of flow along the manifold, the last circular flow front before the hyperbolic profile starts, similarly the last linear flow front, and the asymptote if the radial entrance section of the channel were extended to an infinitesimal point.

The cell is constructed as a "jigsaw" of four components: An upper channel wall (fig. 7.1.A, fully polished), a lower channel wall (fig. 7.1.B), the inlet manifold (fig. 7.1.C), and the outlet manifold (fig. 7.1.D). These are all Perspex, and are sandwiched between two glass plates, which are in turn backed by steel plates. The steel plates (e.g. fig. 7.1.E) feature viewing apertures and provide support and stress distribution. The entire assembly is held together with 15 through bolts, in addition to two lateral clamps (e.g. fig. 7.1.F) which serve to press the central cell components together. The cell can be disassembled and reassembled for modifications or thorough cleaning. When assembled, the flow passage, between the glass walls, has a width of about 8.4mm. The contraction features 118 degree inlets and exits, hyperbolic profiling, and a minimum channel height of 2.61mm. The walls start to taper at a vertical separation of 21.42mm. For vertical flow fronts this corresponds to a total Hencky strain at "constant" extension rate of 2.10, or based on circular flow fronts as introduced in chapter 5 and an initial span of 25.75mm, a total Hencky strain of 2.29. The laser beam enters through a glass window on top of the upper channel wall (fig. 7.1.G), coupled to the Perspex by the index-matched oil, and serves to alleviate scatter and laser damage to the face. The upper and lower channel walls are machine cut, processes such as laser cutting would leave birefringent stresses, potentially leading to future crazing, and cannot guarantee true 90 degree edges.

For the inlet and outlet of each phase, two ports are provided (e.g. fig. 7.1.H). The ports must clear o-ring grooves and narrow to 3mm diameter as a result (fig. 7.1.I). Upstream shear and pressure drop is kept to a minimum by using pair of ports, as well as proving flexible in use. An additional "drain" port on the outlet manifold (fig. 7.1.J) allows any stubborn fluid droplets to be removed separately. Four K-type thermocouples (e.g. fig. 7.1.K) are also installed in the channel, encapsulated in resin, one immediately before and after the contraction per phase. This permits redundancy, comparability (0.1°C is the limit for K-type resolution), and checks on the temperature of each phase in the measurement zone.

The inlet and outlet manifold contain a number of components. Firstly, near the outlet manifold is a set of two copper TEM grids on a 4.18mm high support, for length scale calibrations (fig. 7.1.L). The "table" form of the support permits transmission illumination, and the grids are secured by solvent-welding. The finer grid (Agar Scientific Athene AEI, 35µm holes at 75µm between centres, Agar Scientific Ltd. (2017)) is used predominantly in this work and is shown under conventional microscopy in figure 7.2 to prove the grid is not appreciably distorted. Secondly the inlet manifold contains a "slit" flow distributor (fig. 7.1.M). The inlet manifold has a width of 25mm, a depth of 6mm (bounded by Perspex at the rear face, fig.

7.1.N), and an arc length from the inlet to the channel centre of about 87mm over an angle of 54 degrees. The slit distributor causes the flow to pass through two parallel faces, spaced 2.4mm apart and over a flow length of 30mm. The dominance of pressure drop through the slit, compared to the inlet manifold, produces a reasonably even inlet flow distribution. Design was based on the relations of Bahrami et al. (2006) for pressure drop in the rectangular manifold, and equation 7.1 below (Pritchard, 2011) for pressure driven flow between infinite parallel plates as an approximation to the slit. The slit was subdivided into elements containing Q flowrate, by width increment W, $a = 0.0024m$ and $L = 0.03m$. Figure 7.5 below show the predicted relative velocities along angular position of the slit (ignoring the through bolt along the channel centreline). The interface is assumed to be at the channel centreline (e.g. zero degrees in the plot): the flow rate passing along the manifold (and thus pressure gradient) falls along the manifold length and eventually reaches zero at this location, hence the flattening of the profile towards this point. We can see that velocities are similar to within 25%, a compromise against increasing upstream shear and pressure drop, and the complexity of profiling the distributor. The velocity distribution is of course independent of the pressure drop across this system.

$$Q = W \frac{a^3 \Delta P}{12 \mu L} \tag{7.1}$$

(From Pritchard (2011))
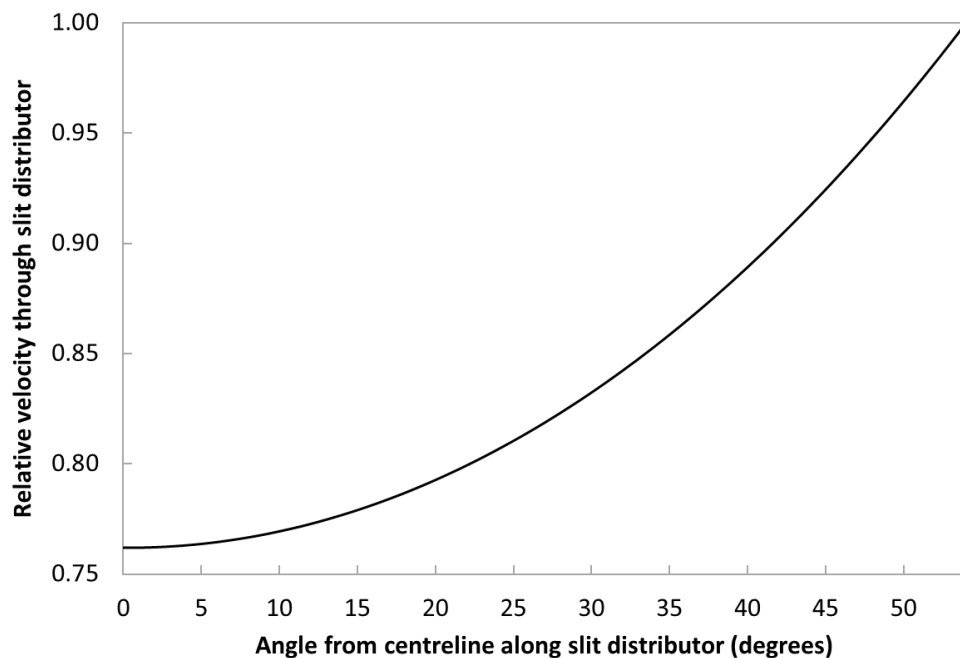
Figure 7.5: Velocity distribution along the inlet slit flow distributor

Thirdly, magnetically moveable baffles are provided in the manifold regions to aid in controlling phase combining and splitting. The inlet baffle (fig. 7.1.O) is plain Perspex, and proved inconsequential in practice, the flow adopting a well-defined and surprisingly flat interface. The outlet baffle (fig. 7.1.P) constitutes a pair of moveable side wall elements, and the entire lower half of the component (central block and side walls) are coated with the surface coating. The central block is dished where the flow impacts, a pointed profile (that shown in the enlarged image of figure 7.3) produced a situation akin to balancing the two phase interface on a knife edge. This splitter design was part of a two leaf strategy: the outlet manifold was originally symmetrical to the inlet manifold, with glass at the front and Perspex at the rear bounding the flow region, and figure 7.6 below shows this configuration under flow conditions for an aqueous PEO / Elite 65 – Synesstic 5 test system. The preferential wetting of the oil phase on the rear Perspex wall resulted in a persistent "stream" of oil (highlighted by the dashed lines), dragged by the increasingly high velocity aqueous phase, all the way to the aqueous outlet port. To address this (and simultaneously to removing a through-bolt through the middle of the flow field), the outlet region was converted to have glass walls on both sides (most important) and this flow splitter added to rigorously enforce the interface location (lesser importance). This issue could have been avoided by simply arranging for the channel to flare directly into a large volume of space, however this is inconvenient to arrange with the upstream planar flow cell design.
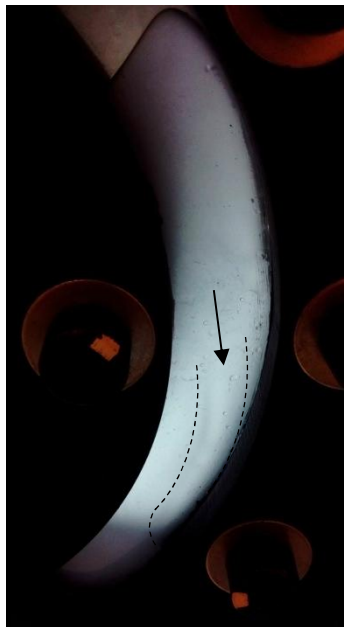
Figure 7.6: Oil phase being dragged to aqueous phase outlet port against the rear Perspex wall (highlighted by dashed lines). Note the interface level has been moved around prior to this image.

In terms of the side walls and sealing provisions, 10mm thick, low iron soda lime toughened glass was used. The substantial thickness was used on two grounds, if at the expense of increasing lens working distances. Firstly, predicting pressure drops for extensional flows is difficult, so an over-engineering approach was adopted: finite element computations in SolidWorks (Dassault Systems., 2012) suggested these windows, supported in the configuration shown, were useable in excess of 6 Bar gauge. Secondly, discussions with colleagues (MacInnes, 2015) underlined the issues of bolting and clamping such windows. Here, sleeving through bolts (e.g. fig. 7.1.Q) prevents metal-glass contact and recommended spacings from stress concentrations (holes, corners etc.) were observed. As neither the toughened glass plates nor the cut steel plates (not annealed) proved flat, the glass plates were bonded to the steel plates by a polyurethane resin (Electrolube UR5528), tough but flexible and conveniently absorbing stray light. A bath-like technique was used for bonding, shown in figure 7.7.

In addition to the issues of the supporting the uneven glass plates, they presented a challenge to seal. Forming a channel narrowest in the centre, and widest at the inlet/out manifold locations) the continuous o-ring that runs around both sides of the 4 central Perspex components failed to seal at the widest points. The solution involved firstly placing a sheet of paper on the lower glass wall, running a bead of commercial builder's silicone, following the path of the o-rings, then covering this with a second sheet of paper, followed by the upper glass wall. After a few hours, the upper wall was removed, and the silicone allowed to set. The paper serving as mould from which the silicone can be peeled (figure 7.8), as well as allowing permeability to the acetic acid vapours. These custom, "graduated" seals (fig 7.1.R), proved extremely successful even with several re-assemblies of the cell. Importantly, no fluid accumulated in the recess above the upper cell halve. Sealing between the manifold sections and the upper and lower cell halves was accomplished with high vacuum putty, applied on the contacting faces immediately below the path of the o-rings (fig. 7.1.S). This is forced out into gaps as the cell is clamped laterally.
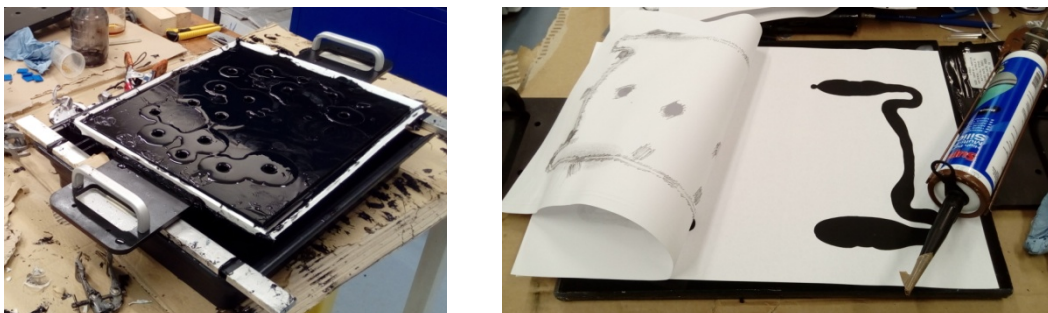
Figure 7.7 (left): Resin bonding process and figure 7.8 (right): production of custom graduated seals.

7.2   Flow loop design

Together with the flow cell, a means is required of pumping both the oil and aqueous test phases through it. The majority of the system adopted is shown in figure 7.9 below, with a full piping diagram in figure 7.10.

Accumulator air/vacuum manifolds

Pressure accumulators

Vacuum manifold

Pump power supply

Balancing gate/needle valves and output isolation ball valves

Cell drain output and valve

Fluid receiver flasks

Diaphragm pumps (x2 per

Dreshler flask to vacuum pump
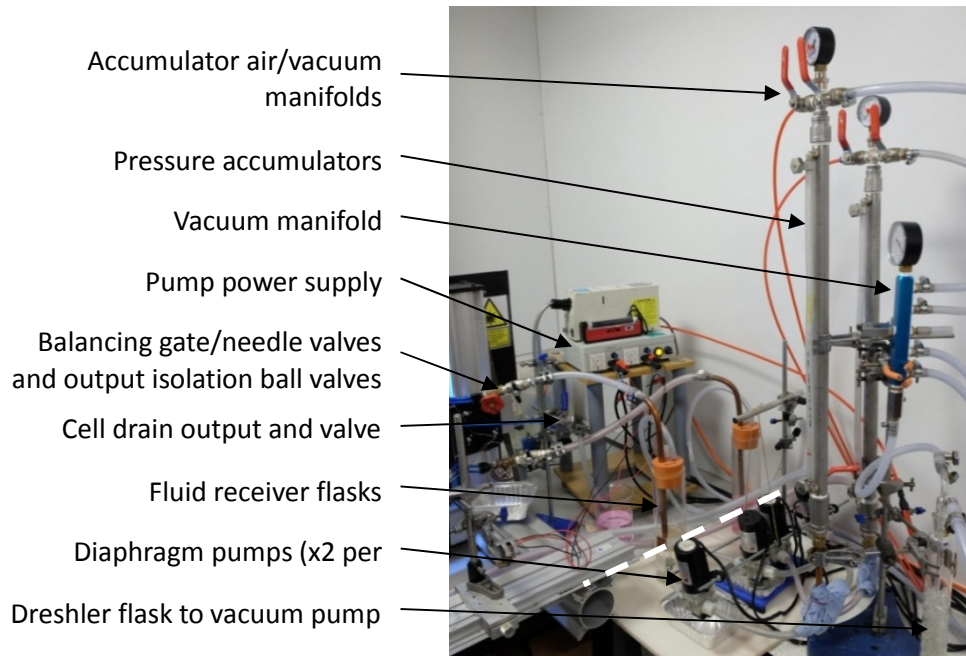
Figure 7.9: Flow loop pumping equipment photograph. Where relevant, labels point to components handling the oil phase and are analogous for components handling the aqueous phase. The white dashed line shows the split between the two independent bench sections (see section 7.4). The foil trays visible (used as drip pans) are in fact vital safety components.
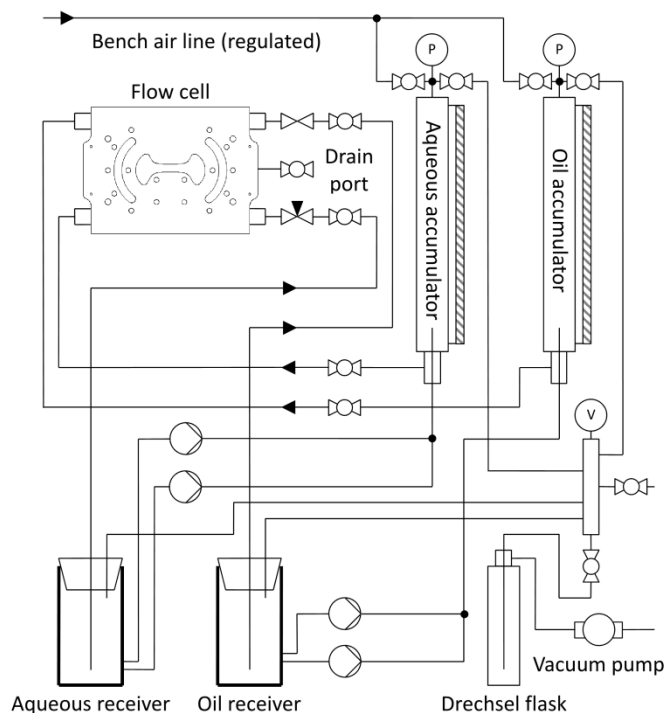
Figure 7.10: Piping and instrumentation diagram

This system features two independent flow loops, one for each phase, permitting long term operation of the experiment during data acquisition. A pair of low voltage positive displacement diagram pumps per phase (Model PLD-1205 and PLD-1206, Pulandi Mechanical and Electrical Equipment Co. Ltd) are suited to handling appreciable pressure drops and complex dynamics of the viscous, non-Newtonian fluids under study, and have the advantage of not damaging solid tracer particles suspended in the flow. Variable flow rate was achieved by electronic PWM (pulse width modulation) control. In later chapters, replacing one pump with a restricted bypass loop was used to achieve low - but still stable - flow rates. The oscillating outputs of these pumps are smoothed by pressure accumulators. Appropriate instrumenting is provided, and air-lines provide a convenient method to shift fluid levels contained within and rapidly flush liquids out during cleaning. The operation of the pressure accumulators requires a surplus volume of fluid within the loops, which is permitted in receivers. The receivers, and to a lesser extent the accumulators, also provide locations for droplets of the opposite phase and bubbles to settle out. The input pipes extend internally higher than the outlet ports of the accumulators as shown in figure 7.10, forcing liquid to flow in the direction of the free liquid surface. Those in the receivers are located as far as practicable from the outlet ports, and deliberately extend under the free surface. Filling of any piping system inevitably introduces bubbles (a hazard to the camera), and the entire system can be in-situ degassed by applying vacuum to the top of both the accumulators and receivers simultaneously via suitable valving (a dreshler flask protects the vacuum pump). The vacuum system also provides a convenient means of pump priming. Shut-off valves and push fit connectors permit the disconnection and reconnection of the flow cell from the piping system. In keeping with minimising upstream shear, pressure drops, and erasing flow history, upstream pipe runs are long and large diameter. The flow history between the aqueous phase accumulators and the inlet manifold is 196cm of 12.5mm ID pipe, followed by 2x 8cm lengths of 4mm ID pipe, then finally narrowing to 2x ~15mm lengths at 3mm ID (as mentioned previously, also see figure 7.1) before reaching the manifold.

Downstream of the flow cell, in addition to shut-off valves, a gate valve on the oil phase and a needle valve on the aqueous phase are provided. The total flow of the two phases entering the flow cell must balance the total leaving, but it is not necessarily the case that that the ratios are equal. Continuous adjustment of the needle valve is required keep the interface in the correct location downstream in the flow cell. This must be done throughout the experiment – so important is this that a webcam was used to keep check remotely. Automatic image recognition and valve control may be desirable in future work, if it can be made sufficiently reliable, as noted in chapter 9.

In terms of quantifying flowrates, as noted in chapter 2 there exists no easy solution for fluids of different or rheologically variable viscosity: the only option is to collect a timed mass sample from that returning to the receivers, at risk of disturbing the balanced outflows and introducing bubbles with the current configuration. Furthermore, for work in section 8.1 and 8.2, knowledge of the flow rate is immaterial as only the velocity profiles themselves are of interest. However, in section 8.3 it is needed to estimate transit times, and timed sampling is performed.

7.3   Laser illumination and synchronisation

As in any other traditional PIV based experiment, illumination is provided by a double cavity Nd:YAG laser (Solo 1 15Hz, New Wave Research Fremont, CA). This is synchronised to a cooled sensor, high dynamic range camera (PCO.1600, PCO AG, Germany), with the ability to capture two frames in a "double shutter" mode with a very low minimum interframing time. Captured images are buffered in onboard RAM in a ring-buffer until being read out. This arrangement permits two images (now referred to as an "image pair") to be taken with interframe times easily less than 1 microsecond, at an overall image pair frame rate of nominally 2Hz. Synchronisation of the whole system is controlled by a Mini-Sync PIV synchroniser (ILA GmbH, Germany). The power of the laser pulses are controlled in the usual fashion by varying the time between firing a laser cavity flash lamp and operating the cavity Q-switch. This is adjusted at each imaging location (minor variations in coupling and illumination distribution) to provide as near as comparable illumination intensity between each image in a pair (improving cross correlation) and to keep sensor saturation to a minimum.

In terms of exposure and laser synchronisation, the system is typical of any other PIV experiment and described here for reference. The start of the first camera image exposure is triggered from the synchroniser, as shown in figure 7.11 (digital oscilloscope screenshot). For this particular camera it is necessary to align the first laser pulse (rising edge of Q switch 1 signal to laser) to fall in the first exposure window of the camera, and the second laser pulse (Q switch 2) to fall in the second exposure window of the camera. The second exposure is the period after the first exposure has finished and the interframing time (120ns) has elapsed, but before the end of the camera "busy" pulse. In this manner, the laser pulse delay, and not the camera exposure timing, controls the delay between images in an image pair. Adjusting delay and exposure settings on both the PIV synchroniser and the camera permit this alignment to be achieved.
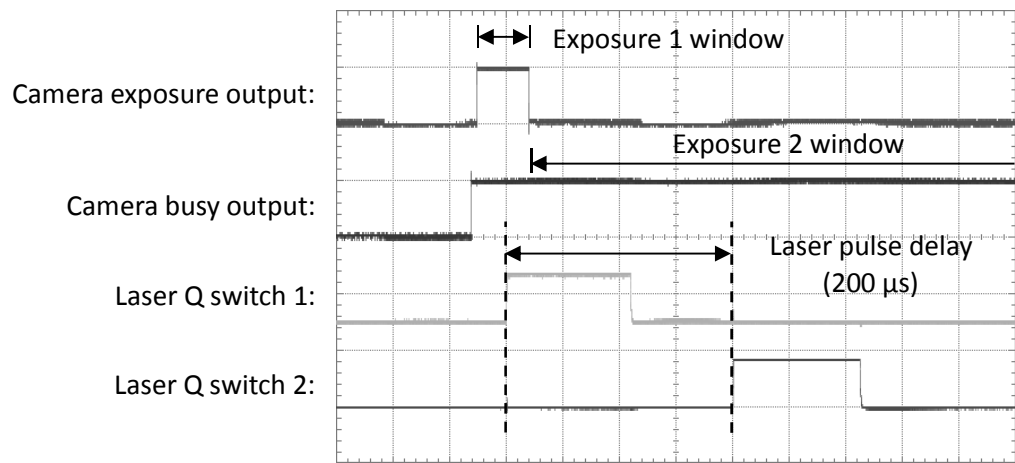
Figure 7.11: Oscilloscope screenshot of laser and camera synchronisation. 50µs per horizontal division, 5V per vertical division, shown here with a 200 µs laser pulse delay.

When cross-correlation is applied to image pairs, as in chapter 8, displacements of about 3-5 pixels are optimum for a 32x32 pixel grid (Beeston, 2016). The rapid acceleration of flow down the channel means initial estimates of appropriate pulse pair delay times must be established, and the synchronisation thus realigned, for each channel imaging location. Assuming velocities to increase in proportion to the reciprocal of the channel height proved quite accurate. This need to adjust timings and some tendencies for timing alignment to shift with variations in laser power made an on-line oscilloscope essential.

In the configuration adopted, as illustrated in figure 7.12 during alignment, the laser output is directed vertically upwards. The beam bounces of a pair of Nd:YAG rated laser mirrors on kinematic mounts, the first mirror sending the beam horizontally, and the second mirror then down vertically through the glass laser insertion window of the flow cell. The second mirror is attached at 45 degrees on a rotary stage (on top of the kinematic mount) to permit beam sweeping up and down the length of the flow cell. The entire of the second mirror assembly can be moved on a translation stage to permit sweeping of the beam across the width of the cell.
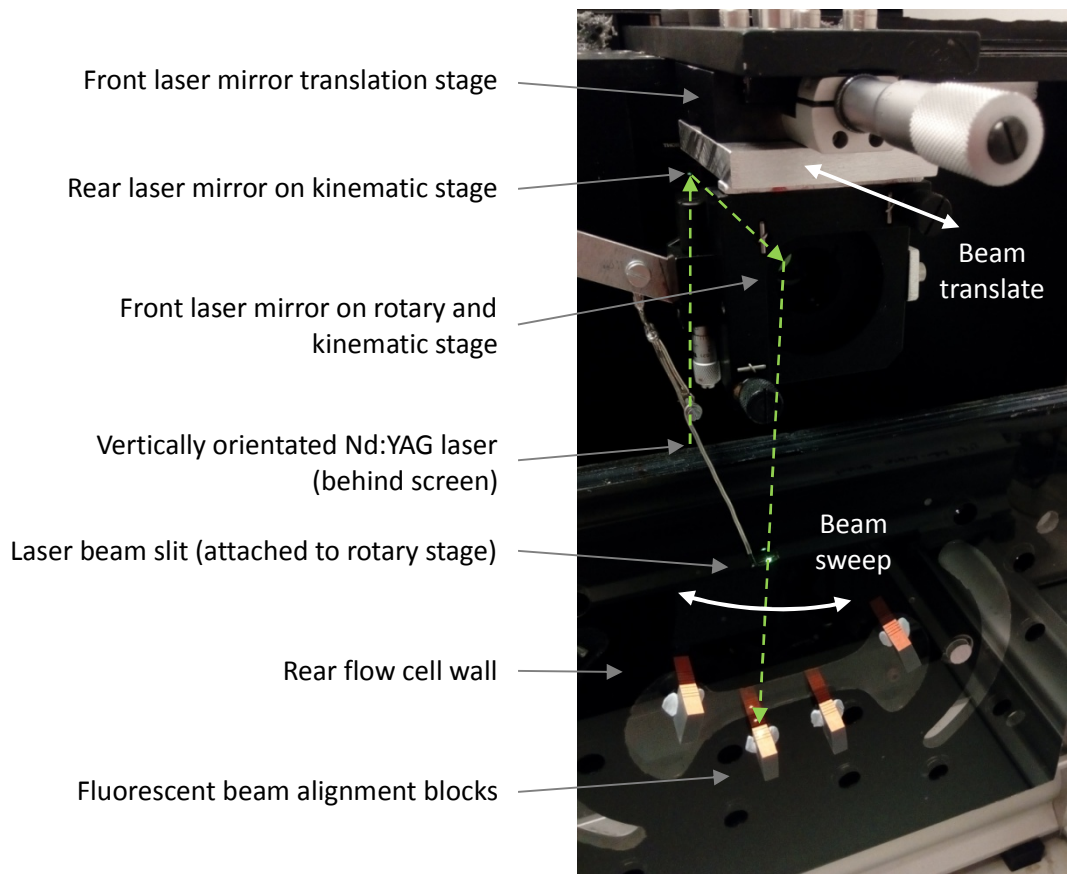
Figure 7.12: Laser illumination configuration and cell alignment process.

Preliminary laser alignment and beam tracking was conducted before the flow cell was assembled, under minimal laser power. Right angled blocks with fluorescent scales denoting the channel centreline are placed at key locations on the rear cell wall. Mirrors and the positioning of the slit are then adjusted accordingly. Loading from bolting the flow cell together is expected to produce a slight shift in this alignment. However, as the focal plane is selected by the imaging lens as previously noted, it is more appropriate to simply rely on this as a "guide", and fine tune the beam positioning for the best image quality across both frames in an image pair.

Despite a laser service and beam overlapping realignment, the alignment - and more particularly the focusing - of the two laser cavities was found to be quite poor, even if use in a beam as opposed to expanded sheet configuration is unusual. The rotating mirror has the added complication of optically rotating beam misalignment. Images typical of pulses from the two laser cavities are shown in figure 7.13, the spacing between two lines on the fluorescent marker being 2.08mm. Different configurations of focussing optics were tried, "configuration 1" was the best found and "configuration 2" an example poorer, non-overlapping configuration. Some configurations produced offsets of millimetres between the illuminated regions.

Correctly aligned beams would be expected to produce no difference, irrespective of laser output optics.
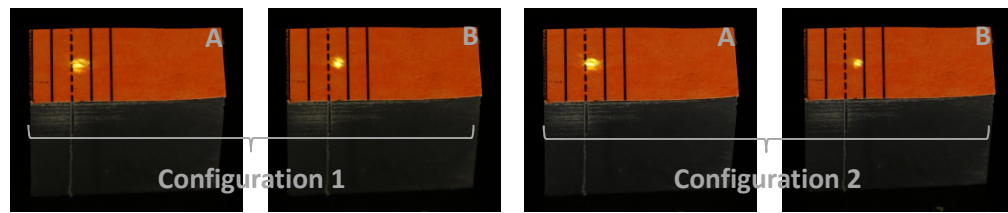
Figure 7.13: Laser beam comparison: cavity A ("A") and cavity B ("B").

To clean up the more defocused beam of figure cavity A, a 0.5mm width slit was incorporated, attached to the rotary stage, and placed as close to the imaging zone as practicable as visible in figure 7.12. The slit width was determined in accordance with the optimum pinhole size as described by Young (1989) with f = 120mm, from slit to cell centreline and λ = 532nm. Such a slit has the disadvantage of limiting how far the beam can be swept from the cell centreline, here to about 1.5mm either side in practice. An upstream "roughing" slit, followed by a fine slit, might permit more flexibility in future work.

7.4   Imaging system configuration

Imaging of the flow field is conducted with an infinity-corrected Edmund optics LWD x10 objective lens (P/N 59-877). This lens permits a wide aperture and a sufficiently long working distance (33.5mm in air) to permit viewing through the glass wall as well as avoiding the steel support plates of the flow cell when imaging obliquely. Rays are brought into focus on the camera sensor by an appropriate 200mm PCX lens (P/N 48-241) situated inside the black enclosure, a PCX lens being optimum for monochromatic light used here. An interchangeable filter card is provided (here, just in front of the sensor, due to certain mechanical restrictions in infinity-space) for fluorescence work in section 7.5. The entire setup is mounted on a X95 based railing and staging system, as shown in figure 7.14 for the oblique (wall-oil) and perpendicular (liquid-liquid) imaging approaches. The lens system can be slid along the flow direction, with a micrometer translation stage being later swapped for a digital scale for accurate X position readout. A second translation stage at 90 degrees permits focussing, and Y height is adjusted with a scissor stag) augmented with a digital micrometer. Note that whilst robust, the scissor stage is certainly not rigid, and even though the lens system was balanced across this stage small variations in tilt produce large shifts in the true vertical lens position, compared to that indicated on the digital micrometer. Measured values are for coarse "position indication" only, and accuracy falls far short of the high precision micrometer. Angular alignment in both cases, and both horizontally and vertically, was performed by a large 60-30

degree protractor, placed against several points on the front of the flow cell. The webcam monitoring the cell outflow condition is also mounted on this railing setup.

Enclosed laser mirrors

Flow cell

Objective and correction prism (section 7.5)

Horizontal translation stage

Focusing translation stage

Horizontal rail and sled

Two-phase outflow remote viewing webcam

Imaging camera and filter card

Vertical digital micrometer and scissor

Horizontal digital scale
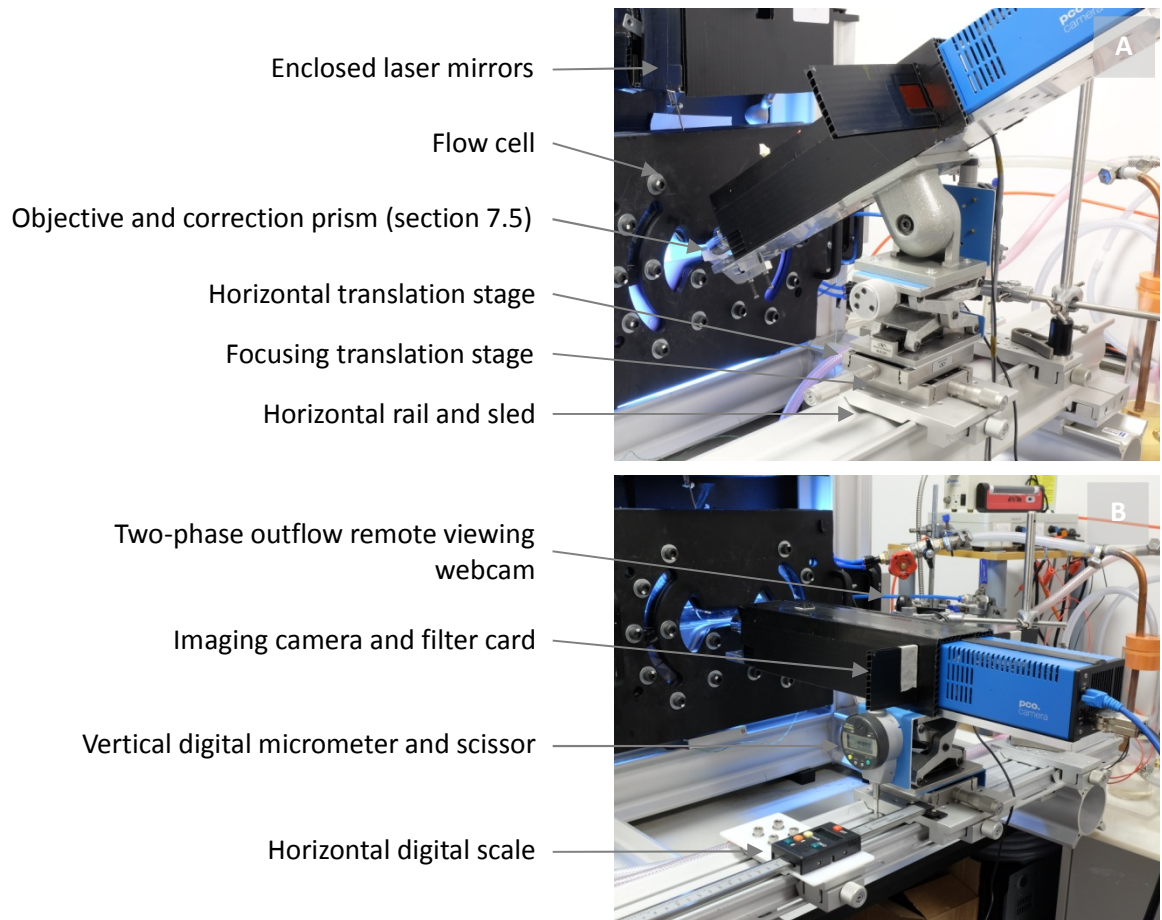
Figure 7.14a and figure 7.14b: Oblique and perpendicular imaging configurations respectfully. Labels between figures A and B are analogous.

Due to the rigidity issues of the scissor stage and the long lens-camera setup, this system is particularly sensitive to vibration, especially in the vertical direction. The diaphragm pumps also generate a significant amount of vibration. As highlighted in figure 7.9 previously, the entire pumping system is located on a mechanically separate worktop to the flow cell and PIV system, with the only coupled vibration being that through the pipes themselves. The pumps are also hung in mid-air, and the flow cell railing system sat on rubber blocks. The cooling fan for the camera Peltier stack generated a finite but practically insignificant amount of vibration.

7.5   Analysis of optics for oblique imaging and correction prism requirement

Early work to evaluate oblique imaging was conducted with a long working distance inspection objective. Here, the Navitar lens from section 4.4 was used with the PCO.1600 camera, the lens being set at maximum zoom, maximum aperture, and minimum focal length. This lens features a significantly longer working length and reduced aperture compared to the main 10x LWD objective (see table 7.4 later). This work showed oblique imaging to be substantially more

complex than simply pointing a lens system at an angle through a transparent wall. Three sets of sample images are shown below for a low seeding density solution of 5µm polyamide particles (Dantec Dynamics PSP-5); glycerol being used to slow settling and to provide a representative refractive index. The solution is contained within a Hellma 110-OS precision 10mm cuvette roughly simulating the 8.36mm width of the main channel, but with a thinner wall (1.25mm per window). Illumination is provided by a white LED torch to avoid scintillation associated with laser sources. Viewing path lengths are reported as "horizontal" since the lens is tracked horizontally through the width of the cell, similarly to the setup in figure 7.14a, rather than being translated on-axis. Tilt angles are relative to the horizontal (cell wall normal), and measured by a plumb line and protractor to ± 1 degrees. Table 7.1 shows increasing angles of tilt at the same path length. Table 7.2 shows increasing path lengths at the same angle of tilt. Table 7.3 shows the effect of moving the position of the focal plane, whilst keeping the same tilt angle and (roughly) the same path length. Original 1600x1200 pixel images are cropped by a standard factor for presentation.

| 0 Degrees tilt | 10 Degrees tilt | 20 Degrees tilt | 30 Degrees tilt |

Table 7.1: Effects of varying lens tilt angle at a horizontal liquid path length of 4.18mm. Image width ~1.2mm.

| 0mm horizontal liquid path length | 1.4mm horizontal liquid path length | 2.8mm horizontal liquid path length | 4.2mm horizontal liquid path length |

Table 7.2: Effects of varying liquid path length at a lens tilt angle of 30 degrees. Distances are from the nearest inner cuvette wall. Image width ~1.2mm.

-0.5mm Horizontal lens shift	-0.2mm Horizontal lens shift	+0.1mm Horizontal lens shift	+0.4mm Horizontal lens shift

Table 7.3: Distortion artefacts as the lens system focus is tracked through the sample at 30 degrees tilt (the circle highlights a particular tracer particle). Distances are relative to 4.18mm from the nearest inner cuvette wall. Image width shown here is 1.2mm.

From table 7.1, we can see that as tilt angle is increased, optical aberrations become increasingly severe. Closing the lens aperture at 30 degrees of tilt restored the image quality to a condition similar to that without tilt, but of course with a deep depth of field. For the much larger aperture x10 microscope objective, we would thus expect far greater distortion, and unusable images at the required angles of tilt, even without considering imaging through a liquid-liquid interface. From table 7.2, we also see that these distortions are a function of the optical path length through the cell, and thus likely due to refractive effects of light rays off centre from the lens aperture. Table 7.3 shows the complexity of the distortion artefacts. As the "focal plane" is moved front to back, relative to a particle, the particle image transitions from a horizontal line, to a distorted "blob", to a vertical line. Also note the distances compared to the stated depth of focus in air for this lens (0.1mm). These distortions are particularly unfortunate, particularly for automatic PIV cross correlation. Firstly, this means the intensity falloff with distance from the focal plane is likely to be slower than if defocused particles took a circular form, thereby serving to increase the depth of "visible" particles. Secondly, the PIV processing assumes that a coordinate shift in a point of light correspond to those of a coordinate shift in a tracer particle. These bright defocused (vertical) lines would cause "ghosting" of the real position of tracer particles across the shear field.

In order to investigate this issue, a geometric ray tracing exercise was conducted. Consider a microscope lens in an ideal environment, focussed on a subject perpendicular to the lens front in air. Rays of light pass from each point on the subject to the frontal lens element, at every point across this element surface. The rest of the lens and optics system then brings them to focus downstream on a camera sensor (or similar). The angles that these rays make with the

190

frontal element are therefore what is required to form a high quality image, regardless of the rest of the lens optics. We can follow these rays in reverse, from the lens, through intermediate mediums, to see how the focussing of rays is being affected. Table 7.4 below summarises the characteristics of the lenses considered. For this modelling, we must also know the shape of the outer frontal surface of the lens. From inspecting both lenses and given their relative working distances, the frontal elements are assumed to be flat.

Lens	Navitar Zoom 6000 system (max aperture and magnification)	Edmund Optics x10 LWD lens
Source	Navitar (2017)	Edmund Optics Ltd. (2016a)
Working distance	92mm	33.5mm
Magnification (as specified)	4.5x	10x
Physical frontal element diameter (measured)	14mm	23mm
Numerical aperture	0.071	0.28
Utilised frontal element diameter	13mm	19.5mm
Depth of focus in air (as specified)	100µm	3.6µm

Table 7.4: Key lens parameters

Calculations were set up in Excel based on Snell's law (equation 7.2). n_1 and n_2 are the refractive indexes of two materials either side of a interface, θ_1 and θ_2 are the angles the rays make relative to the surface normal, respectfully. Rays are then propagated through the series of refractive index boundaries in turn.

$$n_1 \sin \theta_1 = n_2 \sin \theta_2 \qquad\qquad (\,7.2\,)$$

To start with, we consider the Navitar lens in a level configuration without tilt looking at a point at the centre of the field of view. Three rays are traced to the front element from an "imaginary" focal point in air, one to the lens centreline (red) and the other two to the element peripheries (blue). Rays at different points across the field of view were also considered, but negligibly differ from those presented here. These rays are then projected back out and traced through air (n = 1), the cuvette cell wall (1.25mm thick window, n = 1.523), and through the glycerol (taken to be n = 1.474). This is conducted for both the vertical plane in which the tilt is orientated and the horizontal plane, i.e. looking down on the lens system from above, and the results shown in figure 7.15. The rays in the horizontal plane use X axis intersect locations from the vertical plane data (for both interfaces and the line marking 4.18mm) since refraction vertically shifts where they intersect horizontally: i.e. the red ray in the horizontal data is physically same ray as in the vertical data, and must follow an equivalent horizontal plane

(horizontal distances still represent those on the axis of the lens, and are not re-aligned). In all plots subsequently presented, the position of cuvette (or cell) wall has been adjusted to place the focal point of the rays on the horizontal plane (i.e. where the rays intersect) at 4.18mm, measured perpendicular from the inner cell wall. This is shown by the red dashed line. Figure 7.16 then shows the same arrangement, but with 30 degrees of tilt.
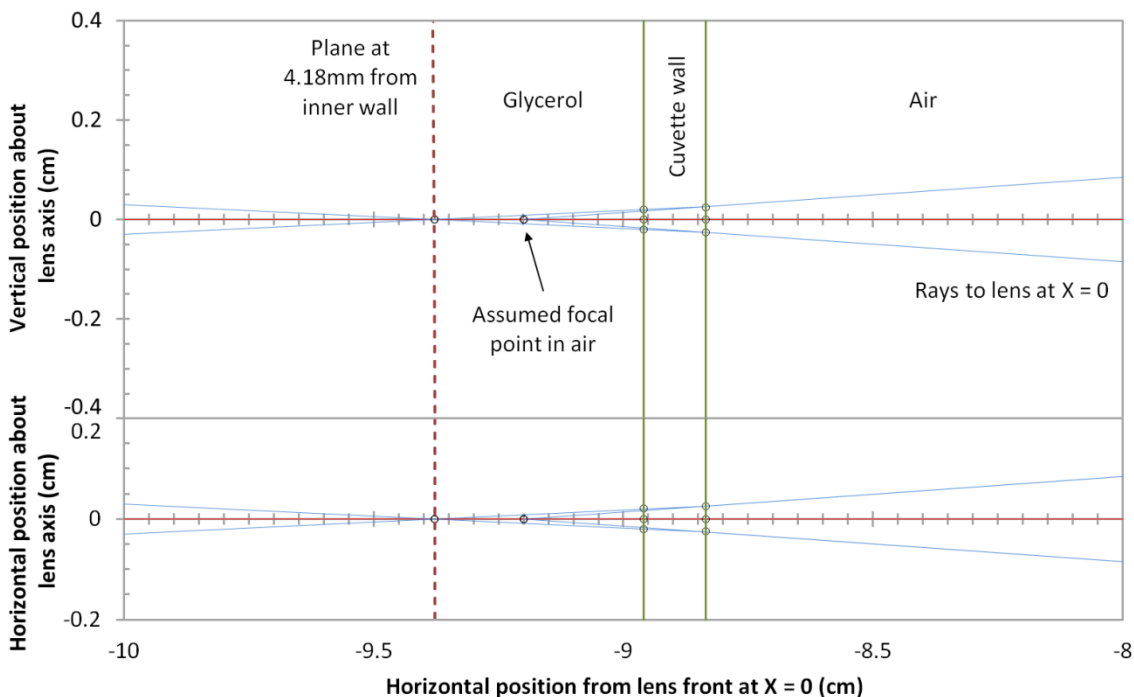
Figure 7.15: Ray tracing of the Navitar lens system and cuvette, with 0 degrees of lens tilt.
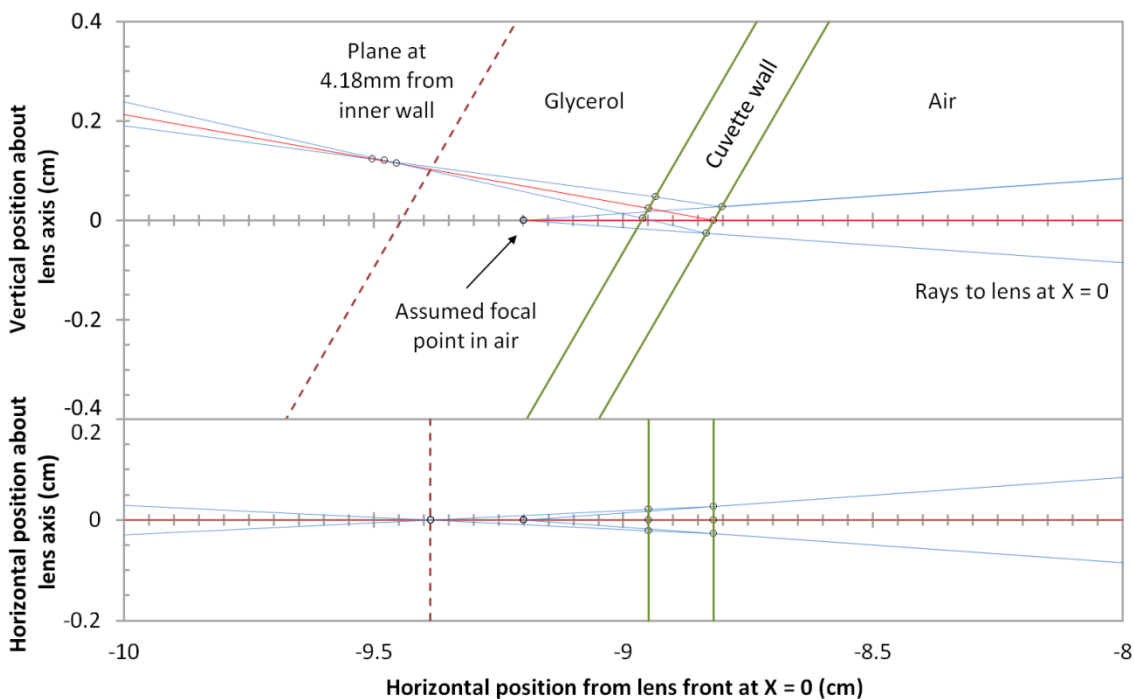
Figure 7.16: Ray tracing of the Navitar lens system and cuvette, with 30 degrees of lens tilt.

In figure 7.15 without lens tilt, we can see a situation which would be reasonably expected. The focal position for rays on both the horizontal and vertical planes has moved from that in air (i.e. the "imaginary" microscopy target) due to the incorporation of different refractive index materials in the viewing path. However, the focal positions in both cases remain well defined and they fall at same location as each other. In figure 7.16 with 30 degrees of tilt however, the rays in the vertical plane no longer form a well-defined focal point, and secondly, the average location of the focal point that they do form falls at a different location than that of the horizontal rays.

This formation of two focal points is the reason why the transition in artefact shape can be seen in table 7.3. This effect is referred to as astigmatism and is usually caused when a misshapen lens has different focal lengths for rays on the horizontal and vertical planes. In the situation in table 7.3, and as illustrated in figure 7.17 below, moving the lens towards a particle places rays in the horizontal plane in focus, and the rays in the vertical plane out of focus, hence particles appearing as "out of focus" lines in the vertical direction. Moving the lens towards a particle produces the converse situation, with no well-focussed point existing between the two. Figure 7.16 shows an offset of about 0.1mm, which a similar magnitude and in the correct direction of that observed in table 7.3 but of an apparently smaller value.
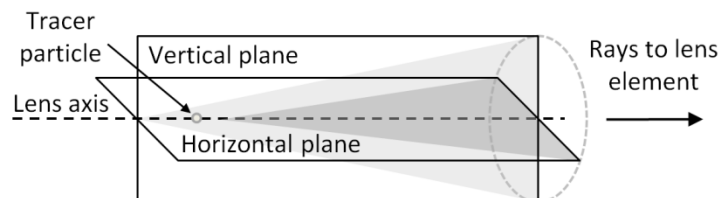
Figure 7.17: Definition of astigmatism (shown here with rays in the vertical plane having a longer focal length than those in the horizontal plane, as per figure 7.16)

In stereoscopic PIV were oblique imaging is used, it is commonplace to include "water prisms" (thin walled triangular tanks) on the side of water filled test-channels to mitigate distortions. These tanks provide a flat surface through which a viewing lens can image as well as an equal refractive index medium as the rest of the test fluid, essentially eliminating astigmatism. This was first suggested by Prasad and Jensen (1995) and later referred to in an associated review (Prasad, 2000). Astigmatism is not mentioned in the former reference, but it is discussed at length around that time by groups such as Zhang and Eisele (1995) with regards to LDA measurements. A photograph of stereoscopic PIV setup incorporating such prisms can be seen in fig. 5.97 of Tropea et al. (2007). Here, a slightly different route to liquid prisms on account of the experimental scale was adopted: a glass Littrow dispersion prism (Edmund Optics P/N 43-

649) with a 30 degree corner, reduced in size for use with the channel viewing apertures. The ideal solution in terms of optics, at least for imaging a single oil phase, would have been to use a Perspex prism with a Perspex channel side walls, which when combined with the index matched oil, yields an equal refractive index path all the way through to the observation area of interest. Whilst Perspex prisms with 30 degree corners are not readily available, such a prism could be machined to any desired angle and polished. There is little choice of angles with commercial glass prisms (excluding Risley pairs, for example) and Littrow prisms are the only convenient option around 30 degrees, however they are precision manufactured. Furthermore, it is possible to show that given the use of glass side walls (which here accommodate twice the viewing path than the oil phase), better optical performance is in fact attained with the use of a glass prism rather than an equivalent Perspex prism.

We now move to modelling the actual setup used in practice. This consists of the thick-walled flow cell (10mm wall thickness, low iron soda lime glass, n = 1.5261 at 532nm) in conjunction with the x10 microscope objective inclined at 30 degrees. The oil phase is now simulated, with a refractive index taken as equal to the average for Perspex previously estimated (1.4941). Figure 7.18 shows the lens system tilted at 30 degrees without a correction prism for comparison, and figure 7.19 shows the 30 degree glass prism (N-BK7 at 532nm: n = 1.5195) situated flush to the cell wall (mechanically the most straightforward configuration). Five light rays are modelled here rather than the three previously. Refractive indexes for glasses are taken from sources in Polyanskiy (2016). Though the prism now provides a face normal to the lens, a 30 degree lens tilt, one readily controllable parameter, may not be strictly optimum on account of the index difference between the oil/wall/prism. 30 Degrees of lens tilt is however simulated here for simplicity. Due to the large lens aperture, even though the lens is tilted above 27.1 degree limit as discussed in section 6.3, rays now enter the lens at angles substantially both above and below this angle. Rays much below the axis of the lens rapidly approach and pass the inclination limit. As a result, we "blank off" the lower half of the lens aperture in the vertical plane, and use rays distributed only between the centreline and the uppermost utilised edge of the frontal element. The red ray still falls along the lens centreline and is still used to dictate the locations where rays in the horizontal plane cross through interfaces.

As can be clearly seen in figure 7.18, without any form of correction, the amount of astigmatism as well as the lack of a clearly defined focal point for the rays in the vertical plane is much more severe for this larger aperture system, as expected. We can also see from figure 7.18 that this system is also suffering from spherical aberration and coma. Spherical aberration

is where rays at different radial positions across a lens have different focal lengths, visible in the inset image for the horizontal focal plane. This is caused by imaging through the substantial wall thickness, and serves to increase the lens's practical depth of focus beyond that in air. Expensive objectives with "correction collars" for use with cover slips correct for such aberration. A ray pattern resembling coma is visible for rays in the vertical plane, where they cross one another at different locations (i.e. why a clear focal point in the ray tracing is no longer evident). Such aberration normally results from an imaging axis being misaligned with a lens axis; nonetheless coma artefacts (the bright heads of vertically distorted particles, resembling comets and their associated tails) can be clearly seen for the Navitar lens in table 7.3. The inclusion of the prism in figure 7.19 dramatically improves the situation, corresponding real world imagery from this scenario is presented in figure 8.1 in the following chapter. The rays in the vertical plane very nearly form a well-defined focal point, which also aligns with the focal point in the horizontal plane, despite the large lens aperture and slight variations in refractive index between different mediums.
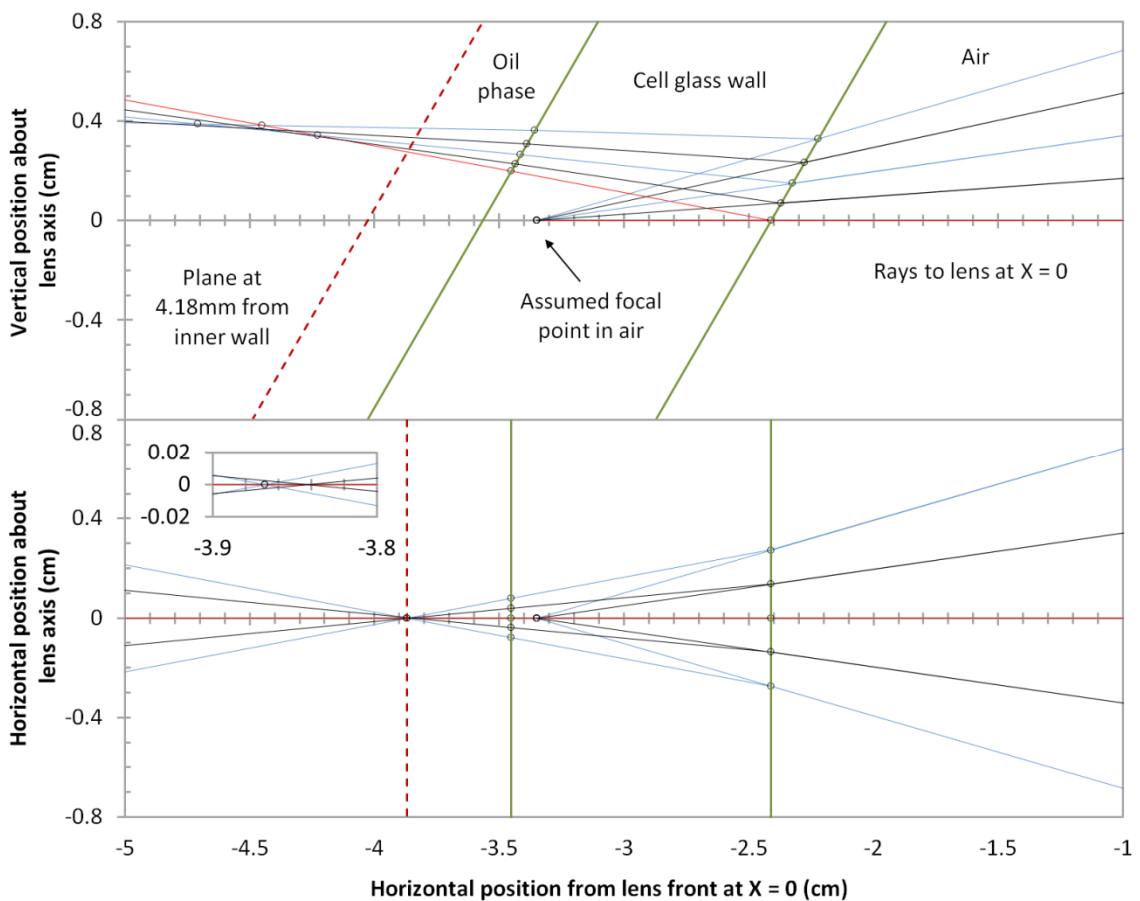
Figure 7.18: Ray tracing of the x10 lens system and flow cell: 30 degrees of lens tilt, no corrective prism, and a single fluid phase. Inset shows detail of the focal point in the horizontal plane.
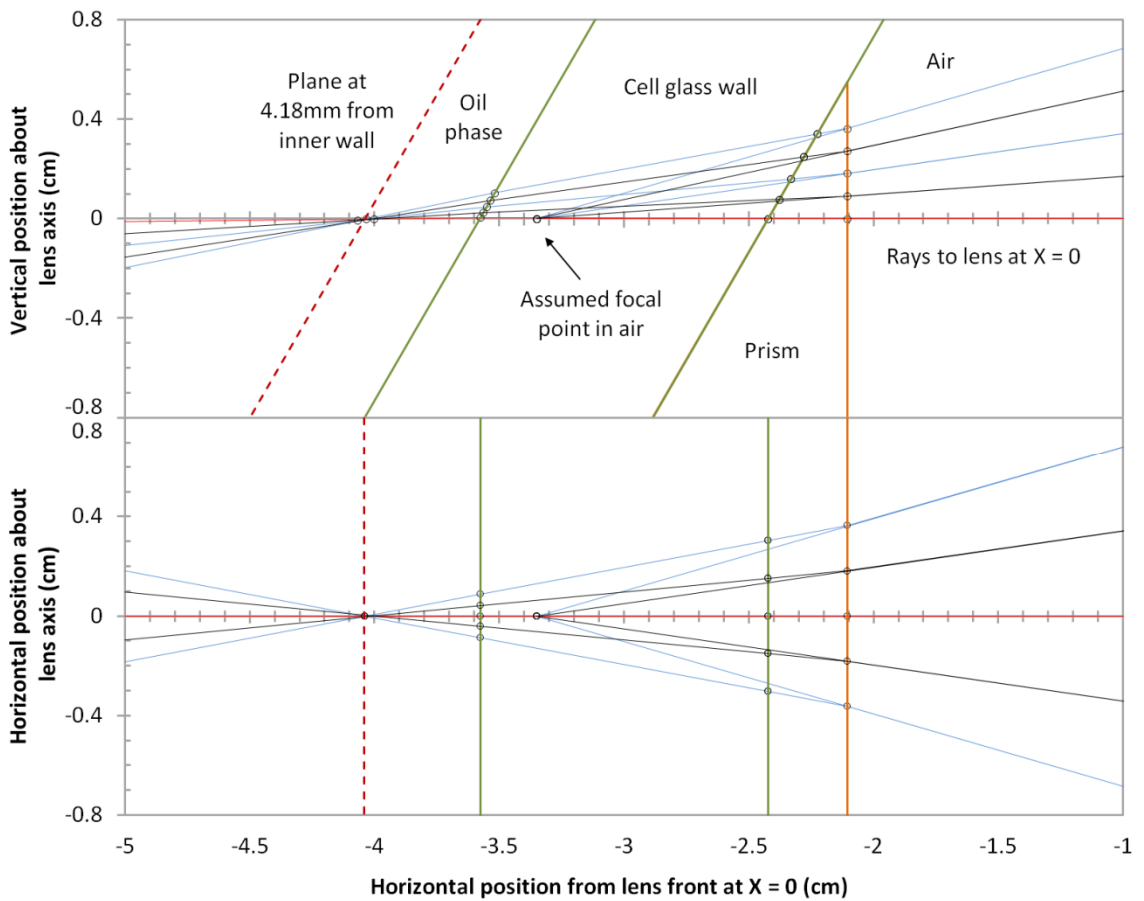
Figure 7.19: Ray tracing of the x10 lens system and flow cell: 30 degrees of lens tilt, with a corrective prism, and a single fluid phase.

The major issues begin when we next consider that we also need to image below the interface: a second obliquely orientated interface which further alters the path of light rays. Here for simplicity the aqueous phase is assumed to have a refractive index equal to that of water (n = 1.333 used here). Figure 7.20 shows the exact same situation as that in figure 7.19, except an interface has been added a small distance above (in terms of cell orientation) where the previous focal position was and the system translated to keep the horizontal focal plane on the cell centreline: this situation closely corresponds to figure 8.3 in the following chapter. The distortions are evident in figure 7.20. It is thus clearly impossible, with one optical configuration, to perfectly satisfy the requirement of simultaneously imaging regions both above and below the interface.
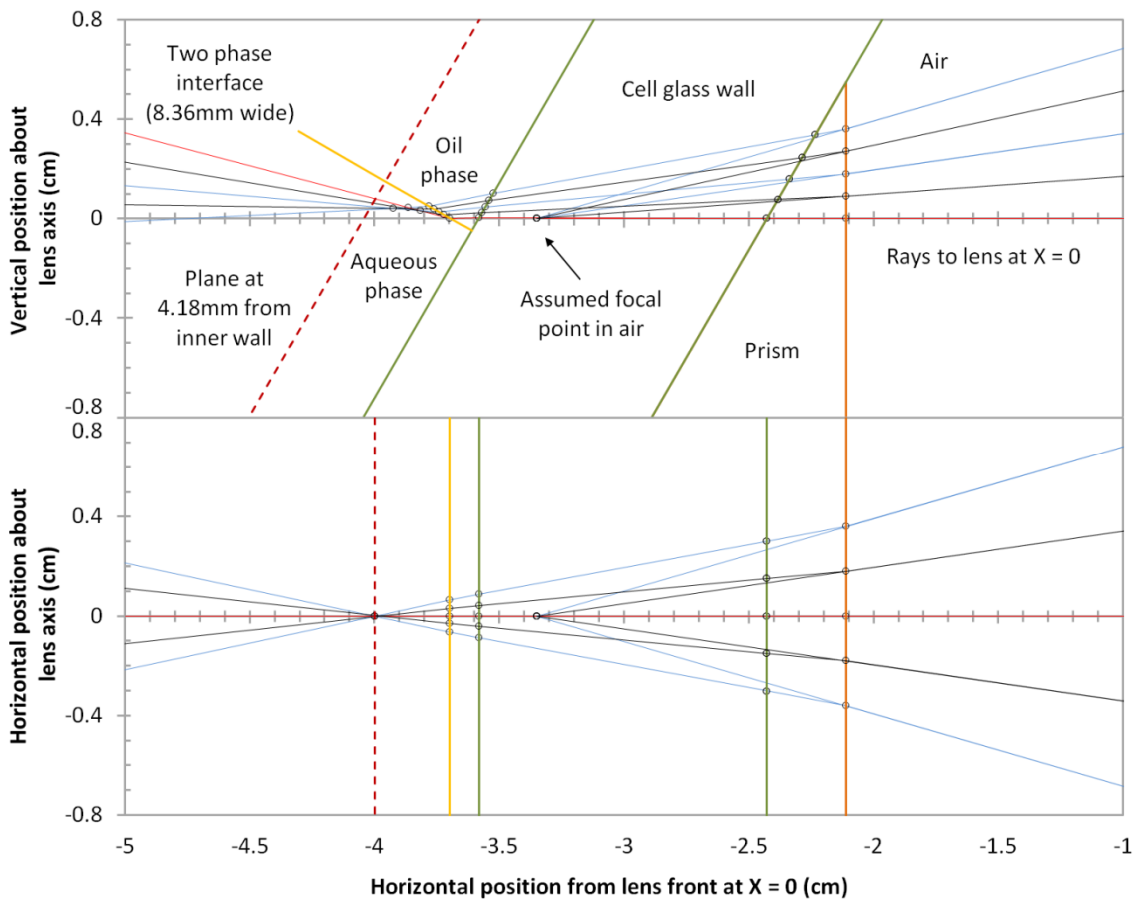
Figure 7.20: Ray tracing of the x10 lens system and flow cell: 30 degrees of lens tilt, with a corrective prism, and two fluid phases.

There are two options at this point. The first is to note that the imaging distance below the interface in figure 7.18 is exaggerated, partially for illustration purposes. If the distance through the interface was zero to the focal point, then there would be no distortions. In reality, we are interested in imaging only a very small distance below the interface, nominally half the field of view height. In this case, distortions may prove manageable. The second option is to consider some form of adaptive optics that can be switched between two optimised configurations for separately imaging the two liquid phases (if necessitating re-registration of the field of view with the interface). The simplest question is to see what happens if the prism is translated and tilted. In fact, there appears to be at least one prism position and tilt that satisfies both the producing a well-defined focal point in the vertical plane and good alignment between the focal points in the two lens planes. This is shown in figure 7.21 (the depth through the interface still being somewhat exaggerated). Note that having the prism moveable means that an optical coupling fluid cannot be used when the prism is against the cell wall for imaging in the oil phase. In this case, the very steep angles rays make between the prism and wall faces, as well as the very small gap, make prism alignment very critical.
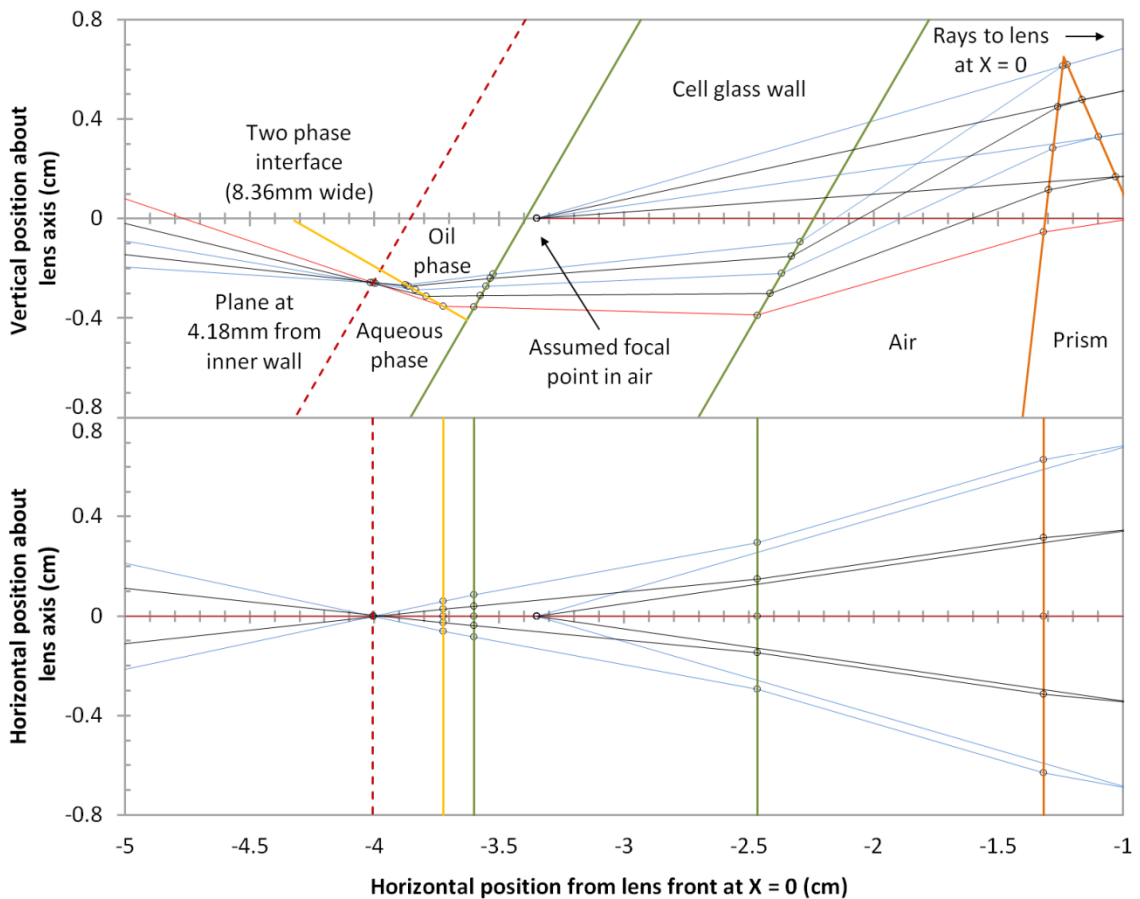
Figure 7.21: Ray tracing of the x10 lens system and flow cell: 30 degrees of lens tilt, with a corrective prism, and two fluid phases. Translation and rotation of the prism have been applied to correct distortions.

At this point, we must realise the level of complexity being entered into. Adaptive optical systems are expensive, demand precision motorised actuators, as well as skilled optical design, far beyond the scope of this PhD. Substantial departures from an assumed flat interface would also render such a system useless. Here, the option of trailing the static prism approach and assuming small path lengths below the interface is taken forward.

Despite the restrictions of implementing adaptive optics, we can conjecture how a more rigorous adaptive optical system might - in future - be achieved. Consider using a long focal length cylinder lens in the vertical plane, in front of the objective. Translating the lens would permit independent correction of astigmatism, and also much more direct correction rather than arbitrarily manipulating the prism. Tilting the lens might offer some arbitrary degree of "corrective" coma, even if the form did not precisely match that of the distortions. A hybrid solution with both a prism and a cylinder lens would permit fine correction with the cylinder lens, and to mitigate the high angle of rays exiting the cell. Drop in spherical aberration correction plates (Edmund Optics Ltd., 2016b) could also be added compensate for the thick

cell walls and to further improve the sharpness of the focal plane. There is, however, a problem. So far, we have considered different ray bundles from across the field of view to be similar, i.e. the field of view was small compared to the optical system being considered. This remained true until the two-phase interface was introduced. This now causes points across the field of view to have substantially different optical situations, each which would necessitate different corrections. Rays close to the front of the objective where such optics would be placed follow essentially the same paths from across the field of view, and thus cannot be discriminated between. In reality, optics downstream of the objective nearer the camera, where points across the field of view can be isolated, would most likely be required.

Figure 7.22 below shows detail of the static prism approach adopted in this work. The prism is supported on an adjustable height "shelf" with a surface parallel to the lens axis. This permits the prism to be sat in a notch, between the cell wall and the shelf, but it must be ensured to be correctly seated each time the lens system is moved. Elite 65 oil is used to hold the prism against the cell wall and act (to a good approximation) as an optical coupling agent. In all work, the front prism face is ensured clean between translations. A paper baffle serves to remove rays below the lens axis.
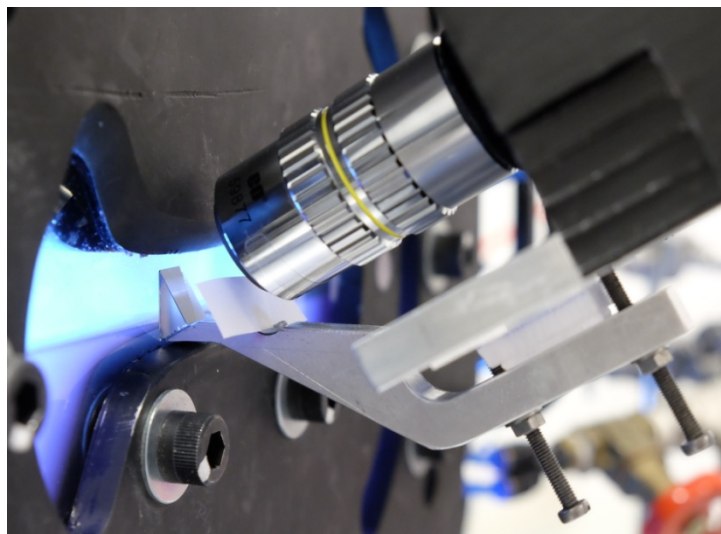
Figure 7.22: Mounting and positioning of the static 30 degree prism

7.6   Test fluids: solution makeup, tracer particles, and fluorescent dyes

In addition to the flow cell and optics, there are a few details with regards preparation of solutions: solvation of test polymers, choice and treatment of tracer particles, and the use of fluorescent dyes that required development. The specifics are given here, and accompany overall details on solution preparation in chapter 8.

Firstly, to fill the experimental setup and provide some excess, about 1.5 litres of each phase is required. With regards the aqueous test solutions, preparation of concentrated solutions on this scale from high molecular weight powdered polymers is not straightforward. The setup shown below in figure 7.23 was arranged, based on a standard 2L media flask. A combination of overhead stirring and heating, as used here, is the only way to sufficiently agitate and prepare such solution volumes. Mixing is assisted with inclined paddles and additional use of a stir bar at the base of flask, the hottest location. A liquid seal (using the liquid solvent) is used to prevent evaporation, without it solution concentration and skin formation would both occur. The liquid seal also mitigates hazards arising from boiling. This arrangement is used for preparing all large volumes of aqueous solutions used in this work.

Overhead stirrer

Liquid seal
(tube immersed into annular trough)

2L Media flask

Inclined paddles

Temperature probe

Stirrer hotplate with oil bath
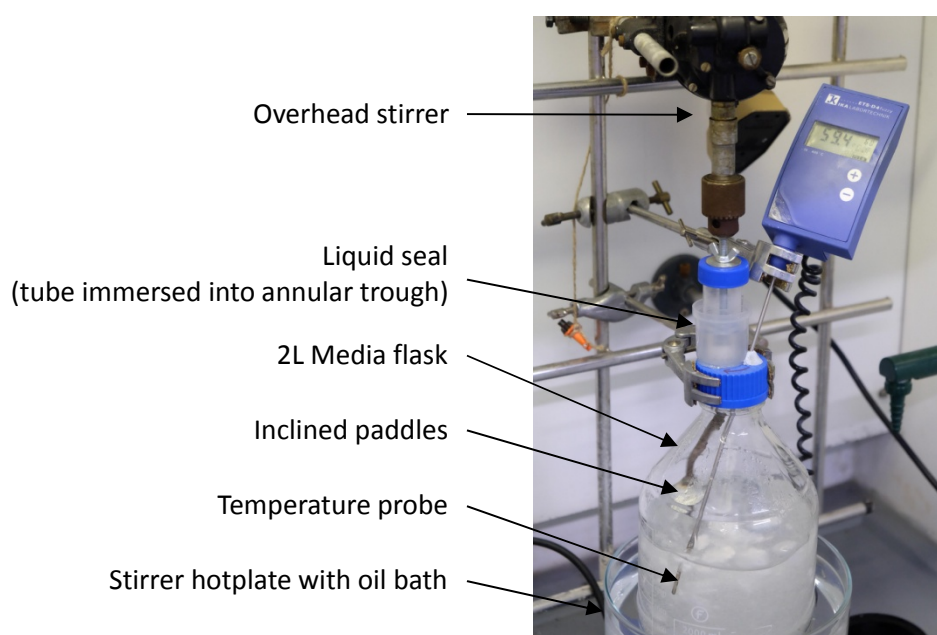
Figure 7.23: Apparatus for solution preparation

To both the aqueous and oil phases, tracer particles need to be added to allow the fluid velocity field to be determined. Papers such as Melling (1997) and Mengel and Moerck (1993) are helpful, but concentrate somewhat more on correct choice of tracers for low viscosity systems (i.e. air) rather than the high viscosity systems here. These particles must be small, such that the particles (or more specifically their images) are ideally just above 1 pixel in size with the lens system used. Having a field of view smaller than the minimum channel height automatically satisfies having small particles relative to the minimum channel dimensions. Smaller than this (or specifically, the formed image of a tracer being smaller than one pixel), and an artefact known as pixel locking occurs, where sub-pixel shifts in position cannot be resolved (Beeston, 2016). Furthermore, certainly particles near or below the wavelength of light would not be desirable (specifically note Melling (1997) for refractive particles). Particles

larger than this is at the expense of spatial resolution, and whilst per particle more light is returned to the camera, this is over more pixels, so image intensity would not presumably benefit. The polyamide PSP-5 5μm particles used in the previous section satisfy this size criterion, but their refractive index is essentially matched to that of the Perspex refractive index matched oil phase (and indeed very close to that of glycerol used for the cuvette images), meaning they would fail to scatter light in this situation. Most other materials have refractive indexes also quite similar. Hollow glass spherical particles bypass this limitation (e.g. Dantec Dynamics' HGS-10), but are not available much below 10μm. Apart from fluorescent (and expensive) PMMA particles, the best solution and that used here is 2μm silver coated solid glass spheres - product SG02S40 from Potters Industries LLC (USA).

Whilst small and highly reflective, two main disadvantages exist with these particles. Firstly, their density (3.6-3.7g/cm^3 true density from manufactures) and thus high density difference to the fluids used, despite their size, means a high rate of settling. This is not a problem in viscous test fluids or modestly viscous reference oils, but it is an issue in fluids such as the 6mPa.s Newtonian reference fluid in the liquid-liquid matched approach. Silver coated PMMA particles which would have a much lower settling rate have in fact been attempted in literature (see Barnickel and Wokaun (1989) and Jeon et al. (2009) for example) but are not available as commercial products. Secondly, as supplied and when viewed under a microscope after manual shaking, particles appear somewhat larger than expected given the 2μm average specified (50th percentile volume fraction). This can be seen after shaking a sample in table 7.5 shortly. Non-coated glass spheres are usually fairly round, and thus the irregularly shaped "particles" in table 7.5 are likely formed by clusters of smaller spherical particles.

If these clusters were due to aggregation, a common approach with the PSP-5 particles (for example) is to aid dispersion is to add a small amount of surfactant though this is not acceptable here on account of the two phase flow. Silver particles however conveniently permit easy surface modification with surface functional groups by thiol chemistry (forming strong covalent metal – thiol bonds). This technique is used to stabilise commercial products in solution (e.g. Sigma Aldrich products 667838 and 673633, using dodecanethiol and decanethiol respectfully to stabilise silver nanoparticles in hexane) and Sperling and Parak (2010) present a general review. Such modification of the silver particles used here was attempted at some length. An acidic (3-mercaptopropionic acid) and two different length alkane chain thiols (1-Octadecanethiol and 1-Octanethiol, c.f. the findings of Bauer et al. (2008)) were considered for the aqueous and oil phases respectfully. Consideration given to possible surface contamination: silver nitrate (photosensitive), silver oxide (Gallardo et al., 2012) and silver

sulphide (see MacLeod and North (1979) for a potentially suitable colloid treatment), as well as potential remaining amines from the production process used as advised by the manufacturers. The required surface density of groups was noted (see Mamun and Hahn (2012) and Giz et al. (1999)) for areas on gold), as well as the air sensitivity of thiols (Loudon, 2009) and conversely the potential requirement of oxygen for surface attachment (Toh et al., 2014). In the end, whilst macroscopic changes in the appearance of samples were visible suggesting surface modification was occurring, no noteworthy improvements were seen under the microscope worthy of reproducing here (however the author does not discourage other individuals from independently attempting this).

Much more dramatic benefits were seen by simple application of high power ultrasound. Table 7.5 elaborates this. Fluid volumes of approximately $10cm^3$ at a seeding density of $2.5mg/cm^3$ were subjected to three different treatments: manual shaking (also part of the series dilution used), an ultrasound bath (2 minutes, 50W), and a ultrasound probe (90 seconds, 50W, 90µm horn tip displacement, manufactured by Sonic Systems, UK). Two different test fluids were used, a 78wt% glycerol – water solution and the Allcosil 200-50 silicone oil of similar viscosities, chosen to illustrate a polar and non-polar system, whilst keeping settling and aggregation rates acceptable and comparable. Solutions are loaded into an optical cuvette and imaged under a microscope (Nikon S Plan Fluor x20 lens, Nikon Eclipse LV100 microscope in transmission illumination, Canon EOS 5Ds camera with adaption lens, focusing just below the upper wall) as soon after treatment and loading as possible.

As table 7.5 clearly shows, with solely manual agitation there is a significant number of particles upwards of 30µm in size, which is rather larger than desirable and greatly exacerbates the settling rate issue. Use of an ultrasound bath produces if anything a minimal reduction in particle size, but nothing significant. Application of the ultrasound probe produces a dramatic reduction in particle sizes (and a reduction in transmitted light, not shown here), with the largest particles visible on the order of 10µm. There is little difference between the glycerol-water and silicone oil systems, showing that untoward aggregation in one of the two systems is not a problem. It would have been thought that the ultrasound bath would have been sufficient to disperse particles, if the size increase was linked to aggregation. However, only the application of very intense ultrasound (the probe used has an energy density many orders of magnitude higher than the bath and in fact appreciably heated the samples) was successful in reducing particle sizes. This suggested that particles are in fact "welded" together by the silver surface layer, and thus requiring high energies to break them apart (noting the product being intended as a bulk conductive filler, and not precision segregated particles). Cospheric LLC

(CA,USA) who offer a similar product (see Cospheric LLC. (2015)), commented that this "welding" effect is known to be a problem. On inquiry, the manufacturers of the particles used stated that such high power ultrasound is in fact part of their size measurement process (Fuerhaupter, 2016), which explains the discrepancy

Treatment	78wt% Glycerol / water	Allcosil 200-50 silicone oil
Manually shaken		
Ultrasound bath (2 min)		
Ultrasound probe (90 seconds)		
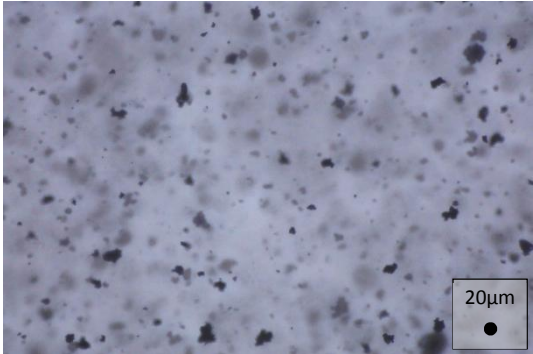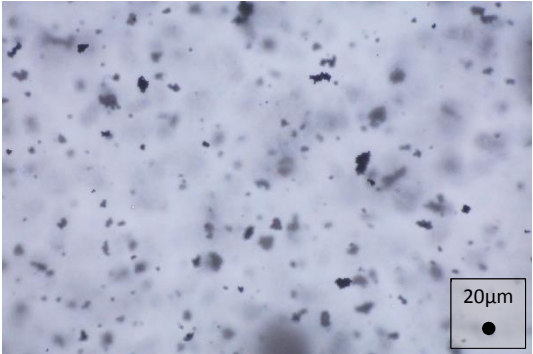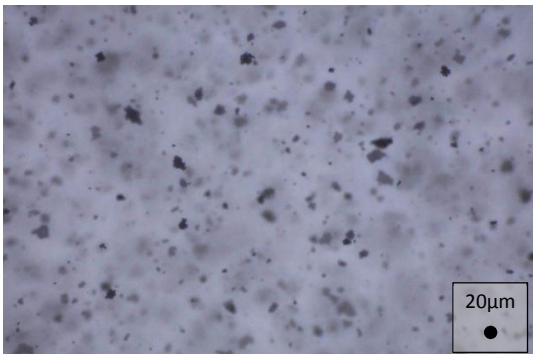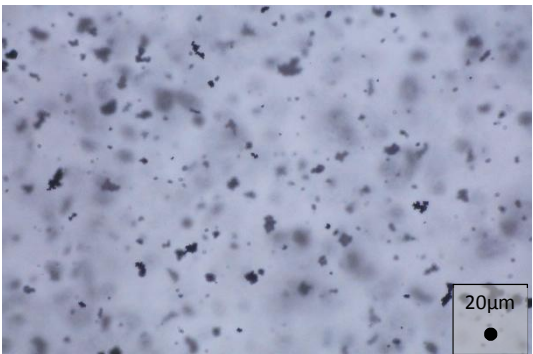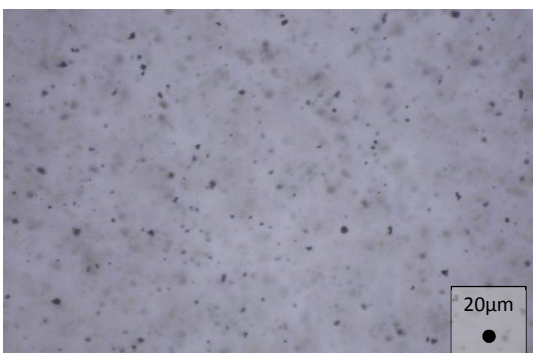
Table 7.5: Comparison of ultrasound treatments applied to the SG02S40 particles dispersed in a water-glycerol solution and the Allcosil 200-50 silicone oil. Scale particles are shown 20μm in diameter.

Whilst even the treated particles are not ideal, with some small clusters still visible (believed to cause some issues in chapter 8), use of an ultrasound probe has sufficiently improved the particle sizes to make them useable. Thus, these treated particles are hence taken forward into chapter 8. The reduction in particle size is also important in terms of settling rates. For 2μm

particles in the low viscosity index matched glycerol – water mixture, they should have a stokes' terminal settling velocity of around 4mm per hour given their density difference (compare this with the 12.5mm pipe bore diameters to the flow cell). In practice, the treated particles provide about a 30 minute useful window before reseeding is required – faster settling than preferred, but manageable. More generally, we recognise that the images in table 7.5 are rather subjective in nature, though they are of a form relevant to the work here (many averages of particle size can be chosen) and show the "welded" clusters. Performing laser particle sizing concurrent with that used by the manufacturers would, in the future, provide comparative data and better technique assessment.

In addition to adding tracer particles, a means is also required of marking the two-phase interface. This is for two reasons: firstly, it is necessary to place the interface across the middle of the imaging field of view when positioning the lens, something which cannot otherwise be discerned from tracer images without processing the velocity fields. Secondly, in the liquid-liquid refractive index matching approach, both the oil and test fluids are also essentially colourless; making it impossible to tell the two phases apart for experimental control or identification of droplets.

The first of these requirements is satisfied by a dye which excites at 532nm and fluoresces at a different wavelength. Ebest Rhodamine B (Acid Red 52, supplied by FastColours LLP, UK) is used for this purpose, soluble in aqueous solutions but not in oil. Using interchangeable bandpass filters at 532nm at the dye emission wavelength (586nm) permits the background light from the dye to be excluded from tracer images, and the bright tracers to be excluded from the duller dye images respectfully. This permits the camera to be easily aligned across the interface before the filters are interchanged and PIV images recorded. At a concentration of 1.35mg/L this dye is sufficient for this purpose. The dye also colours the aqueous phase, however with the 8.3mm path length of the cell, the colouration is almost impracticable. Droplets are virtually impossible to notice and uncertainty can exist as to where the interface actually is. Dramatically increasing the dye concentration is however not desirable, as it strongly absorbs reflected light from tracer particles below the interface and would complicate image thresholding. For a 10mm path length in figure 7.24, 87% of light is transmitted at 532nm at this concentration. Increasing the concentration to a somewhat more visible 10mg/L causes transmission to fall to 43% (or 70% for the 4.18mm cell viewing length). The plots in figure 7.24 use water as a solvent and % is transmission compared to a water filled cuvette, using the same instrument as detailed in section 6.3.
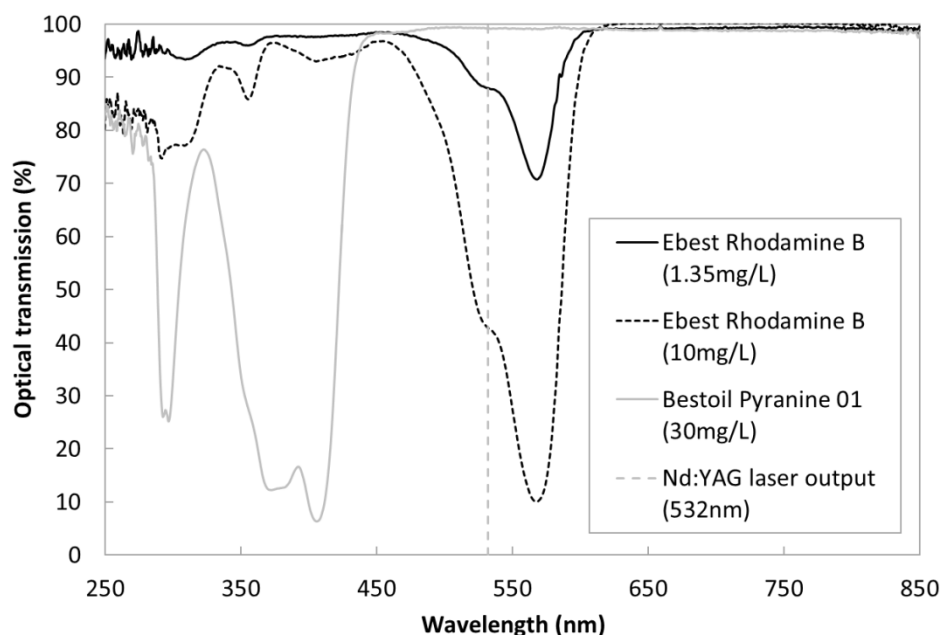
Figure 7.24: Spectroscopic plots of dyes used (path length: 10mm)

Using the Rhodamine dye at such concentrations might be possible, but not preferable. An additional dye that does not absorb at 532nm would be ideal. This is satisfied by Bestoil Pyranine 01 (Anthraquinone, supplied by FastColours LLP, UK), also non-soluble in oil, of which the transmission plot at 30mg/L is presented in figure 7.24. This dye features nil disenable absorption at 532nm, instead strongly absorbing at long wave UV and emitting around blue-green. Use of a black light makes the interface extremely clear and high contrast, both to the eye and the remote monitoring webcam, and much above 30mg/L increasing concentration has reduced practical benefit. Figure 8.19 in the following chapter shows this technique in use.

Concentrations of around 1.35mg/L Ebest Rhodamine B is accordingly used in all following work, and additionally 30mg/L Bestoil Pyranine 01 in the liquid-liquid index matching work. For the 532nm bandpass a proper optical filter is used (unknown origin) and for isolating the rhodamine fluorescence, deep red Perspex has proved excellent (also unknown origin).

Chapter 8.

Experimental results for both optical configurations.

Chapter 8: Experimental results for both optical configurations.

Following directly on from the previous two chapters where the routes for performing the measurements were considered (chapter 6) and the practical implementation (chapter 7), we now present them in practice. As discussed previously, the "wall-liquid" index matching approach permits less restrictions on the choice of test fluids, but features much greater optical complexity, thus the viability of this approach is considered first. The "liquid-liquid" index matched approach is then attempted. The appendix provides raw data as used in this chapter, a summary for the processing workflows, as well as additional processing information.

8.1   Oblique imaging: "Wall-liquid" index matched approach

The viability of the oblique imaging approach is considered to begin with, tested using a viscoelastic aqueous phase, rather than starting with an otherwise simpler Newtonian reference fluid. This was for two reasons. As noted previously, a glycerol-water Newtonian test fluid with a viscosity remotely close to that of the Synesstic 5 / Elite 65 blend would dramatically reduce the refractive index step; thus for legitimate testing a water-polymer solution must be used. Secondly, using a real test system provides experience on system pressure drops, potential instabilities, and the correct choice of phase viscosities for this complex flow situation.

For this work, ~1.5L of the 44.30wt% Synesstic 5 / Elite 65 oil blend and ~1.5L of 4×10^6MW PEO 1.2wt% aqueous solution (Dow Corning Polyox WSR-301) were prepared. This and other grades of PEO were kindly donated from Chempoint (EMEA) and Dow Chemical Company (Europe). Following the details in section 7.6, the aqueous solution was prepared by addition of a measured mass of PEO (±0.01g) to a volume of deionised water (±20ml), followed by stirring with the setup described at 60°C for about 2 days until fully dissolved. To both phases was added 0.06g/L SG02S40 silver particles. These particles were prepared by sonicating a concentrated ($1g/30cm^3$) stock solution in water and the oil blend (typically 120 seconds at the powers previously tested), addition of a measured volume to about $100cm^3$ of the test phase, re-ultrasounding, before shaking or stirring into the bulk of the fluid volumes. The first ultrasound permits the maximum possibility for particle breakup (as well as beneficially reducing viscosity through ultrasound heating). The second ultrasound separates particles and any possible aggregates apart. Rhodamine B dye was also added to the aqueous phase at 1.35mg/L. The prepared solution was used as soon as possible after being prepared. Note that factors such as any remaining fluid in the experimental setup, addition of dyes, tracers, and any draw through of the stirring setup liquid seal (max. 25ml) will all serve to reduce the polymer

concentration. Since the work here is however comparative and these factors small compared to the total solution volume, they are treated as inconsequential.

Imaging was conducted in this work with audibly similar pump RPMs for both the oil and aqueous phases, and imaging conducted at a location 15mm upstream of the contraction apex (corresponding to a height of about 3.65mm at this location). This location is expected to give some of the flattest interface along the channel. The prism and imaging tilt is set up as shown in figure 7.22 previously. Since optical artefacts are expected for tracer particles below the two-phase interface, the seeding density used here corresponds to quite a low level. Rather than using automated image correlation, this permits completely manual particle tracking via a "point and click" approach, which is the most robust method possible. A LabVIEW program was written to allow this to be expediently performed. A long interframe delay (100µs) is used to produce appreciable particle displacements to permit such tracking, and a sufficient number of frames taken and analysed to produce sufficient data (a process that assumes the flow is steady). Figure 8.1 below shows a screenshot of the LabVIEW "point and click" program at a location in the core of the oil phase to illustrate the successful functioning of the correction prism in this phase. The two images of the image pair are placed on different colour planes, and some tracks already drawn can be seen. Tracking is generally restrained to particles that are in focus, and only better particle images in each image pair have been tracked.
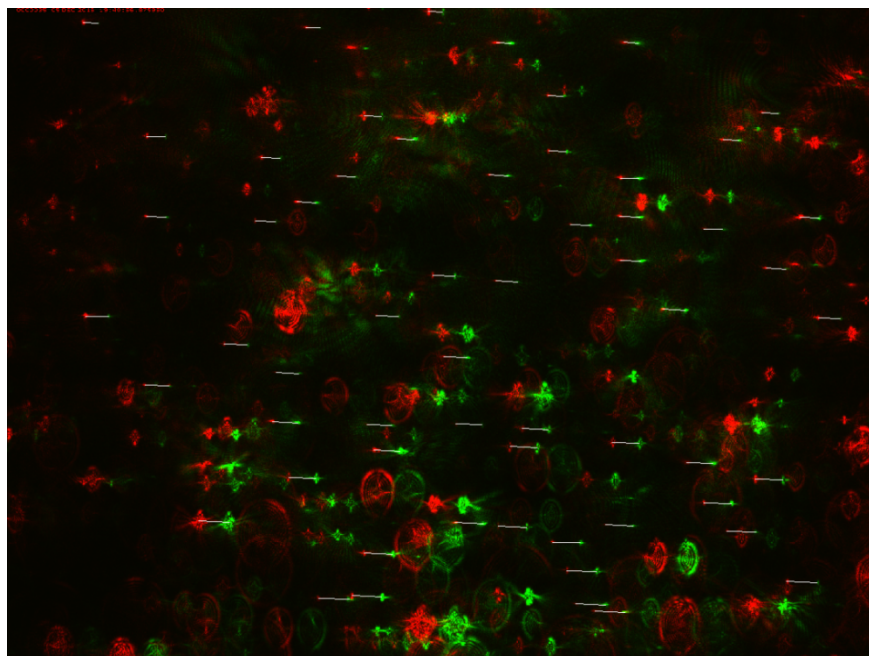
Figure 8.1: Screenshot of the "point and click" LabVIEW program main window for a data set imaging in the core of the oil phase. The correction prism is producing nearly distortion free imagery. Particle tracks already drawn are visible.

Figure 8.2 shows 8 sets of data analysed using this approach taken by translating the lens vertically over the channel height, sweeping between the channel upper and lower walls, and passing through the location of the interface. Raw data is contained within the appendix. Data sets are aligned based on the velocity profiles, and not by the measured lens system height, which was found to align poorly for the reasons noted in section 7.4. Vertical locations are normalised against zero velocity values which are taken to be the location of the (invisible) upper channel wall. Velocities are based on horizontal and vertical length scales (0.000894mm/pixel and 0.00103mm/pixel respectfully) from imaging a calibration grid in the upper oil phase. The apparent aspect ratio here (1.152) closely agrees with that expected in section 6.3 (1.15) for this phase. A line plot also shows the intensity of a horizontal row of 400 pixels from the centre of the images from dye fluorescence imaging, normalised against the maximum values recorded, for identifying the two phase interface location. In this work the Y and X coordinates correspond to the coordinate system of the camera, with the interface being closely aligned. The discretisation of data points against velocity is due to the line drawing approach used operating to integer numbers of pixels.
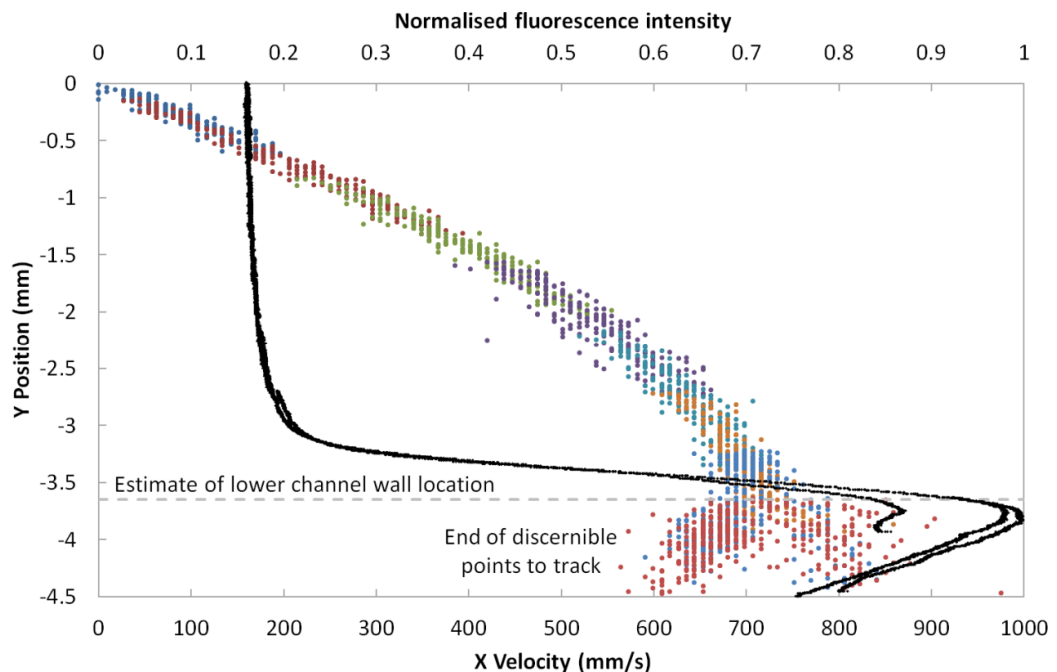
Figure 8.2: Wall – oil RI matched approach velocity plots (coloured data points) and fluorescence data (black traces) for a height sweep near the contraction apex of the flow channel. All lengths are estimated based solely on those in the upper oil phase.

From this data, we can see in the oil phase a fairly clear velocity distribution profile. This rises from zero (i.e. no slip is occurring) at the upper channel wall, and increases with increasing distance from the wall. The fluorescence data then shows a gradual increase in intensity, on account of the oblique viewing angle causing less depth in the lens axis to be fluorescing at the

top of an illuminated volume than at the bottom. Located within this intensity gradient (most likely at the mid-point of which) is situated the two-phase interface. Close to this location, we can see both a split in the velocity profile into two trends in the aqueous phase, and also a considerable increase in scatter. Point plotting ends when disenable artefacts to track are no longer present.

The origin of this split in velocity profiles is evident when we look at data which was being tracked, an example of which is shown below in figure 8.3, straddling the location of the interface. Even a small distance below the interface, regrettably large distortions in tracer particles are produced, far higher than what might have been hoped for. Nonetheless, for this exercise tracking was continued below the interface based on the brightest points of artefacts. What has likely occurred is a combination of coma artefacts and vertically out of focus particles (the horizontally focused component compressing light density into these regions) resulting in bright regions at the very top and bottom of their images being manually tracked. The distance of these bright locations above and below a real particle becomes greater with increasing distortion, i.e. distance below the interface. The result of this is at the same plot locations particles have been tracked which continue to increase in velocity after the interface, i.e. tending towards a velocity profile peak in the aqueous phase, and also particles much closer to the wall, at lower velocities. The increasing scatter in data points is due to the difficulty in tracking "similar" artefacts.
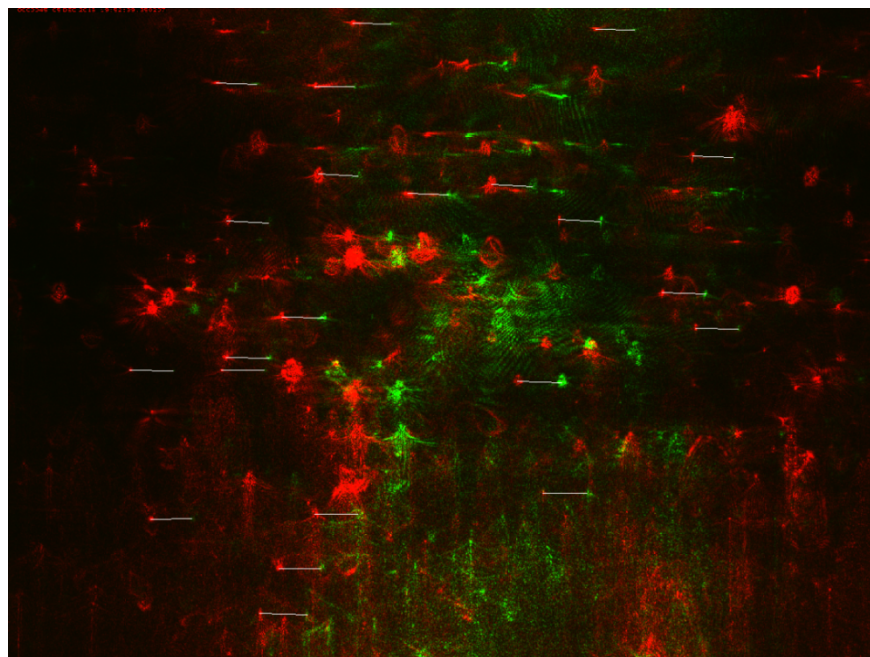
Figure 8.3: Screenshot of the "point and click" LabVIEW program main window for the data set with orange markers in figure 8.2, straddling the interface. Some particle tracks already drawn are visible.

An estimate of the location of the lower channel wall location is also shown in figure 8.2, and it would appear that this roughly coincides with the location of the interface. However, the location is estimated given the known channel height at this location and the apparent upper wall location, rather than via being imaged directly. The manual alignment of the data sets introduces errors, and furthermore, magnification of vertical length scales below the interface compared to those above (see section 6.3) means the real optical location of the lower wall is likely farther from the interface than is shown.

From this experiment, we can conclude that based on the use of a static correction prism, good quality imagery can be attained in the reference oil phase, but not in the aqueous test phase, and thus this experimental approach cannot be used for the purposes required here. However, two useful points can be taken. Firstly, the experiment showed no initial signs of flow instability or oscillation, despite the choice of test phase. Secondly, despite the issues just noted and the phase flow rates not being exactly measured, the oil phase appears to be occupying the majority of the channel height whilst likely travelling slower than the test phase. A reduction in reference oil viscosity below that of the estimates in section 6.3 would be prudent. On this basis, the lower viscosity Allcosil 200-50 silicone oil was chosen for the next section of work, as alluded to in section 6.4.

To highlight the complexity of the interface positioning and why the interface position observation was valuable, consider the estimate of the oil viscosity used here of about 400mPa.s (from section 6.3). The oil thus has a planar extensional viscosity (e.g. see table 1.1) of 1.6Pa.s. Now contrast this with estimates of the shear and extensional viscosities of PEO solutions, both of which contribute to the interface location. A 1.5wt%, $4x10^6$ MW PEO solution has roughly constant (uniaxial, but comparable) extensional viscosity of 30 to 40Pa.s across a broad range of extension rates (Gauri and Koelling, 1997). Assuming that the velocity profile in the aqueous phase in figure 8.2 extends to a peak and taking the length scale change into account gives shear rates, very roughly, on the order of $500s^{-1}$. From data in Ebagninin et al. (2009), and assuming this to be broadly representative thinning for the entire phase, a 1.2wt% $4x10^6$ molecular weight solution has a shear viscosity around 80mPa.s (estimated from figure 2 of the reference). The shear and extensional viscosities thus differ by some $2 - 3$ orders of magnitude; which if individually dictating the interface location, would yield very different results (regards stresses, the extension rates for the phases are equal at the interface; shear rates manifest themselves as pressure drops, more difficult to qualitatively interpret with regards interface location).

211

Before this method is left, supposing imaging below the interface were successful in the future, a true measurement of length scales below the interface rather than an estimation is desirable. This was attempted and is difficult to perform. One method is to place a TEM grid directly below the interface and use it as a reference in the same manner as one above. However, this must be done without disturbing the interface shape, the only way being to place the grid on a fine "fin" at the channel centreline that does not locally attach to the channel walls, and that is cut to leave a calibration pattern at the extreme upper edge of the fin. The interface must then be slowly lowered to within microns of the top of the fin, but without coming into contact, and still assuming that it remains flat across the centre (difficult, with progressive side wall wetting).

Figure 8.4 below illustrates this arrangement and also shows the best imagery that could be attained from such an approach. It can be seen that images are now stretched in Y (as expected, with the grid being a square pattern). However, rough measurements of the grid aspect ratio (~0.7) fall short of the 0.55 aspect ratio predicted. Rather than using this grid approach, a better method would be to incorporate large - and known spherical - particles in the aqueous phase. Horizontal length scales do not change across the interface, and thus a change in apparent aspect ratio would permit the vertical length scales to be found. This method would not suffer from a limited imaging region with the lens focal plane being misaligned to the vertical grid. Furthermore, it would work in not only one calibration run, but in every image set. This means that rather than assuming the interface was centrally level as it was lowered towards a grid (unlikely), it would permit true length scales to be found of the actual interfaces used for PIV data, even if each one was slightly tilted to varying degrees.
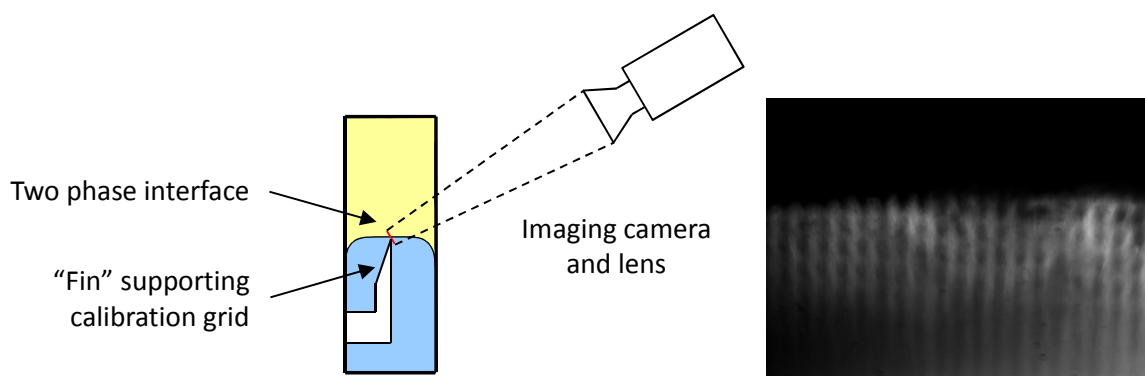
Figure 8.4: Use of an AEI TEM grid (identical to that in figure 7.2, but carefully trimmed) attached to a "fin" positioned immediately below the two phase interface for length scale calibration in the lower phase, left: diagram of arrangement, right: image of a cut TEM grid supported on a fin just below the two phase interface - a frame from a sequence, at the instant prior to interface contact with the grid/fin.

8.2 Perpendicular imaging: "Liquid-liquid" index matched approach – data analysis development and validation experiment

From the "wall-liquid" index matched approach, we now move on to considering the "liquid-liquid" index matched approach, with the lens orientated perpendicular to the cell wall. Raw data for this section is presented in the appendix, along with a summary of the processing workflow developed (figure A.2). For this work, we instead start with a Newtonian glycerol-water solution precisely adjusted to the refractive index of the silicone oil used. This was for two reasons: firstly we end up moving directly onto experimental validation, and secondly, it is considerably easier to fine tune the refractive index of a low than high viscosity system. First, more general aspects of the experiment and associated workflow are presented, followed by specific details. Following the previous work, the flow cell was stripped, thoroughly cleaned, and all pipework flushed with copious quantities of water, hexane for the oil loop, followed finally by ethanol and complete drying to remove all significant traces of previous fluids.

In terms of refractive index matching, a glycerol-water solution (1.6L) was prepared initially at 53.553wt% glycerol as per that determined in section 6.4. Additionally the Ebest Rhodamine B dye was used at 2.5mg/L (slightly increased concentration), and Bestoil Pyranine 01 at 30mg/L. The solution composition was then fine-tuned (via the slope of the index / concentration dependence) using the Abbe refractometer / laser illumination setup. Here, the refractometer was located in the same laboratory (air-conditioned) as the main experiment, and connected to a circulating volume of water as a thermal mass. The 53.553wt% solution was adjusted before loading into the experiment (+8.00g glycerol), and again when loaded as water used to wet the surface coating would serve to disrupt the index match (+2.73g glycerol). The match was again checked and adjusted prior to the bulk of PIV work on this system additional water addition was found to be required (+5.90g), possibly on account of evaporation from various avenues over the time the experiment was left and instabilities in the air-conditioning (oversized for the lab).

Before the 2.73g of additional glycerol was added, an experiment was conducted to estimate the effects of a known level of refractive index mismatch. The two-phase interface was rapidly transitioned through the location of the calibration grids, a process which serves to produce a complex and highly distorted interface shape as it does so. For perfectly matched refractive index between the two phases, and at the matched wavelength, no change in the grid appearance would be expected. In addition to the known mismatch (scale difference of 0.0145, or about 0.00014 in true index n), the white light used here would have generated additional distortion. Figure 8.5 shows a set of equally cropped frames whilst the interface is raised

(bottom to top of images) through the grid location, a process found to produce the most visible aberration. It can be seen that visible aberration does occur, and for this case was on the order of a 5-10 pixel vertical "wobble" in the apparent grid location, which underlines the need for very precise index matching. The same level of wobble was seen on two additional repeat runs. It is difficult to convert this directly to a % error, e.g. of shear rate, as depending on interface shape this will generate both positional and scaling shifts in imagery, but at least this does serve as an indication of errors. Tracer imagery taken across the two-phase interface can be seen in figure 8.7 shortly (the interface being located across the centre of the frames) and it can be seen that the refractive index matching has been successful, leaving no notable optical trace of the interface.

T << 0.5s	T = -0.50s	T = -0.25s	T = 0.0s	T = 0.25s	T = 0.50s	T >> 0.50s
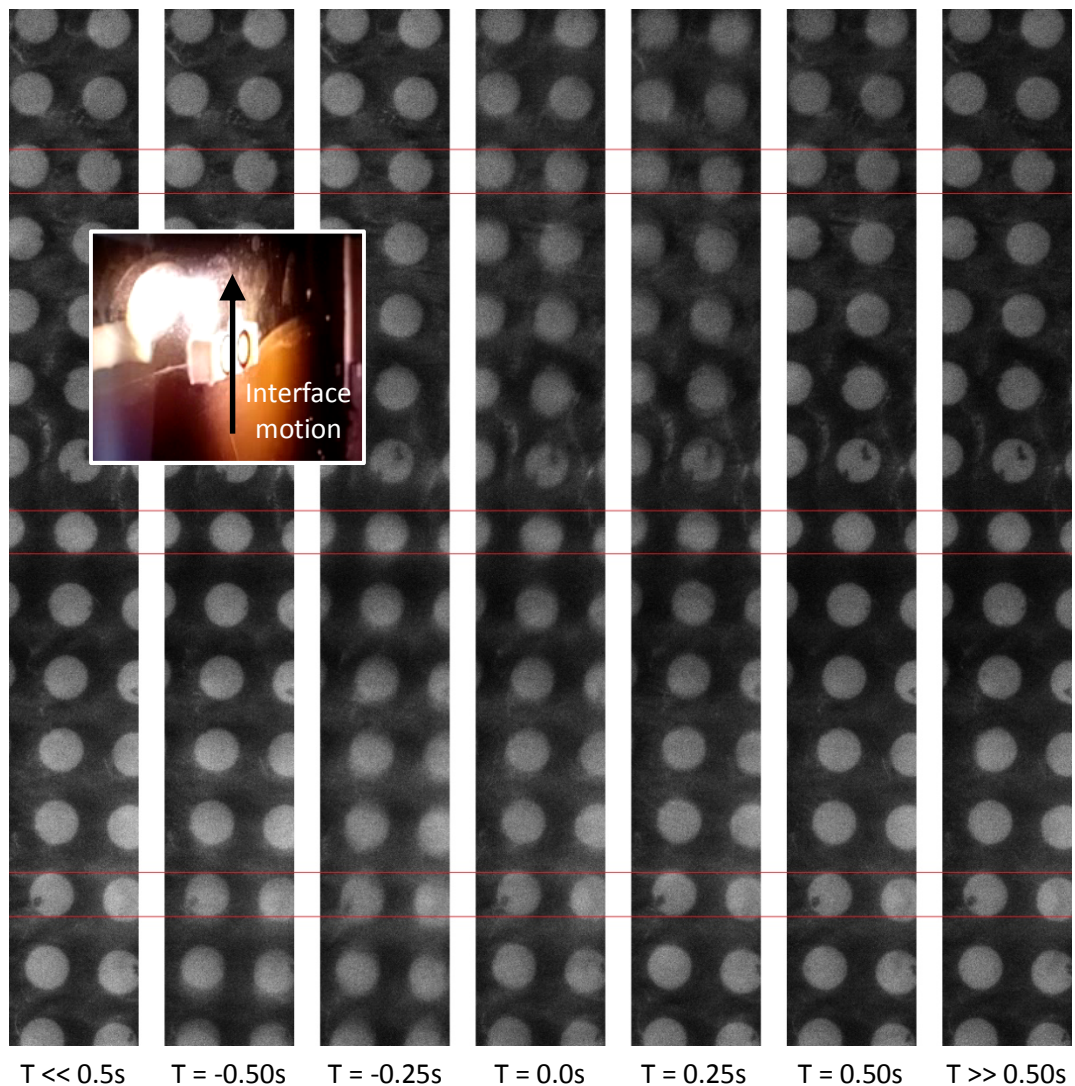
Figure 8.5: Cropped images of the AEI TEM calibration grid (35µm diameter holes) as the interface is moved up over the grid (bottom to top of images). Red lines (1 pixel wide) are added to aid comparison in the observed grid position. Inset: Motion of the interface over the grid carrier.

Building on the use of dyes in section 8.1 to locate the two phase interface, a more accurate and rigorous approach is desired, both to locate the interface, and to permit reorientation of data with respect to the interface. The largest errors in locating the interface vertical position were identified to arise from two main sources: camera movement, when the filters are manually changed; and also from interface movement. Interface movement can arise from both interface wobble between successive PIV images (flow rate unsteadiness, potential upstream or downstream recirculation zones), but also from progressive interface movement arising from slight variations in flow rates and the shifting downstream equilibrium interface position. Camera movement can be corrected for as the interface remains in the same position during the acquisition of PIV images, all other movements cannot. The approach taken here is to take several fluorescence images of the interface both before and after a PIV data set, and furthermore minimise the time taken between this two actions through operating at the highest practical frame rates (8Hz image pairs). Due to the long time taken to save data from the camera buffer when full, the "after" fluorescence images are added to the end of the PIV measurement set before downloading. The images taken give indications of interface wobble between frames and some rough indication of both interface and camera movement (a substantially improved and more robust method is detailed in the conclusions in chapter 9).

To extract interface position from this data, a LabVIEW program was written that extracts intensity values for a narrow averaged column of pixels (5 pixels wide) running from top to bottom of a fluorescence frame. These intensity values are then normalised with respect to a median average located well above and below the interface, and a spline curve fitted to this data. The vertical locations of 35%, 50%, and 65% brightness are then found, this providing a measure of uncertainty of the true interface location within the brightness gradients in the images. This is conducted for vertical strips positioned across the whole frame and linear lines (i.e. the determined position of the interface) fitted for each of these brightness threshold values. Figure 8.6 shows an example fluorescence image, with two fitted intensity profiles for pixel columns, one to the left and one to the right side of the image. The 35%, 50%, and 65% intensity lines determined for this image (from all pixel columns) are also shown. The coordinates of the ends of each of these brightness threshold lines are then separately averaged for all frames pre- and then post- PIV tracer data, the difference giving an interface movement (either from camera disturbance or interface drift). The before and after values are then averaged together, providing a best estimate of the interface position and angle.
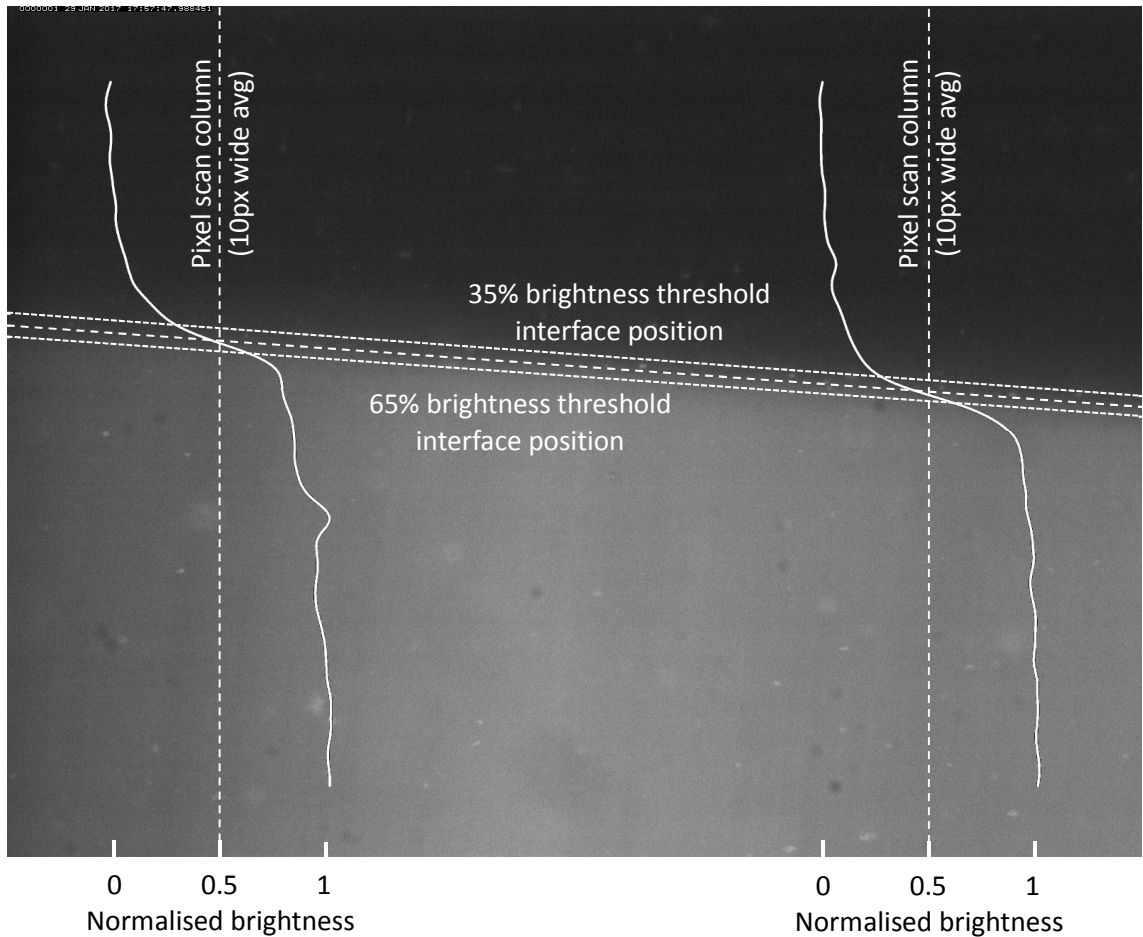
Figure 8.6: Illustration of the procedure for determining the interface position from fluorescence images. Here only two intensity scans are shown (at 300 and 1300 pixels horizontally) at the marked locations. The determined interface positions shown (based on 35%, 50% and 65% normalised brightness) are however fitted from multiple scans across the full image width. This image is from data set 30B in table 8.3.

For this work, rather than manual tracking, automated PIV cross correlation is employed. This presents an additional challenge. Within each interrogation volume (typically 10-30 pixels on each side) at least a couple of tracer particles need to be visible. This demands dramatically higher seeding densities than that used in the previous work, in fact so much higher that the experiment would be impossible on account of test fluid opacity. This is circumvented by operating at a manageable seeding density, taking a large number of frame pairs (170, the camera buffer limit), and performing image stacking. The lens has also been masked with a 10mm aperture to increase the depth of focus, improve the tracer appearance similarity between frames, and to help mask possible refracted tracer images from the upper channel wall. Seeding density for both phases was on the order of 0.16g/L of the silver coated glass particles with this image stacking approach, a level that renders the test fluids essentially opaque when viewed through the diameter of the receiver flasks. The high seeding particle

216

mass density necessitates periodic reseeding of the aqueous phase, and to a lesser extent the silicone oil phase, rendering the above value approximate. Although this seeding density seems significant by eye, this loading level corresponds to a volume fraction of 0.005% and separations between 10µm particles of about 20 particle diameters. This extremely low volume fraction compares very favourably to Mueller et al. (2010) (Newtonian rheology below a volume fraction of 0.01) and the example given in TA Instruments (2013b) (departure from Newtonian rheology above a particle concentration of about 0.2%). Rheological influences from particle-particle interactions are thus not anticipated in this work.

The stacking process is complicated on account of two factors, firstly background illumination, and secondly, large bright out of focus artefacts (and laser interference patterns) from particles just outside of the focal plane, both of which need to be removed. This was achieved in LabVIEW by analysing a masked "doughnut" of pixels (28 Pixels inner by 40 pixels outer diameters used here) around each pixel in an image. The average of this masked group of pixels is multiplied by a scaling factor (x25 used here) and subtracted from the pixel under analysis at the centre of the doughnut. Through this, any bright artefacts generally greater in size than the inner diameter of the mask (about 25µm) subtract themselves out of the image. Artefacts between half the inner diameter and the inner diameter would be reduced in size. Background illumination is also conveniently eliminated by this method.

The program written handles images in their native PCO raw B16 (14bit) format which holds both images in a pair above each other, as visible in figure 8.7. The program levels brightness between frames in an input frame pair prior to processing (via user defined thresholds). Images in the final stacked frame pair are also rotated and translated based on the averaged fluorescence data to place the interface level and in the centre of the images. Rotating PIV images means vectors from cross correlation analysis are conveniently aligned on a grid oriented with the interface, however this requires interpolation which may be at the expense of sub-pixel tracking accuracy. Examples of an input image after filtering (white artefacts passed through the filtering, red areas were eliminated) and the output stacked (summed) image after 170 frames with rotation and translation are shown in figure 8.7. An increased density of tracers can be seen at the interface, this is presumed to be due to pickup of settled particles at the interface upstream. Note: with the present program processing 170 image pairs on a tri-core PC (each image 1600x1200 pixels) takes about two hours to process - program efficiency improvements can be made.
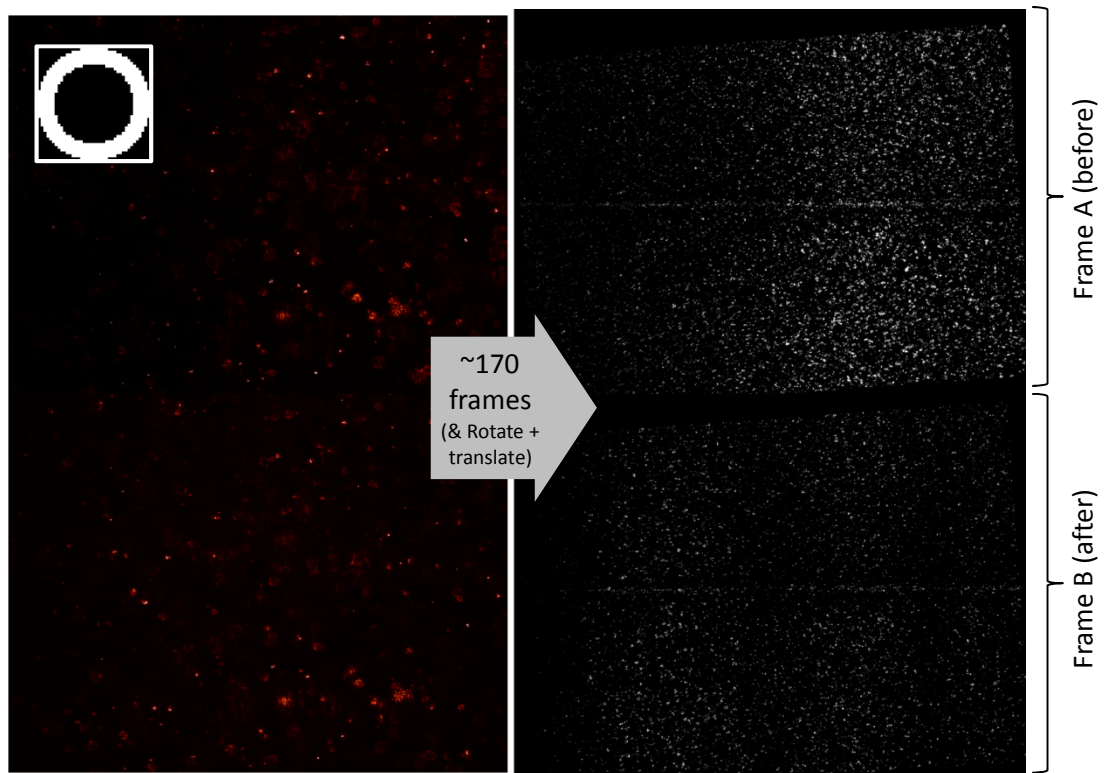
Figure 8.7: Example of a single filtered image frame (left), and the final outputted stacked, rotated, and translated image (right). Image brightness of the filtered image frame has been adjusted for presentation, highlighting out of focus artefacts that would have contributed to the stacked image brightness. Both frames of a frame pair are contained within one file. Inset: Enlarged version of the "doughnut" mask used for analysis.

The output stacked images from this program are then fed into the PIVview2C (PIVTEC GmbH, 2014) PIV correlation software for velocity analysis and raw pixel shift data exported. Table 8.1 shows a summary of the key processing parameters used. Validation filtering conditions summarised in table 8.2 are applied, both internally from the PIVview2C software, and applied externally in LabVIEW to the output data. These effectively filter out vectors from areas of the images with inadequate illumination (usually caused by the second, more tightly focussed laser pulse). Figure 8.8 overleaf shows an example vector field in the PIVview2C to illustrate a typical processed data set and show the drop off in valid vectors to the edges of frames. The input stacked images and output vector fields for all data sets are contained within the appendix, together with information on reading them.

Parameter	Setting
Interrogation windows	32 (H) x 16 (V) pixels, with 50% overlap between windows
Correlation	Standard FFT correlation, uniform window weighting, 9x repeated correlations with multiplication of correlation planes
Interrogation method	Grid refinement interrogation (initial size 64x64 pixels), 5 iterations on final resolution.
Sub pixel shifting and peak fitting	Enabled, based on a least squares Gaussian fit (3x3 points). Restricted correlation peak search area in the vertical direction.

Table 8.1: Summary of key PIV image correlation parameters used

Filtering condition	Criteria
Maximum displacement test	10 pixels (PIVview2C) +2 < dx < +10 pixels (LabVIEW) -3 < dy < +3 pixels (LabVIEW)
Maximum displacement difference (to neighbouring 8 vectors)	1 pixel
Minimum signal to noise ratio	100
Vector Y position	100 < y < 1100 (LabVIEW)
Correlation peak ratio peak 1 – peak 2	99
Outlier replacement	Disabled

Table 8.2: Summary of validation filtering conditions applied both via the PIVview2C software and downstream in LabVIEW.
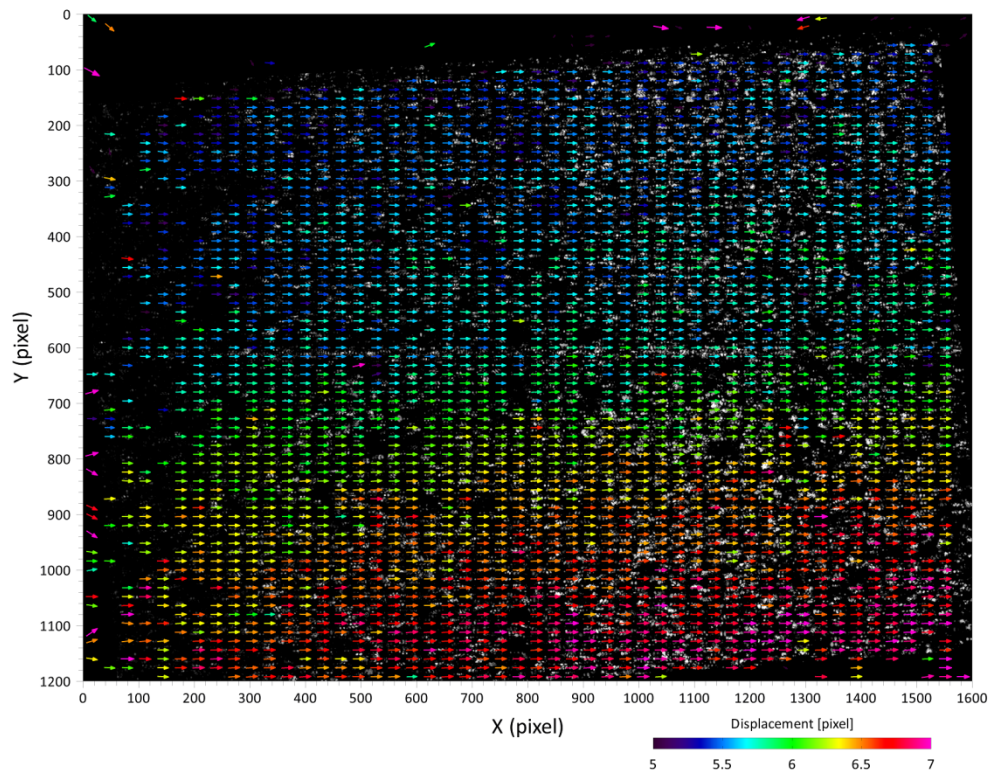
Figure 8.8: Vector field as presented in the PIVview2C software (specifically data set 30B in table 8.3). Every other vector is omitted for clarity and colour scaling used to highlight the velocity gradient.

For the validation work, PIV imagery was taken with an oil flow rate very much lower than that of the aqueous phase. This criteria was found to produce fairly well defined demarcations in shear rates, dominated by the drag from the more viscous, slower moving oil phase, rather than attempting to analyse an interface located towards the top of a velocity profile. Situating the interface on a flat region of the overall channel velocity profile is detrimental for accuracy, shear rates are low and slight changes in the evaluated shear rates from velocity profile scatter would have the most severe effects on the shear rate ratio determined at this location. Flow rates were also reduced as far as possible, with a bypass loop added around the oil pump for stability. In total 9 sets of PIV data (~170 tracer frames, plus before and after fluorescence images) were taken at three different locations travelling down the flow path in the flow channel and "scanned" at three different lateral across the channel width for each of these, the channel centreline and ±1.5mm either side. Length scales in images are 0.000889 mm/pixel based on the calibration grids. The laser illumination mirror position and laser cavity powers were optimised at each location. The lens is moved to place the interface as close to the image centre as possible for each set, and the vertical stage placed under "preload" stress after movement to maximise rigidity. Due to the rate of seeding particle dropout in the aqueous phase, the pumps were switched off and reseeding conducted after the three position "scan" at each flow location was completed. Phase flow rates should be very similar between each three position run. The salient parameters of the tests are summarised in table 8.3 as well as in appendix table A.1. The lens height positions are very approximate for the reasons previously noted. Note that due to refraction effects, for a change in lens distance from the front of the cell of 1.1mm, it was identified from measurement that the focal plane shifts through the cell by 1.48mm, hence the differing beam and lens shifts required. Little change in fluid temperatures occurred across the flow cell as would be expected, but slight changes between performing experimental sets are evident.

Due to the time delay between the fluorescence data at each location in a "scan" across the channel, and in addition vertical movement of the lens, the shape of the interface at a snapshot in time cannot be ascertained. To address this, rapid scans in fluorescence were conducted with corresponding imaging locations at and ±1.5mm either side of the channel centreline at the end of each data set (again tracking illumination accordingly). The interface locating program previously described was used to find the location of the interface at the horizontal frame centres and 50% intensity thresholds, nominally over about 10 frames for each location. These interface positions when combined with the lens height positions are presented in figure 8.9. Linear lines (dashed) are fitted between the three measurement

locations, and the locations of upper and lower channel walls are also indicated at each position down the channel.

Lens lateral position (mm)	Lens height position DTI (mm)	Beam micrometer estimate (mm)	Lens micrometer position (mm)	Interframe time (µs)	Inlet temp' (°C)	Outlet temp' (°C)	Dataset
0 = Centre of contraction	(+) 2.60 = Lower wall at centre of contraction	Maximum shift +/- 1.5mm around midplane	11.1 = Wall closest to camera		Aqueous phase	Aqueous phase	
(+) 87.35 = Far left edge of viewing window	0 = Upper wall at centre of contraction		10 = Midplane (via cal grids) 8.9 = Wall furthest from camera		Oil phase	Oil phase	
	0.643	1.5	8.9		22.2	22.2	30A
29.98	0.443	0	10	14.84	22.5	22.7	30B
	0.239	-1.5	11.1				30C
	1.017	1.5	8.9		22.4	22.4	17_5A
17.46	0.839	0	10	9.48	22.8	22.9	17_5B
	0.757	-1.5	11.1				17_5C
	1.172	1.5	8.9		22.3	22.2	5A
4.93	1.177	0	10	7	22.6	22.6	5B
	1.075	-1.5	11.1				5C

Table 8.3: Accompanying experimental data for the validation data sets (this data is also present in table A.1 in the appendix)
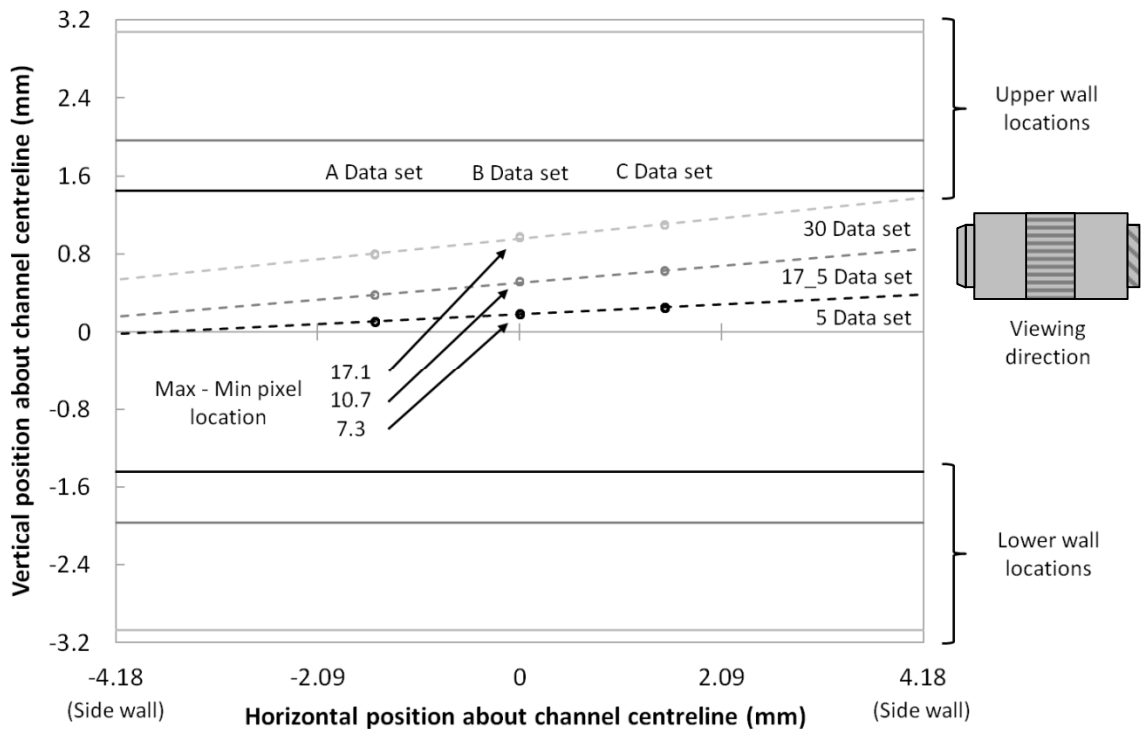
Figure 8.9: Interface locations at three locations across the channel cross section at the end of each experimental run. Dashed lines are linear fits through the measured locations, and the wall positions for each experimental run are colour-coded accordingly.

We can see that – within the limit of the attainable scan distance – that the interface exhibits a degree of tilt across the channel cross section. The level of tilt here is in excess of errors expected with the process used to level the cell, and could be caused by various factors. Flow does occur in narrow gaps between the glass channel walls and the hyperbolic inserts which is visible by eye, and is by no means symmetric either side of the channel. However, compared to the flow through the channel this is quite small. The most likely cause is a combination of non-laterally symmetric flow from the flow distributors (exaggerated by the through bolt) and any asymmetrical wetting occurring in this region, where the surface coating plays no role. Due to the high level of flow inertia in these experiments asymmetric upstream flows would tend to propagate downstream. Apart from the tilt however, the interface is nearly flat in the central measurement region, with only slight upward curvature. The limited interface tilt and curvature and provides confidence, in addition to observations by eye (e.g. figure 8.19 later), that interface is adopting the desired configuration for the measurements intended. The tilt also becomes less significant as the channel narrows: both the most important imaging region, but also the location where flow stresses would be expected to be the most dominant over gravitational effects.

Whilst separate data points for each frame analysed are plotted on figure 8.9 – the scatter of which is characteristic of interface "wobble" between successive image pairs – on the channel length scales they are virtually indistinguishable. However, wobble on pixel length scales is very important for image stacking and vector analysis – the range between the maximum and minimum interface pixel locations is noted for select data points on the channel centreline. We can see this "wobble" becomes less significant downstream as the vertical wall separation reduces (and is why locations further upstream in this particular study were not attempted). This wobble reduction can be explained by assuming wobble to be proportional to the wall spacing. We can also say that further downstream issues with any eddies in the entrance region would expect to be erased (the flow distributor with the central bolt is helpful, but not perfect). A counter argument with regards flow stability also exists however: in a 2D contraction, Reynolds values can be shown to be constant (here, on the order of Re ≈ 500 due to the low viscosity of the aqueous system), but with the vertical walls the Re values upstream (or, at aspect ratios <1) would be expected to be less than those at downstream locations.

We now move onto considering the velocity profiles extracted from the imagery and optimise the required curve fitting processes. The raw data includes noise and scatter, factors that must be very carefully addressed if a pair of accurate velocity derivatives are to be extracted. Figure 8.10 – 8.12 shows velocity profiles (at the three locations scanned across the cell centreline per

figure) for the "30" data set, 8.11 the "17_5" data set, and 8.12 the "5" data set, at locations ~30, ~17.5, and ~5mm upstream of the contraction apex respectfully.

All data hence presented includes filtering of raw vectors to 1 standard deviation either side of the mean values per interface perpendicular location, correction of the interface position, spline curve fitting to mean data with a smoothness factor of 20, and no pixels excluded either side of the interface, unless otherwise stated. These factors are elaborated shortly. Shear rates are determined from the gradients of the spline curves for a very short segment either side of the interface. Legends for velocity profiles in later figures are consistent with figures 8.10 – 8.12.
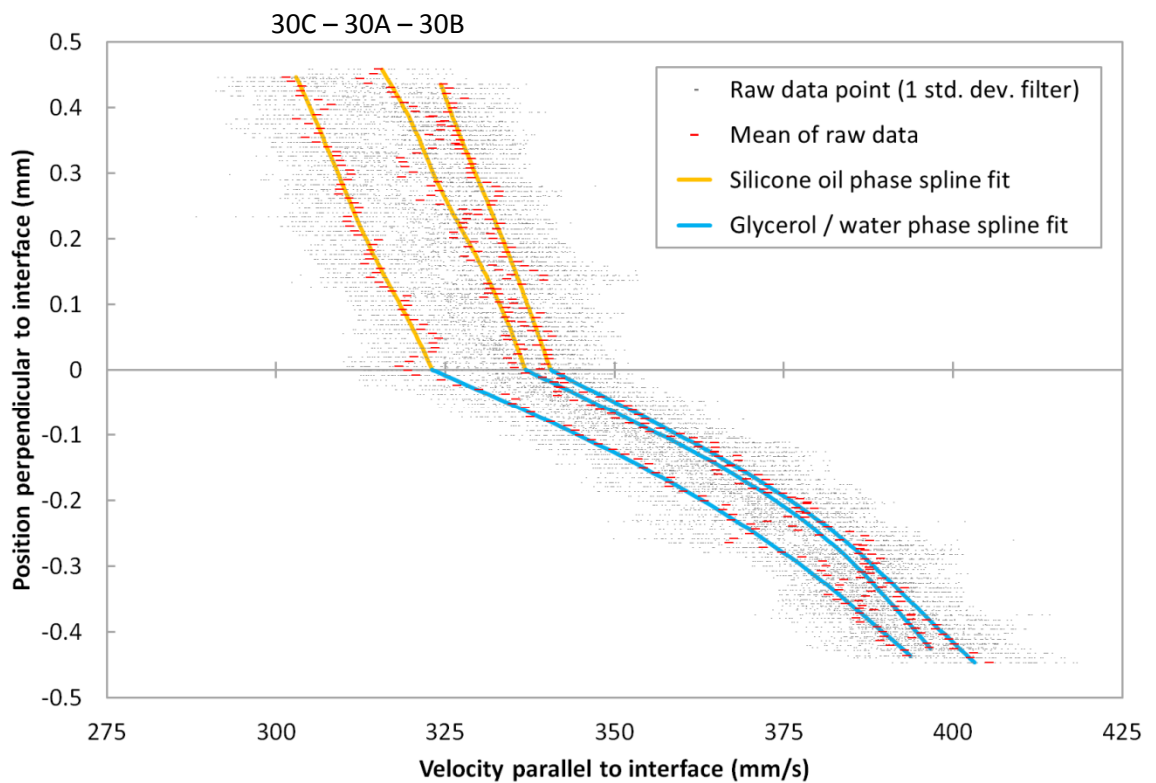
Figure 8.10: Velocity profiles 30mm upstream of the contraction apex at the three locations scanned across the cell centre line
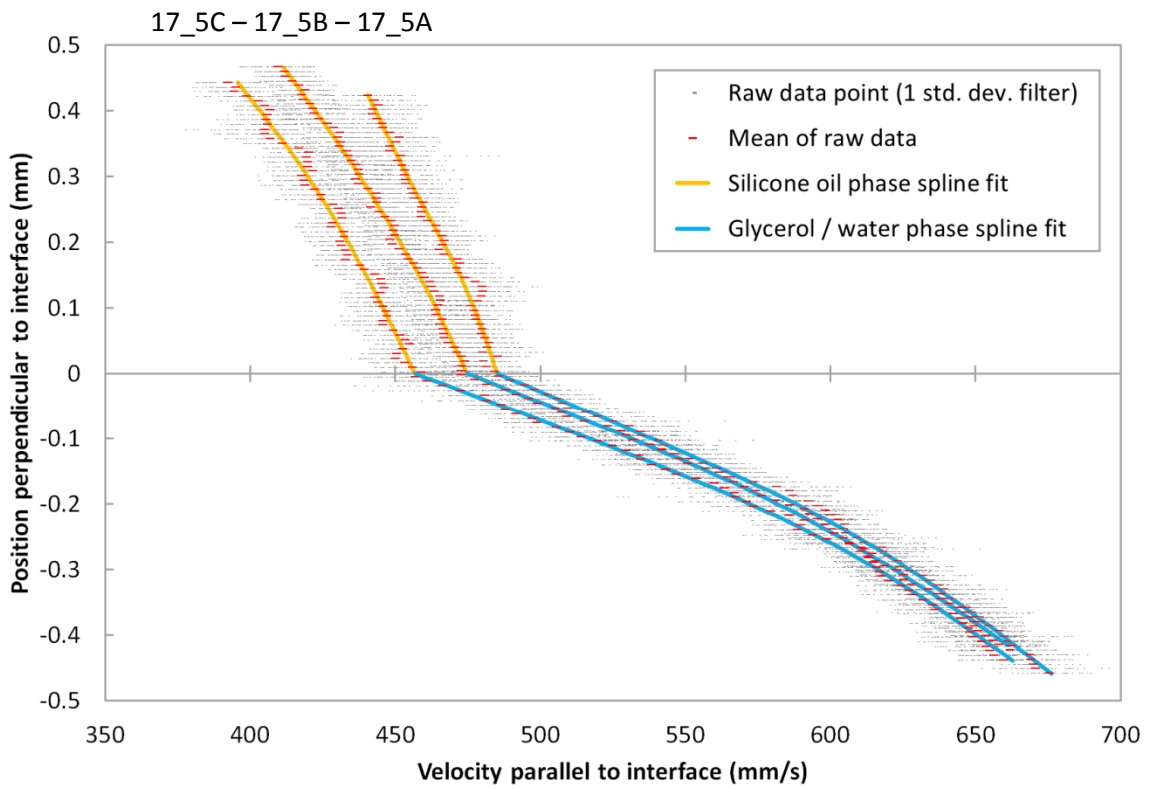
Figure 8.11: Velocity profiles 17.5mm upstream of the contraction apex at the three locations scanned across the cell centre line
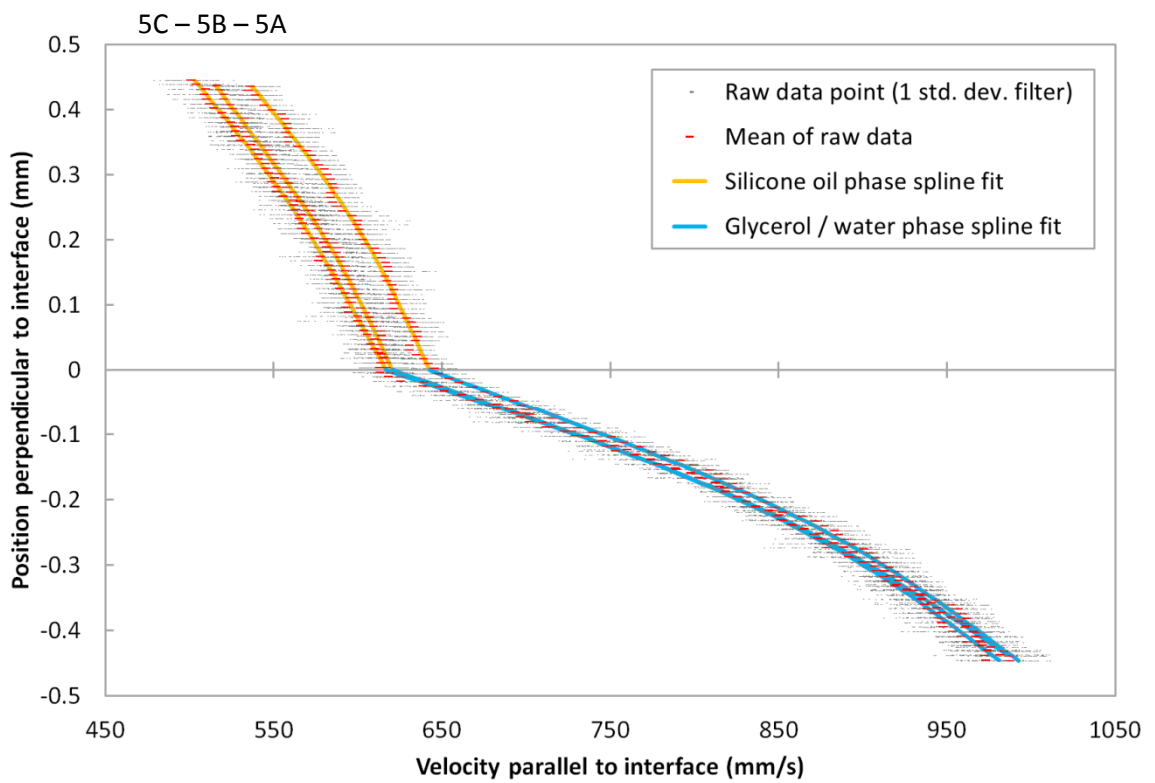
Figure 8.12: Velocity profiles 5mm upstream of the contraction apex at the three locations scanned across the cell centre line

From figures 8.10 – 8.12 we can see that in general, the data sets from each position across the channel width closely agree with each other. Though the scales change in the figures, we also see closer agreement between the data sets close to the contraction apex, which would be expected given the closest approximation to a 2D flow field at this location. In figure 8.10 we see that at the channel centre (set 30B), higher velocities are present than at locations nearer to the side walls (30A and 30C) as expected as here the vertical walls are dominant. Further downstream, interface tilt becomes the dominating factor, with set A's (located furthest from the upper channel wall) featuring the highest velocities. In all data sets, we can see that shear rates are clearly lower in the more viscous oil phase compared to the less viscous aqueous phase. The maximum shear rates running laterally across the channel cross section (between the differences in velocity profiles) are $15s^{-1}$, which compares with shear rates in the aqueous phase of up to around $1000s^{-1}$, favourable in assuming that shear is solely contained within the measurement plane.

In order to fit the data in these graphs, whilst parabolic profiles were found to closely agree with the data, smoothed spline curves have been used, as detailed further in the appendix. Velocity profiles deviating from parabolas are expected with a non-Newtonian shear field, and especially in this case, one also featuring a superposed gradient in extension rates. Whilst a parabola could be used for the oil phase data and a spline curve for the aqueous phase, spline curves have been used to fit profiles in both phases for simplicity.

During the curve fitting process, it was noticed that the interface discontinuities in velocity data appeared to be at different locations to that suggested by the fluorescence data (i.e. deviating from the vertical centre of the realigned images). This was manifested in an apparent "slip" velocity between the spline curve fitted data for the two phases. The analysis program, written to analyse the vector data, was modified to iterate the interface location until the slip velocity reached zero. Figure 8.13 shows how this interface position iteration procedure altered the measured shear rate ratios. We can see that with the exception of data set 17_5B, this iteration procedure has generally caused a convergence of data sets towards the shear rate ratio expected. This convergence shows the assumption of zero interface slip to be essentially valid. The process is also confirmed by noting the apparent concentration of particles in figure 8.7 to be offset from the fluorescence aligned images by +7 pixels, and the same negative shift was required (see data set 30B) in figure 8.13. Shear rate ratios change substantially as vectors are transferred across the interface, however in the apparently flat regions the shear rate ratio is still changing in exported data, but on order 10^{-10}.
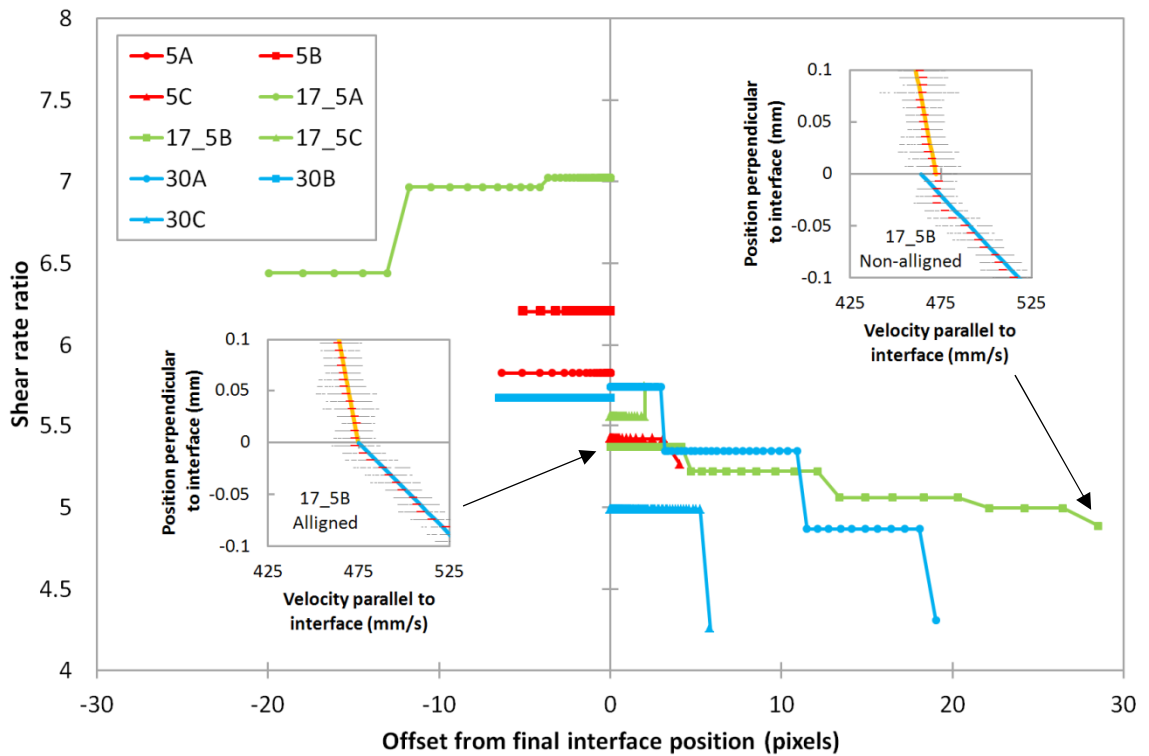
Figure 8.13: Effect of iterating the interface to satisfy zero slip velocity on shear rate ratios determined. Inset plots show cropped velocity profiles for data set 17_5B before and after satisfying the zero slip criteria.

In terms of data on interface position and errors table 8.4 provides a summary. This is condensed into three parameters. The first is the shift in the average interface position from before taking PIV data frames to after, evaluated with a 50% brightness threshold, dependent on interface drift and camera wobble. The second is the worst case maximum minus minimum interface position out of the before and after data sets, a measure of interface wobble frame to frame. The third is the average interface position difference, based on using 65% and 35% thresholds, a measure of the optical uncertainty of interface position. The offsets from correcting for zero slip velocity are also included.

We can see from table 8.4 that with the exception of the "30" data set, that the interface position is essentially reproducible before and after taking the PIV data. The 30 set, being further upstream and the first set to be taken, is more susceptible to interface drift and wetting shifts; care with interchanging the filters may have also improved during the experiment. Data set 30C in particular features a velocity profile notch at the interface location which a shifting interface may in some manner of contributed to. The max-min position information shows the interface to be relatively oscillation free and within the height of one interrogation volume. With regards defining the optical position of the interface, we can see that there exists a

substantial uncertainty band, nominally 20 – 30 pixels. The true interface location within this band may not always reside at a known brightness threshold, depending on how a tilted interface contributes to brightness across an image, and it is likely that fine tuning the true interface position by the zero slip assumption (which produced shifts below this uncertainty range) will always be necessary.

Data set	Interface fluorescence data			PIV data
	Average position shift before to after sets (50% threshold)	Max position – min position for before and after, worst case (50% threshold)	Position of 35% threshold - position of 65% threshold average	Zero slip correction
30A	-32.3	18.5	+30.1	-19.0
30B	-18.1	8.6	+31.6	+6.5
30C	-20.2	11.0	+25.6	-5.8
17_5A	+5.8	19.5	+35.9	+19.9
17_5B	-8.3	12.8	+30.7	-28.5
17_5C	-7.4	6.7	+22.3	-2.0
5A	+4.8	7.6	+28.4	+6.3
5B	+8.0	6.6	+22.2	+5.1
5C	+4.7	3.4	+24.7	-4.1

Table 8.4: Summary of interface position and error information. Positions and shifts are reported with increasing Y value running up a frame, bottom to top.

As part of the fitting process, a number of filtering and fitting parameters were considered: Binning of data points around mean values by standard deviation, exclusion of vectors around the interface, and the smoothness of the spline curves used. In the raw vector fields there is a propensity for erroneous vectors to be located towards the upper and lower frame edges (partly due to image rotation, and hence the Y location filter in table 8.2). Erroneous vectors also exist where intensity falls off on horizontal beam edges, but make it through other filtering criteria. Rather than manually masking images, systematic standard deviation filtering is thus attempted. Since velocities at a particular Y coordinate are clustered around a mean, with a distribution extending from the lowest to the highest values across the frame left to right, filtering by standard deviation also serves to narrow the vertical slide of vectors being considered from a vector field. Excluding vectors a certain number of pixels from the interface investigates whether the overlap of the interrogation volumes (16 pixels high) across the interface is having a detrimental effect. The effects of these criteria are presented in figure 8.14. As can be seen, neither of these parameters have any particularly clear impact on the shear rate ratios determined. As some filtering of outlying points is good practice, and as excluding pixels either side of the interface caused the zero slip minimisation process to

become increasingly unstable, retention of data points within 1 standard deviations of the mean and no exclusion margin are taken forward for future work.
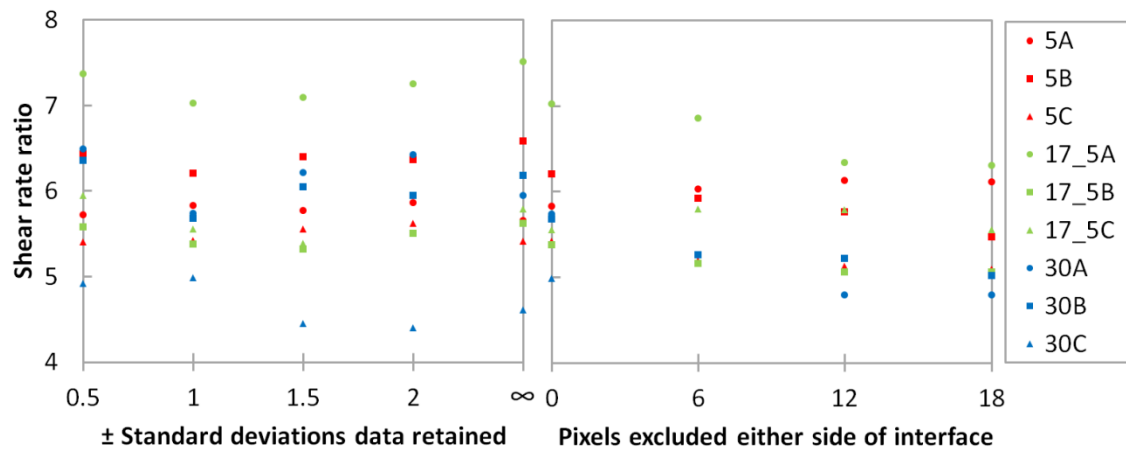
Figure 8.14: Effects of standard deviation filtering and pixel exclusion around the interface on shear rate ratio values determined.

We now consider the impact of differing amounts of smoothing applied to the spline curve fits used. This parameter is critical: the spline curves must accurately following the general data trends whilst rejecting small velocity fluctuations. Figure 8.15 shows differing amounts of the "smoothing" parameter applied to the spline curve fitting function in LabVIEW (as detailed in the appendix), and how this affects both the form of the fitted velocity profiles and the shear rate values determined. For a smoothing parameter of 1.25, the spline curve fits are sensitive to local velocity fluctuations as clear by the insert figures, generating wide (and indeed negative) shear rate ratios. Data sets 30A and 30C are particularly susceptible, featuring "notches" in the velocity profiles at the interface, something excluding pixel margins could strictly help with. At the other extreme, using a smoothing factor of 160 does not correctly follow the velocity profile trends with a resulting flattening behaviour evident. Between these two values, a smoothing factor of 20 is successful at rejecting profile perturbations whilst also avoiding the systematic reduction in shear rate ratio which follows with higher smoothing values. At this smoothing value, data clusters around a shear rate ratio of about 6; comparable to crude ratio viscosity ratio estimate in section 6.4 of 7.6 (a smoothing factor of 10 gives data around a closer ratio of perhaps 7, but with much greater scatter). Of course, these tests are at a temperature of ~22.5°C, not 25°C at which the estimate is based. Glycerol-water mixtures and no doubt the silicone oil feature strong viscosity temperature dependencies, most likely not of equal gradients. RI adjustments will also have shifted the composition, but by an amount insignificant compared to the errors in the viscosity ratio estimate. Note we cannot say choosing a high smoothing factor always means shear rate ratios will be lower than in reality,

different velocity profile situations would likely cause the converse to also occur, and an optimum must be used.
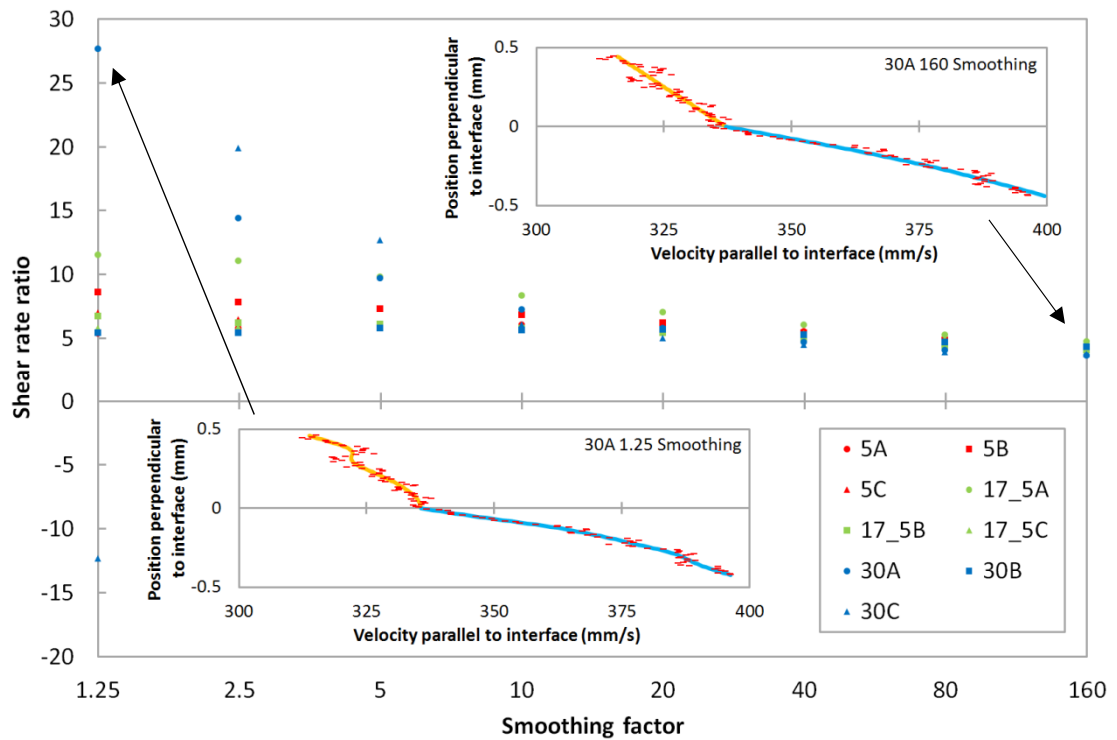
Figure 8.15: Effects of smoothing factor on shear rate ratios and velocity profiles. Inset plots show the effect on the 30A data set velocity profiles (raw data points omitted for clarity).

Aside from evaluating shear rates across the interface, we can also consider whether extension rates along the interface can be found from PIV imagery. This is less important than shear rates and also difficult to perform accurately - extension rates can also be found from increases in the interface velocity between imaging locations, rather than confined within one frame with only a small horizontal velocity gradient. Nonetheless, if it can be found it offers more information on the velocity, and thus temporal space, as a fluid packet propagates down the channel.

In the shear rate determination, we implicitly assumed velocities to be similar at equal distances from the interface, even though a slight increase occurred due to extensional flow, and the data was grouped together. In this case, large changes in velocities are present running perpendicular to the interface, and data sets cannot be grouped together. Extension rates also vary with distance from the interface. However, there is insufficient data contained along the interface to determine the extension rate, with noise being on the order of the true difference between the left and right sides of the imaged region. Fortunately, there is a simple argument by which data can be collapsed to the interface position, which is illustrated in figure 8.16.
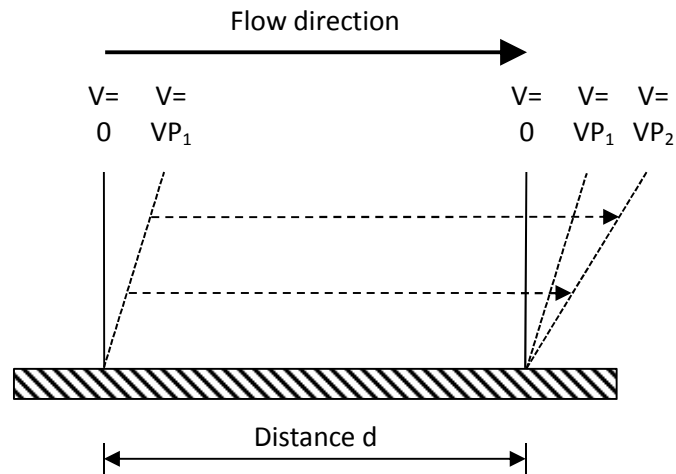
Figure 8.16: Influence of a shear gradient on extension rates. Fluid packets travel a distance d, over which the velocity profile accelerates from V = VP_1 to V = VP_2. The profile is assumed to be linear for illustration purposes.

Consider a distance of wall, d, over the surface of which a shear flow is occurring. Over this distance, the flow is caused to accelerate, e.g. due to a contraction. The velocity profile moves from VP_1 to VP_2 over this distance. It is thus clear that for very close to the wall, over distance d, that a negligible change in velocity will have occurred, with a correspondingly low extension rate. Further from the wall, velocity changes and thus extension rates rise. For a linear velocity profile, extension rates rise in proportion with distance from the wall. More generally for an arbitrary velocity profile, we can say that extension rates are proportional to average velocity. This only holds if the velocity profile "tilts over" uniformly from VP_1 to VP_2. As the average velocities are accurately known from the profiles in figures 8.10 to 8.12, the ratio between the value at a perpendicular coordinate and that at the interface can be used to collapse data onto the interface. Data points at all Y coordinates are used, with the exception of the Y location filter in table 8.2. To exclude far outliers, data points are cut off if they lie further than 0.1m/s from the average interface velocity (reasonable, as a scatter free data set would need extension rates in excess of $140s^{-1}$ extension rate to reach this limit). Standard deviation filtering at each position along the interface is again attempted. A linear profile is fitted through the resulting data using the bisquare method in LabVIEW, providing good outlier rejection. The gradient of this fit provides the extension rate. Figure 8.17 presents the collapsed data (no standard deviation filtering) and bisquare fit for data set 5B. Figure 8.18 presents the effects of standard deviation filtering on the data sets: "Theory" estimates of extension rate are also presented based on the average interface velocity, and assuming the streamline was accelerating perfectly according to the hyperbolic reduction in channel width at the measurement location.
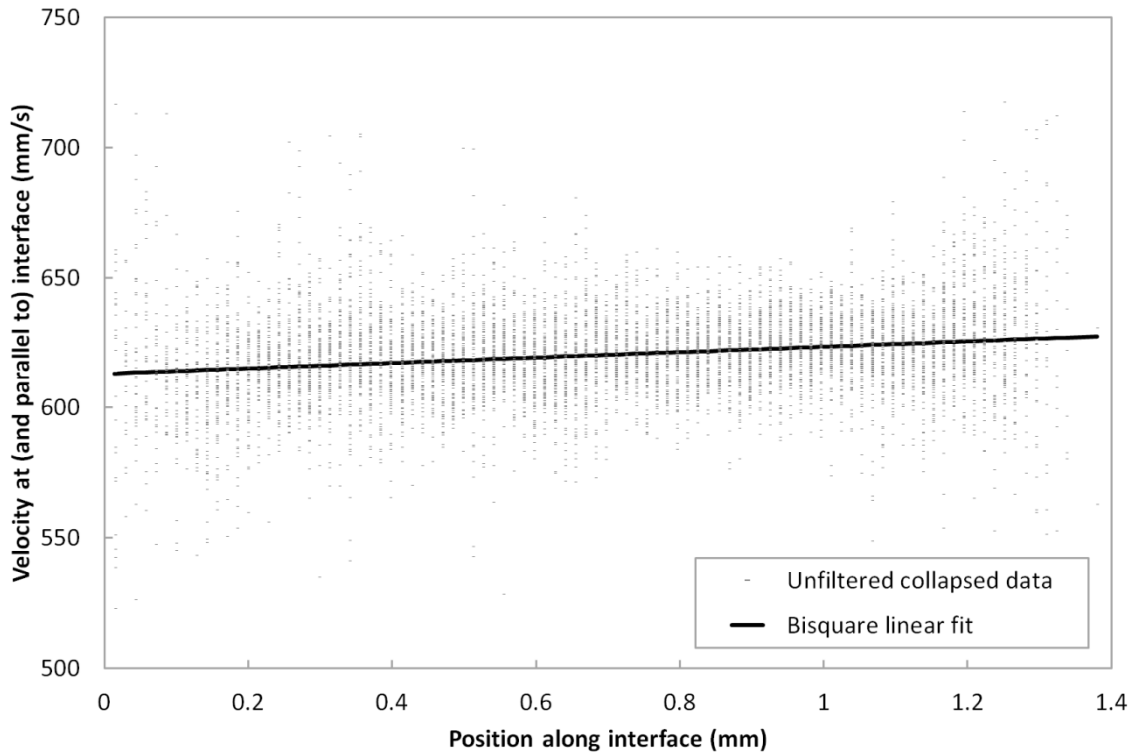
Figure 8.17: Unfiltered collapsed velocity data along the interface for data set 5B and the bisquare linear fit being applied
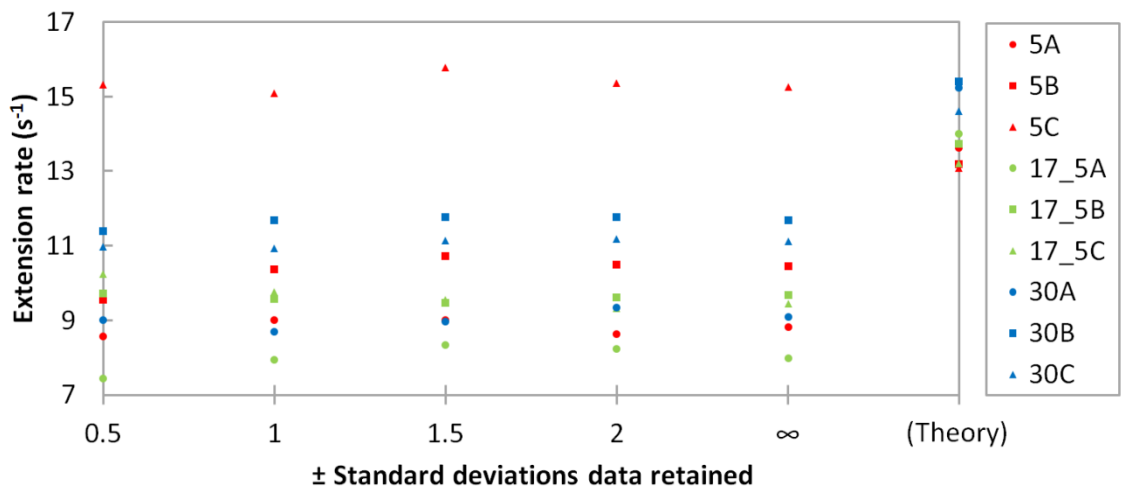
Figure 8.18: Effect of standard deviation filtering before applying the linear data fits on determined extension rates. Theoretical extension rates based on the average interface velocity and the channel geometry at that location are also presented.

From figure 8.17, it is clear that even with the data collapsing performed, there is a significant amount of scatter in the data compared to the velocity difference across the width of the frame, as expected for the short field of view and limited extension rate. As figure 8.18 shows, similarly to that in the shear flow case standard deviation filtering has negligible useful impact

(at low standard deviations, the retained data points clearly fluctuate either side of the linear fit). We can see that all the data sets have extension rates around $9 - 11s^{-1}$, expected as all data sets lie within the hyperbolic contraction region of the channel, and at least in the correct order of magnitude expected from theory. The exception is data set 5C at around $15.5s^{-1}$, lying closer to theory but further from other data sets, though comparable with the scatter of other data sets if they were clustered around some common value. The fact that there is not a substantial discrepancy in interface position for this data set, and similarly that the average velocity is very close to sets 5A and 5B, suggests the difference in extension rate to be an artefact of the (rather approximate) velocity gradient determination process.

To summarise from this initial work with a Newtonian validation test fluid, aside from developing the necessary image analysis processes, it has been shown that from the fluorescence data that the interface is adopting a configuration that is amenable to the 2D flow field assumption sought. This is further supported with velocity profile comparison and shear rate estimates running laterally across the channel cross section. Errors in locating the interface, and the stability of the interface, have been carefully considered and found to be manageable with adjustment of the assumed interface location. With proper choice of filtering parameters (1 standard deviation retention and a smoothing factor of 20), shear rate ratios close to that expected can be successfully extracted with resilience to noise in the velocity profile data. Furthermore, as the values do converge despite the different acceleration rates (with respect to time) of fluid packets at the three measurement locations down the channel, and given the significant velocities and low viscosities used, we can say that fluid inertia does not appear to contribute to these measurements. Extension rate measurements based on the data solely contained within one imaging frame were also attempted. However, taking this forward better accuracy will likely be attainable by evaluating extension rates via the velocity gradients between separate imaging locations.

8.3   Perpendicular imaging: "Liquid-liquid" index matched approach – PEO Test experiment

We now move onto testing a viscoelastic system with the liquid-liquid index matching approach. As previously, raw data is presented in the appendix. For work such a test system, the same solution in section 8.1 was used ($4x10^{6}$ MW PEO at 1.2wt%), except dissolved in glycerol-deionised water solution to satisfy the index matching requirement. An initial glycerol-water percentage was first estimated from regression based on refractive index measurements of a preliminary test sample. Dye levels were used as per the verification work and seeding used at a similar level of 0.16g/L. Seeding particles (previously sonicated in the glycerol/water solvent mixture) and dyes were added during the heating/stirring dissolution process to spread

them throughout the bulk volume. Stirring of the polymer solution at 60°C for about 4 days was required for full solvation, compared to the 2 days previously, likely on account of the poorer solvent used. The refractive index of the prepared aqueous solution was fine-tuned at lab temperature against that of the silicone oil whilst thorough stirring could still be applied, with final glycerol-water ratio of about 52.81wt% glycerol after cumulative adjustments. This solution was then refrigerated until required, and allowed to return to lab temperature before use. The same initial seeding density was utilised for the silicone oil phase, and only the oil phase necessitated infrequent reseeding on account of the high zero shear viscosity of the aqueous phase.

Since the flow cell was previously filled with the required silicone oil and the index matched glycerol water mixture, full dismantling and cleaning of the experiment was not deemed necessary, unlike the previous experiment transition. Instead, the aqueous loop was carefully drained (but not allowed to dry) and filled with the polymer solution. This was then slowly run through the flow cell, displacing the previous glycerol/water mixture, which was collected directly at the pair of outlet pipes and discarded. Note that this process, together with the RI fine tuning, will both serve in addition to those noted in section 8.1, to slightly reduce the polymer solution concentration. Degassing of the test solution was conducted once prior to loading, and again when loaded into the experiment. During experiments, some slight astigmatism of tracer particles very close to the interface was noticed, characteristic of a minor RI mismatch. No attempt was made to correct this as once the experiment is loaded, thorough and even distribution of an adjustment sample throughout the entire rig is difficult (and risky). No evidence of detrimental effects were systematically visible in the velocity profiles recorded.

In terms of flow rate (ratio) choice, we follow the reasoning previously that it is ill-advised to locate the interface on a significantly flat region of the overall channel velocity profile. However, there now exists a trade-off with respect to shear rate: operating with the interface further down the side of a velocity profile peak increases shear rate ratio determination accuracy, but also increases both shear thinning (masking extensional effects sought) and necessitates shear rate ramps to higher peak rates (if over longer timescales) from a comparison shear rheology experiment. It also reduces extension rates attained. Via trial and error to establish the flow rates and timed sample collection to measure them, flow rates of 2.25cm^3/s and 4.27cm^3/s for the aqueous and silicone oil phases respectfully were used for this work. Figure 8.19 shows the flow cell under these flow conditions, and under both UV and laser illumination. Tracers in the oil phase had dropped out to a significant extent by the time the photo was taken.
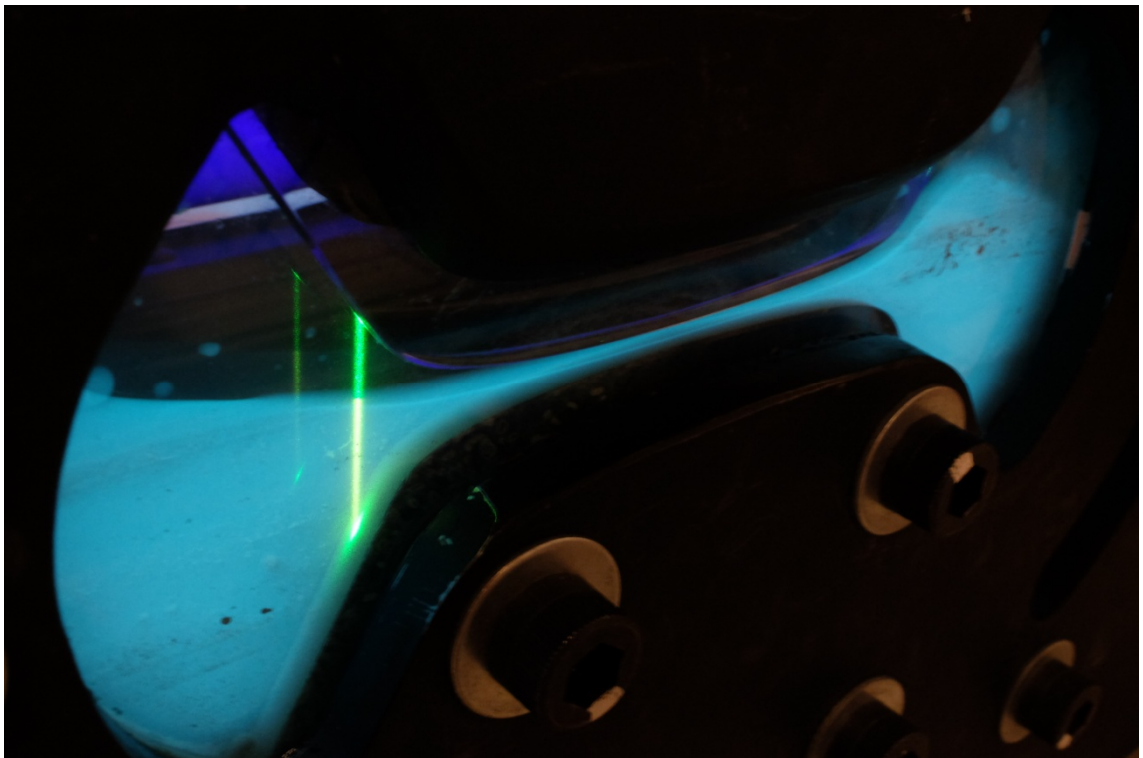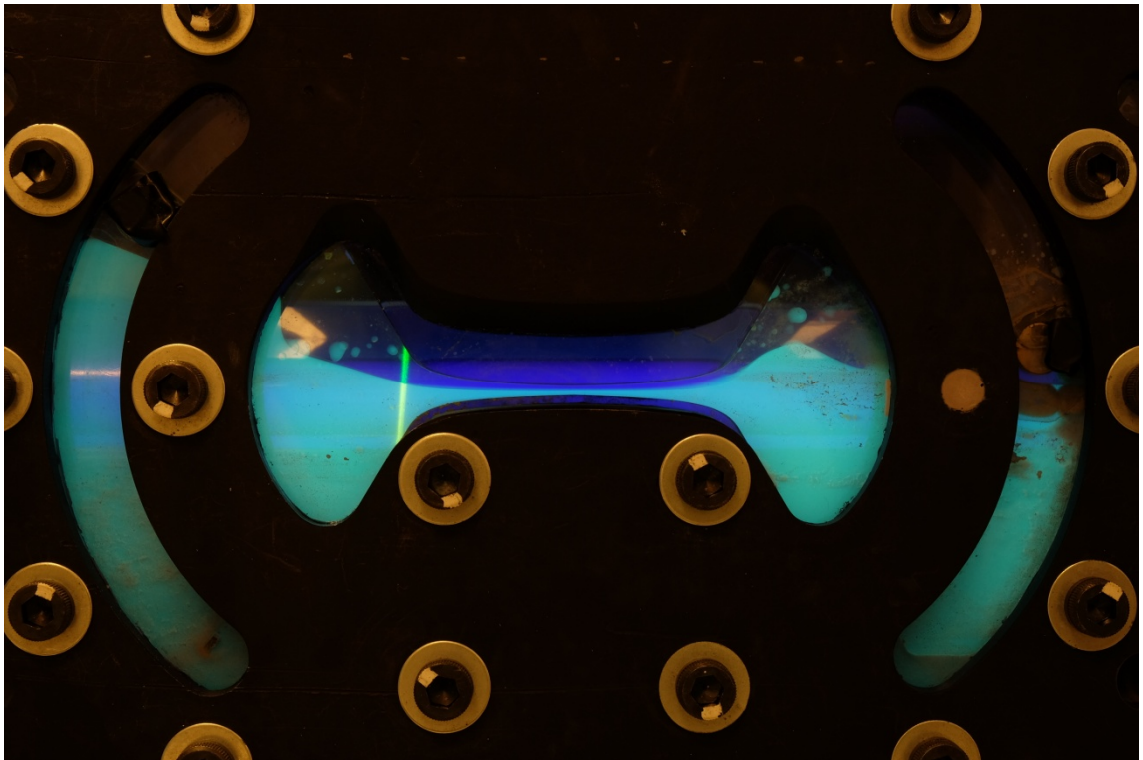
Figure 8.19: Top: Flow cell under flow conditions, with both UV and laser illumination; bottom: inclined view showing interface structure. These photos were taken at different times and will have slightly different interface positions.

Figure 8.19 firstly shows the utility of the dyes, the rhodamine B dye fluorescing orange when illuminated by the green 532nm laser beam, as used for locating the interface, and the pyrannine 01 dye fluorescing green when illuminated by UV (lamp behind the cell) for

experimental control. These photographs were taken at the end of work, hence the accumulation of silver tracer particles on the inside cell walls. Fluorescing islands of the aqueous phase can be seen, these are not droplets, rather stubborn regions that have attached to the cell walls: no travelling droplets were present anywhere in figure 8.19.

In terms of the lateral flow structure, the inclined view in figure 8.19 complements figure 8.9 previously. All work in this section was accompanied by equivalent fluorescence scans to those performed previously, at 3mm upstream of the contraction apex, to confirm the interface was essentially flat at this critical location. What is visible is a strong interface asymmetry far upstream, leaning in the same direction as the profiles in figure 8.9, indirectly linking to the previous discussion.

In terms of the interface profile down the length of the channel, this is affected by the upstream flow splitter, which is set in a location to avoid the central bolt and such that the aqueous phase does not attempt to creep around it (i.e. unbalanced pressures either side), a process that causes droplets to detach and propagate down the channel. The downstream flow splitter is serving minimal purpose here, differential accumulation of fluid principally dictating the interface location. Despite these factors, surprisingly for this highly viscoelastic system the upstream interface is following a nearly linear path and both the upstream and downstream interfaces are very stable, without spatial (or indeed temporal) "wobbles" that might be otherwise expected as tensional strain accumulated or shear thinning occurred. Downstream there appears to be die swell (and the interface position of course still drifts), but this may be coupled to (possible) secondary flows and wetting preferences in this region. Videos are provided via the appendix that show the experiment under flow conditions, as well as a timelapse over the course of an entire experimental run.

The work in this section totalled about 5 hours of continuous, contacting two phase flow, spread over multiple runs. Figure 8.20 shows the receiver reservoirs for the oil and aqueous phases under UV illumination on completion. The relatively small number of droplets of the aqueous phase in the oil receiver (generally formed during experiment start-up, and unchanged from the verification experiment work) and the lack of a significant oil layer on top of the aqueous phase (though PEO is a stabilising agent as previously noted in section 6.4) clearly demonstrates that stable flow contacting and separation has been successfully achieved in this work.
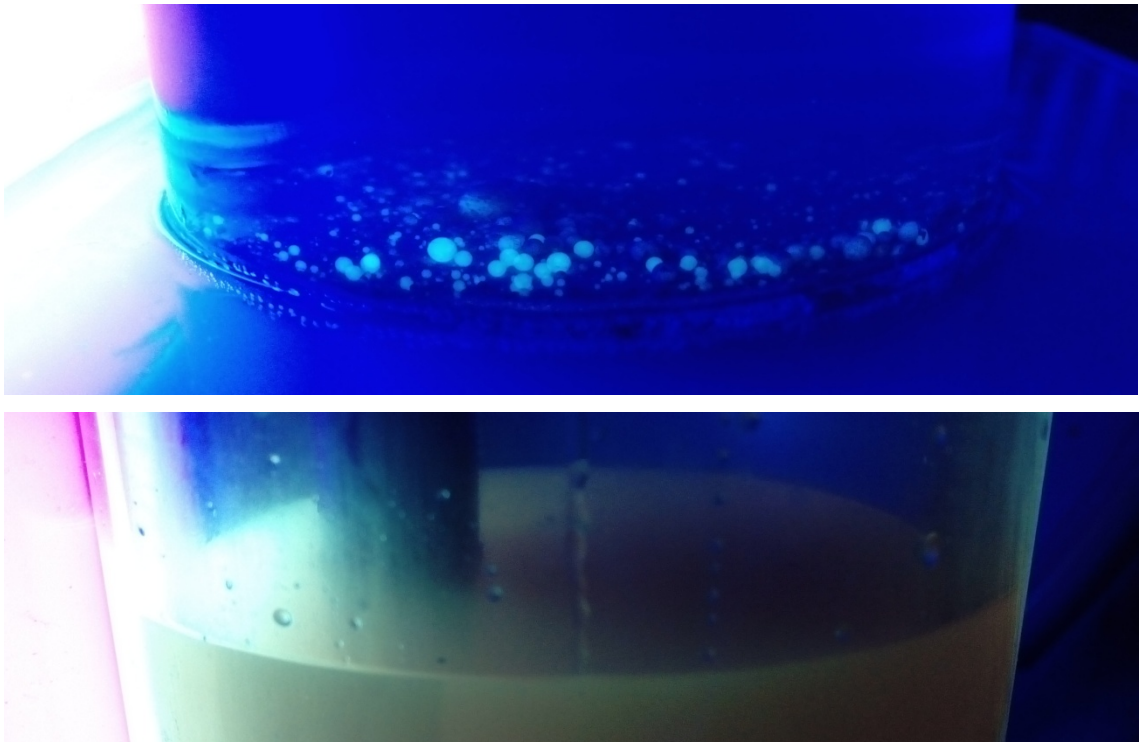
Figure 8.20: Photographs of fluid receivers, under UV illumination, at the end of experimental work. Top: Bottom surface of the oil receiver (showing aqueous phase droplets); bottom: fluid free surface of the aqueous phase receiver (where oil would settle out). Receiver outer diameter: 7cm.

In this section, three repeats (runs 1, 2, and 3) of an experiment were performed where the imaging system is scanned down channel lateral centreline and PIV data taken at between 8 to 10 locations. Measurement locations were added and in some cases moved slightly between runs to address data quality issues upstream (principally from the strong interface tilt) or to investigate further into the expansion region, which can be subject to interface position drift. Distances between the measurement locations are evaluated as straight lines. Average temperatures for these runs between the four thermocouples were 22.7°C, 22.6°C and 22.9°C respectfully, and at the end of each run a sample of the aqueous test solution taken for later analysis in the shear history recreation experiment. Figure 8.21 and 8.22 show velocity profiles at two representative points of interest from run 2: 3mm upstream of the contraction apex, and 28mm downstream, with the largest of differences in shear rate ratio. Figure 8.23 shows results for the aqueous phase shear rate and shear rate ratio between phases for the three repeat experiments (shear rate ratio proportional to aqueous phase shear viscosity). Figure 8.24 shows the same results, except evaluated with 30 pixel exclusion zones either side of the interface (as per those attempted in the previous section). Figure 8.25 evaluates the interface velocity down the channel.
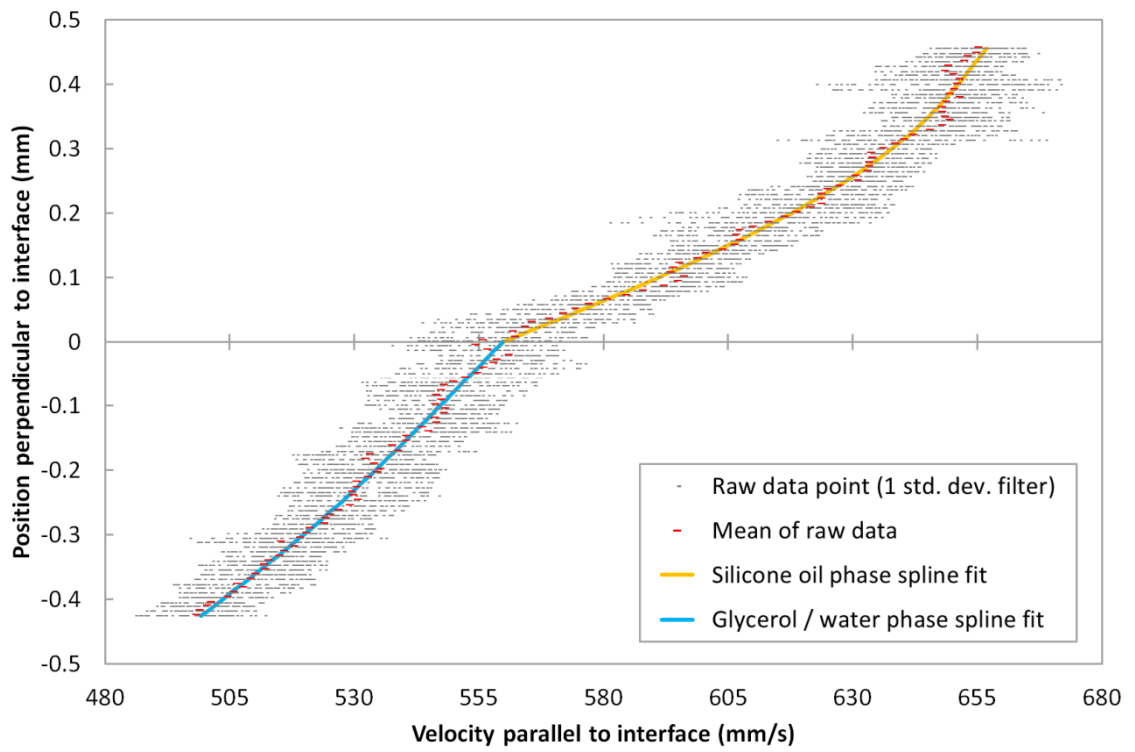
Figure 8.21: Velocity profile across the interface for run 2, at 3mm upstream of the contraction apex (no pixel exclusion zones applied)
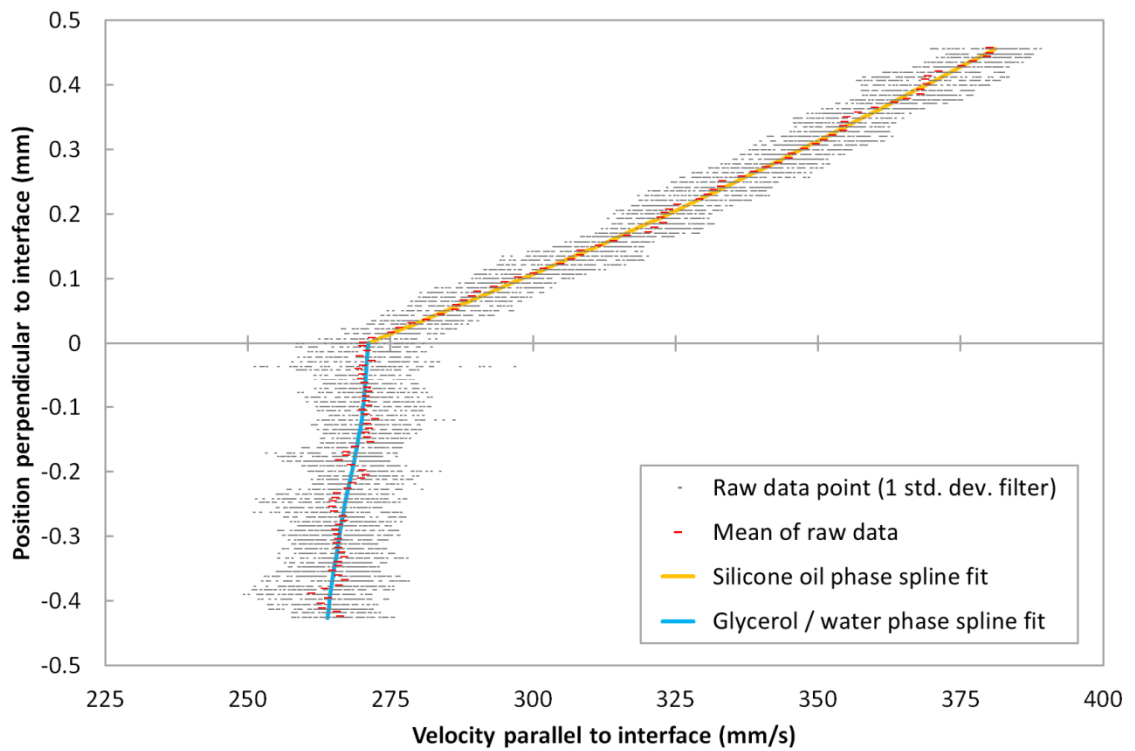
Figure 8.22: Velocity profile for run 2, at 28mm downstream of the contraction apex (no pixel exclusion zones applied)
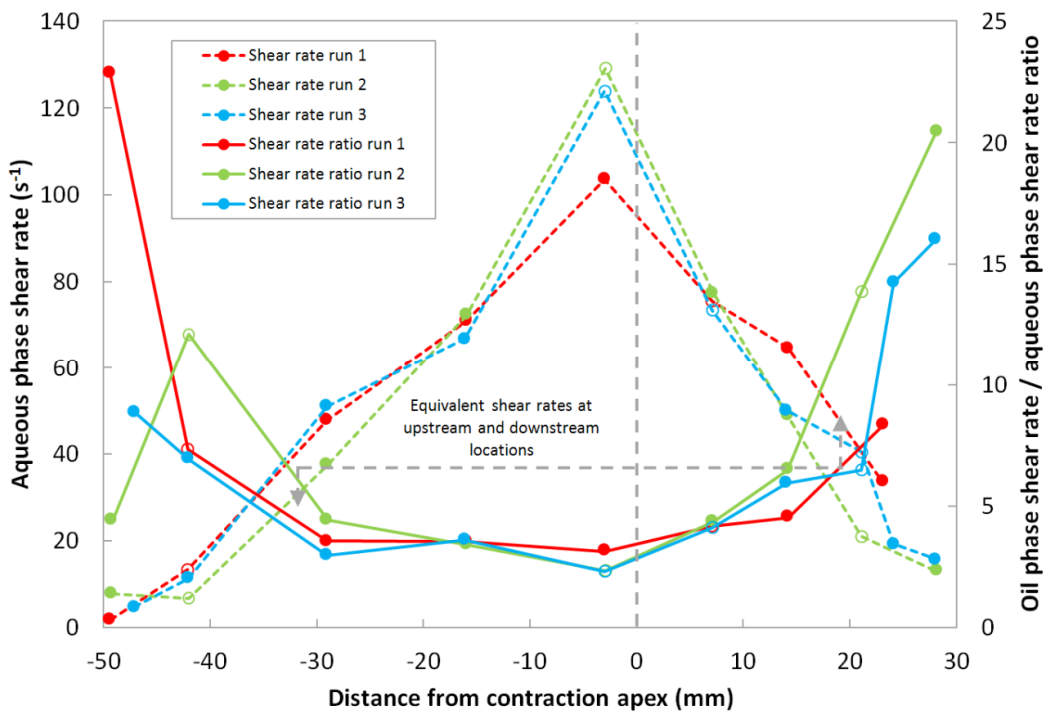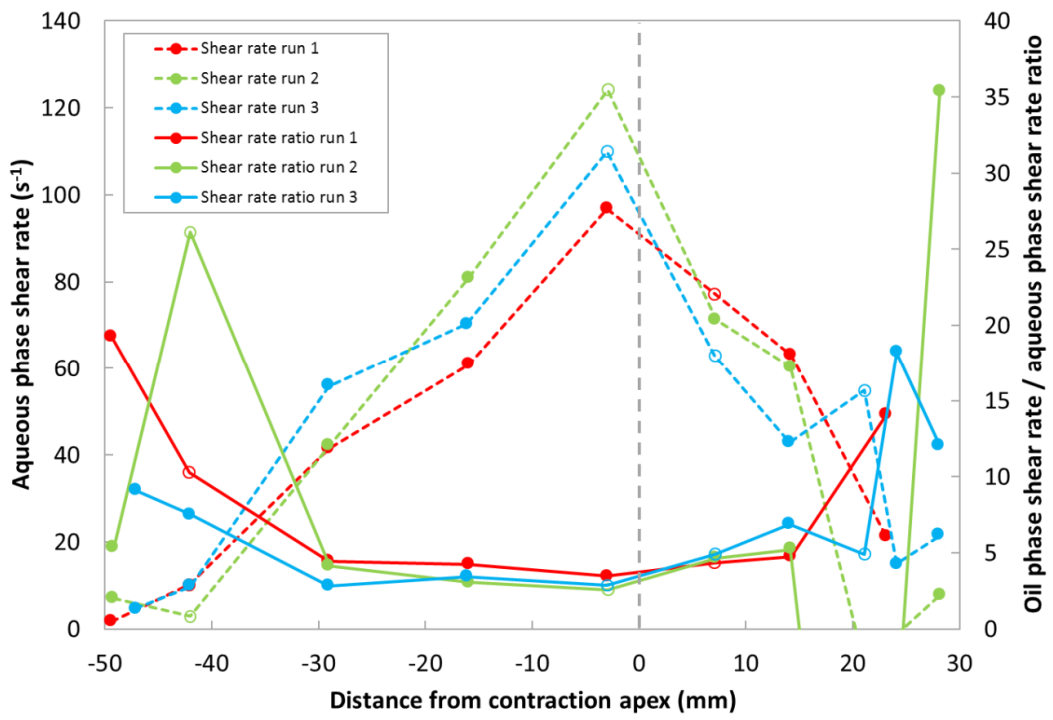
Figure 8.23 (above) and 8.24 (below): Shear rates in the aqueous phase and the ratio between the shear rates in the two phases plotted against linear position through the channel: 0 pixel and 30 pixel exclusion margins either side of interface are applied to data, respectfully. Lines join data points to aid visualisation. Non-filled data points denote reduced-confidence data sets (see text).
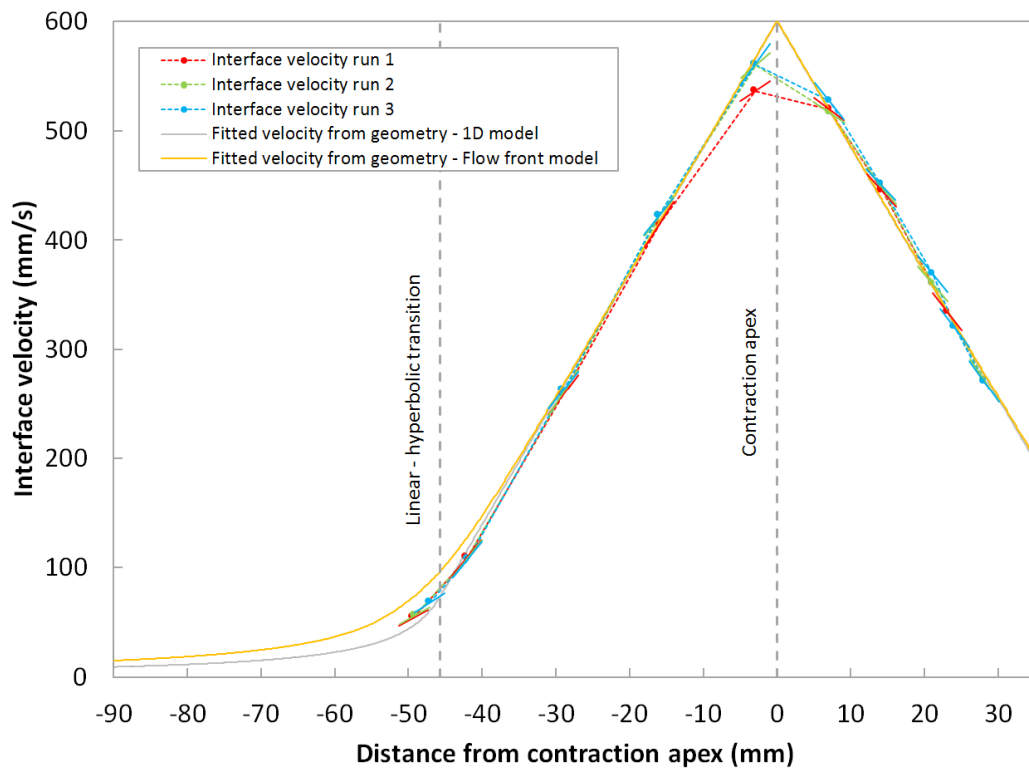
Figure 8.25: Interface velocity against linear position down the channel for the three experimental runs (data points, joined by dashed lines to aid visualisation). Flow exits the distributor at -90mm. Velocity profiles based on a 1D and flow front geometry analysis are plotted, scaled in Y to match the experimental data, both with extension rates of 11.5s^{-1} and -11.5s^{-1} in the contraction and expansion regions, respectfully. Solid lines at data points denote the velocity gradients as determined across the width of PIV images.

We can see from figure 8.23 that as expected for this shear thinning test system, as shear rates rise down the contraction, the shear viscosity of the aqueous test phase falls. As the fluid passes the contraction apex and shear rates fall, the viscosity then rises again. Figures 8.21 and 8.22 clearly show this change in aqueous phase viscosity in terms of velocity profile data. In addition, contrasting to figures 8.10 to 8.12, the lower aqueous phase is now travelling slower than the upper oil phase, which instead now contains the velocity profile peak, a function of the change in viscosities and the choices made with regards flowrates.

There is considerable scatter between the three experimental runs in figure 8.23, with one data point even exhibiting an unphysical negative shear rate ratio (despite the use of the justified smoothing factor in the previous section). When shear rates are higher, the shear viscosities are almost always lower, which fits with the shear thinning description of the test fluid. However, from figure 8.25, we find that the interface velocities between the three runs are

almost identical, suggesting that flow conditions remained most likely constant despite restarting the experiment. Conversely, data scatter would produce the same effect: overestimating the aqueous phase shear rate would cause a reduction in the calculated shear rate ratio (i.e. aqueous phase viscosity). The scatter is due to the inherent difficulties in this experiment: evaluating not one, but two derivatives, with noise, and then calculating the ratio between them. Various data points exhibited "anomalies" near the interface, such as the notches in velocity profiles already mentioned, which have substantial effects on the determined shear rates. Sets containing these are indicated in figure 8.23 and 8.24 by non-filled markers, and figure 8.22 is one such data set. The data set producing the negative shear rate ratio features a particularly large profile notch. There is no clear correlation between positions and when such data sets occurred, suggesting these are random events (e.g. perhaps a bubble caused the interface position to shift mid-way through data acquisition, for example). Due to this, a second attempt is made at applying vector exclusion across the interface in figure 8.24, 30 pixels either side being almost sufficient to eliminate the notch in the negative ratio data set. The basic form of the data is essentially unchanged, but now there is improved agreement between the experimental runs. Note the lack of visible result trends from run 1 – run 3 in figure 8.24, not only are flow rates constant between experiments (figure 8.25), but systematic changes in rheology (oil pickup in the aqueous phase, flow depolymerisation, test solution degradation) are not apparent. Greater time and care was also spent performing the later runs, suggesting the circulating flow around the experiment is not having a detrimental impact. The data for both of these analysis attempts, without and with the exclusion margin, are included in the appendix.

In terms of the data in figure 8.25, apart from the agreement in interface velocities, the data is also extremely well described by simply considering the change flow area against position from geometry, and scaling to match the peak interface velocities around the apex location either by a 1D (grey line) or the flow front approach developed in chapter 5 (orange line). Such agreement might be expected for a low velocity Newtonian flow, but not for the highly complex two phase flow here with significant velocities, and is fortuitous, especially without any positional offset applied. These fits yield constant extension rates before and after the contraction apex (within the hyperbolic region) of $11.5s^{-1}$ and $-11.5s^{-1}$ respectfully, slightly underestimating the true rates in both regions, but not significantly. We also find that velocities in the linear contraction region fall between those predicted by the 1D and flow front models, certainly if a positional offset were applied. Despite the complex flows here and the lack of data into the linear contraction region, this provides some initial proof of the flow front model. Also indicated in figure 8.25 are the velocity gradients if the extension rates determined from

data from within each imaging region held. This data does capture regions where extension rates are changing, but is much less precise than that obtained by evaluating velocity gradients between imaging locations, as expected. With the data used to generate figure 8.25, we can also check whether seeding particles are isokinetic in relation to the flow field. The maximum acceleration rates in the channel approach $7ms^{-2}$. With a seeding particle density of $3.6g/cm^3$ and assuming a diameter of 10μm, the acceleration force acting on such a particle is 1.32×10^{-11}N. By using this as the Stokes drag force on the particle gives a velocity of 2.8×10^{-3} mm/s in a 50mPa.s fluid, e.g. far less than the fluid velocities being measured. The same level of motion is expected due to gravity. Note also that maximum Reynolds values are roughly the order of 50 in the oil phase (e.g. 47.95mPa.s oil, ~700mm/s, 2.61mm high channel) compared to higher value of 500 in the verification work previously. This means that for all work conducted here it is entirely valid to assume the motion of the tracer particles is an accurate representation of the flow field.

There are two key observations to be made from figure 8.24 before we look at constructing a shear history control experiment. Firstly, as shown by the dashed lines at equivalent shear rates in the contraction and expansion regions, the aqueous phase viscosity is lower in the contraction (parallel extension, +ve), and higher in the expansion region (perpendicular extension, -ve). This directly supports the hypothesis and all the evidence in chapter 3. Furthermore, consider the generalised shear rate and Oldroyd-B models, specifically equations 3.10 and 3.35 respectfully. The generalised shear rate model is sensitive to the magnitude of the extension rate, not the direction, whilst the Oldroyd-B model does include coupling to the direction (sign) of the extension rate, in the manner found here. This immediately underlines the shortcomings of the generalised shear rate description when applied to extensional flows. Secondly, from the data in Ortiz et al. (1994) we can estimate the steady state shear viscosity at different values. Extrapolating for a 1.2wt%, 4×10^6MW PEO, 50wt% glycerol solution (η_s = 5.24mPa.s, η_0 = 170Pa.s, λ_E = 24s) gives values based on figure 5b of the reference, very approximately, of 0.85Pa.s at $55s^{-1}$ and 0.6Pa.s at $110s^{-1}$. Given the silicone oil viscosity, these would produce shear rate ratios of 17.7 and 12.5, respectfully. Shear rate ratios in the channel at these shear rates are substantially lower than these estimates, and around 2.5 at the contraction apex. The fact that these are steady state values, not transient, and that many fluids exhibit stress overshoot at the onset of shear both suggest that extensional flow is having a likely influence on reducing shear viscosity. Furthermore, if the relaxation time parameter of 24s is to be believed, the extension rates are about 500 times that required for accumulation of macromolecular strain given the definition in section 5.1. 24 Seconds appears substantial for a relaxation time however, without rheological experiments to confirm it, it must be taken as

read. Whilst intrinsic viscosity values for PEO/water-glycerol solutions are present in the literature which are used with the Rouse and Zimm models to estimate relaxation times (e.g. Mun et al. (1998)), the system used here is well away from the domain of dilute solutions.

Now that data spanning the contraction region has been considered, we investigate the likely flow history further upstream and relaxation times afforded accordingly. Initially, the flow first passes through two pipes of two different diameters and lengths, followed by narrow passages before it reaches the inlet flow manifold of the cell, as detailed in section 7.2 and summarised in table 8.5. The narrower 4mm diameter pipes and 3mm passages generate high velocities and appreciable shearing, and thus cannot be ignored, yet are non-trivial to analyse. Fluid packets travelling near the centreline will experience minimal shear rates and travel at the highest velocities, but also contribute flow over a limited cross sectional area. Fluid packets near the wall travel slower, feature higher shear rates, but also contribute to the overall flow rate over a greater area. Their total accumulated strains (time integrated shear rate) are also much larger, theoretically zero at the centreline and infinite at the wall. We cannot say which fluid packets from the cross sectional area of the inlet pipes will find themselves adjacent to the interface, and a representation of the flow experienced by all fluid packets is thus required. This can be achieved by weighting measures (residence time, shear rate, and total strain) at different pipe radiuses by their contribution to the overall flow rate. A power law velocity profile is assumed given the shear thinning nature of the test fluid used, and n = 0.7 deemed a reasonable estimate. Table 8.5 summarises the results for the three pipe sections subject to the measured flow rate of 2.25cm^3/s. Other parameters of interest are also included, and the power law parameter is also varied for the narrowest pipe sections, illustrating that it only has limited effect on the estimates. This would be expected, as decreasing n produces higher shear rates, but which occupy less of the radial cross section, and thus contributes less to the overall flow rate.

Pipe section	Inner diameter (mm)	Power law index n used	Weighted residence time (s)	Minimum residence time (s)	Weighted shear rate (s^{-1})	Max shear rate (s^{-1})	Weighted total strain
1x 1960mm length	12.5	0.7	107	58.6	5.74	13.0	810
2x parallel 80mm lengths	4	0.7	0.893	0.490	87.5	198	103
2x parallel 15mm lengths	3	0.7	0.0942	0.0516	207	470	25.8
2x parallel 15mm lengths	3	1.0	0.0942	0.0471	227	425	26.7
2x parallel 15mm lengths	3	0.5	0.0942	0.0565	190	530	25.0

Table 8.5: Analysis of shear rates and residence times in upstream aqueous phase pipework

Once the fluid leaves the 3mm passages, it enters the inlet manifold. Given the stream wise flow conditions, we make the assumption that fluid packets on the centreline in the flow channel were also on the centreline in the manifold region (shear from front and back walls is zero in the flow distributor and manifold) and that the passages are sufficiently large that shear rates in other directions are low. Residence timescales however still require estimation. The fluid passes through a short rectangular section roughly 55mm long by a cross section of 16x6mm, before entering the manifold. The manifold features a cross section of 25x6mm, and very roughly, a flow length of 110mm given the flow splitter position used. Once again, analysis is non-trivial as velocities are reducing as fluid propagates along the manifold region. Here, residence times are determined throughout based on the peak velocity of a Newtonian fluid in the manifold, i.e. twice the velocity from flow rate over cross sectional area. This provides a minimum residence time estimate, reflects packets travelling along the lateral centreline, and represents the core flow through which fluid packets propagate until the very end of the manifold at the flow splitter before exiting. The first estimation method would be to assume velocities are instead constant along the manifold, i.e. all flow exits (in some form) at the location of the flow splitter. The peak velocities in the two sections (4.7 and 3.0cm/s) thus provides an underestimation of 4.8 seconds for the residence time before the flow enters the distributor slit. Conversely, if we use the principles for the flow distributor design in section 7.1, as stated the flow rate at the end of the manifold asymptotes to zero which would result in infinite residence times. Between these, the best approximation appears to be a "velocity matching" strategy. Here we tie the peak velocity entering the manifold (3.0cm/s) with an effective "face" velocity entering the distributor (110mm long, 6mm high before transition to the slit, and assuming a uniform entrance velocity across the entire length) of 0.68cm/s. The presence of the through bolt is also neglected. Making the assumption that the velocity falls linearly (for perfect distributor operation) from 3.0 to 0.68cm/s over the 110mm flow length

gives a residence time in this section of 7.0s, or a total of the two passage sections of 8.2 seconds. The approach used here is not entirely arbitrary: The residence time may be longer than 8.2 seconds, but it is unlikely to be shorter. To be shorter would require velocities exceeding the peak for a Newtonian fluid (i.e. localised high velocity streamlines), or a substantially non-linear velocity drop down the manifold, neither of which are expected for the viscous, low velocity, and shear thinning flow here. The slit distributor then adds a further 1.4 seconds (slit width of 2.4mm, entrance arc length 110mm decreasing to 70mm over a path length of 30mm), giving a total time estimate of 9.6 seconds between the inlet passages and the main contracting section of the flow channel. The time history of the channel itself can be estimated by extending the 1D geometry based velocity fit in figure 8.25 (without a positional offset it is a good average representation) back the location where the flow distributor ends at ~90mm from the contraction apex, then applying appropriate numerical integration throughout this region. From 90mm upstream to the apex, the flow duration is only about 2.9 seconds, underlining the need for the previous analysis; despite the approximate nature and the significant errors potentially thus associated. Contrast this also with the previous estimate of λ_E = 24s for this flow system. If this is true, and an accurate reflection of history retention, the experiment permits only one half of λ_E to relax before reaching the measurement zone, and upstream pipework will have an influence.

From this analysis, we now have a full time history description of shear rates that were imposed on the test fluid, both in the PIV measured region, as well as estimates of when and the magnitude of shear rates occurring far upstream. The next task is to fit the shear rate/time profiles of the experimental runs in the contracting section of the channel to some form of suitable profile. The end goal is to program a rheometer, specifically here a TA instruments DHR2, to follow the shear rate rise and fall across the contraction-expansion region, as well as the estimate of upstream shear. Figure 8.26 shows the programming page of the rheometer TRIOS software (TA Instruments, 2016), which accepts functions of strain (i.e. integrated shear rate) against time in up to 4 time domain regions.
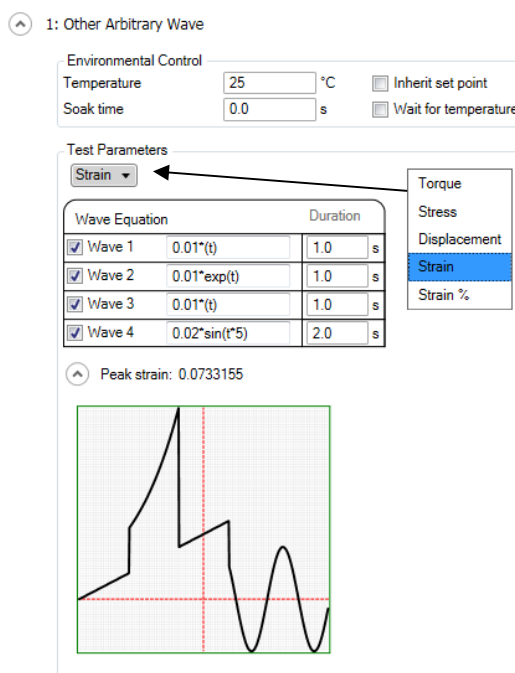
Figure 8.26: Arbitrary wave programming page of the DHR2 rheometer TRIOS software, inset shown of selection menu (TA Instruments, 2016)

Assigning a domain for the long 12.5mm diameter upstream pipe (which also permits sample distribution in the measurement geometry) and a second describing a representative shear pulse of the narrower inlet pipes and flow passages leaves two time domains, one for the shear history before and one for that after the contraction. It is possible to show from dimensional analysis (Chaffin, 2017) that shear rates - and similarly total strain - in a hyperbolic channel increase exponentially with time (this is interesting, given the comments on exponential shear being a "strong" flow in section 3.11). We therefore fit the shear rate / time history data from PIV (for each experimental run) to separate exponential curves before and after the contraction apex which can be readily entered into the software after suitable integration. The exponential curve before the apex is allowed to extrapolate back in time to the end of the shear pulse from the inlet pipes (the strain history description must be continuous). Shear rates in the linear contraction section of the channel would probably be underestimated by an exponential description. Programming limitations however make this complex to circumvent and the shear rates in this section are almost literally zero if the extrapolation is a reasonable description (noting also that the channel side walls and Hele-Shaw flow dictate velocity profiles in this region, not the upper and lower walls, c.f. the comments with regards figure 4 of Cubaud and Mason (2009) made in section 4.1). Figure 8.27 below shows the exponential curve fits in the region of the PIV shear rate data. Time starts at 0 at the inlet of the long 12.5mm diameter pipe run. Fitting has been performed in LabVIEW using the bisquare method, and the analytical intersection point between the fitted equations used to change from the rising to falling

exponential. A fair degree of variability is evident between rise and fall rates for the fits that best describe each data sets, even if they reach similar maximum shear rate values. The impact of this level of discrepancy can only be assessed by running the three experiments separately and comparing the results.
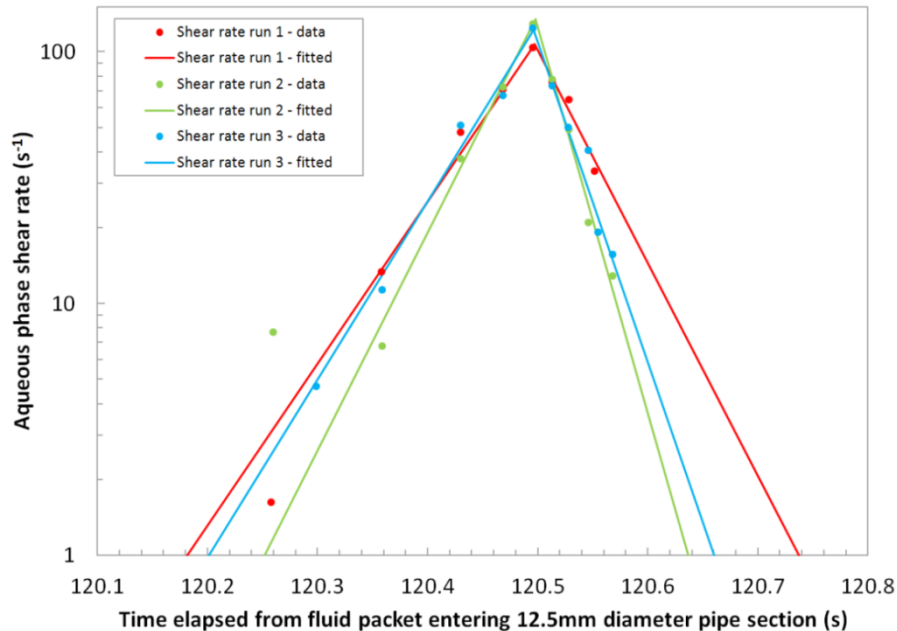
Figure 8.27: Exponential fits to the shear rate against time data in the channel contraction for the three experimental runs. Fit equations are given in table 8.6.

The final programming domains are now summarised in table 8.6 (page 248) for the three experimental runs. In table 8.5, multiplying the weighted residence times by the weighted shear rates does not equal the weighted total strains, the former basis is chosen here. For domain 1, the weighted shear rate is imposed for the weighted residence time. For domain 2, total strain is determined from the weighted shear rates and residence times for the 4mm and 3mm pipe/passage sections, summed for these sections, and converted back to a shear rate. Domains 3 and 4 are the exponential curve fits as shown in figure 8.27 and domain 4 is assigned an arbitrary duration to end the experiment at 125 seconds. Shear rates against time have been integrated to yield strain functions and appropriate integration offsets determined, a process advantageous over curve fitting directly to strain - time data as profiles are inherently continuous: discontinuities, however small, would demand infinite shear rates from the rheometer. Equation parameters, including the integration offsets, are accordingly reported here to a high level of accuracy.

Figure 8.28 shows the preview window from figure 8.26, when programmed with the domain parameters for run 1 in table 8.6. It is clear that the software can be programmed in this

unusual manner required, and sufficiently accurately to avoid discontinuities. The dominance in terms of both time and total strain accumulated of the upstream pipework is also evident.
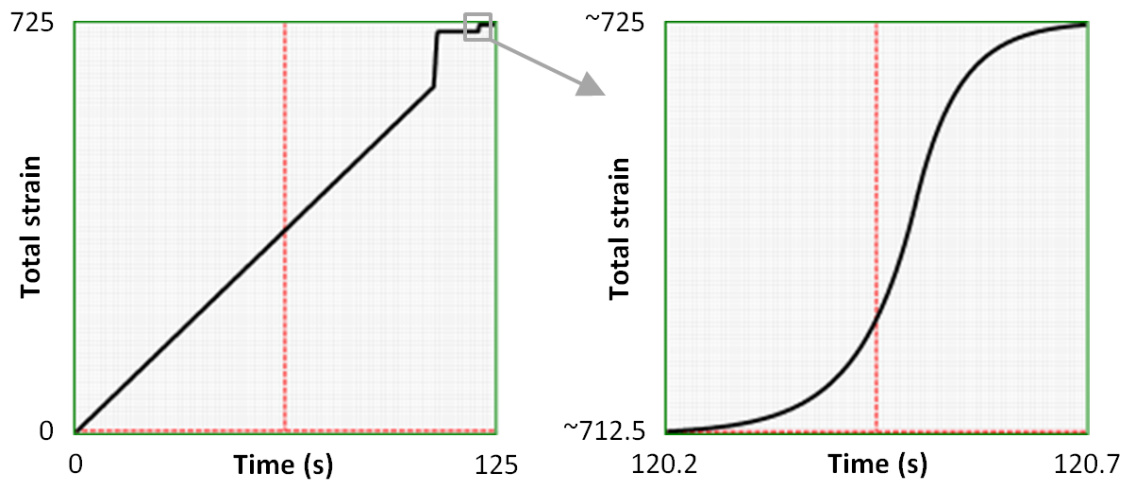
Figure 8.28: Strain vs. time preview window of the rheometer software in figure 8.26, when programmed with the domain parameters for run 1 from table 8.6. Approximate axis labels have been added for indication only. The zoomed region showing the exponential rise and fall in shear rates has been produced by editing the strain equations for domains 3 and 4 to represent a shorter time period of the overall profile for run 1.

It is at this point that, regrettably, no more work can be performed given rheometer issues noted in the thesis preface. The work remaining to be done, when the rheometer becomes available, is described next.

Domain parameters		Run 1	Run 2	Run 3
Set point temperature (°C)		22.7	22.6	22.9
Domain 1: Inlet pipes	Describes	12.5mm diameter pipe section: 107s duration		
	Shear rate (s^{-1})	5.74		
	Strain from t=0	5.74*t		
	Time interval (s)	$0 \leq t < 107$		
	Duration (s)	107		
Domain 2: Inlet pipes	Describes	4mm diameter pipe run: 0.893s duration 3mm diameter passages: 0.0942s duration		
	Shear rate (s^{-1})	98.9 (strain averaged basis)		
	Strain from t=0	614.18+(98.9*(t-107))		
	Time interval (s)	$107 \leq t < 107.99$		
	Duration (s)	0.99 (rounded)		
Domain 3: Exponential rise in shear rate	Describes	Manifold and flow distributor passages: ~9.63s duration (rounded) at ~zero shear rate. Flow leaves distributor at 117.62s into the channel contraction section.		
	Shear rate (s^{-1})	5.769711119* exp(14.80257279* (t-120.3))	2.607847203* exp(19.91794153* (t-120.3))	4.990546623* exp(16.28492426* (t-120.3))
	Strain from t=0	0.3897775880* exp(14.80257279* (t-120.3)) +712.091	0.1309295541* exp(19.91794153* (t-120.3)) +712.091	0.3064519394* exp(16.28492426* (t-120.3)) +712.091
	Time interval (s)	$107.99 \leq t <$ 120.4972318	$107.99 \leq t <$ 120.4979639	$107.99 \leq t <$ 120.4962498
	Duration (s)	12.5072318	12.5079639	12.5062498
Domain 4: Exponential fall in shear rate	Describes	Channel expansion section from intersect of exponential functions to t = 125s.		
	Shear rate (s^{-1})	14.47904106* exp(19.45600996* (120.6-t))	3.669978389* exp(35.29509152* (120.6-t))	5.848730414* exp(29.27448293* (120.6-t))
	Strain from t=0	-0.7441937525* exp(19.45600996* (120.6-t)) +724.81056	-0.1039798519* exp(35.29509152* (120.6-t)) +722.65438	-0.1997893670* exp(29.27448293* (120.6-t)) +723.74349
	Time interval (s)	120.4972318 $\leq t < 125$	120.4979639 $\leq t < 125$	120.4962498 $\leq t < 125$
	Duration (s)	4.5027682	4.5020361	4.5037502
End	Total strain from t=0	724.81056	722.65438	723.74349

Table 8.6: Programming parameters for shear history recreation in a DHR2 rheometer. High levels of precision are required to minimise discontinuities in the strain profiles produced. Rounded values are taken as precise in subsequent calculations. Equations are presented in the format as required by the rheometer software.

8.4   Conclusions

When the rheometer in question is commissioned, the experiments that are required can be split into two sets: those that are critical to generate the comparison extension free data, and those that are desirable, considering additional issues with the shear history recreation experiment.

In terms of critical experiments, firstly, a more accurate value for the reference oil viscosity is required than that provided by the manufacturers to convert the shear rate ratio into an aqueous phase viscosity. This would be performed at 22.7°C, the average of all thermocouple readings in all three experimental runs; and on the same instrument as the aqueous solutions, as calibration errors would thus cancel under comparison. For experimental rigour a shear rate sweep would be performed to demonstrate that this oil was indeed Newtonian. Similar tests would be performed on the glycerol water mixture used in the validation work and the Elite 65 / Synesstic 5 blend used in the wall – oil index matched approach for more accurate viscosity values.

Secondly the rheometer runs described in table 8.6 would be performed using a cone and plate geometry. As part of this, attainment of the shear rate profiles would need to be confirmed, either via the rheometer software, or an external encoder attached to the geometry. Furthermore, it is necessary to check with the shear ramps specified that a Newtonian fluid produces a constant viscosity value, despite contributions to torque from instrument inertia (which should be corrected for) and fluid inertia. Instrument inertia, if an issue, can be corrected for by running the experiment with no sample and subtracting the shear stresses thus recorded, providing the sample presence did not affect the rotation rate profile. Alternatively, if the instrument and geometry inertia were known, the inertial contributions could be calculated. Fluid inertia can be assessed for low viscosity fluids, minimised with low angle cones, and corrected for assuming inertia did not distort the otherwise assumed linear velocity profiles between the cone and plate.

In terms of desirable experiments, the importance of the different sections of upstream shear history would be considered: initially, a direct measurement of test fluid relaxation timescales is sought. Experiments would then be generated lacking representations of different upstream pipe runs, and the resulting viscosity profiles over the exponential shear rate ramp sections compared. An experiment would also be performed where a sequence from table 8.6 is repeated several times (with the same sample still loaded) over a timescale representative of a fluid packet circulating through the entire flow loop, to check for cumulative trends in

rheological behaviour. Necessary precautions against evaporation would be required. Following the comments in section 1.6 about the aging of PEO solutions, a set of suitable tests would also be necessary, given that samples from runs 1 − 3 are now currently in storage. It may be interesting to also perform a standard shear rate sweep on the test fluid and also compare this to the experimental data. If the test fluid exhibits stress overshoot, this would represent the maximum attainable degree of shear thinning at a given shear rate irrespective of time history, and could be compared similarly to the data from Ortiz et al. (1994) previously.

Despite these requirements, we can summarise what has been achieved in this chapter. The wall − oil refractive index matching approach was tested with a representative PEO test solution and analysed manually. The use of a corrective prism was found to yield satisfactory tracer imagery above the interface, but below the interface imagery was unacceptable with severe optical artefacts occurring, even in the limit of small distances below the interface. Comments were also made with regards the differing X and Y length scales, which were found to differ by the expected amount above the interface, but almost impossible to measure experimentally below the interface. Despite this, tracking the interface was attempted, and experience gained in operating the experiment and appropriate choice of reference oil viscosities.

The liquid − liquid index matched approach was then conducted, initially with a Newtonian validation experiment. The impact of refractive index mismatches on imagery was established, LabVIEW programs were developed for determining the interface position from fluorescence data as well as filtering and stacking tracer images, and standardised settings were determined for the PIV software used. The lateral form of the interface across the channel at three locations downstream was checked by fluorescence, and velocity profiles taken laterally across the channel at these three locations compared to check the flow field was indeed essentially symmetric about the channel mid-plane. Correction for errors in judging the interface position from fluorescence were corrected for by minimising the apparent slip velocity across the interface, and errors in both determining the position and frame-to-frame wobble in the interface location studied. Filtering and processing of the velocity profile data was discussed, including standard deviation filtering, excluding vectors either side of the interface, and the appropriate choice of smoothing to apply to velocity profile curve fits: with appropriate parameter choice the shear rate ratio measured coincided closely with that expected given the real viscosity ratio between the two fluids. Determination of extension rates from data within a single measurement location was also attempted, but later found to be inaccurate compared evaluating the change in velocity between measurement locations down the channel.

Using this system, a 1.2wt% 4×10^{6} MW PEO solution in a glycerol-water solvent was then tested at extension (and expansion) rates of $11.5s^{-1}$, with the flow field being found to be both free of instabilities and capable of being ran for many hours without any significant observed transfer of fluid between phases. Three experimental repeats were performed, the shear rates and shear rate ratios agreeing with each other, but featuring an appreciable degree of scatter on account of the inherent difficulties with evaluating derivatives of data. Unexpectedly, interface velocities down the channel were found to almost exactly agree with that imposed by the geometry. Evidence was found, despite the lack of a control shear-recreation experiment at this stage, that parallel extension promotes a reduction in viscosity in this test system, whilst transverse extension promotes a rise at identical shear rates. This supports the hypothesis and evidence presented in chapter 3, qualitatively agrees with the Oldroyd-B model and underlines the shortcomings of the generalised shear rate definition when applied to extensional flows.

Chapter 9.

Conclusions and future work.

Chapter 9: Conclusions and future work.

9.1   Key conclusions

In summary, three main noteworthy achievements were made in this thesis:

- In chapter 4, the challenges of generating a stable, laterally symmetric two phase flow approximating a 2D flow field were realised. A surface coating method was identified through which this could be achieved, and the application method improved to make it mechanically resilient for the task in hand.

- In chapter 5, the design of hyperbolic profiled channels for extensional flow was critically assessed in light of making justified, optimal design decisions. It was found that the hyperbolic shape normally used in literature makes inferences about the inlet region of hyperbolic channels that are unphysical, and negligible consideration is given to this zone in publications. A new profiling strategy was established which predicts a slightly different shape in the inlet region, and placed a maximum useful inlet angle of about 130 degrees on practical channels (the key finding). The assumptions of this strategy were critically evaluated, and the new profiling shape compared to the conventional hyperbolic profile, with slight improvements in extension rate uniformity along the centreline being demonstrated.

- In chapter 8, through the use of two phase flow and determining the shear rates in an oil reference phase and a water/glycerol PEO test phase, initial evidence in support of the hypothesis in chapter 3 has been obtained: that extensional flows affect shear rheology, with extension parallel to the flow direction serving to reduce shear viscosity, and perpendicular to the flow direction serving to increase shear viscosity. The use of two phase flows is the only way such measurements can be performed. This is currently pending recreation of the shear history experienced in the experiments on a conventional shear rheometer, which has been shown as being capable of being programmed in the required manner.

To bring this full circle, in chapter 2 the use of geometric changes to generate a range of shear rates for the purpose of shear rheometry was being discussed. It was noted that such geometric changes cause extensional flow, and from this the hypothesis in chapter 3 established. Based on the findings in chapter 8 to date, we can tentatively conclude that the results from any rheometer based on geometric changes will be influenced by extensional flow, even if it measured shear stresses directly and not pressure drops. Only shear rheometers that generate pure shear flows can be used to accurately probe shear rheology. Similarly, constitutive models must reflect that the effects of both shear and extensional deformations couple, and cannot be treated, or tested, as separate entities.

253

9.2   Future work: Tests to perform

In section 8.4, specifics of future work given the commissioning of a suitable programmable rheometer were described and desirable tests to explore the shear history recreation experiment outlined. Here, a broader overview of future experiments of interest and how the current experimental setup might be improved is discussed.

Firstly, the obvious extensions is simple parameter variation. As noted in section 3.11 the ability to alter the flow rates and their relative ratio between phases permits different shear and extension rates to be applied to a test system, e.g. the current 1.2wt% 4x10^6 MW PEO solution. Different concentrations, and different polymer molecular weights could also be studied, though given the experimental scale decreasing either considerably may not be informative. The warnings about comparing results from such a parameter study given the varying time histories (section 3.11) are however reiterated. More interesting work would study fundamentally different systems. Different polymers could be tested providing they were chemically and biologically stable when left the experiment for long periods of time, and thixotropic systems with isotropic particles were also highlighted as being of interest in section 3.11.

For any new experiment, the choice of a test system would still be limited by the requirements for refractive index matching, suitable reference phase viscosities, and optical clarity. Soluble fluorescent dyes also still need to be added. It seems likely a recirculating flow loop must be used (unless all the improvements in section 9.3 were implemented) which means studies of extruded polymer melts are rather impractical, even if one did fit the above criteria. Volatile solvents are best avoided, partly due to computability with materials and the reference phase, but also as evaporation causes dramatic refractive index mismatches. High levels of birefringence may prove problematic, but the order of magnitude would need to be checked as performed for this work. Particularly dilute or low molecular weight systems requiring high extension rates will also require a smaller scale channel than that used here to prevent flow instabilities. Also note that before further characterisation work was conducted, characterising the operating envelope of the programmable rheometer would be advantageous such that the limits on recreating shear rate ramps are known a priori.

With regards studying thixotropic systems, now we have identified the only practical method is the liquid – liquid index match, the situation becomes still more complex (assuming NMR velocity imaging is still inadequate at the time of reading). Achieving concentrated, but optically transparent suspensions can only be achieved via refractive index matching

techniques, as discussed Wiederseiner et al. (2011): for example, PMMA (Perspex) particles would disappear if dispersed in the Synesstic 5 / Elite 65 oil blend established in section 6.3. Regardless of adding the particles to an aqueous or oil phase, the refractive index of the solid particles, the index of the oil, and the index of the aqueous phase must now all be matched, and the choice of suitable oils is once again the principle limiting factor. Table 9.1 summarises the situation given the candidate particle material refractive indexes provided in the reference and the supplier value for the fumed silica used for the surface coatings in chapter 4. Using base oils from Exxon Mobil as previously detailed in table 6.1, a narrow matching range to silica based particles would be possible, though operating with almost pure glycerol for the aqueous phase is not preferable. Furthermore, note that we cannot simply add fumed silica to either an oil phase (i.e. fortuitously raising the viscosity) or a glycol phase at will. This also has important contrasting impacts on the rheology, as detailed in Khan and Zoeller (1993), Raghavan and Khan (1995) Raghavan and Khan (1997), and Yziquel et al. (1999). If silicone oils are used (and particles added to a low viscosity aqueous phase) matching to POM and PTFE might be possible, providing a candidate blending oil be identified. Most interestingly is if micron sized silicone rubber particles, if they could be sourced, which would provide a near-direct index match automatically.

Oil phase	Aqueous phase	Suitable candidates from Wiederseiner et al. (2011) (Fumed silica from chapter 4)
SpecraSyn Elite 65 – Synesstic 5 blend: 1.4667 – 1.5220 SpectraSyn 2 – Synesstic 5 blend: 1.4418 – 1.5220	Water – glycerol blend: 1.333 - 1.474	Polyvinylacetate (PVA): 1.466 Silica gel : 1.472 Glass: 1.47–1.65 (Fumed silica: 1.46)
Silicone oils (Allcosil 200/50): 1.402	Water – glycerol blend: 1.333 - 1.474	Polysiloxane (Silicone rubber): 1.40 Polyformaldehyde (POM): 1.41 Polytetrafluoroethylene (PTFE): 1.38
PFPE Oils (Krytox): 1.30	Matching not possible	

Table 9.1: Summary of potential particles to create refractive index matched suspensions, whilst also achieving a refractive index match between liquid phases. Figures show refractive indexes, or ranges attainable through blending.

In addition to changing variables and studying different systems, the results could be compared to constitutive models in more detail than the qualitative comments made, and for more advanced models than just the generalised shear rate and Oldroyd-B. The parameters for models could be established from appropriate rheological tests, the entire deformation history

fed into the models directly (simplifying their analysis), and the predictions quantitatively compared to experimental results.

Aside from testing different systems, it was commented in chapter 3 that changes in interfacial rheology may have an impact on the assumption that shear stresses are continuous across the interface. This is an assumption that, before a substantial amount of characterisation were performed, needs additional consideration. As the use of two phase flow appears inescapable for performing these measurements there is no way interfacial rheology can be avoided, however it is also a complex and delicate parameter to even measure. Fortunately in the work with PEO, the polymer is generally a long chain structure with limited branching, bearing little similarity to molecules such as surfactants which would deliberately crowd and straddle an interface. The possibility for changes in fluid properties at an interface may be an important factor in the choice of future test systems.

9.3   Future work: Experimental improvements

We now consider how the experiment might be improved, and reflect on changes if the experiment were rebuilt from scratch. In terms of cell design, the glass walls, despite their difficulty in fabrication and sealing, appear to be having an important role and would be retained. The upstream area of the cell would be made much larger to increase relaxation times beyond the inlet pipes, either by simply extending the upstream area of the cell, or more complex, fairing the cell into a larger upstream "tank", a factor that was practically limited for an initial attempt at the experiment. When the cell was designed, it was not known what level of pressure drops to expect from the extensional flows imposed, and was made capable of withstanding at least a few bars of pressure. In hindsight, the needles in the 10 bar gauges used barely lifted off the end stops, and a less over-engineered construction can be used. The required flow rates were also somewhat overestimated as a consequence (the pump output flow rate was measured and fell almost linearly with increasing backpressure: though positive displacement, the pumps feature safety return values). Through bolts in the flow region would be omitted as they cause particular flow disturbances. With regards thixotropic suspensions however, substantially higher pressure drops would be expected, particularly if dispersed in a modestly viscous oil and glycerol is used as the Newtonian reference phase. The utility of the flow splitters can be debated (e.g. given the issues with the upstream splitter in section 8.3): the experiment should be tried with and without them in the cell. Some method of sealing the narrow passages between the hyperbolic inserts and the glass walls as well as that formed by the flow distributor would be sought: It is preferable to leave the interface away from the cell centreline when not in use to avoid deposit build-up on the walls, a process that also means

the gaps fill with the opposite phase. This is ejected as a slow stream of droplets on experiment start-up. The slightly curved o-ring path on the lower hyperbolic cell half would also be made straight as it led to difficulties in getting the o-ring to stay within the channel during cell assembly. The flow distributor would be retained, the utility of which was evident by looking at upstream flow motion by eye. The location of the calibration grids would also be moved out of the flow path due to the severe flow disturbances they caused. Placing a grid on either side of the hyperbolic inserts (i.e. in the gaps) would best: focusing on the front, then rear walls of the channel and interpolating also gave correct values for the cell centreline position. In figure 8.19, the calibration grids had fortuitously broken off and lodged downstream, though the glue left on the rear wall would have still promoted asymmetrical wetting. The flow system used a substantial number and types of materials in construction and sealing, this may wish to be revised in future designs for chemical compatibility if necessary. Finally, a less crude mass flowrate measurement than opening the fluid receivers during a running experiment to take a timed sample would be preferable.

With regards optics, it is highly unlikely (in the authors opinion) that the wall – oil refractive index matching approach could ever be made to be successful. In terms of the refractive index match for the liquid – liquid approach, though fluid temperature stability between runs was good, the lab temperature was prone to oscillation. Rather than relying on a constant lab temperature for refractive index matching, ultimately the refractometer and flow loop could be augmented with a heater/chiller for stability. The ocular of the Abbe refractometer would also be replaced with an image sensor for the reasons previously noted in section 6.3. The troublesome beam overlapping of the laser system would also be amended and/or a different set of slits used to permit scanning closer to the cell walls, as previously described in section 7.3. Preferably a more accurate method of adjusting or measuring the height of the lens system would also be sought.

By far the most significant change that would be made is to address the issues of interface location. The apparent shift caused by manually exchanging filters was overcome with satisfying zero slip, more importantly however interface movement between frames seems a probable candidate for the troublesome notches seen in velocity profiles. Motorised exchange of filters would solve the former, and if done repeatedly through an automated imaging sequence, potentially the latter. The best solution, however, is to perform both fluorescence and tracer imaging simultaneously, on every frame, and realign (or otherwise select) each frame independently. Using two cameras is both expensive and difficult to satisfy image

registration between cameras. Figure 9.1 instead shows a different approach: separate filters placed over different areas of the same sensor.

Two considerations need to be made: firstly, substantially more illumination intensity is needed for acceptable fluorescence images than tracer imaging. For tracer imaging, in addition to the 532nm band pass a neutral density filter would thus also be required. Secondly, note the image sensor dimensions in figure 9.1. Precision optical filters are supplied in standardised sizes, not amenable to the strips required here. Alternatives (such as the deep red Perspex already used for fluorescence imaging here) would need to be sought and cut to size.
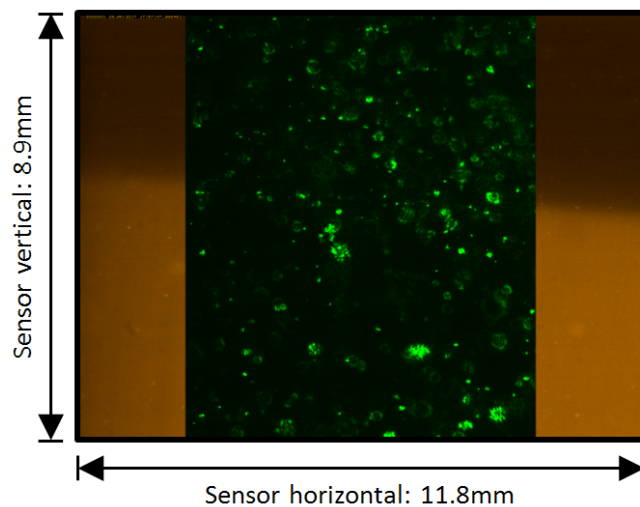
Figure 9.1: Illustration of the segmented filter concept. As drawn here, the 1600x1200 pixel sensor (dimensions indicated) features 300 pixel wide strips at either side devoted to fluorescence imaging, whilst a 1000 pixel wide section in the centre is devoted to tracer imaging. Appropriate filters cover the different sensor areas. Relative brightness is not representative.

A further complication of the use of filters is that they must be placed in image space. An image is only formed on the camera sensor itself, and placing filters in infinity space optical path after the objective will not work. The filter elements must be located immediately against the protective glass window covering the sensor, and even at this location some blurring of one filter region into another will be expected.

There are also improvements that can be made with regards experimental operation. This is a complex experiment to perform, with several steps required between each imaging location which practically limits the number of data points per experimental run:

1. Move camera to new downstream location
2. Enter new laser pulse delay time and associated camera delays
3. Turn up image preview gain, move beam position into frame
4. Switch to fluorescence, move camera vertically to locate interface
5. Switch back to tracer imaging, correct beam position. Optimise beam lateral position.
6. Turn down image preview gain. Check laser pulse A and B intensity (varies with channel position and laser warm-up)
7. Switch to fluorescence, turn up laser pulse A power. Record several frames, name and save image sequence to selected directory.
8. Switch to tracer imaging, turn down laser pulse A power. Turn up laser pulse rate.
9. Start new recording, wait until camera buffer has filled. Stop camera trigger pulses but keep recording.
10. Switch to fluorescence, turn up laser pulse A power. Turn down laser pulse rate. Record several frames onto end of tracer image set. Name image sequence and save to selected directory.
11. Record camera horizontal and vertical position.
12. Turn down laser pulse A power, and return to tracer imaging.

During this period, the interface position in the channel expansion must be continuously monitored and, if necessary, adjusted, and the experiment cannot be stopped until a run has been completed. The synchroniser also caused issues, without a priori testing all laser powers and pulse delays, adjusting a laser cavity power would, beyond apparently arbitrary thresholds, suddenly shift the camera timing, yielding no imagery at all, irrespective of other potential factors as laser power, preview gain, and beam alignment. All these factors together make the experiment quite involved and not entirely stress-free to conduct.

The solution would be to automate as much of the experiment as possible, supposing here that the segmented filters in figure 9.1 are applied. Controlling the lens distance from the cell and the beam mirror by motorising would be useful, allowing rapid interface shape scans at many more points than the three in figure 8.9. Motorising the lens height and downstream position would be less useful: manual beam tracking and alignment checking is still necessary (without substantial optics refinements) and the digital scales could alternatively be automatically read

259

at less cost. The output balancing needle value could also be automatically controlled via image analysis from the interface remote viewing webcam, but safeguards against algorithm failure would be required. The most effective improvement would be the control the main hardware elements of the system from a central program, all of which used here have the potential to be controlled via LabVIEW control. In particular:

- Camera control (dedicated LabVIEW VIs): automatic recording start and saving of image sequences to pre-set directories. Adjustment of preview image gain for alignment and beam power adjustment steps.
- Oscilloscope control (USB, dedicated LabVIEW VIs): automatic adjustment of camera delays and online verification of laser pulse delay time (at least for the current synchroniser)
- Laser synchroniser control (RS232, commands in manual): automatic pre-set values for laser pulse delays. Automatic start and stop of camera triggering, adjustment of pulse rate (if required) and potential online laser power control from frame analysis.

Following this, improvements could also be made to data processing. The image filtering and stacking program could be made more efficient as previously noted. With regards curve fitting, whilst spline curves were justified in as a completely generic fit in section 8.2, parabolic (polynomial order 2) fits appeared to provide a reasonable fit of not just the oil phase, but also the non-Newtonian test phase in section 8.3. Though they may not be an assumption-free representation of the velocity field, in hindsight the errors thus induced would most likely be less than those from kinks and noise in the velocity data when a spline curve fit is used.

Finally, we also recall the conclusions from other chapters, in particular, the channel profiling conclusions in section 5.7. Repeating the stream wise extension rate comparison between the hyperbolic and flow front channel profiles with a different CFD package would be obvious. Extension of the work to axisymmetric channels would be of particular interest, especially to see if the critical inlet angle still occurred. This would be achieved by altering the calculations in the LabVIEW script to model spherical surfaces, rather than circular 2D flow fronts, and accompanying them with axisymmetric CFD simulations accordingly. The contents of chapter 5 would be useful to publish as a standalone guide to (improved) extensional channel design, as no rigorous description of the design considerations is currently present in literature.

References.

Literature and sources cited.

References: Literature and sources cited.

ABEDIJABERI, A., SOULAGES, J., KRÖGER, M. & KHOMAMI, B. 2009. Flow of branched polymer melts in a lubricated cross-slot channel: a combined computational and experimental study. *Rheologica Acta,* 48**,** 97-108.

AGAR SCIENTIFIC LTD. 2017. *Athene Aei Grids Copper 3.05mm* [Online]. Available: http://www.agarscientific.com/tem/grids-athene/round-hole-grids.html [Accessed 02/2017].

AHO, J. & SYRJÄLÄ, S. 2011. Shear viscosity measurements of polymer melts using injection molding machine with adjustable slit die. *Polymer Testing,* 30**,** 595-601.

ANNA, S. L. & MCKINLEY, G. H. 2008. Effect of a controlled pre-deformation history on extensional viscosity of dilute polymer solutions. *Rheologica Acta,* 47**,** 841-859.

ANSYS 2012. Ansys Fluent 14.0.

ARNOLD, D. 2015. *RE: Exol Lubricants: E1600 Base oil information.*

ARRATIA, P. E., GOLLUB, J. P. & DURIAN, D. J. 2008. Polymeric filament thinning and breakup in microchannels. *Physical Review E,* 77**,** 036309.

ASTM INTERNATIONAL 1993. ASTM D2159-93 Standard Test Method for Naphthenes in Saturates Fractions by Refractivity Intercept (Withdrawn 1998). West Conshohocken, PA.

ASTM INTERNATIONAL 2012. ASTM D1500-12 Standard Test Method for ASTM Color of Petroleum Products (ASTM Color Scale). West Conshohocken, PA.

ASTM INTERNATIONAL 2013. ASTM D1238-13 Standard Test Method for Melt Flow Rates of Thermoplastics by Extrusion Plastometer. West Conshohocken, PA.

ASTM INTERNATIONAL 2015. ASTM D341-09(2015), Standard Practice for Viscosity-Temperature Charts for Liquid Petroleum Products. West Conshohocken, PA.

BAHRAMI, M., YOVANOVICH, M. M. & CULHAM, J. R. 2006. Pressure Drop of Fully-Developed, Laminar Flow in Microchannels of Arbitrary Cross-Section. *Journal of Fluids Engineering,* 128**,** 1036-1044.

BARNES, H. A. 1997. Thixotropy—a review. *Journal of Non-Newtonian Fluid Mechanics,* 70**,** 1-33.

BARNICKEL, P. & WOKAUN, A. 1989. Silver coated latex spheres. *Molecular Physics,* 67**,** 1355-1372.

BASAVARAJU, K. C., DEMAPPA, T. & RAI, S. K. 2007. Miscibility studies of polysaccharide Xanthan gum and PEO (polyethylene oxide) in dilute solution. *Carbohydrate Polymers,* 69**,** 462-466.

BAUER, C. A., STELLACCI, F. & PERRY, J. W. 2008. Relationship Between Structure and Solubility of Thiol-Protected Silver Nanoparticles and Assemblies. *Topics in Catalysis,* 47**,** 32-41.

BAUER, W. H. & COLLINS, E. A. 1967. Thixotropy and Dilatancy. *In:* EIRICH, F. R. (ed.) *Rheology Theory and Applications.* New York: Academic Press.

BEADIE, G., BRINDZA, M., FLYNN, R. A., ROSENBERG, A. & SHIRK, J. S. 2015. Refractive index measurements of poly(methyl methacrylate) (PMMA) from 0.4-1.6μm. *Applied Optics,* 54**,** F139-F143.

BEESTON, M. 2016. *RE: Oxford Lasers PIV Laser training session.*

BINDING, D. M. 1988. An approximate analysis for contraction and converging flows. *Journal of Non-Newtonian Fluid Mechanics,* 27**,** 173-189.

BINDING, D. M. & JONES, D. M. 1989. On the interpretation of data from Converging Flow Rheometers. *Rheologica Acta,* 28**,** 215-222.

BIRD, R. B., ARMSTRONG, R. C. & HASSAGER, O. 1977. *Dynamics of Polymeric Liquids,* New York, John Wiley & Sons, Inc.

BIRD, R. B., ARMSTRONG, R. C. & HASSAGER, O. 1987. *Dynamics of Polymeric Liquids,* York, John Wiley & Sons.

BRITISH SOCIETY OF RHEOLOGY 1977. Bulletin. *British Society of Rheology,* 20**,** 13-18.

BRITTON, M. M. 2010. Magnetic resonance imaging of chemistry. *Chemical Society Reviews,* 39**,** 4036-4043.

BROADBENT, J. M., KAYE, A., LODGE, A. S. & VALE, D. G. 1968. Possible Systematic Error in the Measurement of Normal Stress Differences in Polymer Solutions in Steady Shear Flow. *Nature,* 217**,** 55-56.

BROADHEAD, T. O. 1992. *Development of an in-line rheometer for control of reactive extrusion.* Doctor of Philosophy, McGill University.

BROADHEAD, T. O., PATTERSON, W. I. & DEALY, J. M. 1996. Closed loop viscosity control of reactive extrusion with an in-line rheometer. *Polymer Engineering & Science,* 36**,** 2840-2851.

BROOKFIELD ENGINEERING LABORATORIES INC. 2004. *TT-100* [Online]. Available: http://www.brookfieldengineering.com/download/files/TT100Brochure.pdf [Accessed 9/2016].

BROWN, P. S. & BHUSHAN, B. 2015. Mechanically durable, superoleophobic coatings prepared by layer-by-layer technique for anti-smudge and oil-water separation. *Scientific Reports,* 5**,** 8701.

BRUJAN, E.-A. 2011. *Cavitation in Non-Newtonian Fluids: with Biomedical and Bioengineering Applications,* Heidelberg, Springer.

BUDWIG, R. 1994. Refractive index matching methods for liquid flow investigations. *Experiments in Fluids,* 17**,** 350-355.

CAMBRIDGE POLYMER GROUP. 2016. *FiSER™* [Online]. Available: http://www.campoly.com/cpg-services/electronics-and-hardware/instruments/fiser/ [Accessed 9/2016].

CARGILLE LABS. 2016. *Refractive Index (Matching) Liquids* [Online]. Available: http://www.cargille.com/refractivestandards.shtml [Accessed 01/2017].

CARREAU, P. J., KEE, D. C. R. D. & CHHABRA, R. P. 1997. *Rheology of Polymeric Systems, Principles and Applications,* Cincinnati, OH, Hanser/Gardner Publications.

CASANELLAS, L., ALVES, M. A., POOLE, R. J., LEROUGE, S. & LINDNER, A. 2016. The stabilizing effect of shear thinning on the onset of purely elastic instabilities in serpentine microflows. *Soft Matter,* 12**,** 6167-6175.

CHAFFIN, S. 2015. *RE: Discussion with regards the Oldroyd-B model under steady shear and extension.*

CHAFFIN, S. 2017. *RE: Discussion with regards dimensional analysis of hyperbolic extensional flow channels.*

CHATRAEI, S., MACOSKO, C. W. & WINTER, H. H. 1981. Lubricated Squeezing Flow: A New Biaxial Extensional Rheometer. *Journal of Rheology,* 25**,** 433-443.

CHEMOURS. 2015a. *Krytox Performance Lubricants Chemical Stability* [Online]. Available: https://www.chemours.com/Lubricants/en_US/assets/downloads/K-20564-3_Chem_Reactivity_Profile.pdf [Accessed 01/2017].

CHEMOURS. 2015b. *Krytox Performance Lubricants Product Overview* [Online]. Available: https://www.chemours.com/Lubricants/en_US/assets/downloads/Krytox_Overview_LowRes_H-58505-5.pdf [Accessed 01/2017].

CHEN, Y., XUE, Z., LIU, N., LU, F., CAO, Y., SUN, Z. & FENG, L. 2014. Fabrication of a silica gel coated quartz fiber mesh for oil-water separation under strong acidic and concentrated salt conditions. *RSC Advances,* 4**,** 11447-11450.

CHESTERTON, A. K. S., WILSON, D. I., SADD, P. A. & MOGGRIDGE, G. D. 2015. A novel laboratory scale method for studying heat treatment of cake flour. *Journal of Food Engineering,* 144**,** 36-44.

CHRISTANTI, Y. & WALKER, L. M. 2001. Surface tension driven jet break up of strain-hardening polymer solutions. *Journal of Non-Newtonian Fluid Mechanics,* 100**,** 9-26.

CHU, Z., FENG, Y. & SEEGER, S. 2015. Oil/Water Separation with Selective Superantiwetting/Superwetting Surface Materials. *Angewandte Chemie International Edition,* 54**,** 2328-2338.

CINADER, D. K. & BURGHARDT, W. R. 1999. X-ray scattering studies of orientation in channel flows of a thermotropic liquid–crystalline polymer. *Journal of Polymer Science Part B: Polymer Physics,* 37**,** 3411-3428.

COGSWELL, F. N. 1972. Converging flow of polymer melts in extrusion dies. *Polymer Engineering & Science,* 12**,** 64-73.

COGSWELL, F. N. 1978. Converging flow and stretching flow: A compilation. *Journal of Non-Newtonian Fluid Mechanics,* 4**,** 23-38.

COLE-PARMER INSTRUMENT CO. LTD. 2006. *Liquid Pumps – Viscosity Handling Characteristics* [Online]. Available: http://www.coleparmer.co.uk/TechLibraryArticle/625 [Accessed 12/2012].

COLLIER, J. R., ROMANOSCHI, O. & PETROVAN, S. 1998. Elongational rheology of polymer melts and solutions. *Journal of Applied Polymer Science,* 69**,** 2357-2367.

COLLYER, A. A. & CLEGG, D. W. 1998. *Rheological Measurement,* Dordrecht, Springer Netherlands.

COOPER-WHITE, J. J., FAGAN, J. E., TIRTAATMADJA, V., LESTER, D. R. & BOGER, D. V. 2002. Drop formation dynamics of constant low-viscosity, elastic fluids. *Journal of Non-Newtonian Fluid Mechanics,* 106**,** 29-59.

COSPHERIC LLC. 2015. *Conductive Silver Metal Coated Soda Lime Solid Glass Microspheres 2.5g/cc - Classified Grades Product ID: SLGMS-AG-2.5* [Online]. Available: http://www.cospheric.com/SLGMSAG_silver_coated_solid_glass_spheres_beads.htm [Accessed 02/2017].

CROCODILE CLIPS LTD 2000. Crocodile Technology 1.0. 1.0 ed.

CROOKS, R. & BOGER, D. V. 2000. Influence of fluid elasticity on drops impacting on dry surfaces. *Journal of Rheology,* 44**,** 973-996.

CROOKS, R., COOPER-WHITE, J. & BOGER, D. V. 2001. The role of dynamic surface tension and elasticity on the dynamics of drop impact. *Chemical Engineering Science,* 56**,** 5575-5592.

CUBAUD, T. & MASON, T. G. 2009. High-viscosity fluid threads in weakly diffusive microfluidic systems. *New Journal of Physics,* 11**,** 075029.

CURRIE, P. K. 1981. The First Normal-Stress Difference in Shear of Nematic Liquid Crystals. *Molecular Crystals and Liquid Crystals,* 73**,** 1-6.

DAI, S. & TAM, K. C. 2006. Effect of Cosolvents on the Binding Interaction between Poly(ethylene oxide) and Sodium Dodecyl Sulfate. *The Journal of Physical Chemistry B,* 110**,** 20794-20800.

DAIKIN INDUSTRIES, L. 2015. *Demnum Product Information* [Online]. Available: http://www.daikin.com/chm/products/pdfDown.php?url=pdf/tds/tds_dms-1_e.pdf [Accessed 01/2017].

DASSAULT SYSTEMS. 2012. SolidWorks Education Edition 2012. SP4.0 ed.

DAVIES, G. J. G., KNIGHT, D. P. & VOLLRATH, F. 2013. Structure and function of the major ampullate spinning duct of the golden orb weaver, Nephila edulis. *Tissue and Cell,* 45**,** 306-311.

DEALY, J. M. 1990. Challenges in process rheometry. *Rheologica Acta,* 29**,** 519-522.

DEALY, J. M. 1995. Letter to the Editor: Comment on ''Polymer melt lubricated elongational flow'' [Kim, Pendse, and Collier, J. Rheol. 38, 831 (1994)]. *Journal of Rheology,* 39**,** 247-247.

DEALY, J. M. & BROADHEAD, T. O. 1993. Process rheometers for molten plastics: A survey of existing technology. *Polymer Engineering & Science,* 33**,** 1513-1523.

DEALY, J. M., DOSHI, S. R. & BUBIC, F. R. 1992. *Method and apparatus for measuring shear stress*. United States patent application US 5,094,100.

DOSHI, S. R. & DEALY, J. M. 1987. Exponential Shear: A Strong Flow. *Journal of Rheology,* 31**,** 563-582.

DUNBAR, A. 2014. *RE: Discussion relating to applying coatings through airbrushing.*

DUPONT. 2006. *Summary Of Properties* [Online]. Available:
http://www2.dupont.com/Kapton/en_US/assets/downloads/pdf/summaryofprop.pdf
[Accessed 12/2012].

DZIUBINSKI, M. 2012. Hydrodynamic Focusing in Microfluidic Devices. *In:* KELLY, D. R. (ed.)
Advances in Microfluidics. InTech.

EBAGNININ, K. W., BENCHABANE, A. & BEKKOUR, K. 2009. Rheological characterization of
poly(ethylene oxide) solutions of different molecular weights. *Journal of Colloid and
Interface Science,* 336**,** 360-367.

EDMUND OPTICS LTD. 2016a. *10X EO M Plan Apo Long Working Distance Infinity Corrected*
[Online]. Available: https://www.edmundoptics.co.uk/microscopy/infinity-corrected-
objectives/eo-infinity-corrected-long-working-distance-objectives/59877/ [Accessed
02/2017].

EDMUND OPTICS LTD. 2016b. *An In Depth Look at Spherical Aberration Compensation Plates*
[Online]. Available: http://www.edmundoptics.com/resources/application-
notes/optics/an-in-depth-look-at-spherical-aberration-compensation-plates/ [Accessed
01/2017].

EMERSON PROCESS MANAGEMENT. 2014. *Micro Motion Fork Viscosity Meter* [Online].
Available:
http://www2.emersonprocess.com/siteadmincenter/PM%20Micro%20Motion%20Doc
uments/FVM-BRO-MC-001864.pdf [Accessed 09/2016].

ETEBARI, A. 2006. *Wall shear stress measurements in arterial flows.* Doctor of Philosophy,
Virginia Tech and Wake Forest University.

EVANS, M. W. & HEYES, D. M. 1990. Combined shear and elongational flow by non-equilibrium
molecular dynamics. *Molecular Physics,* 69**,** 241-263.

EVERAGE, A. E. & BALLMAN, R. L. 1978. The extensional flow capillary as a new method for
extensional viscosity measurement. *Nature,* 273**,** 213-215.

EXXONMOBIL. 2015a. *SpectraSyn 2 Product Datasheet* [Online]. Available:
http://www.exxonmobilchemical.com/Chem-English/brands/spectrasyn-lo-vis-PAO-
grades-and-datasheets.aspx?ln=productsservices [Accessed 02/2017].

EXXONMOBIL. 2015b. *SpectraSyn Elite 65 Product Datasheet* [Online]. Available:
http://www.exxonmobilchemical.com/Chem-English/productsservices/spectrasyn-
elite-mpao-grades-and-datasheets.aspx [Accessed 01/2017].

EXXONMOBIL. 2015c. *Synesstic 5 Product Datasheet* [Online]. Available:
http://www.exxonmobilchemical.com/Chem-English/brands/synesstic-an-blendstock-
grades-and-datasheets.aspx?ln=productsservices [Accessed 01/2017].

EXXONMOBIL. 2015d. *Synesstic 12 Product Datasheet* [Online]. Available:
http://www.exxonmobilchemical.com/Chem-English/brands/synesstic-an-blendstock-
grades-and-datasheets.aspx?ln=productsservices [Accessed 01/2017].

FAIRCLOUGH, P. 2017. *RE: Discussion with regards the impact of extensional flow on shear
induced crystallisation.*

FEIGL, K., TANNER, F. X., EDWARDS, B. J. & COLLIER, J. R. 2003. A numerical study of the
measurement of elongational viscosity of polymeric fluids in a semihyperbolically
converging die. *Journal of Non-Newtonian Fluid Mechanics,* 115**,** 191-215.

FRICKE, A. K. & CRISALLE, O. D. 1999. Development of viscometers for kraft black liquor. Final
report - phases I, II, IIA, and III. ; Chemical Engineering Department, University of
Florida, Gainesville, FL 32611-6005, USA (US).

FRITZ, H. G. 1989. Sensorentwicklung und Automatisierungstendenzen im Bereich der
Kunststoffaufbereitung. *Stuttgarter Kunststoffkolloquium,* 11.

FUERHAUPTER, H. 2016. *RE: SG02S40 Size measurement processes.*

GALINDO-ROSALES, F. J., ALVES, M. A. & OLIVEIRA, M. S. N. 2013. Microdevices for extensional
rheometry of low viscosity elastic liquids: a review. *Microfluidics and Nanofluidics,* 14**,**
1-19.

GALINDO-ROSALES, F. J., OLIVEIRA, M. S. N. & ALVES, M. A. 2014. Optimized cross-slot microdevices for homogeneous extension. *RSC Advances,* 4**,** 7799-7804.

GALLARDO, O. A. D., MOIRAGHI, R., MACCHIONE, M. A., GODOY, J. A., PEREZ, M. A., CORONADO, E. A. & MACAGNO, V. A. 2012. Silver oxide particles/silver nanoparticles interconversion: susceptibility of forward/backward reactions to the chemical environment at room temperature. *RSC Advances,* 2**,** 2923-2929.

GAURI, V. & KOELLING, K. W. 1997. Extensional rheology of concentrated poly(ethylene oxide) solutions. *Rheologica Acta,* 36**,** 555-567.

GENNES, P.-G. 1979. *Scaling Concepts in Polymer Physics,* Ithaca, United States, Cornell University Press.

GIBBS, S. J., HAYCOCK, D. E., FRITH, W. J., ABLETT, S. & HALL, L. D. 1997. Strategies for Rapid NMR Rheometry by Magnetic Resonance Imaging Velocimetry. *Journal of Magnetic Resonance,* 125**,** 43-51.

GIJSEN, F. J. H., GOIJAERTS, A., VAN DE VOSSE, F. N. & JANSSEN, J. D. 1997. A new method to determine wall shear stress distribution. *Journal of Rheology,* 41**,** 995-1006.

GIZ, M. J., DUONG, B. & TAO, N. J. 1999. In situ STM study of self-assembled mercaptopropionic acid monolayers for electrochemical detection of dopamine. *Journal of Electroanalytical Chemistry,* 465**,** 72-79.

GLASSCOCK, J. A., SMITH, R. S., VANAJEK, J. & WINTER, J. G. 2003. An in-line micro-Fourier rheometer. *Review of Scientific Instruments,* 74**,** 4925-4929.

GLEISSLE, W. & SCHULZE, V. 1993. *Verfahren und Vorrichtung zur kontinuierlichen Viskositätsmessung*. European patent application EP 0 595 276 B1.

GLYCERINE PRODUCERS' ASSOCIATION 1963. Physical properties of glycerine and its solutions. *Glycerine Producers' Association.* New York (Available also at: http://www.aciscience.org/docs/physical_properties_of_glycerine_and_its_solutions.pdf [Accessed 01/2017]).

GOLOSHEVSKY, A. G., WALTON, J. H., SHUTOV, M. V., ROPP, J. S. D., COLLINS, S. D. & MCCARTHY, M. J. 2005. Nuclear magnetic resonance imaging for viscosity measurements of non-Newtonian fluids using a miniaturized RF coil. *Measurement Science and Technology,* 16**,** 513.

GÖTTFERT WERKSTOFF-PRÜFMASCHINEN GMBH. 2014. *Online Rheometer* [Online]. Available: http://www.goettfert.com/images/stories/downloads/produkte/Brochure_Online-Rheometer_eng.pdf [Accessed 9/2016].

GUILLOT, P., MOULIN, T., KÖTITZ, R., GUIRARDEL, M., DODGE, A., JOANICOT, M., COLIN, A., BRUNEAU, C.-H. & COLIN, T. 2008. Towards a continuous microfluidic rheometer. *Microfluidics and Nanofluidics,* 5**,** 619-630.

GUILLOT, P., PANIZZA, P., SALMON, J.-B., JOANICOT, M., COLIN, A., BRUNEAU, C.-H. & COLIN, T. 2006. Viscosimeter on a Microfluidic Chip. *Langmuir,* 22**,** 6438-6445.

HALFORDS. 2017. *Halfords 15W40 Mineral Petrol & Diesel Oil 2L* [Online]. Available: http://www.halfords.com/motoring/engine-oils-fluids/engine-oil/halfords-15w40-mineral-petrol-diesel-oil-2l [Accessed 02/2017].

HALOCARBON PRODUCTS CORPORATION. 2016. *Physical Properties Halocarbon Oils* [Online]. Available: http://www.halocarbon.com/physical-properties/ [Accessed 01/2017].

HASANZADEH, M., MOTTAGHITALAB, V. & REZAEI, M. 2015. Rheological and viscoelastic behavior of concentrated colloidal suspensions of silica nanoparticles: A response surface methodology approach. *Advanced Powder Technology,* 26**,** 1570-1577.

HAWARD, S. J., ODELL, J. A., LI, Z. & YUAN, X.-F. 2010. The rheology of polymer solution elastic strands in extensional flow. *Rheologica Acta,* 49**,** 781-788.

HAWARD, S. J., OLIVEIRA, M. S. N., ALVES, M. A. & MCKINLEY, G. H. 2012. Optimized Cross-Slot Flow Geometry for Microfluidic Extensional Rheometry. *Physical Review Letters,* 109**,** 128301.

HE, K., DUAN, H., CHEN, G. Y., LIU, X., YANG, W. & WANG, D. 2015. Cleaning of Oil Fouling with Water Enabled by Zwitterionic Polyelectrolyte Coatings: Overcoming the Imperative Challenge of Oil–Water Separation Membranes. *ACS Nano,* 9**,** 9188-9198.

HINCH, E. J. 2003. *Lecture 2: Constitutive Relations* [Online]. Available: http://www.damtp.cam.ac.uk/user/hinch/teaching/whoi/lecture02.ps [Accessed 02/2017].

HOLLAND, C. 2015. *RE: Discussion with regards producing rapid shear rate ramps on commercial rheometers.*

HOLLAND, C. 2016. *RE: Discussion with regards to natural extensional channel profiles.*

HOPCROFT, M. A., NIX, W. D. & KENNY, T. W. 2010. What is the Young's Modulus of Silicon? *Journal of Microelectromechanical Systems,* 19**,** 229-238.

HORVAT, M., AZAD EMIN, M., HOCHSTEIN, B., WILLENBACHER, N. & SCHUCHMANN, H. P. 2013. A multiple-step slit die rheometer for rheological characterization of extruded starch melts. *Journal of Food Engineering,* 116**,** 398-403.

HOWARTER, J. A., GENSON, K. L. & YOUNGBLOOD, J. P. 2011. Wetting Behavior of Oleophobic Polymer Coatings Synthesized from Fluorosurfactant-Macromers. *ACS Applied Materials & Interfaces,* 3**,** 2022-2030.

HOWARTER, J. A. & YOUNGBLOOD, J. P. 2007. Self-Cleaning and Anti-Fog Surfaces via Stimuli-Responsive Polymer Brushes. *Advanced Materials,* 19**,** 3838-3843.

HOWARTER, J. A. & YOUNGBLOOD, J. P. 2008. Self-Cleaning and Next Generation Anti-Fog Surfaces and Coatings. *Macromolecular Rapid Communications,* 29**,** 455-466.

HOWARTER, J. A. & YOUNGBLOOD, J. P. 2009. Amphiphile grafted membranes for the separation of oil-in-water dispersions. *Journal of Colloid and Interface Science,* 329**,** 127-132.

ISRAELACHVILI, J. N., TANDON, R. K. & WHITE, L. R. 1979. Measurement of forces between two mica surfaces in aqueous poly(ethylene oxide) solutions. *Nature,* 277**,** 120-121.

J. ALLCOCK & SONS LTD. 2012. *Technical Data Sheet Allcosil 200/50* [Online]. Available: http://www.allcocks.co.uk/files/lib/84/Allcosil%20200-%2050%20cSt%20-%20TDS%20(04-12).pdf [Accessed 01/2017].

JAISHANKAR, A., HAWARD, S., HALL, N. R., MAGEE, K. & MCKINLEY, G. 2012. Shear History Extensional Rheology Experiment II (SHERE II) Microgravity Rheology with Non-Newtonian Polymeric Fluids. *American Society for Gravitational and Space Research (ASGSR) 28 Nov. - 2 Dec. 2012.* New Orleans, LA; United States.

JAKOB, B. & RUTHARDT, A. 2014. *New die design for a rapid rheological characterization of polymers (Application Notes LR-67)* [Online]. Karlsruhe: Thermo Fisher Scientific. Available: https://tools.thermofisher.com/content/sfs/brochures/LR67-e-New-Die-Design.pdf [Accessed 09/2016].

JAMES, D. F. 1991. Flow in a converging channel at moderate reynolds numbers. *AIChE Journal,* 37**,** 59-64.

JAMES, D. F., CHANDLER, G. M. & ARMOUR, S. J. 1990. A converging channel rheometer for the measurement of extensional viscosity. *Journal of Non-Newtonian Fluid Mechanics,* 35**,** 421-443.

JAMES, D. F., MCLEAN, B. D. & SARINGER, J. H. 1987. Presheared Extensional Flow of Dilute Polymer Solutions. *Journal of Rheology,* 31**,** 453-481.

JAMES, D. F. & SARINGER, J. H. 1980. Extensional flow of dilute polymer solutions. *Journal of Fluid Mechanics,* 97**,** 655-671.

JAMES, D. F. & SARINGER, J. H. 1982. Flow of dilute polymer solutions through converging channels. *Journal of Non-Newtonian Fluid Mechanics,* 11**,** 317-339.

JAMES, D. F. & WALTERS, K. 1993. A Critical Appraisal of Available Methods for the Measurement of Extensional Properties of Mobile Systems. *In:* COLLYER, A. A. (ed.) *Techniques in Rheological Measurement.* Dordrecht: Springer Netherlands.

JAYAPRAKASH, M. S., SHIVAKUMAR, K. & SHASHIDHAR 2013. *Viscosity, Ultrasonic, Refractometric and Morphological Studies of PEO/HPMC Blend in Water at 30°C and 50°C.*

JEON, Y.-M., GONG, M.-S. & CHO, H.-N. 2009. Preparation of silver/PMMA beads via the in sito reduction of a silver alkylcarbamate complex. *Macromolecular Research,* 17**,** 2-4.

JOHNSTON, S. B. 2016. *RE: Chemours: PCTFE oil miscibility with Krytox.*

JONES, D. M., WALTERS, K. & WILLIAMS, P. R. 1987. On the extensional viscosity of mobile polymer solutions. *Rheologica Acta,* 26**,** 20-30.

KHAN, S. A. & LARSON, R. G. 1991. Step planar extension of polymer melts using a lubricated channel. *Rheologica Acta,* 30**,** 1-6.

KHAN, S. A. & ZOELLER, N. J. 1993. Dynamic rheological behavior of flocculated fumed silica suspensions. *Journal of Rheology,* 37**,** 1225-1235.

KIM, H. C., PENDSE, A. & COLLIER, J. R. 1994. Polymer melt lubricated elongational flow. *Journal of Rheology,* 38**,** 831-845.

KNEPPE, H. & SCHNEIDER, F. 1981. Determination of the Viscosity Coefficients of the Liquid Crystal MBBA. *Molecular Crystals and Liquid Crystals,* 65**,** 23-37.

KOTA, A. K., KWON, G., CHOI, W., MABRY, J. M. & TUTEJA, A. 2012. Hygro-responsive membranes for effective oil–water separation. *Nat Commun,* 3**,** 1025.

KROHNE, I. 2012. *VISCOLINE – New Generation Rheometer for continuous in-line measurement of process viscosity* [Online]. Available: http://www.krohne-downloadcenter.com/dlc/FL_VISCOLINE_en_121030.pdf [Accessed 9/2016].

KURTZ, S. S. & WARD, A. L. 1936. The refractivity intercept and the specific refraction equation of Newton. I. development of the refractivity intercept and comparison with specific refraction equations. *Journal of the Franklin Institute,* 222**,** 563-592.

KWON, G., POST, E. & TUTEJA, A. 2015. Membranes with selective wettability for the separation of oil–water mixtures. *MRS Communications,* 5**,** 475-494.

LAUN, H. M. & HIRSCH, G. 1989. New laboratory tests to measure rheological properties of paper coatings in transient and steady-state flows. *Rheologica Acta,* 28**,** 267-280.

LEE, J.-D., SO, J.-H. & YANG, S.-M. 1999. Rheological behavior and stability of concentrated silica suspensions. *Journal of Rheology,* 43**,** 1117-1140.

LEE, W., WALKER, L. M. & ANNA, S. L. 2011. Competition Between Viscoelasticity and Surfactant Dynamics in Flow Focusing Microfluidics. *Macromolecular Materials and Engineering,* 296**,** 203-213.

LEEUNGCULSATIEN, T. & LUCAS, G. P. 2013. Measurement of velocity profiles in multiphase flow using a multi-electrode electromagnetic flow meter. *Flow Measurement and Instrumentation,* 31**,** 86-95.

LEEUWEN, M. B. V. 1997. *ELECTROMAGNETIC FLOWMETERS.* M.Sc, Eindhoven University of Technology.

LI, J., YAN, L., LI, W., LI, J., ZHA, F. & LEI, Z. 2015. Superhydrophilic–underwater superoleophobic ZnO-based coated mesh for highly efficient oil and water separation. *Materials Letters,* 153**,** 62-65.

LIU, X. M., THOMASON, J. L. & JONES, F. R. 2009. The concentration of hydroxyl groups on glass surfaces and their effect on the structure of silane deposits. *Silanes and Other Coupling Agents.* Brill Academic Publishers.

LOUDON, M. 2009. *Organic Chemistry*, Roberts & Company Publishers.

MACINNES, J. 2015. *RE: Discussion with regards toughened glass windows.*

MACLEOD, I. D. & NORTH, N. A. 1979. Conservation of Corroded Silver. *Studies in Conservation,* 24**,** 165-170.

MACOSKO, C. W. 1994. *Rheology : principles, measurements,and applications,* New York, VCH Publishers, Inc.

MACOSKO, C. W., OCANSEY, M. A. & WINTER, H. H. 1980. Steady planar extension with lubricated dies. *VIII International Congress on Rheology, September 1 - 5.* Naples: Plenum Press.

MACOSKO, C. W., OCANSEY, M. A. & WINTER, H. H. 1982. Steady planer extension with lubricated dies. *Journal of Non-Newtonian Fluid Mechanics,* 11**,** 301-316.

MAIR, R. W. & CALLAGHAN, P. T. 1996. Observation of shear banding in worm-like micelles by NMR velocity imaging. *EPL (Europhysics Letters),* 36**,** 719.

MAMUN, A. H. A. & HAHN, J. R. 2012. Effects of Solvent on the Formation of Octanethiol Self-Assembled Monolayers on Au(111) at High Temperatures in a Closed Vessel: A Scanning Tunneling Microscopy and X-ray Photoelectron Spectroscopy Study. *The Journal of Physical Chemistry C,* 116**,** 22441-22448.

MARCELLA MASTROMATTEO, S. C., MARIAPIA IANNETTI, VALENTINA CIVICA, GRAZIA SEPIELLI, MATTEO ALESSANDRO DEL NOBILE 2012. Influence of Heat Treatment on the Quality of Functional Gluten-Free Spaghetti. *Food and Nutrition Sciences,* 3**,** 433-440.

MARTIN, H. P., BROOKS, N. J., SEDDON, J. M., LUCKHAM, P. F., TERRILL, N. J., KOWALSKI, A. J. & CABRAL, J. T. 2016. Microfluidic processing of concentrated surfactant mixtures: online SAXS, microscopy and rheology. *Soft Matter,* 12**,** 1750-1758.

MCLEISH, T. C. B., CLARKE, N., DE LUCA, E., HUTCHINGS, L. R., GRAHAM, R. S., GOUGH, T., GRILLO, I., FERNYHOUGH, C. M. & CHAMBON, P. 2009. Neutron flow-mapping: Multiscale modelling opens a new experimental window. *Soft Matter,* 5**,** 4426-4432.

MELLING, A. 1997. Tracer particles and seeding for particle image velocimetry. *Measurement Science and Technology,* 8**,** 1406.

MENGEL, F. & MOERCK, T. Prediction of PIV recording performance. 1993. 331-338.

MERKLINGER, H. M. 2010. *Focusing the View Camera* [Online]. (Previously in print: ISBN 0-9695025-2-4). Available: www.trenholm.org/hmmerk/FVC161.pdf [Accessed 01/2017].

MIESOWICZ, M. 1946. The Three Coefficients of Viscosity of Anisotropic Liquids. *Nature,* 158**,** 27-27.

MORRISON, F. A. 2014. *Shear Viscosity Measurement in a Capillary Rheometer* [Online]. Available: http://www.chem.mtu.edu/~fmorriso/cm4655/lecture_2_cm4655.pdf [Accessed 09/2016].

MUELLER, S., LLEWELLIN, E. W. & MADER, H. M. 2010. The rheology of suspensions of solid particles. *Proceedings of the Royal Society A: Mathematical, Physical and Engineering Science,* 466**,** 1201-1228.

MUN, R. P., BYARS, J. A. & BOGER, D. V. 1998. The effects of polymer concentration and molecular weight on the breakup of laminar capillary jets. *Journal of Non-Newtonian Fluid Mechanics,* 74**,** 285-297.

MYKHAYLYK, O. O., CHAMBON, P., IMPRADICE, C., FAIRCLOUGH, J. P. A., TERRILL, N. J. & RYAN, A. J. 2010. Control of Structural Morphology in Shear-Induced Crystallization of Polymers. *Macromolecules,* 43**,** 2389-2405.

NATIONAL INSTRUMENTS 2012. LabVIEW 2012.

NAVITAR. 2017. *Zoom 6000® Lens System* [Online]. Available: https://navitar.com/products/imaging-optics/high-magnification-imaging/zoom-6000/ [Accessed 02/2017].

NEGRI, M., CIEZKI, H. K. & SCHLECHTRIEM, S. 2013. Spray behavior of non-newtonian fluids: correlation between rheological measurements and droplets/threads formation. *EUCASS Proceedings Series – Advances in AeroSpace Sciences,* 4**,** 271-290.

NGUYEN, N.-T., YAP, Y.-F. & SUMARGO, A. 2008. Microfluidic rheometer based on hydrodynamic focusing. *Measurement Science and Technology,* 19**,** 085405.

NPL. 2016. *Kaye and Laby Online* [Online]. Available: www.kayelaby.npl.co.uk [Accessed 09/2016].

NYSTRÖM, M., TAMADDON JAHROMI, H. R., STADING, M. & WEBSTER, M. F. 2012. Numerical simulations of Boger fluids through different contraction configurations for the development of a measuring system for extensional viscosity. *Rheologica Acta,* 51**,** 713-727.

OBER, T. J., HAWARD, S. J., PIPE, C. J., SOULAGES, J. & MCKINLEY, G. H. 2013. Microfluidic extensional rheometry using a hyperbolic contraction geometry. *Rheologica Acta,* 52**,** 529-546.

OLIVEIRA, M. S. N., ALVES, M. A., PINHO, F. T. & MCKINLEY, G. H. 2007. Viscous flow through microfabricated hyperbolic contractions. *Experiments in Fluids,* 43**,** 437-451.

OLIVEIRA, M. S. N., PINHO, F. T. & ALVES, M. A. 2008. Extensional Effects in Viscoelastic Fluid Flow through a Micro-Scale Double Cross-Slot. *AIP Conference Proceedings,* 1027**,** 982-984.

OMEGA ENGINEERING. 2006. *Strain gage technical data* [Online]. Available: http://www.omega.co.uk/techref/pdf/STRAIN_GAGE_TECHNICAL_DATA.pdf [Accessed 12/2012].

OMEGA ENGINEERING. 2009. *Practical Strain Gage Measurements* [Online]. Available: http://www.omega.co.uk/techref/pdf/StrainGage_Measurement.pdf [Accessed 01/2013].

OMEGA ENGINEERING. 2015. *Precision Strain Gage* [Online]. Available: http://www.omega.com/pressure/pdf/SGD_LINEAR1-AXIS.pdf [Accessed 9/2016].

ORTIZ, M., KEE, D. D. & CARREAU, P. J. 1994. Rheology of concentrated poly(ethylene oxide) solutions. *Journal of Rheology,* 38**,** 519-539.

PABEDINSKAS, A., CLUETT, W. R. & BALKE, S. T. 1991. Development of an in-line rheometer suitable for reactive extrusion processes. *Polymer Engineering & Science,* 31**,** 365-375.

PADAKI, M., SURYA MURALI, R., ABDULLAH, M. S., MISDAN, N., MOSLEHYANI, A., KASSIM, M. A., HILAL, N. & ISMAIL, A. F. 2015. Membrane technology enhancement in oil–water separation. A review. *Desalination,* 357**,** 197-207.

PANDEY, A. & LELE, A. 2007. Exploring the utility of an axisymmetric semi-hyperbolic die for determining the transient uniaxial elongation viscosity of polymer melts. *Journal of Non-Newtonian Fluid Mechanics,* 144**,** 170-177.

PARAMETRIC TECHNOLOGY CORP. 2000. Pro/DESKTOP 2000i2.

PCO AG. 2017. *PCO: Software (Camware)* [Online]. Kelheim, Germany. Available: https://www.pco.de/support/software/sensitive-cameras/pco1600/ [Accessed 8/2017].

PENDSE, A. & COLLIER, J. R. 1995. Letter to the Editor: Response to ''Comment on 'Polymer melt lubricated elongational flow' '' [Kim, Pendse, and Collier, J. Rheol. 39, 247 (1995)]. *Journal of Rheology,* 39**,** 249-249.

PERATECH HOLDCO LIMITED. 2016. *What is QTC?* [Online]. Available: https://www.peratech.com/what-is-qtc.html [Accessed 9/2016].

PETRIE, C. J. S. 2006a. Extensional viscosity: A critical discussion. *Journal of Non-Newtonian Fluid Mechanics,* 137**,** 15-23.

PETRIE, C. J. S. 2006b. One hundred years of extensional flow. *Journal of Non-Newtonian Fluid Mechanics,* 137**,** 1-14.

PIPE, C. J. & MCKINLEY, G. H. 2009. Microfluidic rheometry. *Mechanics Research Communications,* 36**,** 110-120.

PITT, M. J. 2000. The Marsh Funnel and Drilling Fluid Viscosity: A New Equation for Field Use. *SPE Drilling & Completion,* 15**,** 3-6.

PIVTEC GMBH 2014. PIVview2C v3.5.9.1. Göttingen, Germany.

POLYANSKIY, M. 2016. *Refractive index database* [Online]. Available: http://refractiveindex.info/ [Accessed 01/2017].

POLYSCIENCES INC. 2016. *Poly(ethylene oxide), MW 100000 (PEO 100K)* [Online]. Available: http://www.polysciences.com/default/catalog-products/monomers-polymers/polymers/poly-ethylene-glycol-polymers/poly-ethylene-glycol-and-poly-ethylene-oxide/polyethylene-oxide-mw100000/ [Accessed 02/2017].

POWELL, R. L., MANEVAL, J. E., SEYMOUR, J. D., MCCARTHY, K. L. & MCCARTHY, M. J. 1994. Note: Nuclear magnetic resonance imaging for viscosity measurements. *Journal of Rheology,* 38**,** 1465-1470.

PRASAD, A. K. 2000. Stereoscopic particle image velocimetry. *Experiments in Fluids,* 29**,** 103-116.

PRASAD, A. K. & JENSEN, K. 1995. Scheimpflug stereocamera for particle image velocimetry in liquid flows. *Applied Optics,* 34**,** 7092-7099.

PRITCHARD, P. J. 2011. *Introduction to Fluid Mechanics Chapter 8 (ME3250 Fluid Dynamics I lecture notes)* [Online]. University of Connecticut. Available: http://www.engr.uconn.edu/~wchiu/ME3250FluidDynamicsI/lecture%20notes/ch08.pdf [Accessed 01/2017].

PU, Y., CHAUDHRY, S., PARIKH, M. & BERRY, J. 2015. Application of in-line viscometer for in-process monitoring of microcrystalline cellulose-carboxymethylcellulose hydrogel formation during batch manufacturing. *Drug Development and Industrial Pharmacy,* 41**,** 28-34.

RAGHAVAN, S. R. & KHAN, S. A. 1995. Shear induced microstructural changes in flocculated suspensions of fumed silica. *Journal of Rheology,* 39**,** 1311-1325.

RAGHAVAN, S. R. & KHAN, S. A. 1997. Shear-Thickening Response of Fumed Silica Suspensions under Steady and Oscillatory Shear. *Journal of Colloid and Interface Science,* 185**,** 57-67.

RHEOLOGY SOLUTIONS. 2012*. OLR Series 1000* [Online]. Available: http://www.onlinerheometer.com/downloads/olr001.pdf [Accessed 9/2016].

ROBIN, F., ENGMANN, J., TOMASI, D., BRETON, O., PARKER, R., SCHUCHMANN, H. P. & PALZER, S. 2010. Adjustable Twin-Slit Rheometer for Shear Viscosity Measurement of Extruded Complex Starchy Melts. *Chemical Engineering & Technology,* 33**,** 1672-1678.

RODD, L. E., COOPER-WHITE, J. J., BOGER, D. V. & MCKINLEY, G. H. 2007. Role of the elasticity number in the entry flow of dilute polymer solutions in micro-fabricated contraction geometries. *Journal of Non-Newtonian Fluid Mechanics,* 143**,** 170-191.

RODD, L. E., SCOTT, T. P., COOPER-WHITE, J. J. & MCKINLEY, G. H. 2005. Capillary Break-up Rheometry of Low-Viscosity Elastic Fluids. *Applied Rheology,* 15**,** 12-27.

ROHRBACH, K., LI, Y., ZHU, H., LIU, Z., DAI, J., ANDREASEN, J. & HU, L. 2014. A cellulose based hydrophilic, oleophobic hydrated filter for water/oil separation. *Chemical Communications,* 50**,** 13296-13299.

RØNNINGSEN, H. P. 2012. Rheology of Petroleum Fluids. *Annual Transactions of the Nordic rheology society,* 20**,** 11 - 18.

S.RÓŻAŃSKA, BRONIARZ-PRESS, L., RÓŻAŃSKI, J., MITKOWSKI, P., OCHOWIAK, M. & WOZIWODZKI, S. 2012. Extensional Viscosity and Stability of Oil-in-water Emulsions with Addition Poly(ethylene oxide). *Procedia Engineering,* 42**,** 733-741.

SAS IP. INC 2011. ANSYS Workbench 2.0 Framework (FLUENT Version 14.0.0, ANSYS Inc.).

SASAKI, S. & NISHI, S. 1996. Synthesis of Fluroinated Polyimides. *In:* GHOSH, M. K. & MITTAL, K. L. (eds.) *Polyimides Fundimentals and Applications.* New York, Basel: Marcel Dekker, Inc.

SCHUBERTH, S. & MÜNSTEDT, H. 2008. Transient elongational viscosities of aqueous polyacrylamide solutions measured with an optical rheometer. *Rheologica Acta,* 47**,** 139-147.

SECOR, R. B., MOCOSKO, C. W. & SCRIVEN, L. E. 1987. Analysis of lubricated planar stagnation die flow. *Journal of Non-Newtonian Fluid Mechanics,* 23**,** 355-381.

SENGUPTA, A., HERMINGHAUS, S. & BAHR, C. 2014. Liquid crystal microfluidics: surface, elastic and viscous interactions at microscales. *Liquid Crystals Reviews,* 2**,** 73-110.

SHAW, M. T. 1975. Flow of polymer melts through a well-lubricated, conical die. *Journal of Applied Polymer Science,* 19**,** 2811-2816.

SHIRAKASHI, M., ITO, H. & JAMES, D. F. 1998. LVD measurement of the flow field in a constant-extensional-rate channel. *Journal of Non-Newtonian Fluid Mechanics,* 74**,** 247-262.

SIGINER, D. A. 2014. *Stability of Non-Linear Constitutive Formulations for Viscoelastic Fluids,* Springer International Publishing.

SIGMA-ALDRICH CO. LLC. 2012. *Silica, fumed: Product information* [Online]. Available: http://www.sigmaaldrich.com/content/dam/sigma-aldrich/docs/Sigma/Product_Information_Sheet/1/s5130pis.pdf [Accessed 02/2017].

SIGMA-ALDRICH CO. LLC. 2017. *181986 Aldrich, Poly(ethylene oxide), average Mv 100,000, powder* [Online]. Available: http://www.sigmaaldrich.com/catalog/product/aldrich/181986?lang=en&region=GB [Accessed 02/2017].

SNELLING, G. R. & LONTZ, J. F. 1960. Mechanism of lubricant-extrusion of teflon tfe-tetrafluoroethylene resins. *Journal of Applied Polymer Science,* 3**,** 257-265.

SOLTEX INC. 2016. *Acetylene Black -01* [Online]. Available: http://soltexinc.com/wp-content/uploads/2016/10/TDS_AB-01-FINAL.pdf [Accessed 02/2017].

SOULAGES, J., MCKINLEY, G., HALL, N., MAGEE, K., CHAMITOFF, G. & FINCKE, E. 2010. Extensional Properties of a Dilute Polymer Solution Following Preshear in Microgravity. *Earth and Space 2010.* American Society of Civil Engineers.

SOULAGES, J., SCHWEIZER, T., VENERUS, D. C., HOSTETTLER, J., METTLER, F., KRÖGER, M. & ÖTTINGER, H. C. 2008a. Lubricated optical rheometer for the study of two-dimensional complex flows of polymer melts. *Journal of Non-Newtonian Fluid Mechanics,* 150**,** 43-55.

SOULAGES, J., SCHWEIZER, T., VENERUS, D. C., KRÖGER, M. & ÖTTINGER, H. C. 2008b. Lubricated cross-slot flow of a low density polyethylene melt. *Journal of Non-Newtonian Fluid Mechanics,* 154**,** 52-64.

SOUSA, P. C., PINHO, F. T., OLIVEIRA, M. S. N. & ALVES, M. A. 2010. Efficient microfluidic rectifiers for viscoelastic fluid flow. *Journal of Non-Newtonian Fluid Mechanics,* 165**,** 652-671.

SPERLING, R. A. & PARAK, W. J. 2010. Surface modification, functionalization and bioconjugation of colloidal inorganic nanoparticles. *Philosophical Transactions of the Royal Society A: Mathematical, Physical and Engineering Sciences,* 368**,** 1333-1383.

STEINHAUS, B., SHEN, A. Q. & SURESHKUMAR, R. 2007. Dynamics of viscoelastic fluid filaments in microfluidic devices. *Physics of Fluids,* 19**,** 073103.

SULTANOVA, N., KASAROVA, S. & NIKOLOV, I. Dispersion Properties of Optical Polymers. *In:* JELENKOVIC, B. & STRINIC, A., eds. International School and Conference on Photonics, PHOTONICA09, August 24–28 2009 Belgrade, Serbia. Warsaw: Polish Academy of Sciences Institute of Physics, 585-587.

TA INSTRUMENTS. 2013a. *AAN009 Application of Rheology of Polymers* [Online]. Available: http://www.tainstruments.com/pdf/literature/AAN009e_Application_of_Rheology_to_Polymers.pdf [Accessed 09/2016].

TA INSTRUMENTS. 2013b. *AAN016 Understanding Rheology of Structured Fluids* [Online]. Available: http://www.tainstruments.com/pdf/literature/AAN016_V1_U_StructFluids.pdf [Accessed 08/2017].

TA INSTRUMENTS 2016. TA Instruments TRIOS v4.1.031739. New Castle, Delaware.

TALBOTT, W. H. & GODDARD, J. D. 1979. Streaming birefringence in extensional flow of polymer solutions. *Rheologica Acta,* 18**,** 505-517.

TAYLOR, G. I. 1934. The Formation of Emulsions in Definable Fields of Flow. *Proceedings of the Royal Society of London. Series A,* 146**,** 501.

THE UNIVERSITY OF QUEENSLAND. 2013. *The Pitch Drop Experiment* [Online]. Available: http://smp.uq.edu.au/content/pitch-drop-experiment [Accessed 10/2013].

THERMO FISHER SCIENTIFIC. 2015. *HAAKE™ CaBER™ 1 Capillary Breakup Extensional Rheometer* [Online]. Available: https://www.thermofisher.com/order/catalog/product/398-0001 [Accessed 09/2016].

THERMOHAAKE. 2001. *Online Melt Rheometer* [Online]. Available: http://www.mcik.co.kr/pdf/productpdf_11559.pdf [Accessed 9/2016].

TIAN, G., WANG, M., WANG, X. & JIN, G. 2016. Flow between eccentric cylinders: a shear-extensional controllable flow. *Korea-Australia Rheology Journal,* 28**,** 139-148.

TING, R. Y. & HUNSTON, D. L. 1977. Some limitations on the detection of high elongational stress effects in dilute polymer solutions. *Journal of Applied Polymer Science,* 21**,** 1825-1833.

TOH, H. S., BATCHELOR-MCAULEY, C., TSCHULIK, K. & COMPTON, R. G. 2014. Chemical interactions between silver nanoparticles and thiols: a comparison of mercaptohexanol against cysteine. *Science China Chemistry,* 57**,** 1199-1210.

TORRES, M. D., HALLMARK, B. & WILSON, D. I. 2014. Effect of concentration on shear and extensional rheology of guar gum solutions. *Food Hydrocolloids,* 40**,** 85-95.

TREBBIN, M., STEINHAUSER, D., PERLICH, J., BUFFET, A., ROTH, S. V., ZIMMERMANN, W., THIELE, J. & FÖRSTER, S. 2013. Anisotropic particles align perpendicular to the flow direction in narrow microchannels. *Proceedings of the National Academy of Sciences,* 110**,** 6706-6711.

TROPEA, C., YARIN, A. L. & FOSS, J. F. 2007. *Springer Handbook of Experimental Fluid Mechanics,* Berlin Heidelberg, Springer.

TROUTON, F. T. 1906. On the Coefficient of Viscous Traction and Its Relation to that of Viscosity. *Proceedings of the Royal Society of London. Series A,* 77**,** 426.

VAN AKEN, J. A. & JANESCHITZ-KRIEGL, H. 1980. New apparatus for the simultaneous measurement of stresses and flow birefringence in biaxial extension of polymer melts. *Rheologica Acta,* 19**,** 744-752.

VAN AKEN, J. A. & JANESCHITZ-KRIEGL, H. 1981. Simultaneous measurement of transient stress and flow birefringence in one-sided compression (biaxial extension) of a polymer melt. *Rheologica Acta,* 20**,** 419-432.

VAN HORN, B. L. & WINTER, H. H. 2000. Dynamics of shear aligning of nematic liquid crystal monodomains. *Rheologica Acta,* 39**,** 294-300.

VENERUS, D., GUADARRAMA-MEDINA, T. & SHIU, T.-Y. 2008. A Continuous Lubricated Squeezing Flow Technique to Study the Rheological Behavior of Polymer Melts in Equibiaxial Elongational Flow. *AIP Conference Proceedings,* 1027**,** 1183-1185.

VENERUS, D. C., SHIU, T.-Y., KASHYAP, T. & HOSTTETLER, J. 2010. Continuous lubricated squeezing flow: A novel technique for equibiaxial elongational viscosity measurements on polymer melts. *Journal of Rheology,* 54**,** 1083-1095.

VENOHR, H., FRAAIJE, V., STRUNK, H. & BORCHARD, W. 1998. Static and dynamic light scattering from aqueous poly(ethylene oxide) solutions. *European Polymer Journal,* 34**,** 723-732.

VISSMANN, K. & BEWERSDORFF, H.-W. 1990. The influence of pre-shearing on the elongational behaviour of dilute polymer and surfactant solutions. *Journal of Non-Newtonian Fluid Mechanics,* 34**,** 289-317.

WANG, B., LIANG, W., GUO, Z. & LIU, W. 2015. Biomimetic super-lyophobic and super-lyophilic materials applied for oil/water separation: a new strategy beyond nature. *Chemical Society Reviews,* 44**,** 336-361.

WANG, J. & JAMES, D. F. 2011. Lubricated extensional flow of viscoelastic fluids in a convergent microchannel. *Journal of Rheology,* 55**,** 1103-1126.

WANG, J., JAMES, D. F. & GÜNTHER, A. 2010. Microfluidic Lubricated Extensional Flow of Viscoelastic Fluids. *In:* VERPOORTE, S., ANDERSSON-SVAHN, H., EMNÉUS, J. & PAMME, N. (eds.) *μTAS 2010 14th International Conference on Miniaturized Systems for Chemistry and Life Sciences, 3 - 7 October.* Groningen, The Netherlands.

WANG, J. M. D. A. J. 2013. *Melt Rheology and its Applications in the Plastics Industry,* Dordrecht, Springer Netherlands.

WANG, Z., ELIMELECH, M. & LIN, S. 2016. Environmental Applications of Interfacial Materials with Special Wettability. *Environmental Science & Technology,* 50**,** 2132-2150.

WHORLOW, R. W. 1992. *Rheological Techniques,* New York, Ellis Horwood.

WIEDERSEINER, S., ANDREINI, N., EPELY-CHAUVIN, G. & ANCEY, C. 2011. Refractive-index and density matching in concentrated particle suspensions: a review. *Experiments in Fluids,* 50**,** 1183-1206.

WIKLUND, J. & STADING, M. 2008. Application of in-line ultrasound Doppler-based UVP–PD rheometry method to concentrated model and industrial suspensions. *Flow Measurement and Instrumentation,* 19**,** 171-179.

WILLIAMS, P. R. & WILLIAMS, R. W. 1985. On the planar extensional viscosity of mobile liquids. *Journal of Non-Newtonian Fluid Mechanics,* 19**,** 53-80.

WINTER, H. H., MACOSKO, C. W. & BENNETT, K. E. 1979. Orthogonal stagnation flow, a framework for steady extensional flow experiments. *Rheologica Acta,* 18**,** 323-334.

WUNDERLICH, A. M. & JAMES, D. F. 1987. Extensional flow resistance of dilute polyacrylamide and surfactant solutions. *Rheologica Acta,* 26**,** 522-531.

XPANSION INSTRUMENTS. 2014. *SER Universal Testing Platform* [Online]. Available: http://www.xinst.com/products.htm [Accessed 9/2016].

XUE, Z., CAO, Y., LIU, N., FENG, L. & JIANG, L. 2014. Special wettable materials for oil/water separation. *Journal of Materials Chemistry A,* 2**,** 2445-2460.

XUE, Z., WANG, S., LIN, L., CHEN, L., LIU, M., FENG, L. & JIANG, L. 2011. A Novel Superhydrophilic and Underwater Superoleophobic Hydrogel-Coated Mesh for Oil/Water Separation. *Advanced Materials,* 23**,** 4270-4273.

YANG, J., ZHANG, Z., XU, X., ZHU, X., MEN, X. & ZHOU, X. 2012. Superhydrophilic-superoleophobic coatings. *Journal of Materials Chemistry,* 22**,** 2834-2837.

YOON, H., NA, S.-H., CHOI, J.-Y., LATTHE, S. S., SWIHART, M. T., AL-DEYAB, S. S. & YOON, S. S. 2014. Gravity-Driven Hybrid Membrane for Oleophobic–Superhydrophilic Oil–Water Separation and Water Purification by Graphene. *Langmuir,* 30**,** 11761-11769.

YOUNG, M. 1989. The pinhole camera: Imaging without lenses or mirrors. *The Physics Teacher,* 27**,** 648-655.

YOUNGBLOOD, J. P. 2014. *RE: Discontinuation of Zonyl FSN-100.*

YU, Y., CHEN, H., LIU, Y., CRAIG, V. S. J. & LAI, Z. 2016. Selective separation of oil and water with mesh membranes by capillarity. *Advances in Colloid and Interface Science,* 235**,** 46-55.

YZIQUEL, F., CARREAU, J. P. & TANGUY, A. P. 1999. Non-linear viscoelastic behavior of fumed silica suspensions. *Rheologica Acta,* 38**,** 14-25.

ZAHORSKI, S. 1992. The converging flow rheometer reconsidered: an example of flow with dominating extension. *Journal of Non-Newtonian Fluid Mechanics,* 41**,** 309-322.

ZHANG, G.-D., WU, J.-R., TANG, L.-C., LI, J.-Y., LAI, G.-Q. & ZHONG, M.-Q. 2014. Rheological behaviors of fumed silica/low molecular weight hydroxyl silicone oil. *Journal of Applied Polymer Science,* 131**,** 40722 (1 of 5) - 40722 (5 of 5).

ZHANG, Z. & EISELE, K. 1995. Off-axis alignment of an LDA-probe and the effect of astigmatism on measurements. *Experiments in Fluids,* 19**,** 89-94.

ZHMUD, B. 2014. Viscosity Blending Equations. *Lube Magazine,* 121**,** 22-27 (Available also at: http://www.lube-media.com/documents/contribute/Lube-Tech093-ViscosityBlendingEquations.pdf [Accessed 01/2017]).

ZHU, H. & GUO, Z. 2016. Understanding the Separations of Oil/Water Mixtures from Immiscible to Emulsions on Super-wettable Surfaces. *Journal of Bionic Engineering,* 13**,** 1-29.

ZHU, Y., WANG, D., JIANG, L. & JIN, J. 2014. Recent progress in developing advanced membranes for emulsified oil/water separation. *NPG Asia Mater,* 6**,** e101.

Appendix.

Raw data and summary of flow experiments performed.

Appendix: Raw data and summary of flow experiments performed.

On the following pages is table A.1, which details the organisation of the compressed data repository archive for this work (located at 10.15131/shef.data.5306578) along with additional experimental parameters; and figure A.2, which summarises the data processing workflow as developed in chapter 8 for the main experiments performed. Table A.1 also serves as a summary of all the main velocity profiling experimental work with every run and imaging location used listed.

As shown in table A.1, the archive is split into 6 folders. These folders contain data for the oblique imaging attempt ("Oblique"), Newtonian verification work ("Verification"), the three main experimental runs performed ("Run 1", "Run 2", and "Run 3"), and finally a folder with ancillary videos of experiment operation ("Videos"). Note that in contradiction to the coordinate system visible in figure 8.8, in all data in the repository increasing pixel or mm position values correspond to running from the aqueous to the oil phase, or from an upstream to a downstream location. Lens positional information is referenced differently due to the orientation of readout devices used.

For the oblique imaging attempt, there are two files per imaging location: interface.csv files and track.csv files. Each pair of files is taken at different lens positions, scanning vertically across the channel at a fixed lateral location as specified in table A.1. These files were used to create figure 8.2. The interface files contain fluorescence intensity information extracted from a vertical strip running down a fluorescence frame. The track files contain the position and velocity of manually tracked tracer particles extracted across a number of imagery frames. Unlike the main experimental data, this velocity data has not been rotated to coincide with the interface, however at the lateral location used the interface was essentially horizontal.

For the verification and main experimental run data, there are three types of file per imaging location: .b16, .dat, and .csv files. The numbers in front of the file names relate to the lateral imaging location. Following the workflow summarised in figure A.2, the position information for each data set is given in table A.1, along with data such as temperatures and the interframing times used. Once the interface position was identified from fluorescence the PIV images are filtered, stacked, and rotated to produce a horizontal interface. The .b16 image files were the output of this process. These files can be read with the software for the camera from PCO (PCO AG, 2017). Alternatively, these files may be read by loading them as unsigned 16 bit little endian values , removing the first 512 values, then parsing the remaining data into an array corresponding to the image size (1600 x by 2400 y pixels – containing both frames of the

image pair, one above the other). Whilst when loaded with the PCO software a saturated pixel has a brightness of 16383, a saturated pixel read in via this manner has a value of 65532. These stacked images were then fed into the PIV software for cross correlation, which then yielded the .dat vector files. The important parameters within these files are the ix and iy parameters (pixel position of each vector), dx and dy (pixel displacements of each vector), and the flag parameter, which for vectors that pass the criterion in table 8.2 has a value of 3. These files were then fed into a custom LabVIEW script, converting pixel to spatial shifts with the lengthscale conversion ratio stated in chapter 8. This script sorted vectors by Y coordinate location, conducted standard deviation filtering against velocity for each Y coordinate, revaluated the new mean velocities, corrected the interface position previously aligned from fluorescence by aiming for zero apparent slip (in an iterative manner), excluded pixels near the edge of frames and within a specified margin of the interface, applied velocity profile spline curve fitting, and measured velocity gradients at interface, providing phase shear rates as well as an estimation of extension rates. The .csv files provide data relating to this process, "0px" files are feature application of a zero pixel exclusion margin, and "30px" files a 30 pixel margin. The first two columns in these files provide standard deviation filtered raw data, sorted by Y location. The second two columns provides the mean velocity values from this at each Y location. The next four columns then provide the fitted spline curves points for the oil and aqueous phases.

Within the mean values, a set of 6 "phantom" data points were added, for the Run 1/49velocityprofiles30px.csv data file, these are in rows 68 – 73 of the csv file, ending up on rows 5 – 7 of the oil phase and 68 – 70 of the aqueous phase. These data points are arbitrarily assigned velocities of 0.05m/s, however they are also assigned 1×10^{-10} weighting in the spline curve fit, rather than 1 as applied to all other data points. These points, three per phase and shown in figure A.1 as displayed onscreen, serve to extrapolate the spline curve up to the location of the interface, especially when a pixel exclusion margin is applied to the dataset.

From this group of three data points the velocity gradient, and thus shear rate, was then determined for each phase, and finally thus the shear rate ratio between the two phases. These results are reported at the top of the csv files. In addition the smoothing parameters used for each particular data set are reported (for shear rate determination - pixels excluded either side of interface, standard deviation filtering, balance and smoothing parameters for the spline fit), interface iteration information (final iterated position and apparent slip velocity achieved), the estimated extension rate based on data within this imaging location, the interframe time delay used, and the velocity of the interface (used for determining timescales

between imaging locations, e.g. in figure 8.25). In some cases the apparent slip velocity could not be iterated to below the target threshold chosen of 5×10^{-6} m/s due to data points transitioning either side of the interface location between iterative steps. Representative result pairs for such data sets are denoted A (-ve slip velocity) and B (+ve slip velocity). Average results between these conditions have generally been used, except for instances when large differences were apparent. In this case, the most consistent solution to other surrounding data was used – invariably denoted by the non-filled symbols in figures 8.23 and 8.24.
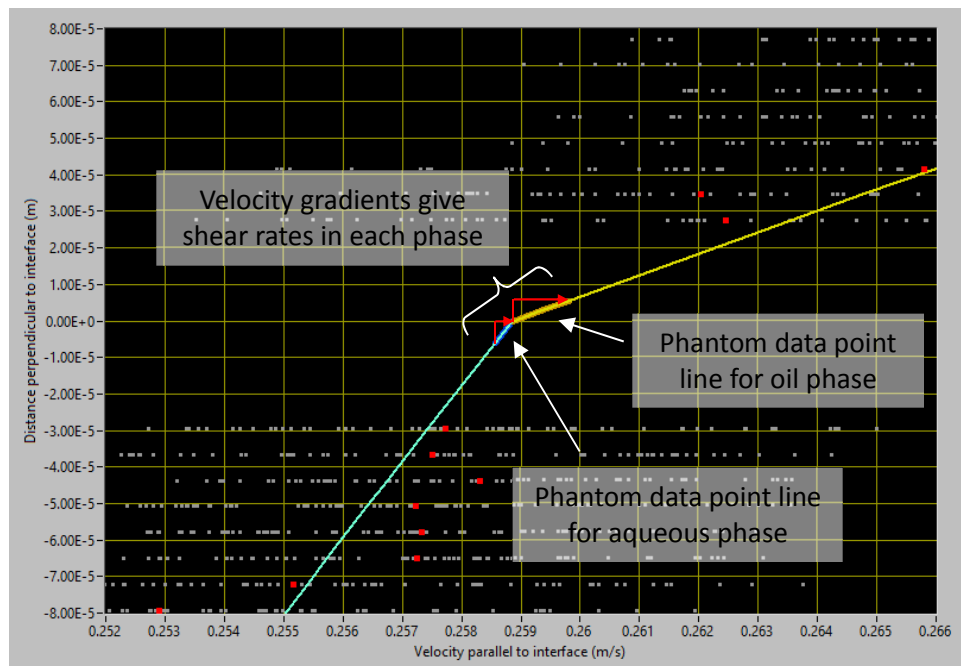

Figure A.1: LabVIEW screenshot highlighting the use of phantom points in the spline curve fits to extrapolate the curves to the location of the interface

(here shown for Run 1/29velocityprofiles30px.csv)

For the purposes of reproducing the spline curve fits used in this work, the NI_AALPro.lvlib:Cubic Spline Fit.vi function in LabVIEW was used. Data was fed in to the function with Y values as velocity parallel to the interface (m/s), X values as distance perpendicular to the interface (m) temporarily shifted by x10,000 (similar order of magnitudes assisting fitting). Weighting values of 1 for each data point were set (except for the phantom points), a smoothness value as specified for the work, and a consistent balance parameter of 0.9 (chosen as it generally appeared successful).

Finally, there are three videos in the data repository. These videos are intended to illustrate the flow stability, and partly, to serve for posterity. "View 1.3gp" and "View 2.3gp" provide two different views of the cell under the same flow conditions utilising the PEO test solution and silicone oil, with the laser running but at a reduced repetition rate compared to the 8Hz used

278

for recording work. "Outflow for run 2.mpeg1" is a time lapse sequence looking at the channel expansion region during the entirety of run 2. This is a recording from the same camera as used for remotely monitoring the interface position / outlet flow balance. The apparent instability of the interface at the start of the video is at flow start-up whilst the correct flow balance is adjusted for and finally achieved. Balance adjustments are also occasionally performed in between taking data sets. Noteworthy observations are the oil droplets caught in the aqueous phase streaming out of the cell just after flow is initiated. These droplets are due to fluid of the wrong phase being trapped in the gap between the hyperbolic inserts and the glass walls whilst the experiment is stationary. The formation of these droplets however ceases after a short period and were not considered detrimental. Various moving concentrations of black detritus can also be seen during this period, which is in fact sedimented groups of seeding particles being swept out of the cell. Towards the end of the video, the microscope lens comes into view as imaging locations are conducted further down the channel. After this, amongst other things two fluorescence sweeps across the horizontal width of the cell near the contraction apex can be seen being conducted (~9:22PM). These are for symmetry confirmation in each run at this critical location, as noted in chapter 8. As the video also shows, in hindsight the moveable outlet flow splitter was of minimal use in these experiments.

Folder / file in repository	Lens lateral position (mm) 0 = Centre of contraction (+) 87.35 = Far left edge of viewing window	Lens height position DTI (mm) (+) 2.60 = Lower wall at centre of contraction 0 = Upper wall at centre of contraction	Horizontal (imaging) position (mm) 0 = Channel centerline -ve = towards lens side of cell	Inter-frame time (µs)	Aqueous inlet, oil inlet (°C) Aqueous outlet, oil outlet (°C)	Oil (reference) phase composition	Aqueous (test) phase composition	Significance of data set
Oblique/0_0…		0.0						
Oblique/0_4…		0.4						
Oblique/0_8…		0.8						Oblique imaging test experiment – Manually tracked particle data. Lens height values are approximate only for reasons previously described.
Oblique/1_2…	15.00	1.2	0	100.00	Not recorded	44.30wt% Synesstic 5 / Elite 65 oil blend	4×10^6MW PEO 1.2wt% aqueous solution	
Oblique/1_6…		1.6						
Oblique/2_0…		2.0						
Oblique/2_4…		2.4						
Oblique/2_8…		2.8						
Verification/30A…		0.643	1.5		22.2, 22.5, 22.2, 22.7			
Verification/30B…	29.98	0.443	0	14.84				
Verification/30C…		0.239	-1.5				53.553wt% glycerol - water aqueous solution (subject to RI adjustments)	Perpendicular imaging Newtonian validation experiment: Scanning at three lateral locations down the channel and checking the horizontal flow symmetry.
Verification/17_5A…		1.017	1.5		22.4, 22.8, 22.4, 22.9	Allcosil 200-50 silicone oil		
Verification/17_5B…	17.46	0.839	0	9.48				
Verification/17_5C…		0.757	-1.5					
Verification/5A…		1.172	1.5		22.3, 22.6, 22.2, 22.6			
Verification/5B…	4.93	1.177	0	7.00				
Verification/5C…		1.075	-1.5					

Run 1/49…	49.07	-1.32		115.00				
Run 1/42…	42.06	0.47		46.60				
Run 1/29…	29.01	1.41		20.36				
Run 1/16…	15.97	1.48	0	13.00	22.6, 22.8, 22.5, 22.7			Perpendicular imaging main experiment: run 1
Run 1/3…	2.98	1.48		9.60				
Run 1/m7…	-7.06	1.38		10.40				
Run 1/m14…	-14.20	1.34		12.40				
Run 1/m23…	-23.10	1.23		17.00				
Run 2/49…	48.96	-1.08		111.68			4×10^{6} MW PEO 1.2wt% dissolved in 52.81wt% glycerol - water aqueous solution (subject to RI adjustments)	
Run 2/42…	41.97	0.44		46.60				
Run 2/29…	28.97	1.42		20.36				
Run 2/16…	15.97	1.47		13.00				
Run 2/3…	2.91	1.46	0	9.60	22.5, 22.7, 22.4, 22.7	Allcosil 200-50 silicone oil		Perpendicular imaging main experiment: run 2
Run 2/m7…	-7.21	1.36		10.40				
Run 2/m14…	-14.16	1.31		12.40				
Run 2/m21…	-21.10	1.23		15.08				
Run 2/m28…	-28.17	1.09		19.48				
Run 3/47…	46.99	-0.48		111.68				
Run 3/42…	41.97	0.51		46.60				
Run 3/29…	29.02	1.35		20.36				
Run 3/16…	16.12	1.46		13.00				
Run 3/3…	2.98	1.41	0	9.60	22.7, 23.0, 22.7, 23.0			Perpendicular imaging main experiment: run 3
Run 3/m7…	-7.10	1.31		10.40				
Run 3/m14…	-14.07	1.32		12.40				
Run 3/m21…	-21.10	1.20		15.08				
Run 3/m24…	-24.10	1.17		17.00				
Run 3/m28…	-28.11	1.07		19.48				
Videos/Outflow for run 2.mpeg1	Timelapse video looking at the channel expansion region during the entirety of run 2 – Fluids as per runs 1 - 3							
Videos/View 1.3gp	Two example videos showing flow through the channel and laser operation – Fluids as per runs 1 - 3							
Videos/View 2.3gp								

Appendix table A.1: Files in compressed data repository archive located at 10.15131/shef.data.5306578: see text for additional information.
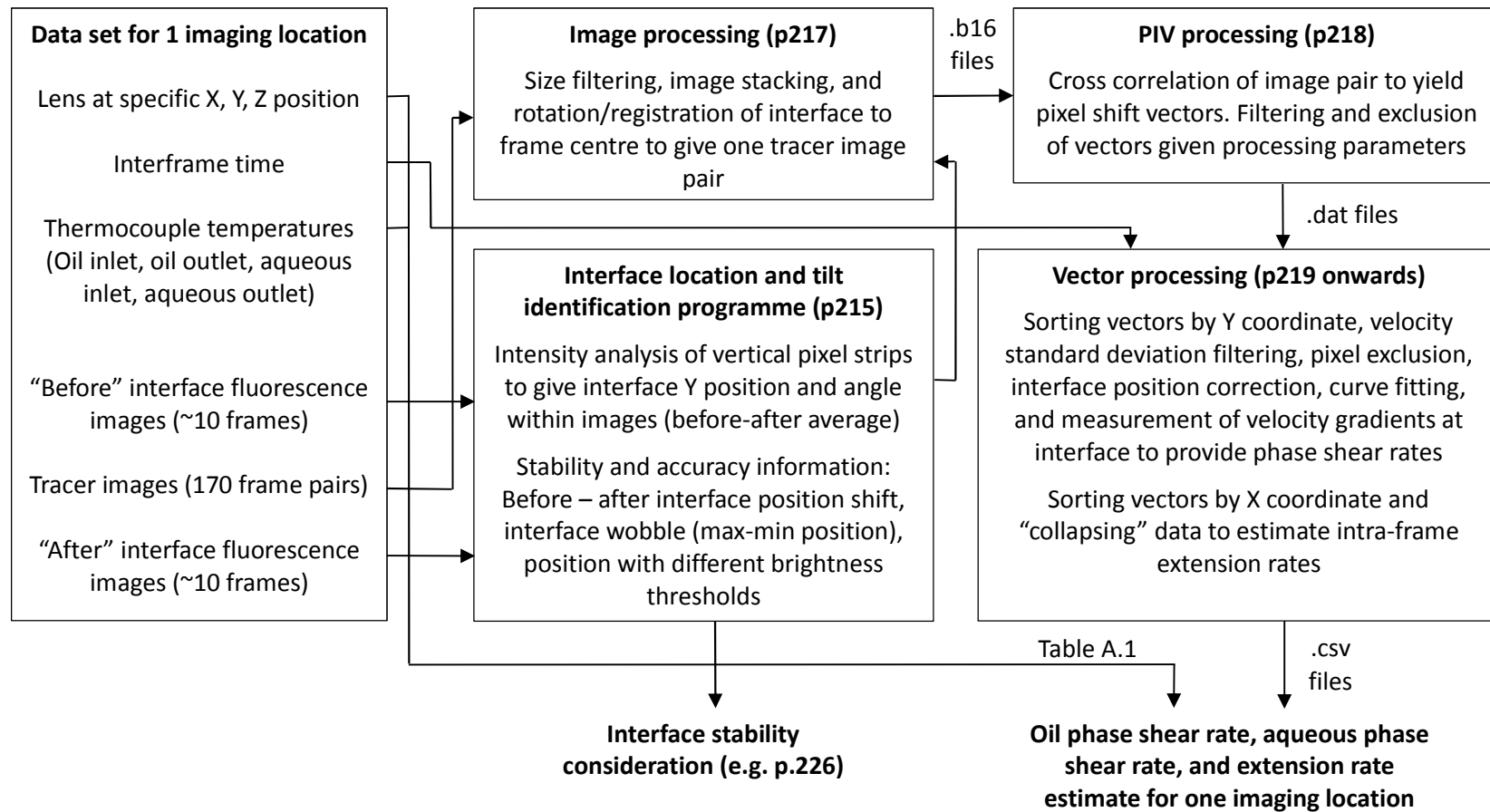
Figure A.2: Summary of the data processing workflow for the Newtonian validation experiment and the three main experimental runs conducted